Technische Universität München
Fakultät für Physik
Nonequilibrium Chemical Physics

Investigation of silicon electrodes functionalized with pyridine for the electrochemical H_2 evolution and CO_2 reduction reaction

Doktorarbeit

Qi Li

März 2019

Technische Universität München
Fakultät für Physik

Investigation of silicon electrodes functionalized with pyridine for the electrochemical H_2 evolution and CO_2 reduction reaction

Qi Li

Vollständiger Abdruck der von der Fakultät für Physik der Technischen Universität München zur Erlangung des akademischen Grades eines Doktors der Naturwissenschaften (Dr. rer. nat.) genehmigten Dissertation.

Vorsitzender:
Prof. Dr. Michael Knap

Prüfende der Dissertation:
1. Prof. Dr. Katharina Krischer
2. Prof. Dr. Christine Papadakis

Die Dissertation wurde am 26. März 2019 bei der Technischen Universität München eingereicht und durch die Fakultät für Physik der Technischen Universität München am 2. Mai 2019 angenommen.

Abstract

Dissolved pyridine has been reported to catalyse or mediate the electrochemical reduction of carbon dioxide in aqueous electrolytes and its conversion to methanol, but the mechanism behind its efficiency improvement of the electrochemical methanol production has not been understood. In order to further determine the positive effect pyridine has on reduction reactions, the electrocatalytic activity of pyridine immobilized on silicon electrodes was investigated with respect to the hydrogen evolution and CO_2 reduction reaction. An electrografting procedure was developed to graft 3-diazopyridine (either in situ generated or as a synthesized diazonium salt) covalently onto a planar, H-terminated n-type silicon electrode, yielding a partial surface coverage of less than a monolayer, as evidenced in XPS measurements in conjunction with EIS measurements. Compared to the initially H-terminated electrodes, the 3-pyridine-terminated silicon electrodes showed a remarkably improved reactivity for the hydrogen evolution reaction. The positive HER onset shift was predicated on the protonation of the grafted pyridine / pyridinium molecules in an acidic electrolyte, as the onset shift vanished in weakly acidic solutions with a pH higher than the $pK_a \approx 5$ of the grafted pyridine layer. In EIS measurements, the grafted 3-pyridine-terminated silicon electrodes exhibited a larger total capacitance compared to an H-terminated electrode in an acidic environment, likewise pointing towards the modification of the electrode|electrolyte interface with a layer of the immobilized, protonated pyridinium molecules. In contrast to the improved reactivity for HER, the grafted 3-pyridine-terminated silicon electrodes showed no improved reactivity for the electrochemical carbon dioxide reduction, as evidenced using product analysis tools such as NMR and gas chromatography established in the thesis, and the faradaic efficiency of the hydrogen production was only slightly improved during the bulk electrolysis in weakly acidic, carbon dioxide saturated electrolytes, diverging from reports of the catalytic or mediative effect of dissolved pyridine on the carbon dioxide reduction to methanol. This non-existent reactivity increase due to the grafted pyridine layer seems to fit into the emergence of a critical view concerning the favourable effects of pyridine on the CO_2 reduction reaction presented in literature.

Zusammenfassung

Die Anwesenheit von gelösten Pyridin in einem wässrigen Elektrolyten hat laut Literaturberichte eine katalytische oder unterstützende Wirkung auf die elektrochemische Kohlenstoffdioxidreduktion. Dabei ist die Art und Weise, wie Pyridin an dieser Reaktion beteiligt ist, bisher nicht bekannt. Um seine Wirkung auf elektrochemische Reaktionen weiter zu beleuchten, wurde in dieser Arbeit den Einfluss von auf der Oberfläche von Siliziumelektroden immobilisierten Pyridinmolekülen auf die elektrochemische H_2- und CO_2-Reduktion untersucht. Eine elektrochemische Graftingprozedur mit 3-Diazopyridin Kationen wurde entwickelt, um Pyridinmoleküle kovalent auf eine wasserstoffterminierte, flache Siliziumoberfläche zu binden. Die so hergestellte Pyridinschicht zeigte in XPS- und EIS-Messungen eine kleinere Bedeckung als eine voll geschlossene Monolage auf der Si-Elektrode. Die 3-Pyridin-terminierte Siliziumelektroden zeigten eine signifikant Verbesserung der Wasserstoffentwicklungsreaktion in sauren Elektrolyten. Die aktivierende Eigenschaft der Pyridinschicht hängt mit der Protonierung von immobilisiertem Pyridin zu Pyridinium ab, da sie in schwach sauren Elektrolyten verschwand, wenn der pH Wert der Lösung über der Säurekonstante für Pyridinium $pK_a \approx 5$ lag. Mit EIS-Messungen konnte gezeigt werden, dass, verglichen mit H-terminierten Siliziumelektroden, Elektroden mit einer gegrafteten 3-Pyridinschicht eine größere Gesamtkapazität über die Silizium|Elektrolyt-Grenzfläche besitzen. Diese Eigenheit hängt ebenso wie die aktivierenden Eigenschaften von der Protonierung der Pyridinschicht ab und deutet auf die Modifikation der Grenzfläche durch die geladenen Oberflächenmoleküle hin. Im Gegensatz zur Wasserstoffentwicklung zeigten die mit 3-Pyridin gegrafteten Siliziumelektroden keine verbesserte Reaktivität im Bezug auf die CO_2-Reduktion. Dieses Resultat für die 3-Pyridinschicht reiht sich ein in die aufkommende Kritik and Zweifel am bisherigen Wissensstand bezüglich der katalytischen Wirkung von Pyridin auf die elektrochemische Kohlestoffdioxidreduktion.

Table of Contents

Chapter 1

Motivation & overview

Carbon dioxide (CO_2) as a greenhouse gas can absorb and emit infrared radiation from the surface of the earth, leading to heat trapping, and thus contributes to the natural greenhouse effect [1], which results in an average surface temperature of 14° C on earth [2]. The rise of anthropogenic CO_2 production has lead to an increase of the CO_2 concentration in the atmosphere to over 410 [3] μmol per mol dry air or parts per million (ppm) in present day from $\approx$ 275 ppm at 1700 before the industrial evolution [4] resulting in global warming. In order to limit and reduce the man-made greenhouse effect and thus to stop the rise of the global temperature, great effort is undertaken to limit the CO_2 output into the atmosphere by several sequestering and filtering methods. The collected CO_2 is then to be "stored" or utilized in carbon capture and storage (CCS) facilities [5–7], effectively removing its additional impact on the "natural" atmospheric carbon cycle, leading to so-called negative CO_2 emission [8, 9].

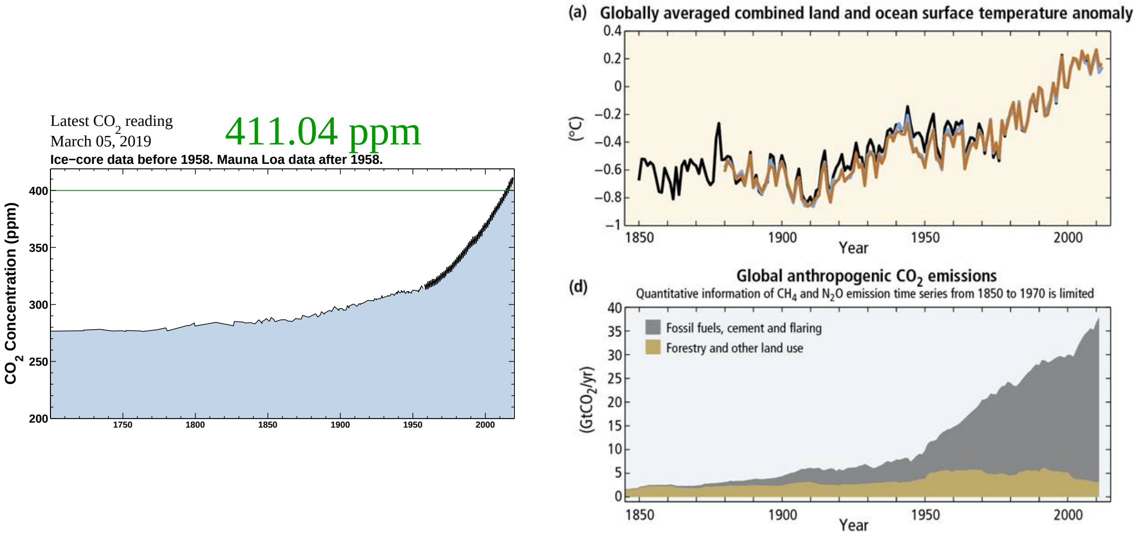

Figure 1.1: Left: Development of the atmospheric CO_2 concentration in ppm from 1700 up to present day. Original figure from [3]. Data comprised of ice measurements from Law Dome, Antarctica [4] and from the Mauna Loa Observatory [10]. Right: (a): rise in averaged combined land and ocean surface temperature anomaly compared to average surface temperature [2]. (b): corresponding rise of the global anthropogenic CO_2 emissions from 1850 to present day. Original figure from [11].

The combustion of hydrocarbons like natural gas, oil/gasoline and coal covers a majority of the energy production worldwide [12], but it also releases huge amounts of carbon dioxide into the atmosphere and continuously depletes the limited fossile resources. Renewable energy generated by wind and sunlight provides sustainable electric energy, but it exhibits strong output fluctuations on multiple time scales (hourly, daily, seasonal). To level these fluctuations, electric energy produced from renewable sources could be converted into chemical energy stored in molecular bonds. These chemical energy storages or chemical batteries can then buffer the energy production of renewable energy sources and the created chemical energy carriers with a comparable energy density per volume (Lower heating value of methanol: 15.6 MJ/L; LHV of gasoline: 34.2 MJ/L [13]) can be used as an alternative energy carrier to gasoline, diesel and natural gas in the transportation and energy sector.

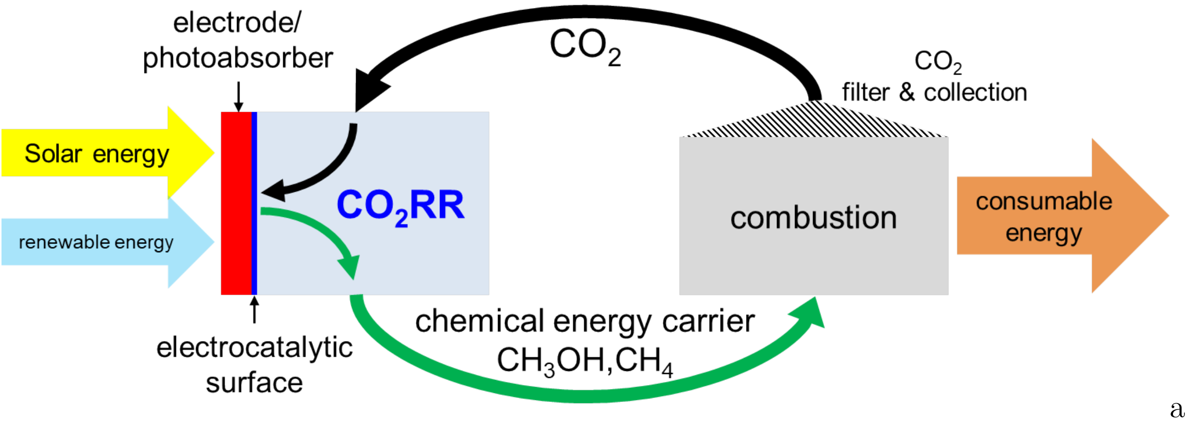

Figure 1.2: Scheme of the artificial CO_2 cycle where the (photo)electrochemical CO_2 reduction reaction (CO_2RR) is used to buffer or store solar and electric energy from renewable sources by forming chemical energy carriers such as methane (CH_4) and methanol (CH_3OH) from CO_2 at the electrode/photoabsorber with a suitable electroactive surface. The carriers can then be used in combustion reactions to be converted into consumable energy (electric, kinetic, thermal). Through filtering the exhaust, the collected CO_2 is again used as feedstock for the CO_2RR, thus closing the cycle.

A way to both create an energy storage with high energy density using renewable electric energy (or directly sunlight) and make use of the sequestered and existing CO_2 feedstock is to develop an efficient (photo)electrochemical process to convert CO_2 (back) to hydrocarbons. These could be natural gases like methane or alcohols like methanol and ethanol. A scheme of such an artificial CO_2 cycle is depicted in figure 1.2. The electrochemical reduction of CO_2 to form these products is possible, but usually suffers from high overpotential needed and "slow/sluggish" kinetics, due to the fact that the molecule itself has a high reduction potential of -1.9 V vs SHE and multiple proton and electron transfer steps are required to produce the desired product molecules [14].

$$\mathrm{CO_2} + 6\mathrm{H}^+ + 6e^- \rightarrow \mathrm{CH_3OH} \quad \mathrm{E_{redox}} = -0.38\,\mathrm{V\,vs\,SHE} \tag{1.1}$$

$$\mathrm{CO_2} + e^- \rightarrow \mathrm{CO_2^-} \quad \mathrm{E_{redox}} = -1.9\,\mathrm{V\,vs\,SHE} \tag{1.2}$$

For the production of methane and ethylene, copper electrodes have shown the highest faradaic efficiencies (FE) for the CO_2 reduction on metal electrodes in an aqueous electrolyte [15, 16], i.e., at a certain applied electrode potential a major part of the reaction current was consumed by the reduction of CO_2 to form the product molecule. Liquid products such as ethanol and methanol were also found as reduction products on copper, but their efficiencies were 10 to 1000 times smaller than for the main reaction products such as methane [16]. Other metal electrodes were often either poisoned or rendered inert by the adsorption of reduction products such as CO on platinum, and only yielded small amounts of product molecules usable for energy storage [17]. This situation prompted the search for an improvement of the CO_2 reduction reaction (CO_2RR) towards its conversion efficiency and selectivity towards energy carrier molecules, especially for liquid reduction products such as methanol.

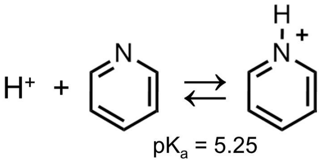

Figure 1.3: Scheme of the pyridine / pyridinium redox pair with its $pK_a = 5.25$ [13, 18].

The first report of pyridine (see fig.1.3) mediated, electrochemical reduction of CO_2 was published in 1993 by Bocarsly et al. [19]. CO_2 reduction on "electrolytically" / electrochemically charged [20], "preloaded" H-terminated palladium (Pd) electrodes with dissolved pyridine was conducted in an unbuffered, weakly acidic electrolyte (0.5 M Na_2SO_4), in which methanol and formaldehyde were detected using mass spectrometry and gas chromatography measurements. The faradaic efficiency (FE) for methanol production at about 30 % was astonishingly high. The authors emphasized the importance of the protonated pyridinium molecule being present during the reduction. At the same bulk pH around 5 they detected no methanol when they replaced pyridine with N-methyl-pyridine in the electrolyte, effectively preventing the protonation of the nitrogen molecule. Additionally, the mild reduction potential i.e. low overpotential during galvanostatic electrolysis measurement of $\approx$ -0.75 V vs SCE or -0.21 V vs RHE (pH 5) was pointed out as a positive feature of the system compared to the high overpotentials usually needed for the reduction reaction. Pd electrodes were known to reduce CO_2 to CO and formic acid [20] albeit at much higher overpotentials (FE_{CO}=15%, FE_{FA}=15%; -1.14 V vs RHE (pH 7)). The same catalytic behaviour was found again on Pt electrodes [21–26] with CO_2 reduction in 0.5 M KCl with 10 mM pyridine producing formic acid ($FE_{FA} \leq 11\%$), formaldehyde and methanol ($FE_{MeOH} \leq 22\%$). The corresponding cyclic voltammogram (CV) in figure 1.4 shows a significant current increase in the cathodic region around -0.7 V vs SCE when pyridine is included in the electrolyte, which was interpreted as an enhancement of the CO_2 reduction.

Methanol as the main product of the reduction reaction of CO_2 on Pt electrodes was up to that point a new and remarkable result, as only CO and formic acid formation had been reported before [28]. Pyridinium was therefore credited as the main reason and a first reaction mechanism was proposed, where neutral pyridinyl radicals as the reduction product of pyridinium homogeneously reduced CO_2 step by step to formic acid, formaldehyde and finally methanol [21]. The electron transfer was proposed to occur after the formation and decomposition of a carbamate zwitterion as a transition state (see right side of fig. 1.5) which was observed in a reaction of pyridine vapor with $(CO_2)_m^-$ clusters via vibrational predissociation spectroscopy [29] and via electrospray

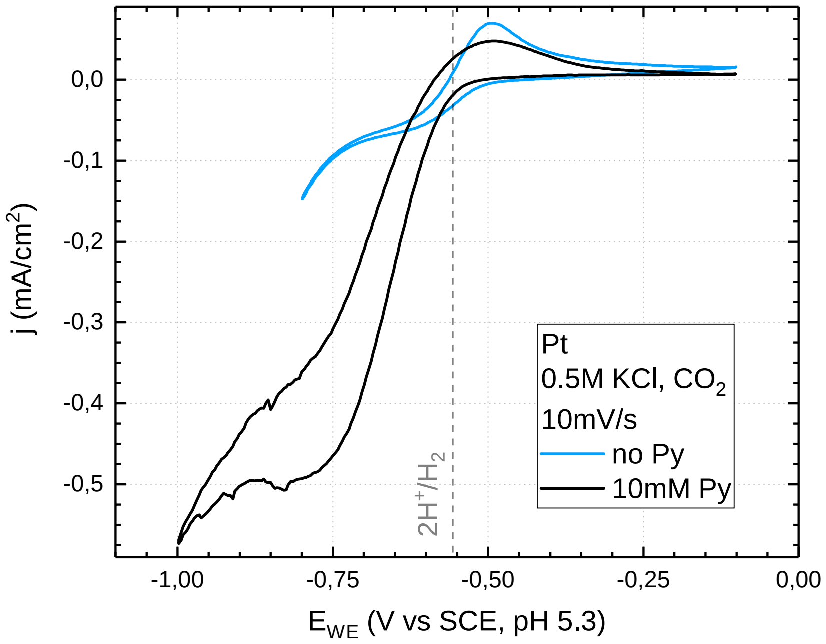

Figure 1.4: Cyclic voltammogram (CV) of CO_2 reduction on a platinum (Pt) electrode in an electrolyte without (blue) and with 10 mM pyridine (black). The grey dashed line indicates the redox potential for $2H^+/H_2$ redox pair in the electrolyte used. Electrolyte: 0.5 M KCl, purged with CO_2 (pH 5.3). Scan rate: 10 mV/s. Data from the master thesis of Andreas Heine [27].

ionization mass spectrometry with photogenerated pyridinyl molecules [30].

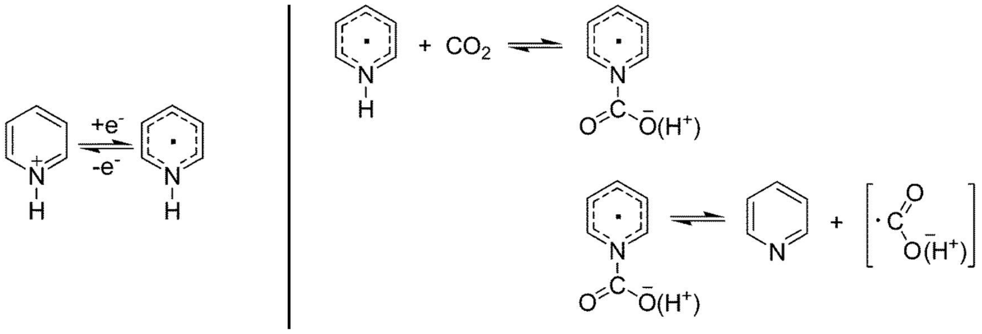

Figure 1.5: Proposed reaction scheme for pyridinium / pyridinyl radical redox pair (left) and for the reduction of CO_2 to formate via the formation of the carbamate intermediate. From [21].

Since then Jaramillo and coworkers detected trace amounts of methanol produced during the CO_2 reduction on Pt in 0.1 M $KHCO_3$ at higher overpotentials of -0.75 V vs RHE [31]. In addition to metal electrodes, (photo)electrochemical CO_2 reduction on semiconducting materials such as p-GaP, p-GaAs, FeS_2, p-$CuInS_2$ and p-CdTe yielded also formic acid and/or methanol [32–38]. As the main characteristic, reduction yields of methanol reached over 90 % in some cases [32,37]. Also, while the faradaic efficiency for CO_2 reduction to methanol on p-GaP was remarkable, p-GaP and p-GaAs electrodes were already known to support the reduction of CO_2 to methanol [39–43] but suffered from photocorrosion [44,45] over extended reduction periods. In summary, the main impact of pyridine on CO_2 reduction at the mentioned (photo)electrodes seems to be the following:

- Increase of faradaic efficiency of reduction products such as methanol on electrodes where CO_2 reduction to methanol is already possible / has been reported.
- Decrease of required overpotential from several hundreds of mV to values close to / near RHE.

From these observations the role of pyridine on the improvement of the CO_2RR to produce methanol seems to be difficult to discern and to separate from the reaction taking place at the electrode without pyridine mediation. At the beginning of this thesis the question arose, if the effect of pyridine on reduction reactions such as CO_2RR can be better distinguished when the reactions are taking place on an otherwise electrochemically less reactive electrode with *immobilized pyridine molecules at its surface.* If pyridine was the reaction center at which the subsequential reduction of CO_2 to methanol occured [21], then immobilizing them on the surface of the electrode should improve the electron transfer onto the pyridinium/pyridyl radical redox pair, which has been reported to be surface sensitive, i.e., dependent on the material of the electrode [46]. Otherwise, if pyridine "only" mediates or interacts as an stabilizing agent for the CO_2RR at the surface, the immobilization of the pyridine molecules at the electrode|electrolyte interface should likewise have a positive effect on the overall reduction reaction.

In this thesis crystalline silicon (Si) was chosen as an electrochemically rather inactive electrode or, possibly, photoelectrode. The crystal orientation of Si(111) was selected, since electrodes with that orientation can be etched to achieve an atomically flat, hydrogen terminated (H-terminated) surface [47]. Hydrogen evolution on H-terminated silicon electrodes requires large overpotentials of ≈ -0.7 V vs SHE [47–49] while the reduction of CO_2 is reported to only yield formic acid and small amounts of methane [50–53]. If immobilized pyridine could improve the reactivity of silicon electrodes for reduction reactions such as CO_2RR, then modified p-type silicon photoelectrodes could (at least partially) drive the reduction reaction using solar illumination, as the bandgap of silicon $E_\mathrm{g} = 1.12$ eV matches the spectrum of sunlight very well, leading to a theoretical solar-to-electric energy conversion efficiency of over 30 % [1,54,55]. Even photoelectrochemical CO_2 reduction fully driven by illumination could be considered using multi-junction cells, as such cells have already been used for the photoelectrochemical water splitting totally driven by sunlight [56]. These kind of tightly integrated photo-driven catalytic devices are predicted to rival and even surpass separated photovoltaic / electrolysis systems in production costs for hydrogen production. Amongst the reasons, integrated photoelectrochemical hydrogen evolution systems have shown a slightly increased efficiency, because the kinetics of the reaction improved with higher temperature due to the radiative heating of the photoelectrochemical cell [57].

Numerous surface modification methods for functionalizing a silicon surface with organic molecules have been reported [58] with the goal of achieving the controlled formation of a monolayer of immobilized molecules directly bound to the silicon surface via Si-C bonds, leading to rigid, self-assembled monolayers (SAMs).

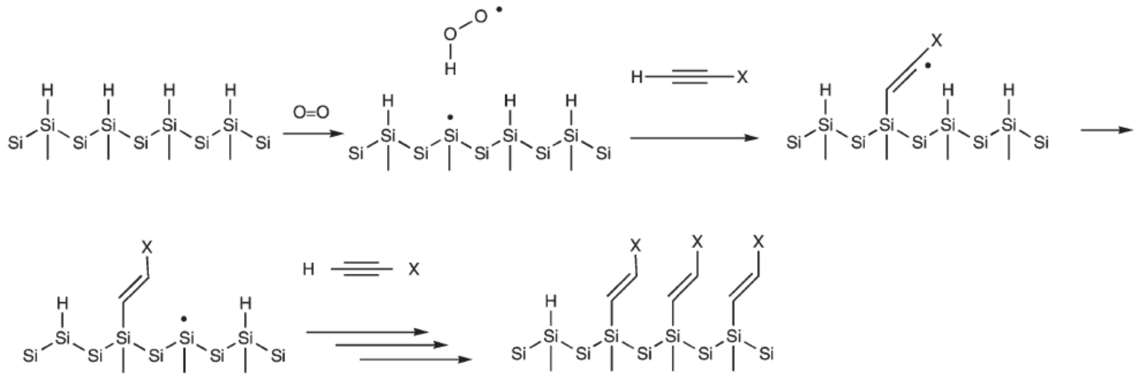

Figure 1.6: Schematic reaction scheme for the hydrosilylation of an H-terminated silicon surface with ethyl-X molecules and its autocatalytic formation of Si-C bonds between the molecules and the silicon surface. Here, X=pyridine [59, 60]. Original figure from [61].

In prior collaborations with the WACKER chair of molecular chemistry (Technical University Munich, Chemistry Dept.) and AK Wintterlin (Ludwig-Maximilians-Universität, Chemistry Dept.), hydrosilylation (as seen in figure 1.6) of ethyl- and vinylpyridine was used to functionalize H-terminated silicon surfaces, but the resulting pyridine layer was believed to partially consist of several monolayers, as the radicalized ethyl- and vinylpyridine intermediates could form a polymer [59, 60]. Electrochemical measurements of such modified silicon samples were inconclusive as to the overall effect of such a functionalized pyridine layer. In order to gain more control on the functionalization process, the electrochemical grafting of diazonium molecules (Ar-N_2^+ [62]) was considered as an alternative surface modification method in this thesis [63].

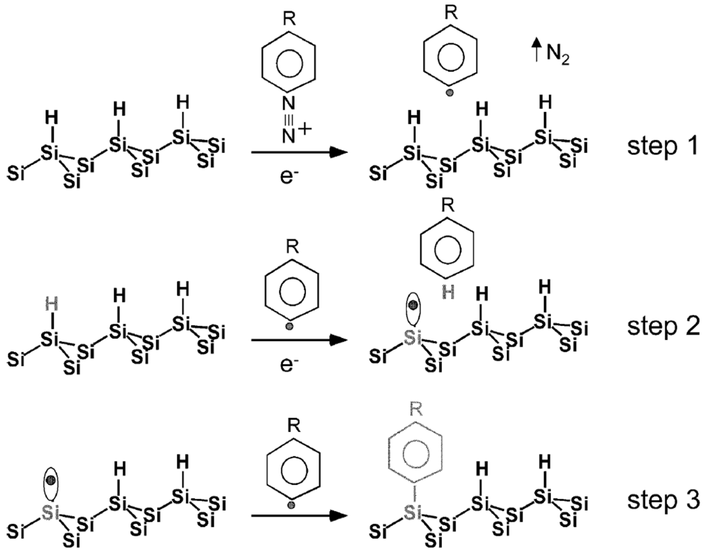

Figure 1.7: Model for the formation of a phenyl-R layer on an H-terminated Si (111) surface by electrochemical reduction of an aryl-diazonium salt Ph-Ar-N_2^+. Original figure from [64].

As shown on figure 1.7, the reduction of the diazo group -N_2^+ (step 1) leads to the electrochemically controlled production of radical molecules, which then attack (step 2) and subsequently bind with the silicon surface (step 3). In addition to the prospect of a higher degree of control of the process via control of the applied potential, a *direct* Si-C bond is formed between the grafted molecule and the surface, leading to a minimal distance of the fixed molecule to a surface, where it typically does not adsorb to. Allongue and coworkers successfully grafted 4-bromobenzene and 4-nitrobenzene diazonium onto H-terminated silicon (111) surfaces to achieve closed monolayers as determined by X-ray photospectroscopy (XPS) and Rutherford backscattering (RBS) measurements [65–67]. Because of the similar sizes of pyridine and benzene, it was believed that a similar grafting procedure with some kind of a pyridine diazonium would yield closed SAM of immobilized pyridine molecules directly bound to the silicon surface.

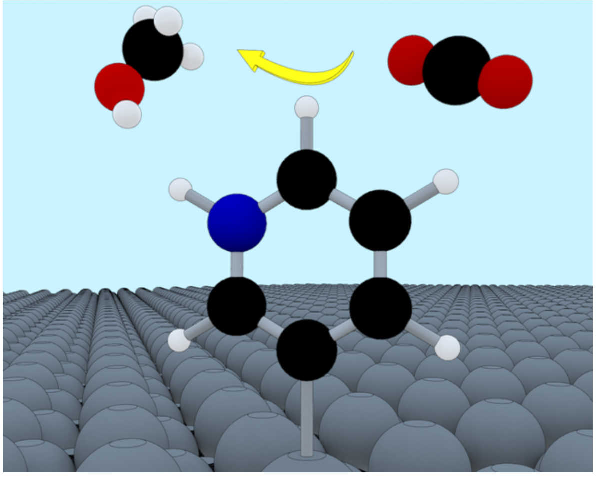

Figure 1.8: Illustration of a grafted 3-pyridinium molecule on Si (111) surface with the suggested conversion of a CO_2 molecule to CH_3OH in an aqueous electrolyte.

The goal of this thesis is to investigate the effect of a functionalized layer of pyridine molecules as a reported electrocatalytic molecule on an otherwise electrochemically inert silicon electrode for the hydrogen evolution and CO_2 reduction reaction, as illustrated in figure 1.8. This task was divided into the following steps:

- First, a functionalization method was developed, in which pyridine was immobilized on the silicon surface by electrografting. The functionalized surface was characterized using XPS measurements.
- Then, the modified silicon electrodes were electrochemically characterized. Thereby they showed a remarkable, improved reactivity for the hydrogen evolution reaction (HER) in acidic electrolytes.
- The final goal of the presented electrochemical experiment was to investigate the electrochemical reduction of CO_2 on the modified silicon electrodes, including a complete analysis of its reaction products. With these studies, the question can be answered, if the heterogeneous catalysis of CO_2 reduction using bound pyridine instead of homogeneous catalysis using dissolved pyridine is possible.

During the duration for the thesis, three bachelor thesis and one master thesis were completed under the partial supervision of the author [27, 68–70]; results from these works are included in the thesis.

Chapter 2

Theoretical background

2.1 Electrochemistry

A brief overview of the basics of the electrochemical experiments described in this thesis is given here. It is mainly based on [1,71,72]. Generally, an electrochemical experiment similar to the ones described in this thesis is conducted at the interface of a metal or semiconductor *electrode* and a conducting *solution* or *electrolyte* (| denotes a phase boundary, here solid|liquid). Reduction or oxidation of electrolyte components in the vicinity of the electrode or of the electrode itself can be driven by a potential gradient across the electrode|solution interface, which leads to an electron transfer across the interface. One refers to a cathodic reaction or current if the electrode emits electrons and an anodic reaction or current if the electrode accepts electrons, i.e.,

$$\text{cathodic reaction or reduction of species A: A} + \text{e}^- \rightarrow \text{A}^-$$

$$\text{anodic reaction or oxidation of species B: B} \rightarrow \text{B}^+ + \text{e}^-$$

Usually, one is not interested in reactions with the solvent, but with dissolved species, which may carry with them a shell of inert solvent molecules.

2.1.1 Measuring potentials

One can distinguish two potentials of a phase 'α'. The *outer* potential or *Volta* potential ψ_α represents the work required to bring a point charge from vacuum to just outside the phase 'α', distant enough to avoid image interactions with the phase boundary (about 0.1 - 10 μm). The *inner* potential or *Galvani* potential ϕ_α is the the work needed to bring the point charge from vacuum to inside the phase. It is equal to the sum of the outer potential ψ_α and the *surface* potential $\chi_\alpha = \phi_\alpha - \psi_\alpha$. To bring a charged particle 'i' into this phase, work must be done against its inner potential ϕ_i^α in addition to the work required by the chemical potential μ_i^α, i.e., the energy needed to add an uncharged particle of species 'i' to phase 'α'. Together, they form the *electrochemical potential* of a species 'i' in a phase 'α':

$$\tilde{\mu}_\mathrm{i}^\alpha = \mu_\mathrm{i}^\alpha + \mathrm{z_i} e \phi_\alpha \tag{2.1}$$

with the elemental charge e. $\mathrm{z_i}$ denotes the charge number of species 'i'. In a metal electrode, the electrochemical potential of the electrons $\tilde{\mu}_e^\mathrm{el} := \tilde{\mu}_e^\mathrm{m}$ is also known as the

Fermi energy defining the average energy state of available electrons in phase 'α' [72]. In the solution, one considers a *redox couple*, i.e., a pair of chemically identical species with different oxidation levels.

$$\mathrm{Ox} + e^- \rightleftarrows \mathrm{Red} \tag{2.2}$$

Analogous to electrons being added to an electrode, there is an electrochemical potential of electrons of that redox couple in the solution s which is defined by the difference in the electrochemical potentials of the species 'Red' and 'Ox' in case for one electron to be added to a species 'Ox' in order to reduce it to yield a species 'Red'.

$$\tilde{\mu}_e^{\mathrm{s}} = \tilde{\mu}_{\mathrm{Red}}^{\mathrm{s}} - \tilde{\mu}_{\mathrm{Ox}}^{\mathrm{s}} \tag{2.3}$$

When an electrode is in contact and in equilibrium with a solution containing one redox couple and $\tilde{\mu}_e^{\mathrm{el}} = \tilde{\mu}_e^{\mathrm{s}}$, the difference of the Galvani potentials between the electrode and the solution takes an equilibrium value $\mathrm{E}_{\mathrm{redox}}$[1].

$$\mathrm{E}_{\mathrm{redox}} = \phi_{\mathrm{el}} - \phi_{\mathrm{s}} + \frac{\mu_e^{\mathrm{el}}}{e} \tag{2.4}$$

These equilibrium potentials of redox couples inside the solution are usually referenced against the *Standard Hydrogen Electrode* (SHE), whose absolute potential for the reaction

$$\mathrm{H}^+ + e^- \rightleftarrows \frac{1}{2}\mathrm{H}_2 \tag{2.5}$$

is estimated at $\mathrm{E}_{\mathrm{SHE}} \approx 4.44$ V against the vacuum level [73] under *standard condition* (at activity 1 for both H_2 (fugacity · partial pressure) and protons (≈ 1 M (molar, $\frac{\mathrm{mol}}{\mathrm{liter}}$) concentration of acid) and 298 K. The SHE potential defines the zero-point of the electrochemical potential scale, and the redox reaction denoted in 2.2 changes to 2.6.

$$\mathrm{Ox} + \frac{1}{2}\mathrm{H}_2 \rightleftarrows \mathrm{Red} + \mathrm{H}^+ \tag{2.6}$$

The potential of a redox couple in equilibrium with the electrode $\mathrm{E}_{\mathrm{redox}}$ can then be given in reference to the potential of the SHE. Figure 2.1 shows an idealized electrochemical measurement setup for measuring the potential of the electrode in question or *working electrode* (WE) against the SHE as the *reference electrode* (RE) consisting of a platinum (Pt) electrode connected with the WE via a voltmeter (V) or potentiostat.

---

[1] Per definition, $\mathrm{z}_{\mathrm{Red}} = \mathrm{z}_{\mathrm{Ox}} + 1$.

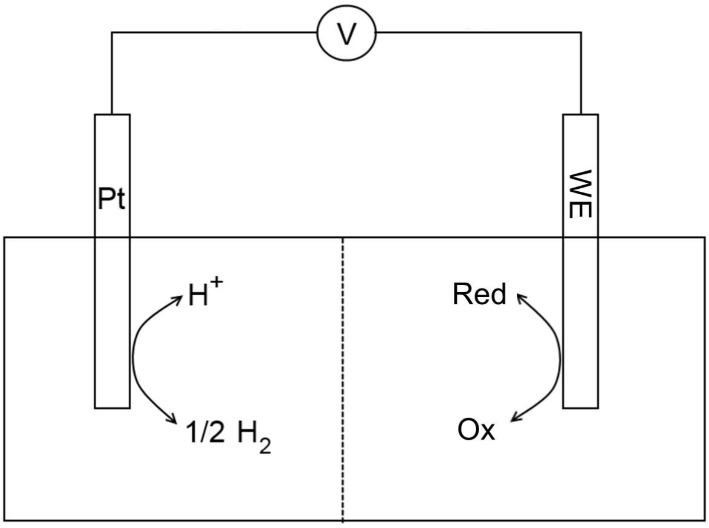

Figure 2.1: Scheme of an idealized measurement of the potential of the working electrode WE on on the right against SHE as reference electrode RE on the left. Original from [1].

$E_{redox,0}$ values at standard conditions (i.e. 298 K and activities of all redox species $a_i = 1$), can be found in textbooks [18, 72, 74]. Usually the observed reactions do not take place under these standard conditions. To obtain equilibrium potentials at non-standard conditions, the *Nernst equation* is used:

$$E = E_0 + \frac{RT}{F} ln \frac{a_{ox}}{a_{red}} \tag{2.7}$$

with the gas constant R, the Faraday constant $F = N_a \cdot e$, i.e., the total charge of one mole (Avogadro number $N_a = 6.022 \cdot 10^{23}$ mol^{-1}) of electrons, and the activities of oxidized and reduced species $a_{ox,red}$, e.g. concentrations of liquid species or partial pressures of gaseous species multiplied by an activity coefficient. When potentials of redox reactions involving protons in electrolytes with different pH values are compared, it is useful to compare them against the *reversible hydrogen electrode* (RHE). The zero point of the scale is shifted with respect to the pH value:

$$0\,\mathrm{V\,vs\,RHE} = 0\,\mathrm{V\,vs\,SHE} + \mathrm{pH} \cdot 0.059\,\mathrm{V} \tag{2.8}$$

Several reference electrodes other than SHE or RHE are used, depending on the electrolytes in which they are deployed and the possible contaminations their usage would introduce into the electrolyte. In this experiment a *saturated calomel electrode* (SCE) and a *saturated mercury sulfate electrode* (MSE) were used as RE. Their standard potentials are

$$\begin{aligned} 0\,\mathrm{V\,vs\,SCE} &= 0.244\,\mathrm{V\,vs\,SHE} \\ 0\,\mathrm{V\,vs\,MSE} &= 0.64\,\mathrm{V\,vs\,SHE} \end{aligned} \tag{2.9}$$

Using a voltmeter or potentiostat (V in figure 2.1) to measure the potential difference between the WE and the RE in equilibrium, the potential one obtains is also called the *open circuit potential* E_{ocp} since in equilibrium there is no net current flowing at the WE.

2.1.2 Electrochemical double layer

When electrode and electrolyte are brought in contact and the electrochemical potentials of the electrons in the respective phases align, excess charges of opposite sign and equal magnitude in the two phases, i.e., electrons in the electrode and ions in the electrolyte respectively, accumulate at the electrode|electrolyte interface. Hence a space charge region is formed at the interface which is called the *electrochemical double layer*. While an excess charge density forms in close vicinity of the electrode surface of a metal electrode, an excess of oppositely charged ions form a compact layer in the electrolyte in close proximity and parallel to the electrode called the *Helmholtz layer* or *Stern layer* and behind that a diffuse ion layer called *Gouy-Chapman layer*, where the excess ion density exponentially drops back to zero towards the bulk electrolyte. The extension of the diffusive layer strongly depends on the concentration of the electrolyte; in concentrated electrolytes (≥ 0.1 M) the effect of the diffuse layer can be neglected. A model of the combined Gouy-Chapman-Stern layer i.e. Helmholtz layer together with a diffuse layer of excess ions with a hydration shell (i.e. shell made up of solute / H_2O molecules) near the electrode is shown in figure 2.2. The closest distance between the electrode and the ions in the Stern layer is denoted as d_{Stern}, which is roughly the radius of the hydration shell.

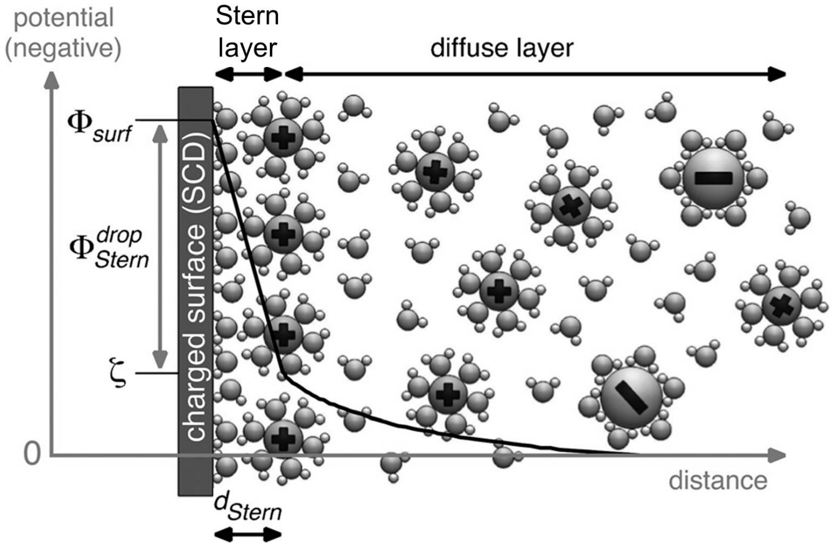

Figure 2.2: Model of the combined Gouy-Chapman-Stern electrochemical double layer near an electrode with a negative surface charge density (SCD) and dilute electrolyte. Most of the surface or inner potential ϕ drops in the Stern layer up to the electrokinetic potential ζ [75], while the rest vanishes exponentially in the diffuse layer towards the bulk or the electrolyte. Original from [76].

2.1.3 Electron-transfer reactions

Up to here electrode and electrolyte were presumed to be in equilibrium; the electrochemical potentials of electrons 'in' the redox pair in solution and in the electrode are aligned and the WE is at the open circuit potential $E_{ocp} \mathrel{\hat{=}} E_{redox}$. Oxidation and reduction reactions do take place at E_{redox}, but they cancel each other out, leading to a net current of zero. When the potential at the WE is shifted $E_{WE} \neq E_{redox}$, there is an

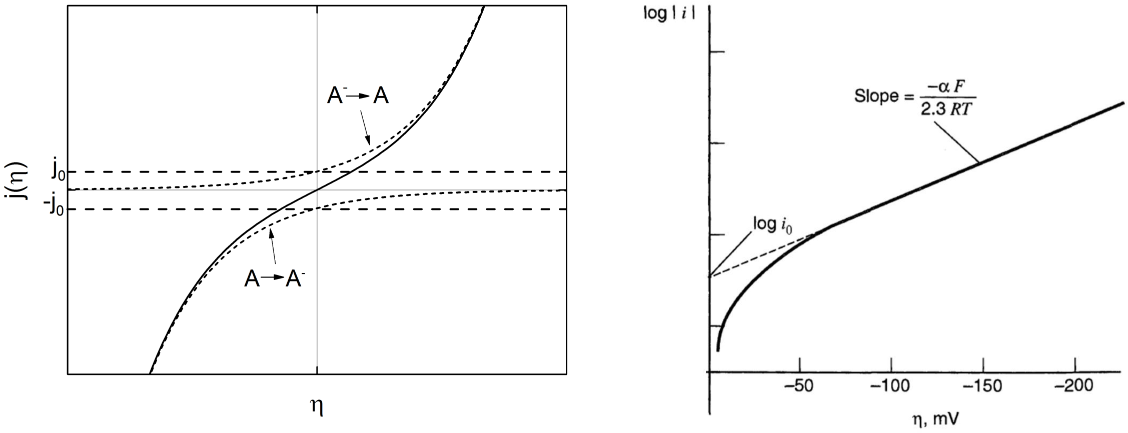

Figure 2.3: Left: Current-overpotential characteristics at the working electrode according to the Butler–Volmer equation 2.11 for $\alpha = 0.5$ (solid curve) and the anodic and cathodic partial currents corresponding to both summands in equation 2.11 (dashed curves). Original from [1] p.115. Right: Tafel plot of the current overpotential characteristic at the working electrode according to the Butler–Volmer equation at high η (eq: 2.12). Original from [72] p.103

overpotential η present, with which a net reaction or faradaic current can be driven.

$$\eta = \mathrm{E}_{\mathrm{WE}} - \mathrm{E}_{\mathrm{redox}} \tag{2.10}$$

For a simple, so called outer sphere electron-transfer, i.e. the reactants are at a distance of at least a solvent layer away from the electrode and only one electron is exchanged at a time without breaking or altering chemical bonds of the reactant, the current density j of the reaction is composed of the rates of oxidation and reduction reactions depending on the overpotential, and can be expressed with the *Butler-Volmer equation*:

$$\mathrm{j} = \mathrm{j}_0 \left[\exp\left(-\frac{\alpha \mathrm{F} \eta}{\mathrm{RT}} \right) - \exp\left(-\frac{(1-\alpha)\mathrm{F}\eta}{\mathrm{RT}} \right) \right] \tag{2.11}$$

with the symmetry factor α describing the symmetry of the oxidation / reduction reaction of the redox couple and the *exchange current density* j_0. The left side of figure 2.3 shows $\mathrm{j}(\eta)$ of a redox couple A^-/A comprised of oxidative ($\mathrm{A}^- \rightarrow \mathrm{A}$) and reductive ($\mathrm{A} \rightarrow \mathrm{A}^-$) partial currents i.e. the two exponentials in equation 2.11. Their intercept points with the grey ordinate at $\eta = 0$ denotes the size of j_0.

The exchange current density can be used to give a qualitative evaluation of how "efficient" current is generated by overpotential or how "well" a certain electrode "promotes" the reaction. At high η only one of the partial currents dominates the total current density.

$$\mathrm{j} \approx \mathrm{j}_0 \exp\left(-\frac{\alpha \mathrm{F} \eta}{\mathrm{RT}} \right) \tag{2.12}$$

As can be seen on the right of figure 2.3, the plot the logarithm of j versus η, also called *Tafel plot*, can be linearly fitted at high overpotentials. At $\eta = 0$, the fit curve intersects the current axis at the exchange current density j_0.

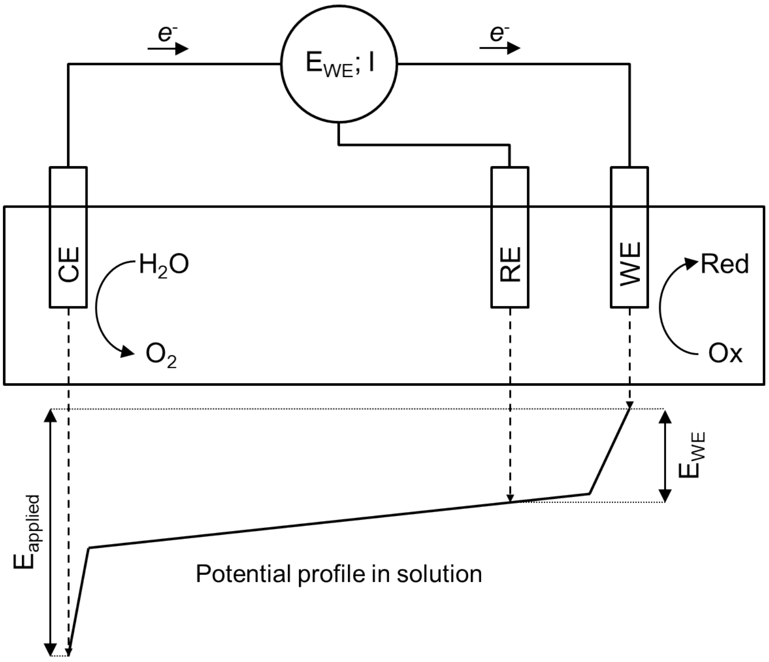

Figure 2.4: Scheme of the three-electrode setup and its potential profile.

In this thesis, an electrochemical experiment investigating such electron transfer processes deploys a *three-electrode setup* immersed in the electrolyte (fig. 2.4), with the investigated reaction taking place at the *working electrode* (WE). When a potential is applied using a potentiostat to shift the potential between working and reference electrode (RE), the faradaic current produced by the electrochemical reaction at the WE is balanced or supplied by the *counter electrode* (CE). In figure 2.4 H_2O is oxidized to oxygen (O_2) at the CE in order to counterbalance the assumed negative current from the investigated reduction reaction taking place at the WE. With the addition of the CE, the potential of WE can be adjusted independently from the reactions taking place at the CE.

Cyclic Voltammetry

Next to a constant applied potential, the main electrochemical measurement technique used in the thesis is *Cyclic Voltammetry.* Rather than staying constant, the potential of the WE is swept from an initial starting potential E_i to a final or turnaround potential E_f with a sweep or scan rate v.

$$E_{WE}(t) = E_{WE,i} + vt \tag{2.13}$$

Then v changes sign and the WE potential is swept back again to E_i, thus completing the cycle. Redox reactions with redox potentials inside the potential range between the two potentials or scanning range can be driven by the temporarily applied overpotential during the sweep and thus detected and their reaction currents quantified. In figure 2.5 a cyclic voltammogram (CV) of a redox couple A/A^- with its redox potential E_{A/A^-} is depicted. The negative current density of the scan down (to the left) rises exponentially as described in the Butler-Volmer equation 2.11, but then tapers off when the reactant A is depleted in the double layer, resulting in a peak-like current drop off. On the back scan up (to the right) the produced A^- is subsequently oxidized back to species A, as the potential returns to the initial potential E_i. The emergence of these two peaks of similar size positioned around E_{A/A^-} during the CV points towards the redox reaction $A \rightleftarrows A^-$ as being reversible; a cathodic or anodic current density without the corresponding current density of an opposite sign signifies a totally irreversible reaction, such as the electrografting process described later in chapter 4.1.

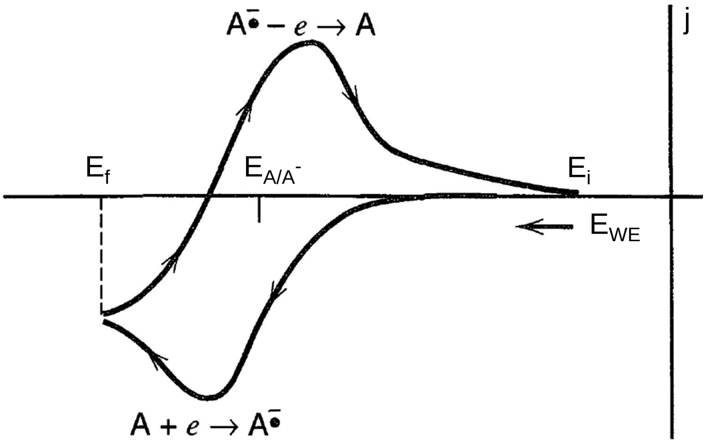

Figure 2.5: Plot of a CV of the A/A^- redox couple. Original from [72] p.227.

Electrochemical Impedance Spectroscopy

Another measurement technique used in this thesis is Electrochemical Impedance Spectroscopy (EIS). In EIS the frequency dependence of the investigated electrochemical system, e.g. processes taking place at the electrode|electrolyte interface or the double layer itself, is investigated by superimposing a sinusoidal perturbation potential $E_{WE,p}(t) = E_p \sin(\omega t)$ to some set potential E^0_{WE} and recording the current response $I(t) = I_r \sin(\omega t + \varphi)$ with the perturbation amplitude E_p, response current amplitude I_r, angular frequency $\omega = 2\pi f$ and the phase shift φ between $E_{WE,p}(t)$ and $I(t)$. Figure 2.6 shows an exemplary time evolution of $E_{WE,p}(t)$ and $I(t)$.

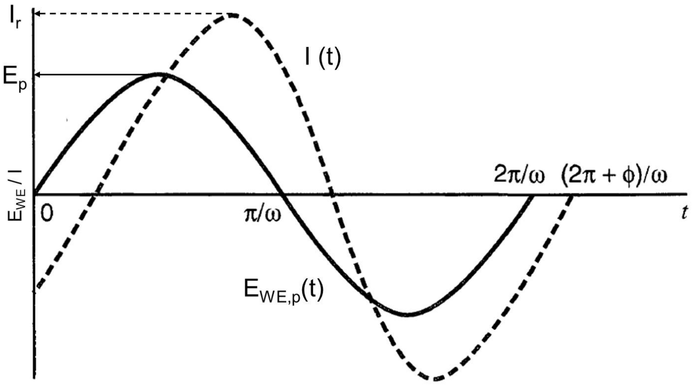

Figure 2.6: Plot of the perturbation potential $E_{WE,p}(t)$ and current response I(t) versus time. Original from [72] p.371.

The ratio of $E_{WE,p}(t)$ and $I(t)$ yields the complex impedance $Z(\omega)$ of the system, consisting of a real part Z_r and an imaginary part Z_i with $i = \sqrt{-1}$.

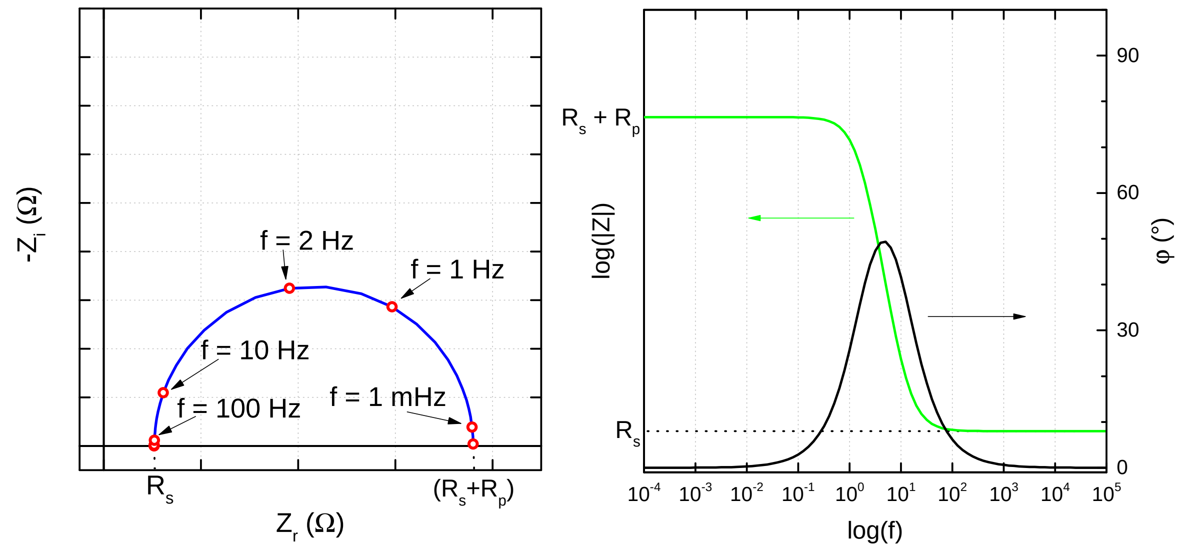

Figure 2.7: Left: Nyquist plot of the impedance spectrum of the equivalent circuit shown in figure 2.8. Right: Bode plot of the same impedance spectrum. $\mathbf{R_S} = 3.9 \cdot 10^2\,\Omega$, $\mathbf{R_P} = 6.6 \cdot 10^5\,\Omega$, $\mathbf{C_P} = 1.4 \cdot 10^{-6}$ C.

$$Z(\omega) = \frac{\mathrm{E_{WE,p}}}{\mathrm{I}} = \mathrm{Z_r} + i\mathrm{Z_i} \tag{2.14}$$

Real and imaginary part of the complex impedance are linked by the phase difference φ between $\mathrm{E_{WE,p}}$ and I.

$$\tan\varphi = \frac{\mathrm{Z_i}}{\mathrm{Z_r}} \tag{2.15}$$

Changing ω leads to a spectrum of impedance values over the investigated frequency range. Two typical plots of such an impedance spectrum are shown in figure 2.7.

In the Nyquist plot on the left side, -$\mathrm{Z_i}$ is plotted versus $\mathrm{Z_r}$ (blue curve), while in the Bode plot on the right side, the logarithm of the magnitude of the impedance |Z| (green curve) as well as the phase shift φ (black curve) are plotted versus the logarithm of the frequency f. One can try to find an *equivalent circuit* consisting of electrical components such as resistors and capacitors and use it to fit the impedance spectrum of the electrochemical system. The impedance of a resistor with resistance R and an capacitor with an capacitance C are given by:

$$\begin{aligned} Z_{\mathrm{resistor}}(\omega) &= \mathrm{R} \\ Z_{\mathrm{capacitor}}(\omega) &= -\frac{i}{\omega\mathrm{C}} = \frac{1}{i\omega\mathrm{C}} \end{aligned} \tag{2.16}$$

One such equivalent circuit is shown in figure 2.8, where one resistor with the resistance $\mathrm{R_S}$ is connected in series with a parallel connection of a resistor with the resistance $\mathrm{R_P}$ and capacitor with the capacitance $\mathrm{C_P}$. This circuit can be used to model an electrochemical double layer, where $\mathrm{R_S}$ represents the resistance from the electrolyte, $\mathrm{C_P} \mathrel{\hat{=}} \mathrm{C_{dl}}$ the double layer capacity and $\mathrm{R_P} \mathrel{\hat{=}} \mathrm{R_{ct}}$ the charge transfer resistance of the double layer.

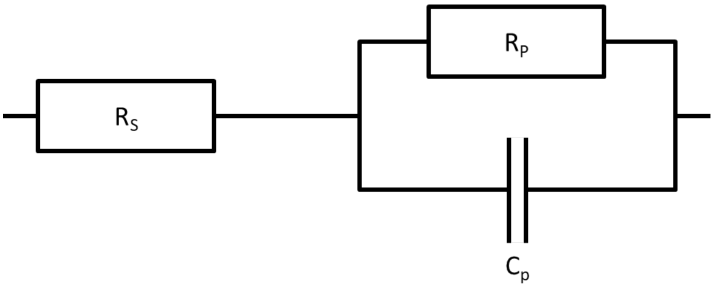

Figure 2.8: Simple equivalent circuit of an electrochemical cell.

The half circle in the Nyquist plot and the sigmoidal shape of |Z| in the Bode plot stem from the simulated EIS impedance values of the equivalent circuit in figure 2.7 and exhibit some of its main features, namely:

- At high frequencies, i.e., the left end of the half circle in the Nyquist plot, the capacitor acts like a bypass for the parallel resistor, and the half circle intercepts the Z_r scale at $\mathrm{R_S}$. In the Bode plot |Z| plateaus at $\mathrm{R_S}$ on the high frequency side.
- At low frequencies, i.e., the right end of the half circle, the capacitor acts like an open switch, and the half circle intercepts the Z_r scale at the combined resistance of $\mathrm{R_S+R_P}$. In the Bode plot |Z| saturates at $\mathrm{R_S+R_P}$ on the low frequency side.

The total impedance of the equivalent circuit can be calculated by the sum of the impedances of the circuit parts.

$$\begin{aligned} Z_{\mathrm{tot}}(\omega) &= Z_{\mathrm{R}}(\omega) + Z_{\mathrm{R/C}}(\omega) = \\ &= \mathrm{R_S} + \left(\frac{1}{\mathrm{R_P}} + i\omega \mathrm{C_P}\right)^{-1} = \\ &= \underbrace{\left(\mathrm{R_S} + \frac{\mathrm{R_P}}{1+\omega^2 \mathrm{R_P^2 C_P^2}}\right)}_{\mathrm{Z_{tot,r}}} + i \underbrace{\left(\frac{-\omega \mathrm{R_P^2 C_P}}{1+\omega^2 \mathrm{R_P^2 C_P^2}}\right)}_{\mathrm{Z_{tot,i}}} \end{aligned} \tag{2.17}$$

2.2 Semiconductor electrodes

The previous sections have assumed a metal electrode in contact with the electrolyte. In this thesis, semiconducting silicon electrodes were used[2]. Unlike metal electrodes, where the Fermi energy E_{F} of electrons in the highest occupied or filled energy state [3] in the electrode lies inside of a quasi continuous range of available energy states (or inside an energy band), the Fermi level in an intrinsic semiconductor lies between two energy bands. At room temperature, the energetically lower one is nearly completely filled with electrons (*valence band*, highest filled energy state at E_{vb}) and the upper one practically empty (*conduction band*, lowest available energy state at E_{cb}) due to the temperature dependent Fermi distribution of electron energies, while inside the *band gap* ($E_{\mathrm{g}} = E_{\mathrm{cb}} - E_{\mathrm{vb}}$), there are no available energy states. Hence, the electric

---

[2] The overview is mainly based on [1, 48, 77].

[3] at T = 0 K

conductivity in semiconductors is far smaller than in metals. The electronic band structures of the two electrode types are schemed in figure 2.9.

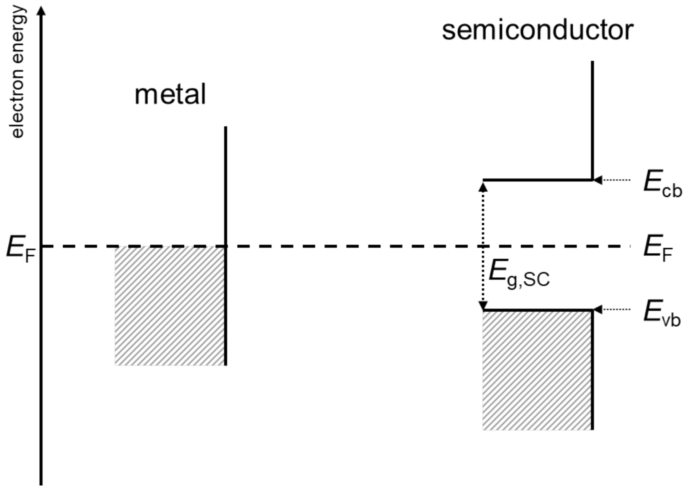

Figure 2.9: Schematic illustration of the band structures of a metal (left) and semiconductor (right).

The conductivity of a semiconductor can be improved by doping the intrinsic semiconductor with atoms which possess a different valency. As depicted in figure 2.10 for silicon and its valency of four, dopant atoms such as phosphorus (P, valency: 5) or boron (B, valency: 3) embedded into the silicon lattice introduce additional electrons or holes (i.e. electrons missing from the lattice, with positive charge e) and thus shift E_F from about the middle of the band gap towards the conduction band or the valence band. Phosphorus-doped silicon is an n-type or n-doped semiconductor with E_F closer to the conduction band, while boron-doped silicon is a p-type or p-doped semiconductor with E_F closer to the valence band:

$$\begin{aligned} \mathrm{n-type:}\quad E_\mathrm{F} &= E_\mathrm{cb} - \mathrm{kT}\frac{\mathrm{N_{cb}}}{\mathrm{N_D}} \\ \mathrm{p-type:}\quad E_\mathrm{F} &= E_\mathrm{vb} + \mathrm{kT}\frac{\mathrm{N_{vb}}}{\mathrm{N_A}} \end{aligned} \tag{2.18}$$

with the effective densities of states in the conduction and valence bands for silicon, respectively $\mathrm{N_{cb}} = \mathrm{N_{vb}} = 2 \cdot 10^{19}\,\mathrm{cm^{-3}}$, the Boltzmann constant k, temperature T and the densities of donor (i.e. electron donating) atoms $\mathrm{N_D}$ and acceptor (i.e. electron capturing/accepting) atoms $\mathrm{N_A}$, respectively.

The main difference of a semiconductor|electrolyte interface to a metal|electrolyte interface is that because of the low conductivity relative to metals, the space charge region formed by the potential difference between the semiconductor electrode and the electrolyte is also extended inside the semiconductor due to the accumulation or depletion of electrons near the interface, changing the energetics there and leading to the bending of the energy bands near the surface of the electrode. The total potential drop between electrode and electrolyte is split into two parts, the one across in the space charge layer in the semiconductor $\Delta\phi_\mathrm{SC}$ and the one across the electrochemical double layer or Helmholtz layer $\Delta\phi_\mathrm{H}$.

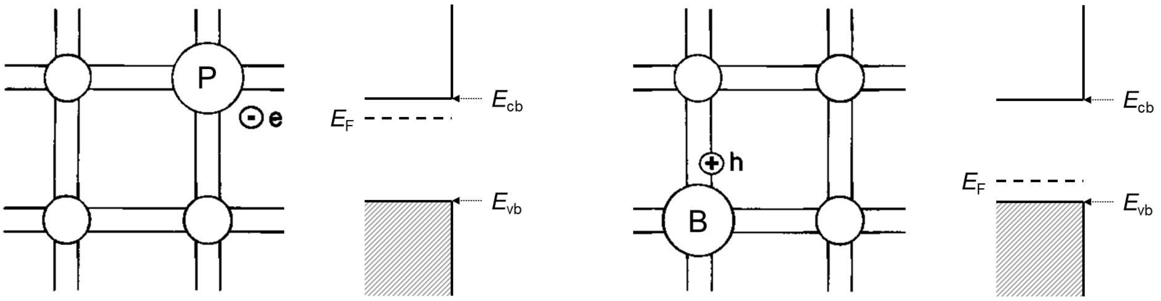

Figure 2.10: Left: Schematic illustration of the inclusion of a donor, phosporus atom (P) in the silicon lattice and the energetics of an n-type semiconductor. Right: Schematic illustration of the inclusion of an acceptor, boron atom in the silicon lattice and the energetics of a p-type semiconductor. Original figure from [77] p.48.

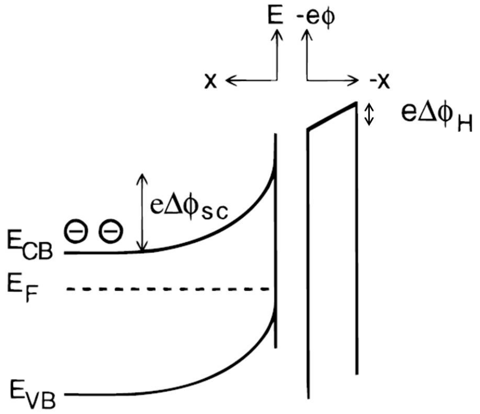

Figure 2.11: Schematic illustration of the band structure of an n-type silicon/electrolyte interface under depletion conditions in the dark illustrating the splitting of the total potential difference in two potential drops across the space charge layer $\Delta\phi_{SC}$ and across the Helmholtz layer $\Delta\phi_H$. Original figure from [78].

When the electrolyte is more conductive than the semiconductor, the majority of the potential drop happens inside the semiconductor, as is depicted in figure 2.11, making the interface similar to a semiconductor|metal or *Schottky contact.* The *flat band potential* $E_{fb} = E_{fb}/e^-$ denotes the situation where the applied potential counteracts the potential difference in the space charge region, thus eliminating excess charges near the interface and the resulting band bending. One can record the capacity of the space charge layer C_{SC} versus the potential of the silicon working electrode in the depletion region using EIS. With the so called *Mott-Schottky* (MS) relation, one then can fit the MS plot to the potential at which ${C_{SC}}^{-2}$ goes to zero, i.e. where no excess charges are left on the idealized space charge capacitor.

$$\frac{A^2}{C_{SC}^2} = \frac{2}{e\epsilon_{Si}\epsilon_0 N_D}(E_{WE} - E_{fb} - \frac{kT}{e}) \tag{2.19}$$

where A is the area of the electrode, e the elemental charge, ϵ_{Si} the permittivity of silicon ($\epsilon_{Si} = 11.9$ [48]), N_D the doping density, $E_{WE} - E_{fb}$ the potential of the silicon electrode relative to its flatband potential E_{fb}, k the Boltzmann constant and T the temperature.

In electron-transfer reactions through the space charge layer both the valence band

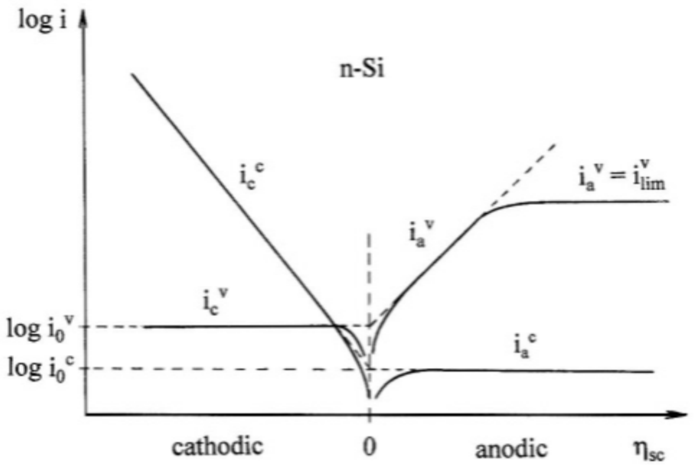

Figure 2.12: Schematic, logarithmic plot of the partial currents of valence and conduction bands versus the overpotential in the space charge layer η_{SC} for n-type silicon. Original figure from [48] p.25.

and the conduction band contribute to the overall current, but typically the major part of the current will come from the energy band that is closer to the electrochemical potential of the redox couple. As depicted in figure 2.12, for n-type silicon electrode the cathodic current of the conduction band (denoted in the figure as $i_c{}^c$) grows exponentially with more negative overpotential $-\eta_{SC}$, while it stays constant in the anodic region due to the approximately constant number of empty states in the conduction band under depletion conditions, i.e., at anodic overpotentials $+\eta_{SC}$. Analogously, the cathodic current of the valence band (denoted in the figure as $i_c{}^v$) stays constant in the cathodic region due to the number of filled states in the valence band at cathodic overpotentials $-\eta_{SC}$, while $i_a{}^v$ grows exponentially with more positive overpotential $+\eta_{SC}$ until $i_a{}^v \rightarrow i^v_{lim}$ saturates at high $+\eta_{SC}$ due to the limited amount of minority charge carriers (acceptors or holes in the case for n-type silicon). For reduction reactions at modest faradaic currents, n-type silicon shows a net current of $i_c = i_c{}^c + i_c{}^v$, which should qualitatively exhibit the same exponential current-potential characteristics as described for metal electrodes in equation 2.11.

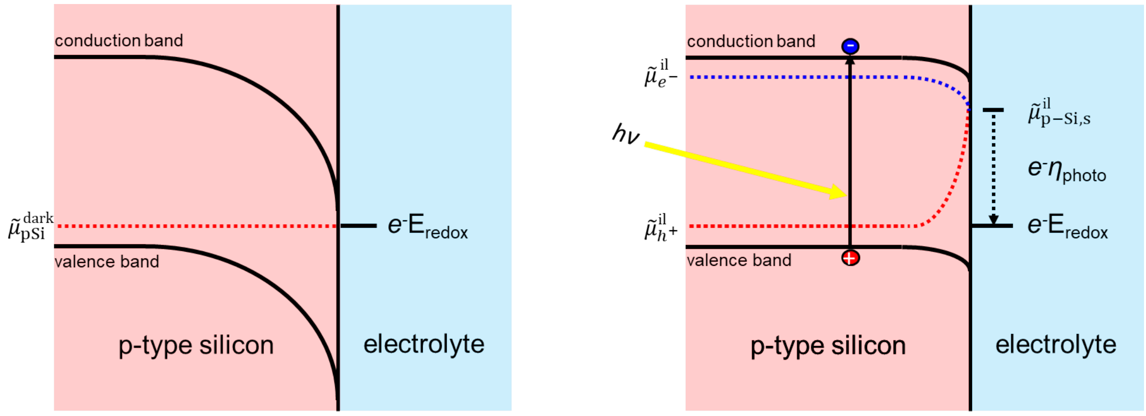

Figure 2.13: Scheme the energy levels of a p-type semiconductor (red) in contact with an electrolyte (blue) containing a redox pair with $e^-\mathrm{E}_{\mathrm{redox}}$ in equilibrium without illumination (left) and when illuminated by light with a photon energy $h\nu > E_g$ (right).

Semiconductor electrodes show a rather small exchange current density compared to metal electrodes, but on semiconductor electrodes electrochemical reactions can be partially driven by illumination. Light with a photon energy $h\nu > E_{\mathrm{g}}$ can be absorbed and creates electron-hole pairs in the semiconductor as shown schematically in figure 2.13. In the case of a moderately doped p-type silicon electrode (p-Si), the created photo-electrons form their own Fermi level or quasi electrochemical potential $\tilde{\mu}^{\mathrm{il}}_{\mathrm{p-Si},e^-}$ close to the conduction band after thermalization, in addition to the quasi electrochemical potential $\tilde{\mu}^{\mathrm{il}}_{\mathrm{p-Si},h^+} \approx \tilde{\mu}^{\mathrm{dark}}_{\mathrm{p-Si}}$ of the holes, effectively increasing the limiting current $\mathrm{i}_{\mathrm{lim}}$ from figure 2.12. In figure 2.13 energy band diagrams without (left) and with (right) illumination are depicted. Without illumination a p-type silicon is in equilibrium with a solution containing a redox species with a suitable redox potential $\mathrm{E}_{\mathrm{redox}}$, which is energetically higher than $\tilde{\mu}^{\mathrm{dark}}_{\mathrm{p-Si}}$. At equilibrium, the resulting band bending downwards at the Schottky contact leads to the formation of a quasi n-doped semiconductor near the electrode|electrolyte interface, where $\tilde{\mu}^{\mathrm{dark}}_{\mathrm{p-Si}}$ is close to the band edge of the conduction band. The emergence of electrons from the electron-hole pairs created in this space charge region by illumination leads to a reduction of the band bending and the effective increase of $\tilde{\mu}^{\mathrm{il}}_{\mathrm{p-Si,s}}$ at the surface, where the quasi electrochemical potentials $\tilde{\mu}^{\mathrm{il}}_{\mathrm{p-Si},e^-}$ and $\tilde{\mu}^{\mathrm{il}}_{\mathrm{p-Si},h^+}$ merge. The (photo-) electrons at the semiconductor|electrolyte interface can then drive the reduction reaction of the redox couple in the electrolyte with $e^-\mathrm{E}_{\mathrm{redox}} < \mu^{\mathrm{il}}_{\mathrm{p-Si,s}}$, effectively applying a photo-generated overpotential η_{photo}. Figure 2.14 shows the effect of the photo-generated overpotential on the j-E_{WE} characteristic of a reduction reaction. The current response of the illuminated p-type silicon electrode is very similar to the j-E_{WE} curve of an n-type silicon electrode with the same doping concentration in the dark. The illumination leads to a shift of the j-E_{WE} curve towards lower overpotentials.

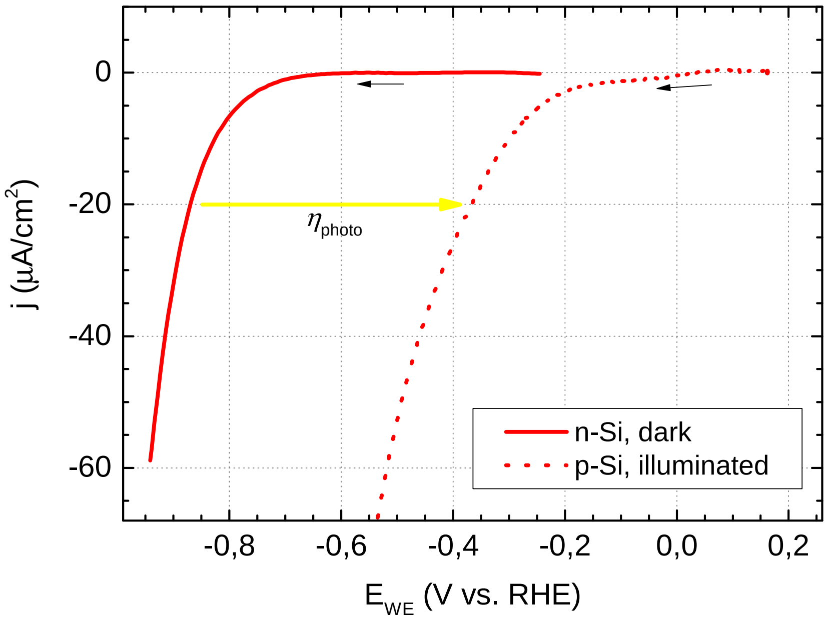

Figure 2.14: Exemplary j-E_{WE} characteristics of an n-type silicon electrode (solid line) and an illuminated p-type silicon electrode (dotted line) with the same doping concentration doping concentration $\mathrm{N}_{\mathrm{A}} = \mathrm{N}_{\mathrm{D}} \approx 10^{15}\,\mathrm{cm}^{-3}$. The yellow arrow denotes the photo-generated overpotential η_{photo}.

2.3 Surface characterization via X-ray photoelectron spectroscopy (XPS)

In order to investigate the surface modification of silicon electrodes modified with a layer of immobilized pyridine, the functionalized surface needs to be characterized with respect to its chemical composition and morphology in the unmodified state, and subsequently the change thereof after the surface modification process. In this thesis X-ray photoelectron spectroscopy (XPS) was deployed for the surface characterization of the modified silicon electrodes. The following explaination is mainly based on [79, 80].

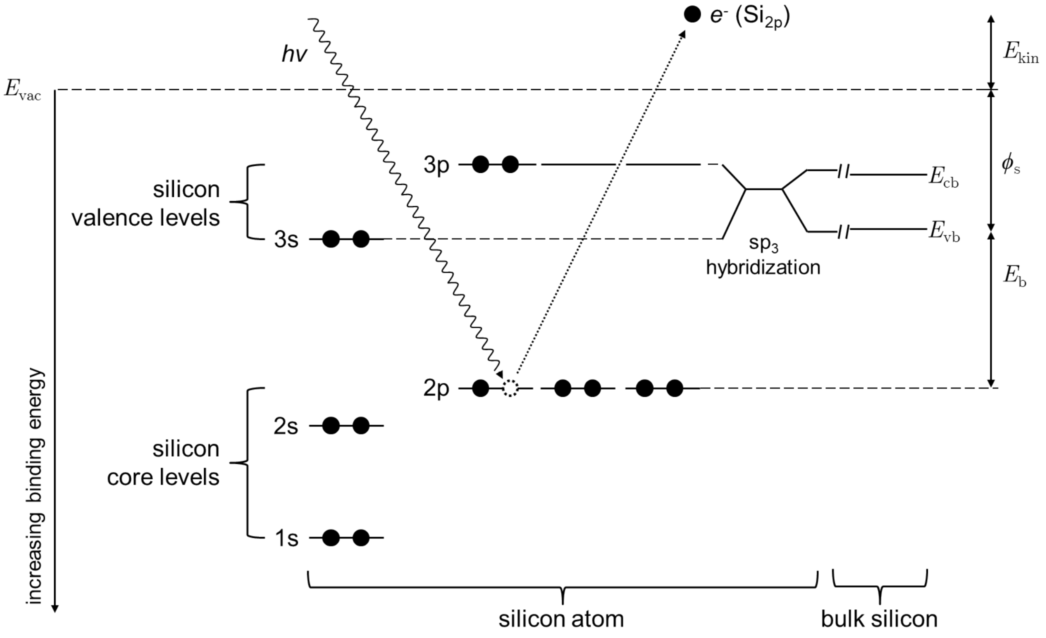

Figure 2.15: Illustration of the electron (black dots) configuration on the valence and core energy levels of silicon, when an electron (white dot with broken line) from the 2p core energy level absorbs an X-ray photon with a suitable photon energy $h\nu$ and is emitted (dotted line). The 3s and 3p valence levels hybridize to sp_3 orbitals, which form a dimer of bonding and anti-bonding states. With subsequent atom addition towards bulk silicon formation, these bonding and anti-bonding states develop into the valence and conduction bands with their band edge energies E_{vb} and E_{cb}. On the right, the energy of the photon $h\nu$ is qualitatively divided into the components E_{kin}, ϕ_s and E_b of the Si_{2p} photoelectron.

XPS is based on the photoelectric effect, where, due to X-ray radiation with a suitable energy $h\nu$ on a sample, photoelectrons from the sample are emitted with a kinetic energy E_{kin}, as illustrated in figure 2.15:

$$E_{kin} = h\nu - E_b - \phi_s \tag{2.20}$$

which depends on the work function of the sample ϕ_s and the initial binding energy of the emitted electron E_b. Depending on the atom, the bound electrons are distributed on a number of core energy levels and the valence levels, which take part in the formation of molecular orbitals and energy bands, as the considered atom is part of a solid state lattice. These core level electrons are mainly targeted for the XPS measurements in this thesis and denoted with the spectroscopic nomenclature for principle quantum number n, followed by a letter for the angular quantum number $l = 0, 1..., n-1$. For example, the main XPS peak of silicon is denoted $\mathrm{Si}_{2\mathrm{p}}$, i.e. they stem from electrons in core level 2p with an angular momentum quantum number $l = 1$. Even though the core level electrons do not form bonds with neighbouring atoms in the solid state, the chemical state of the atom and thus their binding energies are influenced by the neighbouring atoms (due to electrostatic shielding of the nuclear charge from all other electrons in the atom), which leads to differences in the corresponding binding energies. The binding energy of 2p electrons of a silicon atom bound to two oxygen atoms as part of silicon dioxide (SiO_2) $E_{\mathrm{b,Si2p}}(\mathrm{SiO}_2) \approx 103$ eV is for example higher than $E_{\mathrm{b,Si2p}}(\mathrm{bulk}) \approx 99.5$ eV of 2p electrons of silicon atoms in bulk silicon. These chemical shifts can be used to detect not only the occurrence of different chemical species but also the type of molecular structures certain atoms are part of. While X-rays have a penetration depth of ≈ 100 μm into the sample, only photoelectrons from a depth of ≤ 10 nm from the surface of the sample can escape. XPS is therefore considered to be highly surface sensitive.

Experimental setup of an XPS instrument

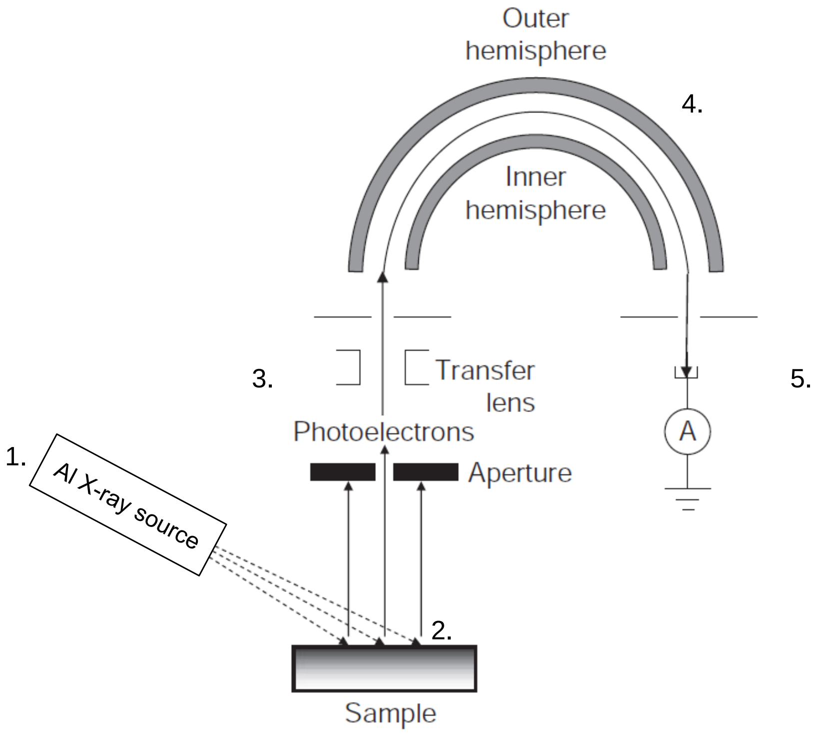

Figure 2.16: Illustration of an XPS instrument and its main components as used in this thesis. Original figures from [80] p. 45, 54.

An XPS instrument, as used for this thesis, requires a vacuum with a pressure of $\leq 10^{-6}$ Pa (very high vacuum (VHV) or ultra high vacuum (UHV)) in order to minimize the interaction of photoelectrons with the remaining gaseous environment after their emission from the sample. The following components of an XPS instrument are housed in such a vacuum chamber, as depicted in figure 2.16:

1. The source of the X-ray radiation is the X-ray tube (1.) aimed at the sample (2.). Inside the X-ray source an electron beam is directed at an X-ray anode, in this thesis an aluminium (Al) electrode. The ejection and subsequent re-filling of Al_{1s} core electrons produces $\mathrm{K}\alpha$ X-ray radiation with a photon energy of $h\nu(\mathrm{Al}-\mathrm{K}\alpha) = 1486.6$ eV.

2. The sample (2., grey gradient) is irradiated with the Al $\mathrm{K}\alpha$ X-ray radiation, which leads to the production of photoelectrons due to the photoelectric effect. Photoelectrons which are emitted perpendicular to the surface of the irradiated sample can then enter the detector beam path. In this position one detects the most amount of photoelectrons, i.a. electrons originating from a few bulk atom layers in addition to the surface. For a more surface sensitive XP spectrum the sample can be tilted in relation to the detector beam path to achieve a take-off angle $\theta < 90°$ in order to minimize the bulk photoelectron signal relative to the surface signal.

3. Before entering the hemispherical analyser, the electrons are de-/accelerated to a constant kinetic energy E_{pass} using the transfer lens system. In the so-called fixed analyser transmission (FAT) mode, the transfer lens or system of lenses select the kinetic energy of the photoelectrons. Therefore, the energy resolution is independent of the kinetic energy of the photoelectrons. The choice of a low pass energy E_{pass} increases the resolution of the analyser but reduces its sensitivity (and vice versa for an high E_{pass}).

4. A concentric hemispherical analyser (CHA) with entrance and exit slits is used to guide or pass the electrons with the kinetic energy E_{pass} to the detector. In FAT mode, the inner and outer hemisphere with their radii $\mathrm{R}_{\mathrm{hs,in}}$ and $\mathrm{R}_{\mathrm{hs,out}}$, respectively, are set to the constant potentials $\mathrm{E}_{\mathrm{hs,in}}$ and $\mathrm{E}_{\mathrm{hs,out}}$:

   $$\begin{aligned} \mathrm{E}_{\mathrm{hs,in}} &= E_{\mathrm{pass}}\left(3-\frac{\mathrm{R}_{\mathrm{hs,in}}+\mathrm{R}_{\mathrm{hs,out}}}{\mathrm{R}_{\mathrm{hs,in}}}\right) \\ \mathrm{E}_{\mathrm{hs,out}} &= E_{\mathrm{pass}}\left(3-\frac{\mathrm{R}_{\mathrm{hs,in}}+\mathrm{R}_{\mathrm{hs,out}}}{\mathrm{R}_{\mathrm{hs,out}}}\right) \end{aligned} \tag{2.21}$$

   In the end, the energy resolution of the analyser ΔE is dependent on the pass energy, the radii of the hemispheres and the average slit width w.

   $$\Delta E \approx \frac{\mathrm{w}}{2(\mathrm{R}_{\mathrm{hs,in}}+\mathrm{R}_{\mathrm{hs,out}})}\cdot E_{\mathrm{pass}} \tag{2.22}$$

5. The photoelectrons, which passed the analyser, are multiplied by a channeltron or channel electron multipliers (CEM) and finally detected by an anode collector or charge collector devices (CCD).

The resulting spectrum plots the intensity of the detected electrons versus their kinetic energy in the instrument $E_{\mathrm{kin,XPS}}$, which is determined by the de-/acceleration fields in the transfer lens system.

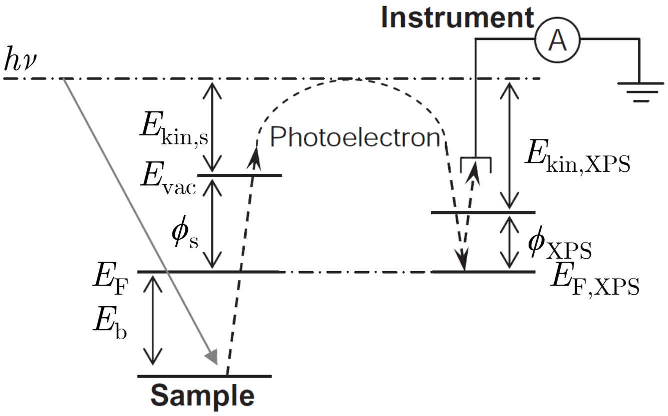

Figure 2.17: Illustration of the energy levels of the sample and the XPS instrument which is in electrical contact with the sample and shares its Fermi energy level E_{F}. Original figure from [80] p.67

As is illustrated in figure 2.17, once the sample and instrument are electrically in contact, their Fermi energy levels align. By constructing the XPS instrument in such a way that the work function of the instrument $\phi_{\mathrm{XPS}} < \phi_{\mathrm{s}}$, the binding energy E_{b} can be determined using the instrument-specific work function ϕ_{XPS} and $E_{\mathrm{kin,XPS}}$. Therefore E_{b} becomes independent of the often unknown work function of the sample ϕ_{s}:

$$\begin{aligned} E_{\mathrm{b}} &= h\nu - E_{\mathrm{kin,s}} - \phi_{\mathrm{s}} = \\ &= h\nu - E_{\mathrm{kin,XPS}} - \phi_{\mathrm{XPS}} \end{aligned} \tag{2.23}$$

The spectrum plotted versus the binding energy E_{b} contain peaks at certain energies, which can then be related to tabulated, known binding energies for atoms and their chemical shifts [79], as can be seen in chapter 4.2.

2.4 Product analysis

Product analysis tools were deployed to distinguish and quantify possible reaction products stemming from the electrochemical bulk CO_2 reduction electrolysis measurements conducted in chapter 7. The liquid part of those reaction products are reported to be comprised of small hydrocarbon molecules such as formic acid (FA), formaldehyde, methanol (MeOH) [19] as well as traces of ethanol (EtOH) and propanol (PrOH) [25] for electrolytes containing pyridine. The gaseous products meanwhile might include hydrogen (H_2) and carbon monoxide (CO), although both species have not been specifically measured, rather assumed [21] or implictly / electrochemically detected [25]. Prior work on the pyridine mediated CO_2 reduction reaction on platinum electrodes in this group reported the detection of electrochemically produced methanol using High Performance Liquid Chromatography (HPLC) instrument [81], but the detected signal was as small as the detection limit of the HPLC, which was around the concentration of about 0.1 mM or, as a ratio[4], $c_{\mathrm{MeOH}} = \frac{0.1\,\mathrm{mM}}{55.56\,\mathrm{M}} \leq 2$ ppm. Following this result and reported (state of the art) detection limits of ≈ 0.1 ppm [16,25], one of the goals in the master thesis of Andreas Heine [27] was improving the detection limit achievable in our lab using HPLC, Gas Chromatography (GC) and Nuclear Magnetic Resonance (NMR). The detection limit of ≈ 0.1 ppm was only reached using NMR. Therefore, ^{1}H-NMR was used to detect liquid CO_2 reduction products, while GC was used to detect the gaseous reaction products.

2.5 Gas Chromatography (GC)

Gas Chromatography (GC) measurements were conducted to detect possible gaseous CO_2 reduction products. The following explanations are based on [82].

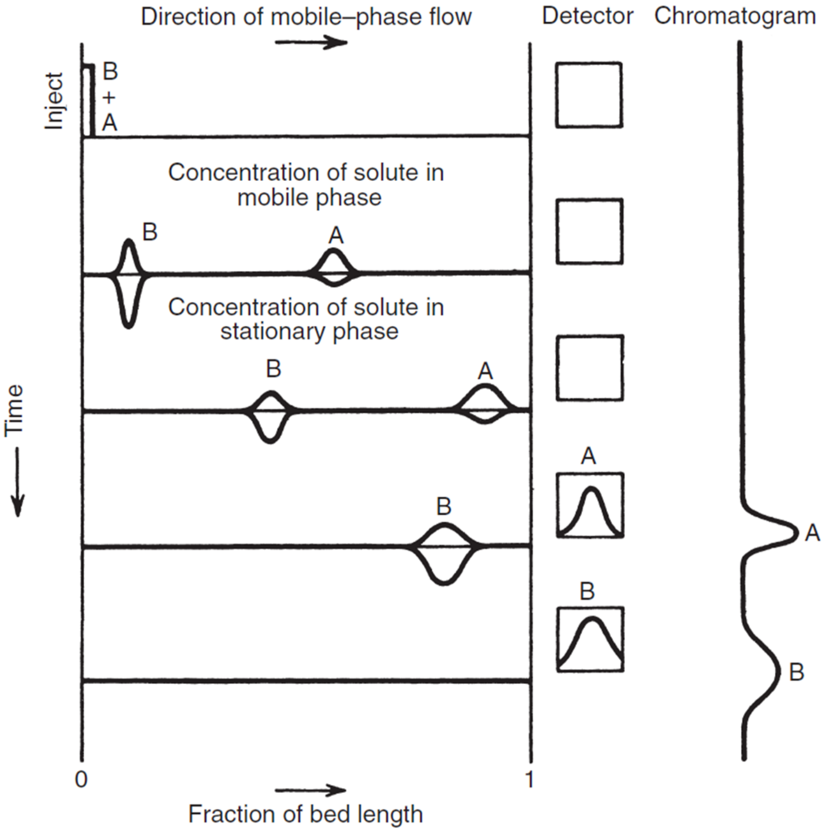

Figure 2.18: Scheme of the separation of a mixture of solute A and B through a column of a certain bed / column length and the resulting chromatogram (right side). Each line represents a snapshot of the column at a certain time. Original graph taken from [82], p. 18.

As can be seen in figure 2.18, in a GC measurement a gas sample consisting of different species or solutes are transported in a *mobile phase* or carrier gas through a column, which possesses a surface material or *stationary phase*. The differences in ad- and desorption characteristics of the solutes with the stationary phase lead to a separation of the solutes during the time they are carried through the column. At

---

[4] $c_{H_2O} = 55.56$ M

different retention times the separated solutes are finally detected in a suitable detector. The basic setup of a GC is shown in figure 2.19.

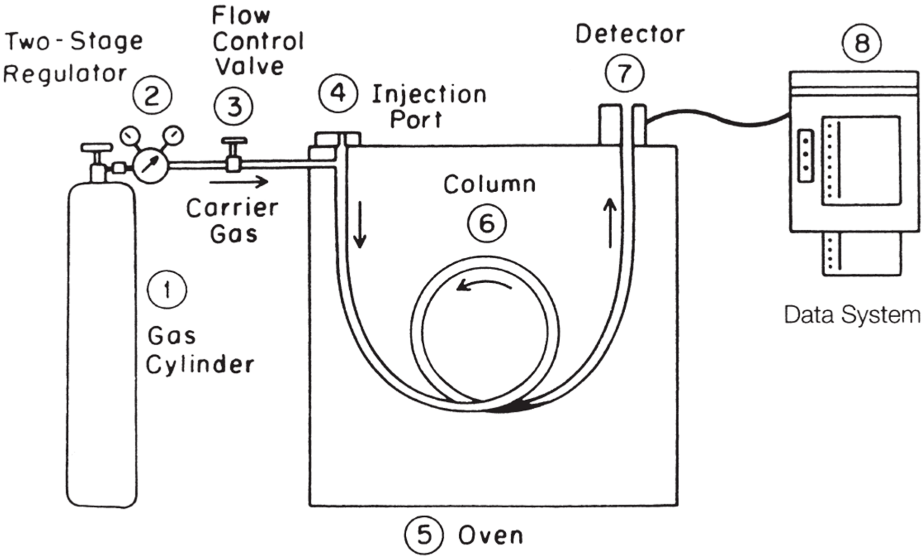

Figure 2.19: Scheme of the basic GC setup. Original graph taken from [82], p. 25.

2.5.1 Resolution

The resolution of a GC instrument R_S denotes the degree by which two solutes A and B producing two Gaussian peaks in the detector with their base widths $w_{b,A}$, $w_{b,B}$ are separated by a distance d, as seen in figure 2.20.

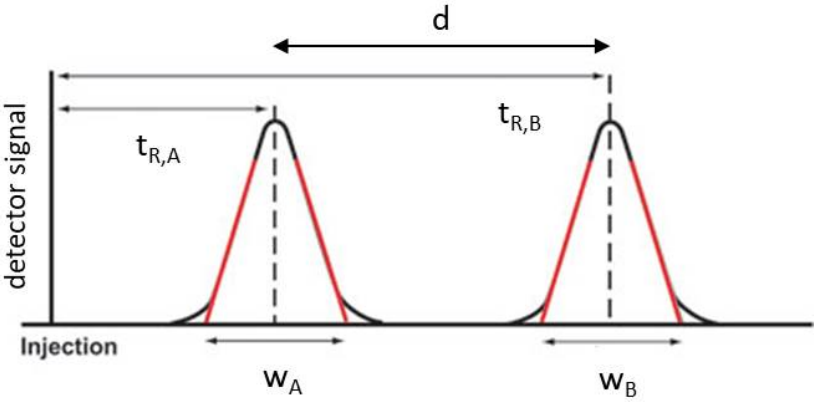

Figure 2.20: Scheme of two separated peaks from solutes A and B. Original adapted from [83].

$$R_S = \frac{t_{R,B} - t_{R,A}}{\frac{w_{b,B}+w_{b,A}}{2}} = \frac{2d}{w_{b,B} + w_{b,A}} \tag{2.24}$$

If the neighbouring peaks with equal area have the same base width $w_{b,A} = w_{b,B} = w_b$, then equation 2.24 simplifies to:

$$\mathrm{R_S} = \frac{\mathrm{d}}{\mathrm{w_b}} \tag{2.25}$$

For adequate separation, one strives for $\mathrm{R_S} \leq 1$, i.e., the peaks are not yet merging. Both d and $\mathrm{w_b}$ are dependent on the length of the column L. The retention time difference depends linearly on L, while the width of the peak increases with $\propto \mathrm{L}^2$. Therefore, $\mathrm{R_S}$ is inversely proportional to the square root of the length of the column. A longer column leads to a better separation of the solutes, but also longer retention times and thus a longer measurement time.

$$\mathrm{R_S} \propto \frac{\mathrm{L}}{\mathrm{L}^2} = \frac{1}{\sqrt{\mathrm{L}}} \tag{2.26}$$

2.5.2 Column and temperature control

GC columns contain the stationary phase, typically a liquid polymer material with polar / unpolar groups or substitutions, which then interacts with polar or unpolar solutes, respectively, due to van-de-Waals forces (unpolar) and hydrogen bonds (polar). Contaminations in the carrier gas helium, usually oxygen (O_2) or nitrogen (N_2), can contaminate or oxidise the stationary phase, leading to unreliable chromatograms and the degradation of the column, so very pure He gas sources and external gas purifiers are needed to prevent gas contaminations. The stationary phase is coated on a solid support, either a capillary or a so-called packed column, which was used for this thesis.

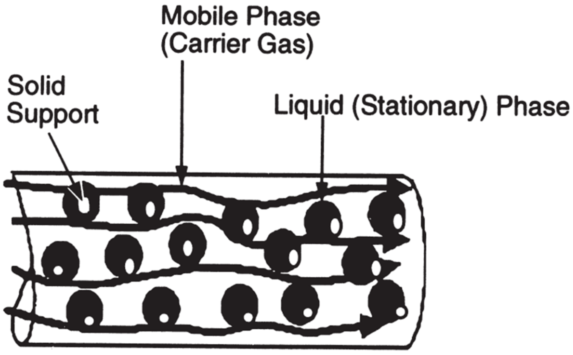

Figure 2.21: Cross section of a packed GC column. Original adapted from [82] p.24.

As depicted in figure 2.21, a packed column is usually made out of stainless steel or carbon and filled with particles that are coated with the liquid stationary phase, effectively forming a mesh, where the mobile phase carrying the gas sample is pushed through. In the column used here, the support is made of a carbon material. The number '80/100' on the specification sheet refers to the mesh or net formed by the particles, as in the so formed holes are smaller than a mesh 80 (diameter $\varnothing < 177\ \mu$m) but bigger than mesh 100 ($\varnothing > 149\ \mu$m). Due to their higher surface area and increased loading of the stationary phase, packed columns are usually used for separation of gas samples where maximum interaction of the otherwise relatively dilute sample with the stationary phase is ensured. For the detection of volatile, liquid species a capillary column was tested for our GC setup [27], but its detection limit was worse than the established HPLC detection limit of 2 ppm.

Next to the selection of a suitable stationary phase or column type, the choice of the temperature at which the column is kept during the measurement is the second important factor in determining or tuning the separation characteristics of the GC. Generally speaking, increasing the temperature of the column will decrease the net interaction of the gas sample with the stationary phase, therefore decreasing the retention times of all solutes. Though this might negatively impact the resolution of the column, it can also greatly decrease the measurement time. In the case of this thesis, where the gas sample is taken from the gas overhead of the electrolysis cell, water vapour is a major part of the gas sample, which can be retained for a long time in the stationary phase, leading to baseline shifts in the chromatogram and possible partial clogging of the column and diminished reproducibility of consecutive GC measurements. The programmed temperature ramps shown in figure 3.12 remove most of the water vapour from the column during a measurement while retaining separation of the gaseous solutes at the beginning of the temperature ramps.

2.5.3 Barrier Ionization Discharge (BID) Detector

The separated solutes exit the column and are then carried to a detector. Different types of detectors are available for GC, depending on the types of different solutes which need to be detected. In our GC instrument a Barrier Ionization Discharge (BID) detector [84] is implemented, as shown in figure 2.22.

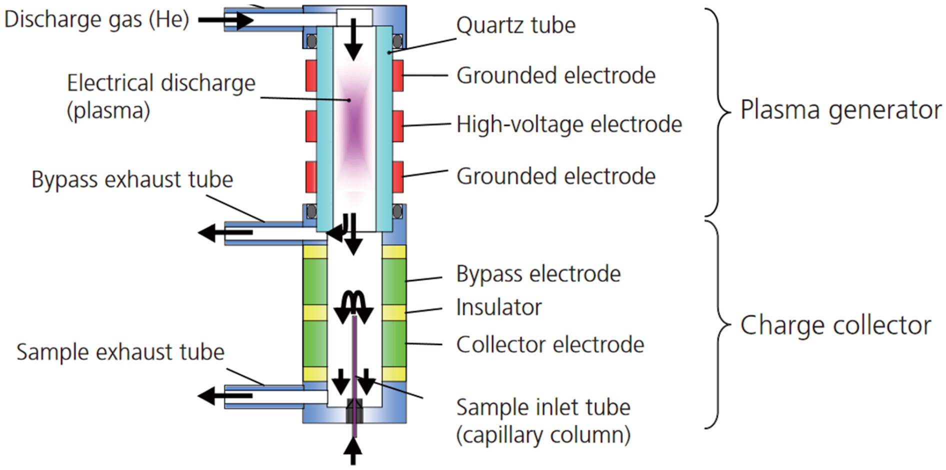

Figure 2.22: Cross sectional diagram of a BID. Original from [84].

In a BID a helium plasma is created using an alternating electric field [85] in a quartz tube and then mixed with the carrier gas containing the separated solutes streaming out of the sample inlet tube. Once the exited state of diatomic He_2 relaxes back to the dissociative 2He ground state ($He_2(A^1\Sigma_u^+) \rightarrow 2He(1S^1) + h\nu$) a photon with the energy $h\nu = 17.7$ eV is emitted, also known as the Hopfield emission [86]. These photons then ionize the solutes which subsequently create a signal at the collector electrode. BID detectors offer increased sensitivity compared to other detector types towards both CO_2, CO, methane, ethylene etc. as well as H_2 vapour and are therefore suitable for trace analysis of gaseous species. Its sensitivity towards H_2O vapour can be detrimental for measurements containing water vapour, as it can lead to interfering baseline shifts of the chromatogram due to a dominating water vapour signal.

2.6 Nuclear Magnetic Resonance (NMR)

^{1}H Nuclear Magnetic Resonance (NMR) was used as the product analysis tool for liquid reaction products in the electrolyte. The following explanations are based on [87] and [88]. NMR makes use of the intrinsic angular momentum or spin of a nucleus L.

$$L = \sqrt{l(l+1)}\hbar \tag{2.27}$$

with the spin quantum number l and the reduced Planck's constant $\hbar$. l can have integral and half-integral values (0, 1/2, 1, etc.) for different nuclei. For protons (^{1}H) $l = 1/2$. The projection of the spin on the z-axis parallel to a stationary magnetic field $\vec{B}_0$ can have the discrete values of $L_z = \hbar m$ with the magnetic quantum number m, which can take the values l, $l-1$, ... ,$-l$. A nucleus with a spin is also associated with a magnetic moment μ of the nucleus.

$$\mu = \gamma L \tag{2.28}$$

where the ratio between L and μ is called the magnetogyric ratio γ. When a number of identical nuclei is placed in a stationary magnetic field $\vec{B}_0$, their spins orient themselves along the magnetic field and can take up $2l+1$ orientations. Due to the interaction of the magnetic field $\vec{B}_0$ with the magnetic dipole of one nucleus, the energy of that dipole is now

$$E = \vec{\mu} \cdot \vec{B}_0 = \mu_z B_0 = \gamma m \hbar B_0 \tag{2.29}$$

For protons with $m = -1/2, +1/2$, there is now an energy difference between nuclei aligned parallel or anti-parallel to $\vec{B}_0$, resulting in the so called Zeeman energy levels.

$$\Delta E = E_{-1/2} - E_{1/2} = \gamma \hbar B_0 \tag{2.30}$$

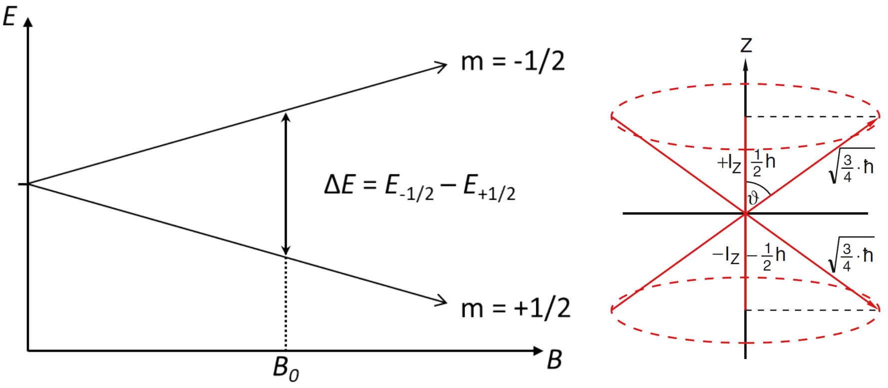

Figure 2.23: Left: Scheme of Zeeman energy level splitting due to an external magnetic field $\vec{B}_0$. Right: Scheme of two $l = 1/2$ spins precessing parallel and antiparallel to $\vec{B}_0$, which is parallel to the z-axis. Original graph taken from [89].

In the classical model depicted in figure 2.23, the spin of the nucleus L precesses around $\vec{B}_0$ at an angle ϑ with $\cos\vartheta = \frac{L_z}{L} = \frac{m}{\sqrt{l(l+1)}}$ at the orbital frequency called the Larmor frequency ν_L.

$$\nu_\mathrm{L} = \frac{\gamma}{2\pi} B_0 \tag{2.31}$$

When such a nucleus in the lower energy level absorbs radiation with the Larmor frequency ν_L, it can transition to the higher energy level.

$$\Delta E = \gamma \hbar B_0 = h \nu_\mathrm{L} \tag{2.32}$$

A small excess of nuclei exists on the lower energy level of a spin-1/2 system such as ^{1}H at low temperature, due to a Boltzmann distribution.

$$\frac{\mathrm{N}_{-1/2}}{\mathrm{N}_{+1/2}} = \exp\left(\frac{\Delta E}{\mathrm{kT}}\right) \tag{2.33}$$

with the Boltzmann constant k, temperature T and $\mathrm{N}_{-1/2}$, $\mathrm{N}_{+1/2}$ being the number of nuclei on the respective higher and lower energy level, leading to a net magnetization $\vec{M} = M \cdot \hat{e}_z$.

2.6.1 The source of the NMR signal

It is this net magnetization M which subsequently can be perturbed by applying a sinusoidally oscillating magnetic field $\vec{B}_1$ in the xy-plane perpendicular to the stationary magnetic field $\vec{B}_0$ with the Larmor frequency ν_L. Only with the right frequency $\nu_0 = \nu_\mathrm{L}$ can the magnetic perturbation field $\vec{B}_1$ effect a net magnetization in the xy-plane, which was zero before the perturbation. In a rotating frame with x', y' rotating with the Larmor frequency ν_L around the z-axis, the now stationary perturbation field $\vec{B}_1$ pointing in the x'-direction can turn the net magnetization $M_{y'}$ completely into the x'y'-plane parallel to the y'-axis, as depicted in figure 2.24. Such a pulse is called 90° pulse.

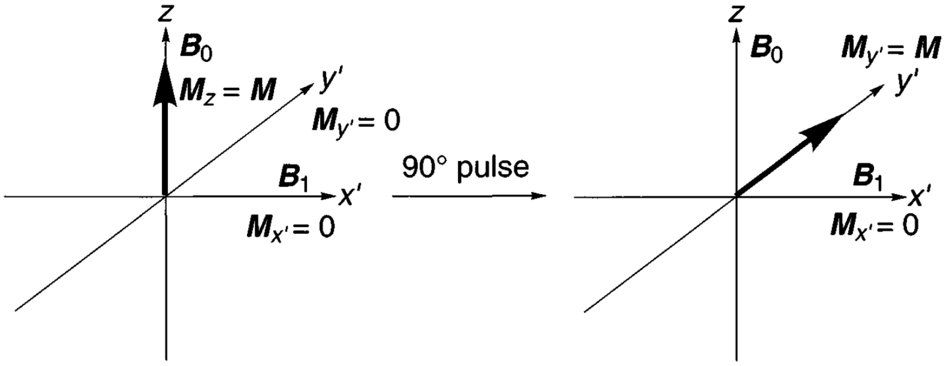

Figure 2.24: Scheme of a 90° pulse applied to the net magnetization M, leading to a $M_{y'}$ parallel to the y'-axis. Original graph taken from [87].

Once the perturbation field $\vec{B}_1$ is switched off, the turned net magnetization relaxes back to its initial state parallel to z-axis, i.e., $M_{y'}$ declines back to zero. The diminishing magnetization in y'-direction can induce a current in the detection or receiver coils placed in the x'y'-plane, which has to be insensitive to $\vec{B}_1$ created by the transmitter coils. A sample consisting of only one type of nuclei produces a decaying cosine signal, which, once subtracted from the spectrometer frequency, yields the so called Free Induction Decay (FID) signal. Fourier transformation of the FID yields a frequency function, where at the Larmor frequency a peak appears with a line width inversely proportional to the characteristic time constant of the decay envelope of the FID.

2.6.2 The chemical shift

The spin of the ^{1}H nucleus is partially shielded by the electron and its motion around the proton, which creates a magnetic field opposing the stationary magnetic field $\vec{B}_0$. The Larmor frequency has to be augmented by a screening constant σ reflecting this shielding.

$$\nu_\mathrm{L} = \frac{\gamma}{2\pi} B_0 (1 - \sigma) \tag{2.34}$$

Chemical bonds as well as neighbouring molecules modulate the density of electrons at the hydrogen nuclei in the sample, changing their shielding which leads to ^{1}H nuclei possessing not one but multiple Larmor or resonance frequencies. In order to perturb nuclei with different resonance frequencies, a short pulse of a monochromatic magnetic field $\vec{B}_1$ with a bandwidth of frequencies is applied to the sample. The resulting FID consists of the superposition of all decaying cosine functions, as seen in figure 2.25, exemplarily for two frequencies.

The resonance frequencies of the differently shielded nuclei are commonly plotted in reference to a marker substance with known Larmor frequency $\nu_\mathrm{L,m}$. The ratio of the frequency difference between the unknown and the marker substance to the marker frequency is called the *chemical shift* δ.

$$\delta = \frac{\nu_\mathrm{L} - \nu_\mathrm{L,m}}{\nu_\mathrm{L,m}} \tag{2.35}$$

A commonly used marker molecule is tetramethylsilane $(CH_3)_4Si$ (TMS) with a known resonance frequency of $\nu_\mathrm{L,TMS} \approx 400$ MHz ($B_0 = 9.39$ T). δ is usually expressed in parts per million (ppm). Exemplarily, the spectrum of ethyl bromide is shown in figure 2.26, which is very similar to the signals of ethanol (compare it to the peaks from ethanol in the calibration figure 3.10).

Spin-Spin coupling

Often times the hydrogen atoms of different parts of a molecule and their spins affect their respective resonance frequencies, leading to a splitting of the resonances. In the case of ethanol, the spins of the hydrogen atoms from the CH_2- group lead to a splitting of the CH_3 resonance peak into a main peak with no coupling (the two spins of the CH_2-group are anti-parallel and cancel each other out) flanked by two smaller peaks due to the perturbation of the overall spin of the CH_2- group, as seen on the right side in figure 2.27, with their peak height ratio of 1:2:1 due to the two possible spin configurations for zero net spin compared to the single configurations for net spin $\sum m = \pm 1$. In the same fashion, the three hydrogen atoms in the CH_3 group perturb the resonance frequency of the protons in the CH_2- group into splitting into four peaks, now with a

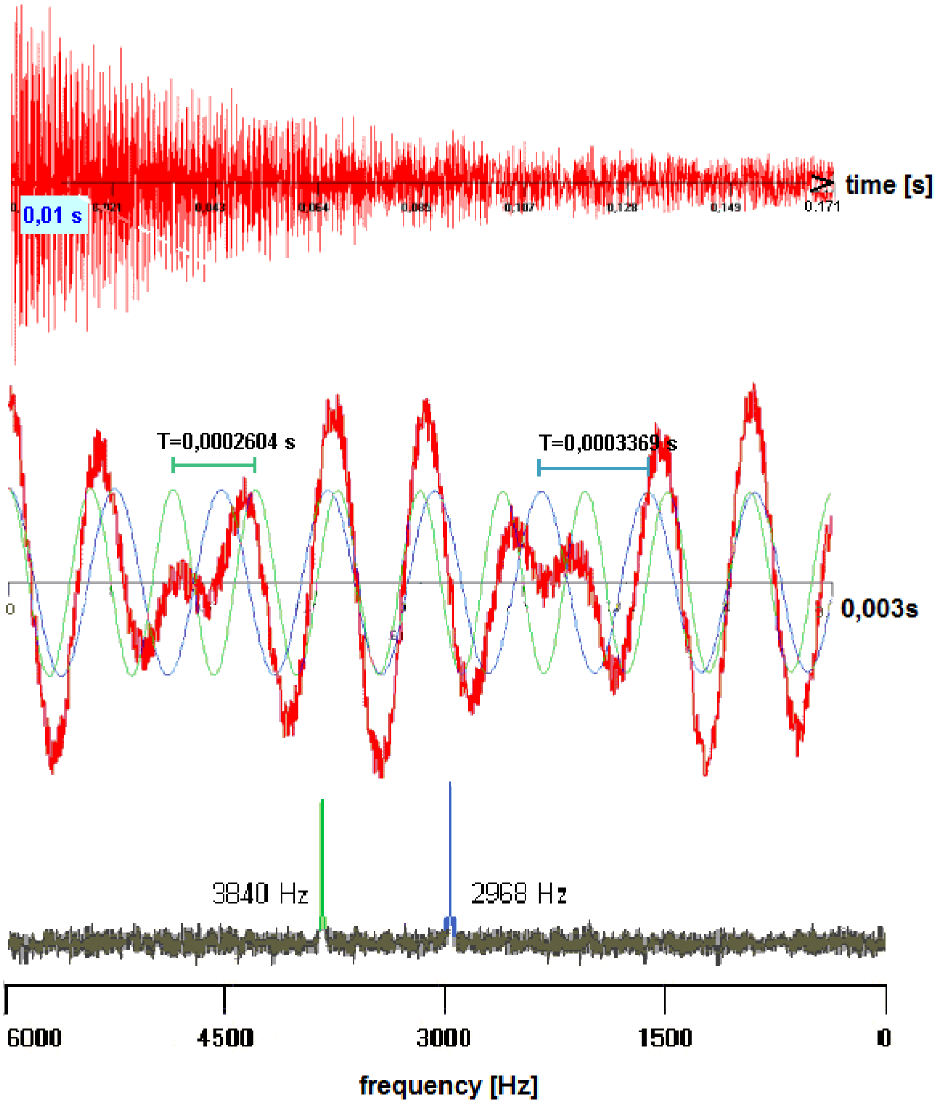

Figure 2.25: Examplary FID composed of two decaying cosine functions with two different resonance frequencies and the resulting Fourier-transformed plot. Taken from [27], adapted from [90].

height ratio of 1:3:3:1, as seen in the left side of figure 2.27. The coupling constant J denotes the magnitude of the coupling interaction.

The number of resulting peaks due to the spin-spin coupling is called multiplicity $N = 2l+1$. This fine structure of the resonance peaks can be used to further determine the chemical species in question and their respective molecular shapes.

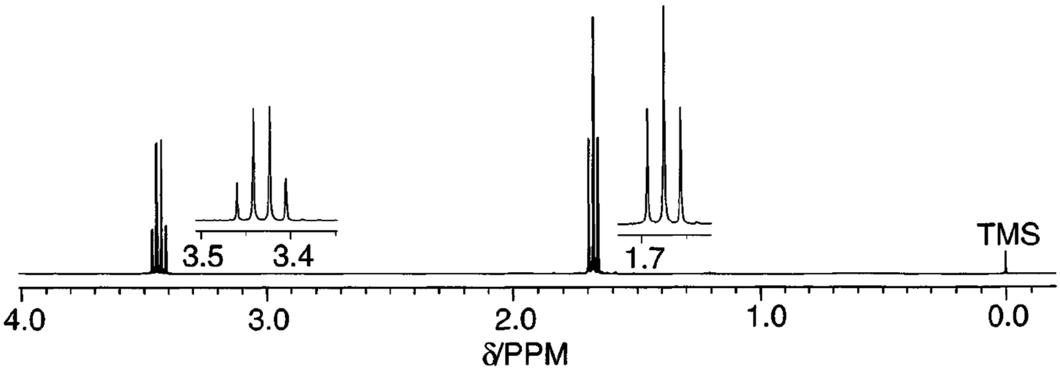

Figure 2.26: NMR spectrum of ethyl bromide (CH_3CH_2Br) in $CDCl_3$, with the CH_3 and CH_2- signals enlarged. 400 MHz ^1H NMR. Original figure taken from [87]

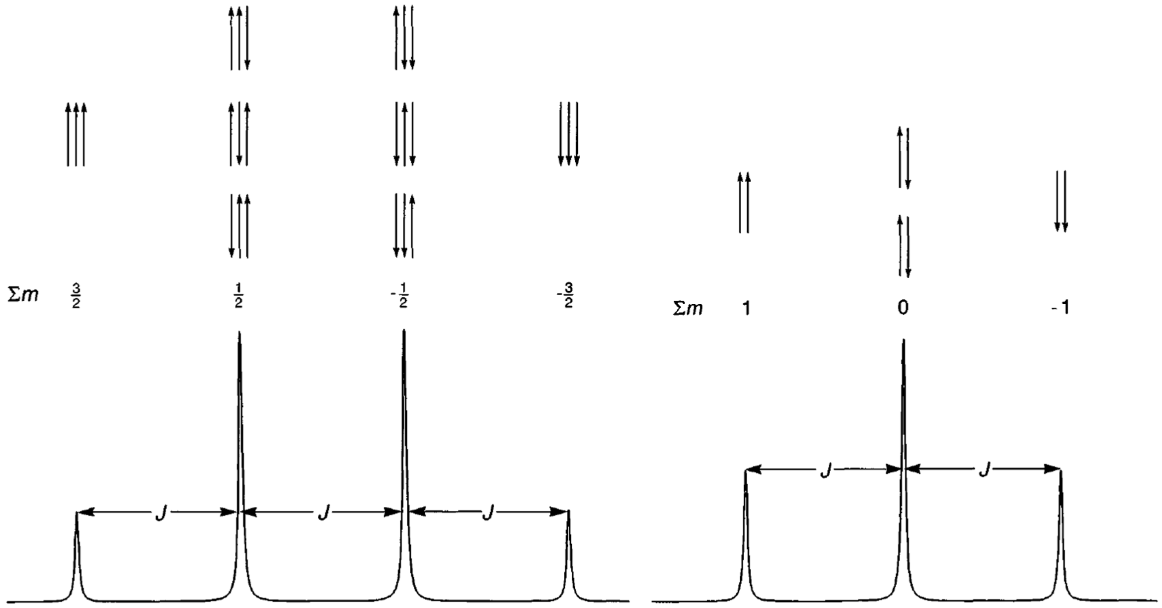

Figure 2.27: Left: Scheme of the splitting of the CH_3 resonance peak due to the spin-spin coupling with the two protons in the CH_2- group into a triplett. Right: Scheme of the splitting of the CH_2 resonance peak due to the spin-spin coupling with the three protons in the CH_3- group into a quartet. Original figure taken from [87].

2.6.3 Water suppression

The samples measured in the NMR instrument are taken directly from the electrolyte and consist mainly of H_2O. The solvent or H_2O signal would therefore dominate the resulting NMR spectrum and either cover up signals of other electrolyte components such as reaction products in the decaying flanks of its peak, or the ratio of signal strengths of non H_2O components farther away from the H_2O peak would fall into the noise range of the detector, if it is matched up with the signal strength of H_2O. Water suppression has to be applied to dampen the signal of H_2O. Before the actual perturbation pulse (pulse number 3 in figure 2.28) the sample is treated to a presaturation step and an exitation step [91]. The simplest presaturation step consists of a low amplitude, continuous perturbation field with the H_2O frequency, which leads to the saturation of the spins from water hydrogen atoms in the x'y'-plane. Hopefully, there are no spins of water hydrogen atoms left in the z direction, which could be perturbed by the final perturbation pulse. The excitation step usually features several magnetic field pulses of the perturbation field with the goal of enhancing the net magnetization of the non-solvent species while reducing the net magnetization of the solvent. For the thesis, the preparation and excitation steps are exemplarily schemed in figure 2.28.

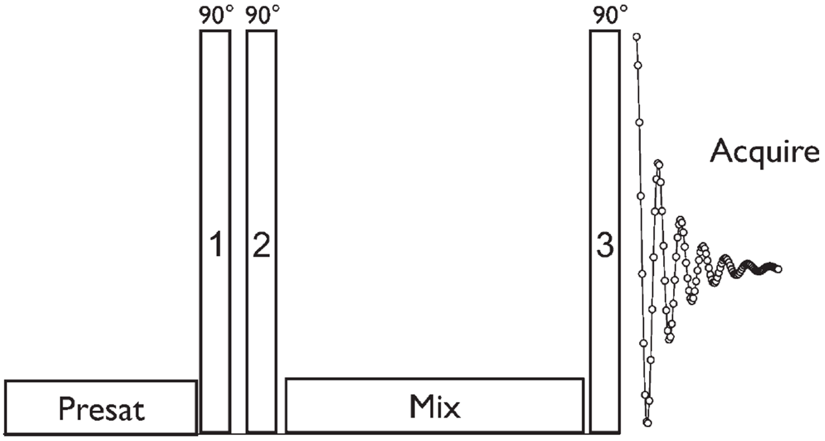

Figure 2.28: Scheme of a water suppression procedure with presaturation / exitation steps called NOESY-1D, similar to the suppression method used for the NMR measurements in chapter 3.5.1. Original figure taken from [92].

Chapter 3

Experimental details

In this chapter the experimental details of the measurements conducted in the following result chapters are presented, including the design and installation of experimental setups used in the thesis as well as the preparation of the electrodes and other components of the measurements.

3.1 Materials and cleaning procedures

The chemicals listed in table 3.1 were used as bought. Ultrapure H_2O (specific resistance: 18.2 MΩcm, trace of organic content (TOC) 1 ppm) was provided by a Purelab Ultra ultrapure water purification system (ELGA, USA). All glass ware was cleaned in a two step process, which consisted of soaking in 0.1 M nitric acid (HNO_3) overnight and afterwards soaking in 1 M potassium hydroxide (KOH), followed by thoroughly rinsing in ultrapure H_2O. All PTFE, PCTFE and Viton parts were cleaned in concentrated Caro's acid ($1:1$ mixture of 96% sulfuric acid (H_2SO_4) and 40% hydrogen peroxide (H_2O_2)) and cooked in hot H_2O ($\approx 80°$ C) overnight to remove residual H_2O_2, PMMA beaker was soaked in 1% potassium permanganate ($KMnO_4$) and subsequently in 30% hydrochloric acid (HCl).

3.2 Silicon substrate preparation

For the experiments in this thesis, silicon wafer from Si-Mat Silicon Materials, Germany were used (CZ, 3 inch diameter, one side polished, (111) orientation, 0.5 ° miscut, n-doped with phosphorus, 1-10 Ωcm or p-doped with boron, 5-25 Ωcm). From the wafers, quadratic samples (11.8×11.8 mm^2) were cut using a mechanical diamond scriber and broken using clean microscope slides. The cut wafer was rinsed with isopropanol and blow dried with argon gas (Ar), while the glass slides were wiped with isopropanol after each sample to mitigate possible scratching of the samples due to small particles from scribing and wafer breaking. After this step, the Si sample were only handled using (cleaned) PTFE tweezers and holders to minimise scratching and contaminations. As a pre-cleaning step, the samples were ultrasonicated in acetone, isopropanol, and ultrapure H_2O for 5 min. each. When changing the cleaning solution, the samples were rinsed with the subsequent solution to avoid possible solution residues due to condensation. The samples were then blow dried with Ar and oxidized in an oxygen

Chemical species	Concentration	Purity grade	Company	Usage
H_2SO_4	96 %	Suprapur	Merck	Electrolyte
HF	40 %	Suprapur	Merck	Electrolyte
3-aminopyridine	-	99 %	Sigma Aldrich	Electrolyte
4-aminopyridine	-	99 %	Sigma Aldrich	Electrolyte
$NaNO_2$	-	99.999 %	Alfa Aesar	Electrolyte
Sodium acetate	-	Emsure	Merck	Electrolyte
KCl	-	Suprapur	Merck	Electrolyte
K_2SO_4	-	Suprapur	Merck	Electrolyte
HCl	30 %	Suprapur	Merck	Electrolyte
NH_4F	40 %	VLSI	Honeywell	Etching
H_2SO_4	95-97 %	Emsure	Merck	Cleaning
H_2O_2	30 %	-	Sigma Aldrich	Cleaning
$KMnO_4$	-	Normapur	VWR Chemicals	Cleaning
HCl	30 %	Normapur	Merck	Cleaning
HNO_3	68%	Normapur	VWR Chemicals	Cleaning
Methanol	100 %	Normapur	VWR Chemicals	Cleaning, NMR
Ethanol	100 %	Normapur	VWR Chemicals	Cleaning, NMR
Isopropanol	100 %	Normapur	VWR Chemicals	Cleaning, NMR
Acetone	100 %	Normapur	VWR Chemicals	Cleaning, NMR
Pyridine	100 %	Normapur	VWR Chemicals	NMR
Formaldehyde	37 %	ACS reagent	Sigma Aldrich	NMR
Formic acid	99 %	Chromanorm	VWR Chemicals	NMR
D_2O	99.85 atom % D	-	Sigma Aldrich	NMR
Argon	-	$\leq$ 99.999 %	Westfalen	Electrolyte
CO_2	-	$\leq$ 99.995 %	Westfalen	Electrolyte
He	-	$\leq$ 99.9999 %	Westfalen	GC

Table 3.1: Chemicals used for the experiments described in this thesis.

plasma (5 min., $p_{O_2} = 1.4$ mbar, 200 W, Technics Plasma 100-E, Germany) in order to obtain a clean silicon surface with a smooth, amorphous 1-2 nm thick oxide layer on top. Before an electrochemical experiment one of these (oxidized) samples was loaded onto a PTFE sample holder, which held the sample in an upright position during all same cleaning steps mentions above as well as etching steps to enhance the solutions flow off the samples (see fig. 3.1).

The sample was ultrasonicated subsequently in acetone, ethanol, and ultrapure H_2O for 5 min., being rinsed between the cleaning steps with the subsequent solution during the change of the cleaning solution.

Etching of the cleaned sample was conducted in concentrated ammonium fluoride (NH_4F, 40% wt or 18 M, Honeywell) for 10 min. in the dark. While the rough backside of the sample was eventually covered by H_2 bubbles during the etching step [47, 93, 94], the polished side remained empty. Bubble formation on the polished side of the silicon sample would point towards scratches and other irregularities on the surface at which the etching process and thus H_2 evolution was increased [93]. Such samples were excluded from further use due to possible promotion of unwanted charge transfer processes [47, 95]. When removing it from the etching solution, the etched sample should be hydrophobic [47, 96, 97] and become dry instantly. Droplets remaining around the edges and bevels of the sample were carefully removed using laboratory wipes, taking

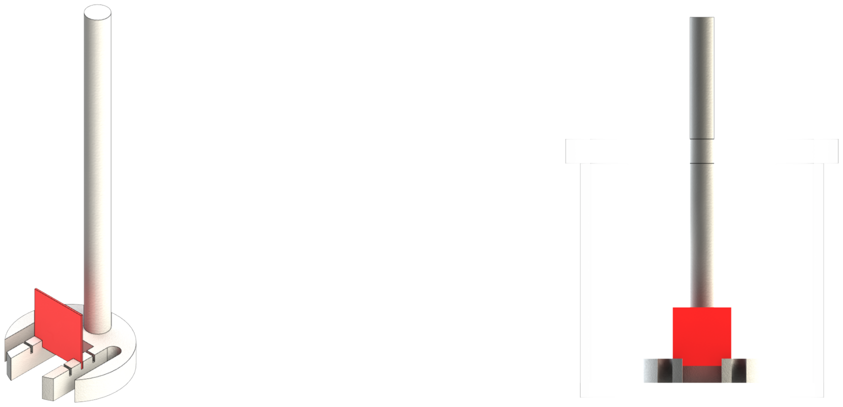

Figure 3.1: 3D drawing of the PTFE sample holder used for handling the silicon sample (red) inside the beaker during the cleaning and etching steps.

care not to touch the etched surface. The etched silicon sample was then mounted onto the electrode holder or electrolysis cell described in the following chapters 3.4.1 and 3.4.2. The goal of the etching step was to remove the oxide layer ontop of the silicon electrode and obtain an atomically flat, hydrogen terminated (H-terminated) silicon surface [47,93,94,96,98,99]. In 40% NH_4F as the etching solution, the steps perpendicular to the (111) plane are preferrably etched, leading to the formation of atomically flat (111) terraces with the maximum terrace width depending on the miscut angle to the (111) plane [47, 94, 100, 101]. Ex-situ and in-situ scanning tunneling microscopy (STM) and electrochemical STM (ECSTM) measurements of etched samples show the formation of theses silicon bi-layer steps with a step height of 3.14 Å.

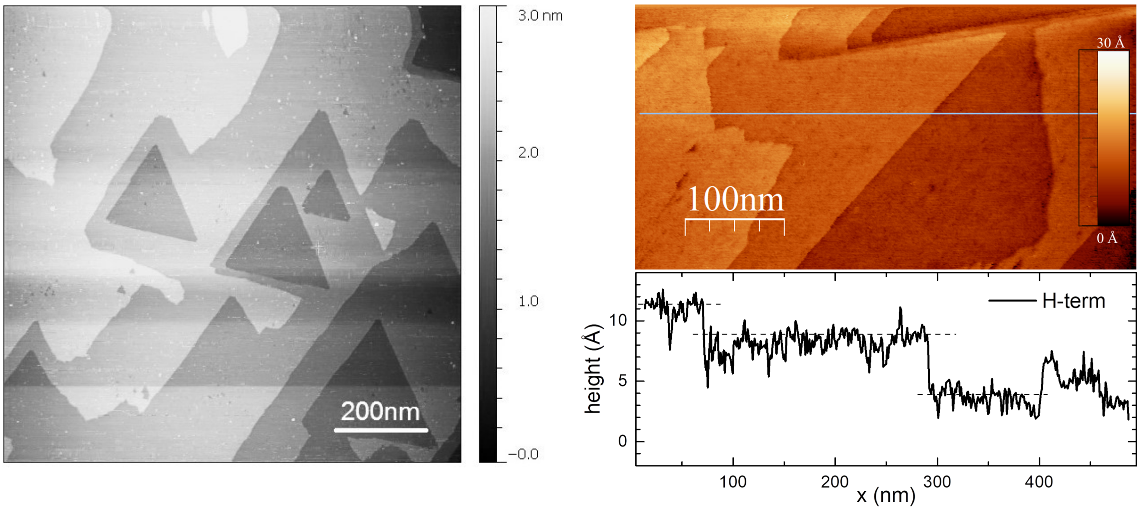

Figure 3.2: STM pictures of an H-terminated Si(111) sample as obtained by the described etching procedure. Left: Ex-situ STM in N_2 atmosphere. Measurement by Dr Alexander Solovev[1];. Right: In-situ ECSTM in 0.1 M H_2SO_4, purged with Ar. Measurement by Francesco Casablanca[1]. Original data from [102].

A few triangular shaped depressions were also observed in figure 3.2. These cor-

---

[1] Non-equilibrium Chemical Physics, Technical University Munich Physics Department

respond to etch pits, which form when oxygen (O_2) is present in the etching solution [93, 94, 103], but the limited occurrence of these etch pits was accepted without purging the NH_4F solution with Ar to remove O_2 as suggested in the literature. Especially in the beginning of the thesis the oxygen plasma step proved very useful for the removal of point-like or rectangular defects on the terraces [93] otherwise often visible in the STM pictures, as seen in figure 3.3.

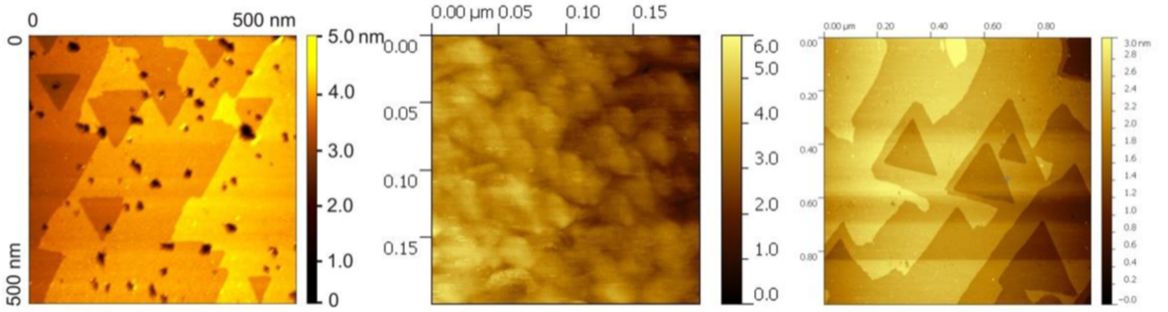

Figure 3.3: Ex-situ STM pictures of an etched Si(111) sample without plasma oxidation (left) featuring dark defects of unknown origin, a plasma oxidized silicon sample before etching (middle) and finally a plasmaoxidized sample after etching without the defects. Measurement by Dr Alexander Solovev. Original from the bachelor thesis of Sebastian Lindner [68].

3.3 XPS measurements

For the first set of measurements (figures 4.16, 4.17, 4.19) a custom XPS instrument with an aluminium (Al) Kα X-ray source (nonmonochromatic, hν = 1486.6 eV) and a hemispherical analyzer (VSW Atomtech Ltd., UK) was used. The analysis spot is circular with an area of approximately 1 cm^2. The XP spectra were fitted with Doniach-Sunjic functions [104]. The rest of the measurements were conducted using an XPS instrument with a non-monochromatic XR-50 Al Kα X-ray source (SPECS, Germany) and a Phoibos 100/150 Hemispherical Energy Analyzer (SPECS, Germany). The X-ray source was operated at 350 W (12 kV, 29.2 mA), the slit in front of the analyser set at 7 × 20 mm^2. The detector was set to Large Area mode (LA) with an acceptance area / source size of 5 mm and a pass energy of E_{pass} = 10 eV. Data analysis of XP spectra was performed using OriginPro (Originlab, USA) including its Shirley background subtraction and fitting. Silicon samples were cut down to about 4 × 10 mm^2 using a diamond cutter and then fixed on the XPS sample holder in such a way that an H-terminated silicon sample and a grafted 3-pyridine-terminated silicon sample could be placed next to each other on a single XPS sample holder with a space of $\approx$ 3 mm between them. Before fixing them on the holder, silicon samples were cleaned and etched as described above and blow-dried using Ar or nitrogen (N_2) gas. The time between gas drying and insertion into the vacuum load lock was under 2 min. Using the sample manipulator, one could then move either of the samples in and out of the detector beam path.

3.4 Electrochemical measurements

Electrochemical measurements were controlled mainly by a Zennium potentiostat / galvanostat with a frequency response analyzer (FRA) unit (Zahner, Germany). Some electrochemical measurements, for example electrolysis measurements, were controlled using the SP-300 potentiostat (Biologic, France) and the PGU-10V-1A-IPS-S potentiostat (IPS, Germany). For electrochemical impedance measurements the CE and RE were shorted using a 100 nF capacitor in order to minimize the high frequency resistance above 100 kHz during EIS measurements. If not stated otherwise, measurements were conducted inside a Faraday cage in the dark. For illuminating p-doped silicon electrodes a HighLED LED (LINOS, USA) illumination source was used, which had a wavelength of 633 nm and an intensity of 1.33 mW/cm^2 (as decribed in the bachelor thesis of Sebastian Lindner [68]). The intensity was determined with a handheld photometer in an empty, dry glass beaker while the LED was positioned outside of the beaker tangential to the outer glas wall. Data analysis of the electrochemical measurements was performed with OriginPro, while fitting of the electrochemical impedance spectra (EIS) data plotted as Nyquist plots [72] was performed using Zview (Scribner, USA) or EIS Spectrum Analyser [105] by applying the described equivalent circuit (see fig. 2.8).

3.4.1 Electrochemical Cell

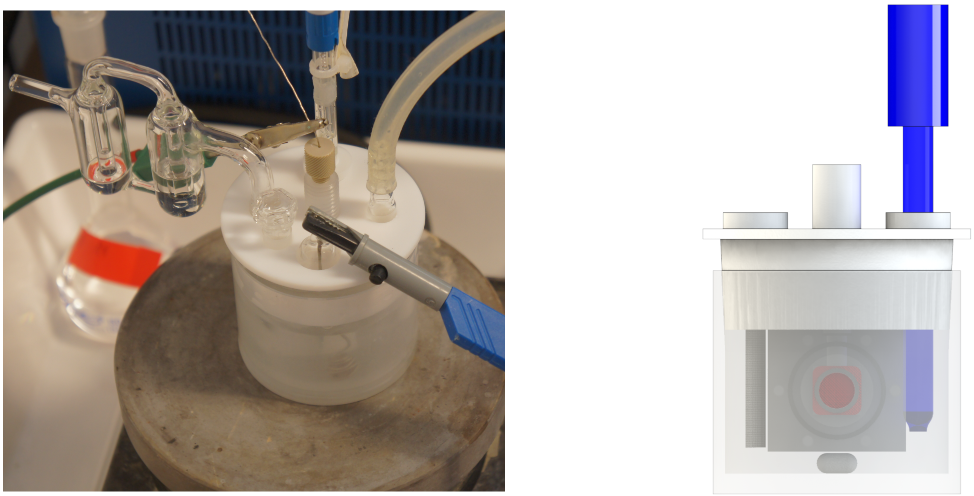

Figure 3.4: Picture (left) and 3D drawing (right) of the electrochemical cell. The three electrodes depicted in the rendering are colorcoded as follows: RE (blue), silicon WE (red) and glassy carbon CE (gray). Picture from the master thesis of Andreas Heine [27].

The electrochemical experiments were carried out in an one-compartment PTFE / PMMA three electrode electrochemical cell (see fig. 3.4) with the silicon sample mounted on a custom built PCTFE electrode holder as the working electrode, a saturated calomel reference electrode (SCE) or a saturated mercury sulfate reference electrode (MSE), and a glassy carbon counter electrode.

The custom PCTFE electrode holder in figure 3.5 pressed the sample onto a 9 × 1 O-ring (Viton, Alwin Höfert, Germany), which also determined the geometrical area

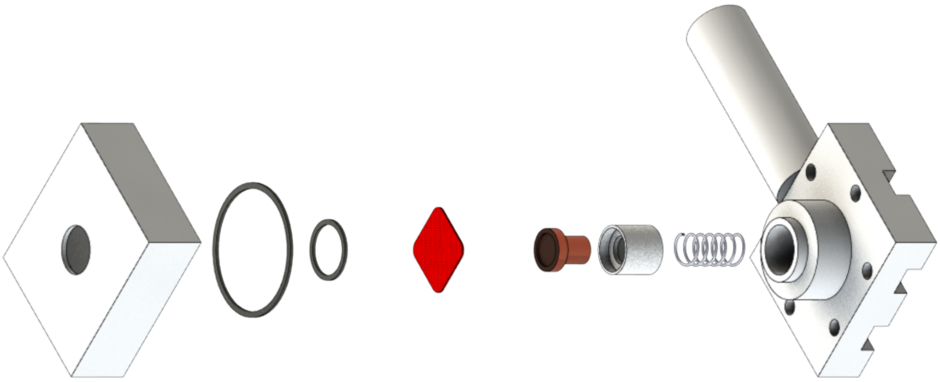

Figure 3.5: 3D drawing of the components of the custom PCTFE electrode holder with the silicon electrode (red), the pair of Viton O-rings (black) in front of the electrode, and the copper stamp containing the GaIn eutecticum behind the electrode.

of the electrode in contact with the electrolyte (0.63 cm^2). Another, larger O-ring was used to seal off the inside of the holder against electrolyte leakage. A spring-loaded copper stamp holding the gallium indium (GaIn) eutecticum [47] pressed against the back side of the electrode to ensure electrical contact. The electrolyte was purged via a small glass frit with Ar or CO_2 gas, and in some cases stirred during the measurements with a magnetic stirrer. Reference electrodes were rinsed copiously before and after each measurement and otherwise stored in a saturated KCl (for SCE) or saturated K_2SO_4 solution (for MSE). Glassy carbon electrodes were stored in Caro's acid and cooked in hot H_2O overnight to remove residual H_2O_2. A PTFE covered stirring fish (∅ 5 mm, VWR) was used to stir the electrolyte, also stored in Caro's acid and cooked in hot H_2O. The electrolyte was purged with Ar or CO_2 for at least 30 min. in an external glass container before introduction into the cell. WE, RE, and CE were connected to the potentiostat in a "dry" or empty cell. Afterwards the pre-purged electrolyte was introduced into the dry cell. The heights of the RE and CE were adjusted in such a way that the rising electrolyte level would contact the CE first, then the RE and the silicon WE last to ensure that the silicon electrode would be potentiostatically controlled and set at a (cathodic) resting potential to prevent its possible oxidation, once it comes into contact with the electrolyte. The electrolyte was then purged with Ar or CO_2 for 30 min. before the first electrochemical measurement. After the end of a measurement the cell and the external electrolyte container were first emptied using syringes and filled up with ultrapure H_2O for three times in order to wash off electrolyte residuals.

3.4.2 Electrolysis Cell

Electrolysis measurements were carried out in a dedicated, custom PCTFE three compartment cell (see fig. 3.6), where the main compartment with the working electrode is separated from the two compartments housing reference and counter electrode, respec-

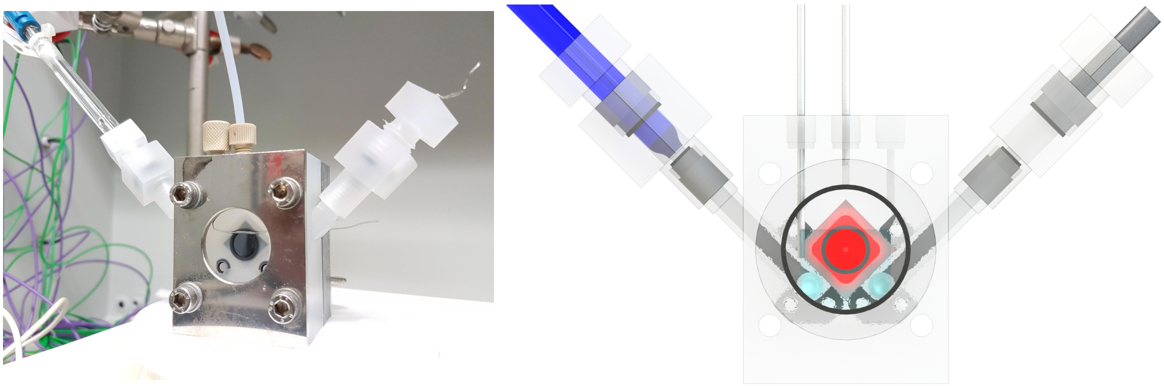

Figure 3.6: Picture and 3D drawing of the electrolysis cell. The three electrodes depicted in the rendering are color-coded as follows: RE (blue), silicon WE (red) and glassy carbon CE (gray).

tively, by Nafion membranes (Nafion117), as depicted in figure 3.7. In order to ensure an electrolysis product concentration comparable to electrolysis experiments from literature [16, 25], the volume of the main compartment is sized such that the ratio of active electrode area and electrolyte volume was approximately 1 cm^2 to 1 ml. With the electrolysis cell, sometimes also a Pt wire was used as the CE. Ar or CO_2 was bubbled through the electrolyte in the main compartment via a thin PTFE tube during degassing. All PTFE, PCTFE parts and Viton O-rings were cleaned in Caro's acid overnight and subsequently cooked in hot H_2O overnight. Pt wire and glassy carbon CEs were cleaned in separate Caro's acid baths and again cooked in hot H_2O overnight. The Nafion membranes were punched out of the bulk Nafion sheet, wiped with acetone-drenched Kimtech wipes and ultrasonicated in acetone, isopropanol and H_2O 5 minutes each. Then the pre-cleaned membranes were cleaned in Caro's acid overnight and finally stored in H_2O till cell assembly. Initially, the membrane had a yellowish / brownish tint and expanded when it came in contact with acetone due to absorption. After the cleaning step in Caro's acid membranes turn transparent and regain their actual size before the acetone bath. This difference in color can be seen in the left picture of 3.8. In this state, the Nafion membranes offered sufficient conductivity even after month-long storage in H_2O without additional reactivation in boiling sulfuric acid or Caro's Acid.

Electrolyte was purged with CO_2 gas for at least 30 min. externally before introduction into the RE and CE compartments using pipettes. After connecting all electrodes the WE compartment was half-filled with electrolyte in order to establish electrical contact between RE and CE. Then, under potentiostatic control the WE compartment was fully filled, contacting the silicon WE with the electrolyte. The WE compartment was purged in CO_2 through a PTFE tube submerged in the electrolyte for at least 30 min. again after bringing the WE in contact with the electrolyte. During electrolysis measurements the gas tube was pulled out of the electrolyte. Otherwise, due to pressure gradients inside the tube, electrolyte tended to be pushed into the gas tube and out of the WE compartment. A PTFE covered stirring fish (∅ 1 mm, VWR) was used to stir the electrolyte. Before the experiment it was also stored in Caro's acid and cooked in hot H_2O. The position of the stir fish and the external stir motor can be seen in the picture on the right in figure 3.8.

At the end of measurements the WE compartment was emptied using a glass syringe

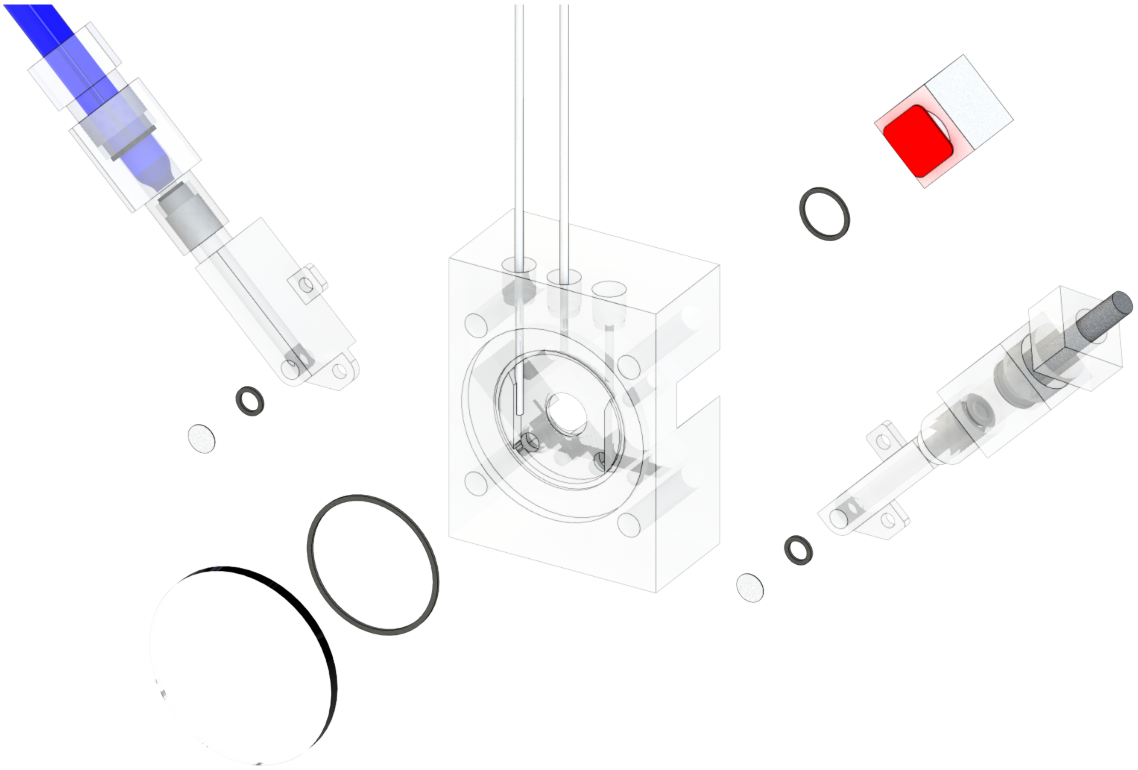

Figure 3.7: 3D drawing of the main components of the electrolysis cell exhibits the placement of the transparent Nafion membranes in front of the small O-rings separating the RE and CE compartments from the main WE compartment, respectively. The O-ring setup used for sealing the silicon electrode is identical to the one used for the sample holder depicted in figure 3.5. The three electrodes depicted in the rendering is color-coded as before: RE (blue), silicon WE (red) and glassy carbon CE (gray).

with an PTFE tube adapter in order to analyze the resulting electrolyte sample for electrolysis samples. Due to the sensitivity to contamination the glass syringe and PTFE tube was also cleaned in Caro's Acid and boiled in H_2O overnight. The electrolysis cell could be used for several measurements when the WE was washed / emptied and re-filled with ultrapure H_2O at least three times and stored in H_2O. Residual organic species from the prior measurement could be removed in this way and would not be detectable via NMR.

3.5 Product analysis

3.5.1 ^{1}H-NMR measurements

^{1}H-NMR spectroscopy was performed at 300 K using an Avance III 500 System (Bruker Biospin, Germany) with an UltraShield 500 MHz magnet and a SEI 500 S2 probe head (5 mm, inverse ^{1}H/^{1}3C with Z-gradient). For all samples, the ^{1}H-NMR spectra were acquired using the one-dimensional NOESY sequence "noesygppr1d.comp" with presaturation of the residual water signal during the relaxation delay (5 s) and the mixing time (10 ms) using spoil gradients. The acquisition time was 4.1 s. Spectra were the result of 512 scans, with data collected into 64 k data points. The analysed

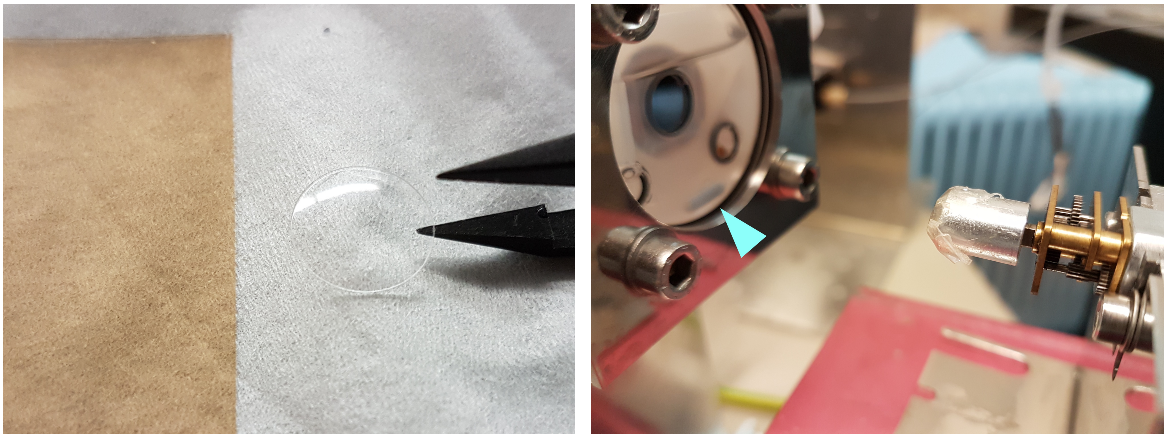

Figure 3.8: Left: Comparison of Nafion sheet in its initial state and a cleaned, ready to use Nafion membrane. Right: Custom built motored electromagnet used for turning the small stir fish (turquoise arrowhead) inside the WE compartment.

solutions (500 μL) were taken directly from the electrochemical cell after electrolysis and mixed with 40 μL of pyridine calibration solution (0.135 M pyridine) and 60 μL D_2O. NMR tubes (Scientific, 178 × 4.97 mm, 500 MHz, DURAN, Germany) were cleaned in fresh / hot Caro's acid overnight, cooked in ultrapure H_2O afterwards and dried with Ar. With the addition of the pyridine calibration solution each H_2O based sample (540 μL) contained 10 mM pyridine.

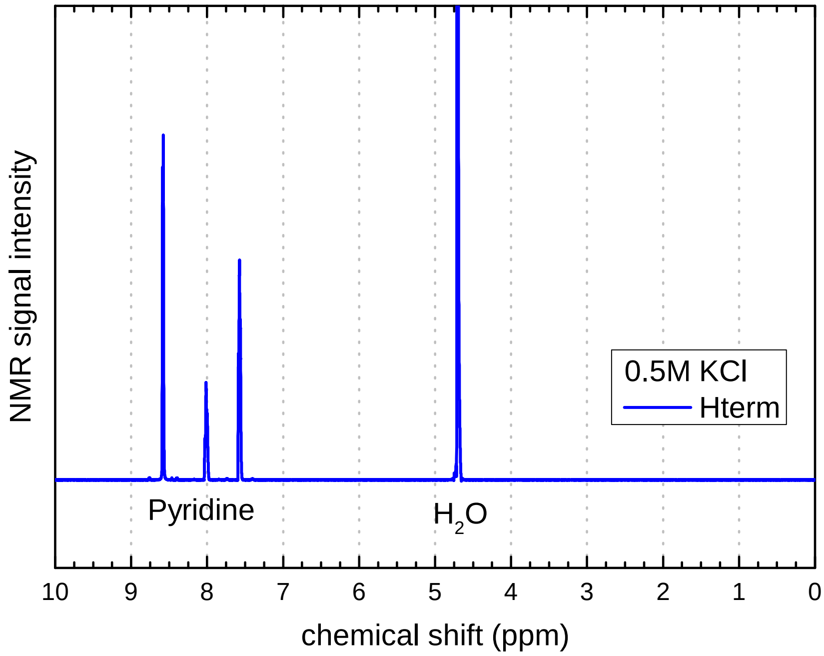

Figure 3.9: NMR spectrum of a clean 0.5 M KCl sample with the added pyridine calibration solution. Same data as in fig. 7.7, electrolysis sample of an H-terminated silicon electrode.

Of the three main pyridine peaks in the NMR, as depicted in figure 3.9, the area of the peak with the highest chemical shift around 8.7 ppm was used as the reference area, to which all other product and contamination peak areas inside of the sample were referenced to. The relative peak sizes were then correlated to known concentrations of the prepared calibration solutions which, using the known electrolyte volume inside the WE compartment, could be calculated into number of moles for the respective chemical species. The sensitivity was such that concentrations lower than 10 μM were detectable using NMR, as can be seen in the calibration plot in figure 3.10.

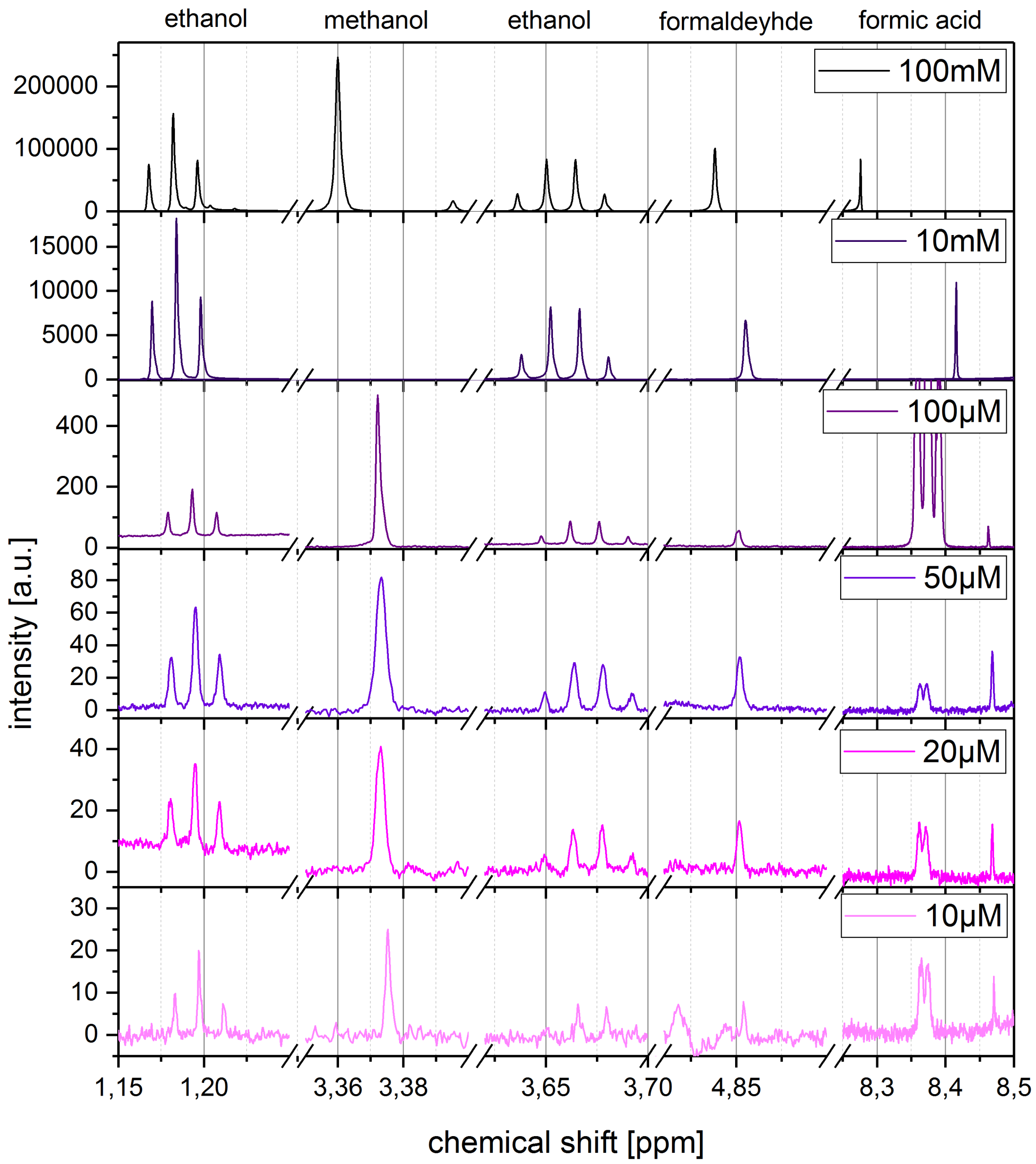

Figure 3.10: NMR spectra of different product and contamination species in 0.5 M KCl in descending concentrations down to 10 μM. Original from the master thesis of Andreas Heine [27].

3.5.2 GC measurements

GC measurements were conducted using a GC2010 Plus GC (Shimadzu, Japan) equipped with a barrier discharge ionization detector (BID 2010 Plus, Shimadzu, Japan) operating at a temperature of 300 °C and a micropacked ShinCarbon ST 80/100 (inner diameter 0.53 mm, length 2 m; Restek GmbH, Germany) column. It is continuously purged by helium (He, purity 6.0, Westfalen AG), which is further refined by two heated gas purifiers. The gas overhead of the electrolysis cell is sampled via semiautomatic sample collection with several valves controlled by the GC: In standby position (Position B), a 6-port valve connects the He supply line over a sample loop of 100 μL volume with the GC column (see Figure 3.11). Over the other two ports, a vacuum pump is connected to the electrolysis cell, both lines equipped with an additional 2-way valve. To draw a gas sample, the 6-port valve switches into position A so that the He line is directly connected to the column, while the sample loop is between vacuum pump and cell. By opening the valve in front of the pump, the sample loop can be evacuated. When this valve is closed and the one in front of the cell is opened, the vacuum inside the sample loop is filled by the overhead gas from the cell containing possible gaseous reaction products. Now, the analyte or carrier gas is transported into the column by switching of the 6-port valve into position B. Before starting the next electrolysis, cell, tubes and pump are purged with CO_2 under a small overpressure which is controlled by an additional pressure controller in the CO_2 supply line directly in front of the cell.

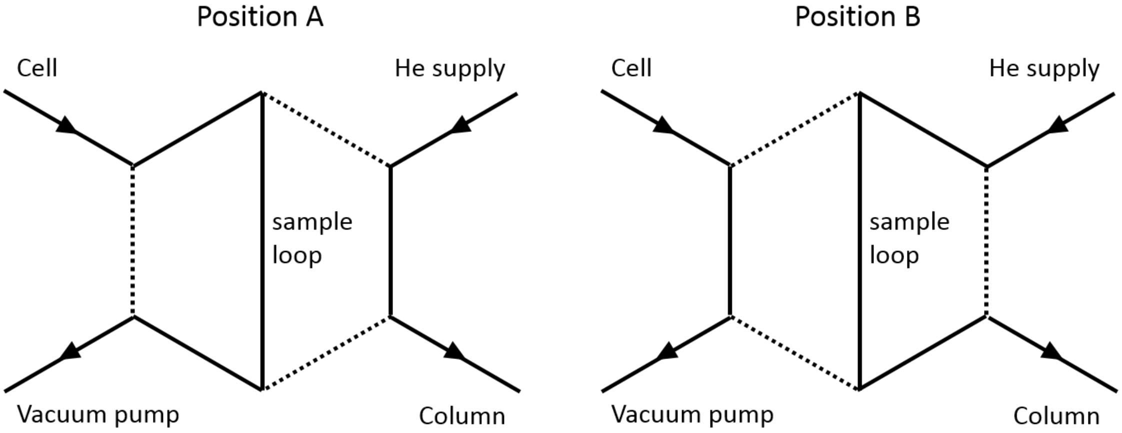

Figure 3.11: Working principle of the 6-port valve. From [106].

In order to achieve a separation of all relevant gas peaks, the measurements started from 60 °C with a ramp of 3 $\frac{°\mathrm{C}}{\mathrm{min}}$ until 80 °C, where the ramp rate was increased to 10 $\frac{°\mathrm{C}}{\mathrm{min}}$ up to a temperature of 150 °C. There, it stayed constant for 4 min and finally ramped up to 200 °C with 40 $\frac{°\mathrm{C}}{\mathrm{min}}$. In parallel, a pressure ramp started at 130 kPa with 12 $\frac{\mathrm{kPa}}{\mathrm{min}}$ up to 250 kPa, where it stayed constant for the rest of the measurement. These parameter developments are plotted in figure 3.12.

The measurement routine has been calibrated using a gas mixture containing 1.08 % hydrogen, 1.01 % carbon monoxide, 1.02 % methane, 1.27 % ethene and 95.6 % carbon dioxide (custom mix by Linde AG, Germany; relative measurement error: 2 %) and the calibration method of the LabSolutions software (GC software from Shimadzu, Japan). Since the BID detector has a very linear behavior and a reproducible dilution of gases could not be guaranteed, only the original gas mixture has been measured three times and the average value for each species have been used. Using LabSolutions the ratio of the detectable gases were detected and finally used to split the partial electrolysis charge, which was left after subtraction of the charge used for the production of the liquid products, i.e., the absolute (calibrated) size of product gas signals were not considered, rather than their ratio. For the measurements in figure 7.3 the gas overhead

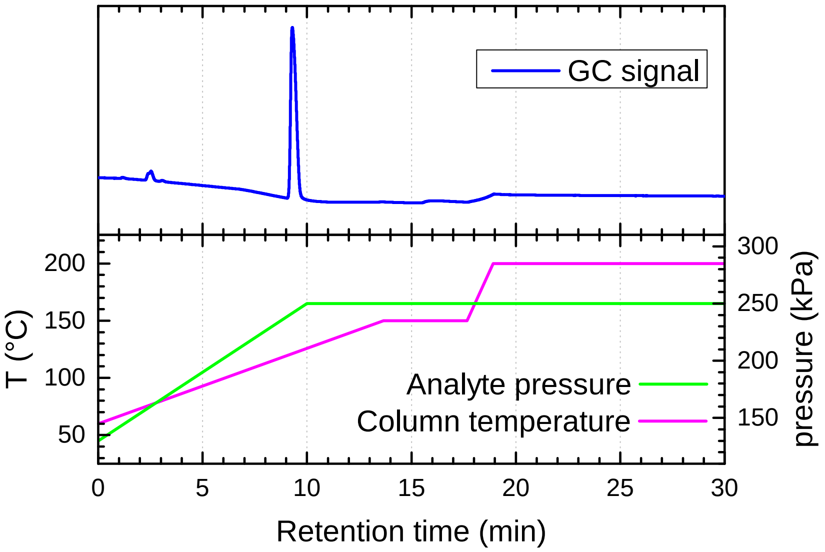

Figure 3.12: GC measurement routine with the column temperature (magenta) and analyte pressure (green) ramps. The corresponding GC signal (blue) is from 7.7.

of the electrolysis cell after electrolysis was sampled using a syringe to manually inject 100 μL of the overhead gas into the built-in injection port of the GC (injection port temperature: 150 °C). Reproducibility obviously was worse when injecting manually, but in the case of these measurements only hydrogen gas was detected, so the higher error margins did not come into play.

Chapter 4

Preparation and surface characterization of silicon electrodes functionalized with pyridine

In this chapter the preparation of silicon electrodes functionalized with immobilized pyridine molecules is described. An electrografting procedure of diazopyridine is developed, which yields a layer of covalently bound 3-pyridine molecules ontop of the silicon surface. The modified surface is characterized with XPS. The measurements presented in this chapter were partly done by Sebastian Lindner, Anton Tosolini and Manuel Windscheid in the course of their respective bachelor theses, which were supervised by the author as part of this thesis [68–70].

4.1 Electrografting (in-situ generated) 3-diazopyridine on silicon electrodes

The cleaned and etched, H-terminated n-type silicon electrodes were electrochemically functionalized in order to immobilize pyridine molecules on the silicon surface. Previous attempts in our group used hydrosilylation of ethyl- / vinyl-pyridine derivatives to immoblize pyridine onto the silicon electrodes [59, 60], but control of the layer thickness and the resulting reactivity of the modified electrode was difficult to attain. In order to improve these parameters during the functionalization process via control of the potential of the working electrode, diazopyridine was electrochemically grafted onto the silicon surface. Grafting diazomolecules had been shown to form covalently bound molecules on glassy carbon [107–109] as well as silicon [64,66,67] electrodes. Diazopyridine was not available as a stable diazonium salt at the beginning of the thesis and was therefore generated in-situ by diazotization of aminopyridine [110] in an acidic solution, during which the reaction of 3-aminopyridine and sodium nitrite ($NaNO_2$) yields 3-diazopyridine in an acidic solution [111] such as 0.5 M H_2SO_4, as depicted in figure 4.1.

Complete diazotation was reported to be reached after 15 s and only small amounts of the decomposition product 3-hydroxypyridine were detected after 2 min. [111]. The decomposition reaction is shown in figure 4.2.

This grafting method for glassy carbon modification was further developed into a

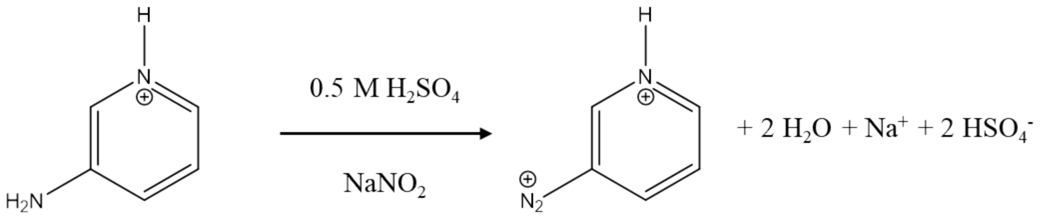

Figure 4.1: Diazotation of 3-aminopyridine in 0.5 M H_2SO_4 [111].

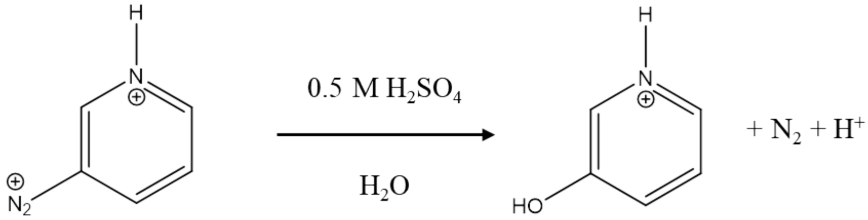

Figure 4.2: Decomposition of 3-diazopyridine to 3-hydroxypyridine in 0.5 M H_2SO_4 [111].

grafting procedure for silicon electrodes. An important aspect was the stability of the in situ generated diazopyridine cations over time. In NMR measurements conducted by Ignaz Höhlein[1] (see figure 4.3), the developing signals of the formed 3-diazopyridine 3 min. after the start of the reaction and its eventual decomposition to 3-hydroxypyridine after 90 min. could be followed. The 3-diazopyridine peaks at δ = 9.45, 9 and 8.75 ppm (maroon spectrum) that were observed 3 min. after the start of the diazotation process disappeared after 90 min., while the 3-hydroxypyridine peaks around δ = 8.0, 7.75 and 7.6 ppm (turquoise spectrum) developed into the main signals 90 min. after diazotation.

4-aminopyridine was also considered in the beginning of the thesis as an alternative precursor molecule, but it tended to decompose quickly to 4-hydroxypyridine during diazotization [112] without forming sufficient amounts of 4-diazopyridine, as can be observed in the ^{1}H-NMR spectra in figure 4.4. Due to the ^{1}H-NMR measurements of the insufficient diazotation of 4-aminopyridine, the more stable 3-aminopyridine was instead chosen as the sole precursor for the grafting process.

The electrografting procedure itself [68] was derived from established grafting procedures with phenyl rings on silicon electrodes [66] and with in-situ generated 3-diazopyridine on glassy carbon [111,113]. The etched electrode was immersed into an electrolyte consisting of 0.5 M H_2SO_4 + 1.8 mM HF + 1 mM 3-aminopyridine, purged with Ar at the open circuit potential (OCP). Later measurements without fluoric acid (HF) required the silicon electrodes being biased at a potential of $E_{WE} \approx$ -0.20 V vs RHE during degassing of the electrolyte. $NaNO_2$ was then added to the electrolyte, which was subsequently stirred for 30 s to initiate the in-situ generation of 3-diazopyridine. Subsequently, without stirring, the potential of the silicon working electrode E_{WE} was ramped towards more cathodic potentials in order to initiate the reductive electrografting process. Figure 4.5 shows consecutive electrografting cyclic voltammograms between -0.07 V and -0.84 V vs. RHE in the resulting grafting electrolyte.

The main reduction peak observed in the first scan at -0.42 V vs. RHE is attributed

---

[1] WACKER-Chair of Macromolecular Chemistry, Chemistry Department, Technical University of Munich

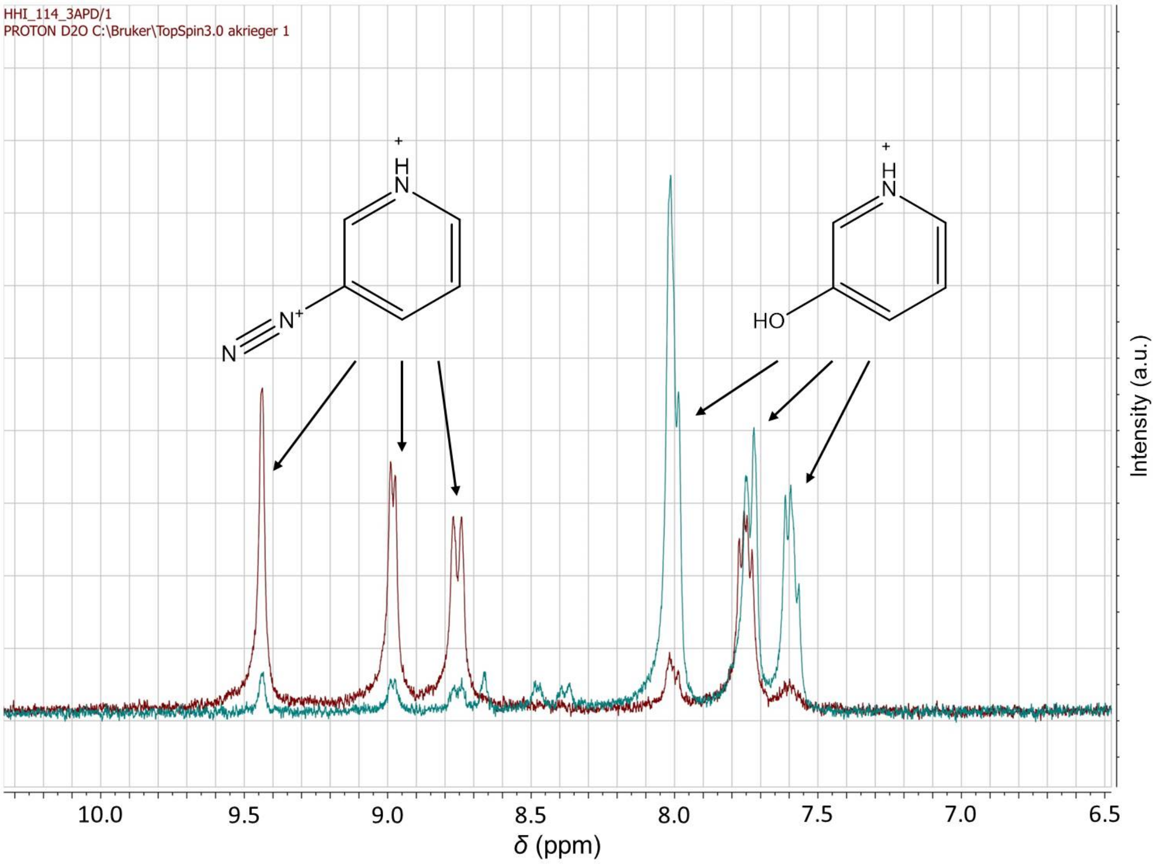

Figure 4.3: NMR spectra of a 1:1 stochiometric mixture of 3-aminopyridine and $NaNO_2$ after 3 min. (maroon) and after 90 min. (turquoise) with developing signals from 3-diazopyridine and 3-hydroxypyridine.

to the reduction of 3-diazopyridine. The thereby generated pyridine radicals abstract hydrogen atoms of the H-terminated silicon surface, leaving, as a first step, dangling bonds. Subsequently pyridine radicals also react with the latter, resulting in the covalent attachment of 3-pyridine to the silicon surface. This process is shown in figure 4.6. In undesired side reactions, pyridine radicals also react with already bound pyridine molecules, leading to patches with branched, polymerized molecule chains [111, 114], as depicted in figure 4.7.

The gradual decrease of the reduction current in figure 4.5 in subsequent CV scans could be attributed the depletion of diazonium cations in the double region, which becomes apparent when comparing the cyclic voltammograms obtained in stirred and unstirred solutions. In a stirred solution, the reduction peak can be observed over several cycles, probably due to an increased transport or replenishment of diazopyridine cations into the double layer. Excess $NaNO_2$ in the grafting solution can also lead to an additional reductive current [111, 115] shown in equation 4.1, though this reduction current does not show a peak-like behaviour [111], rather a current step.

$$NO_2^- + 2H_2O + 3e^- \rightarrow \frac{1}{2}N_2 + 4OH^- \tag{4.1}$$

To minimize this effect, the stochiometric ratio of aminopyridine and $NaNO_2$ was set at 1 : 1.

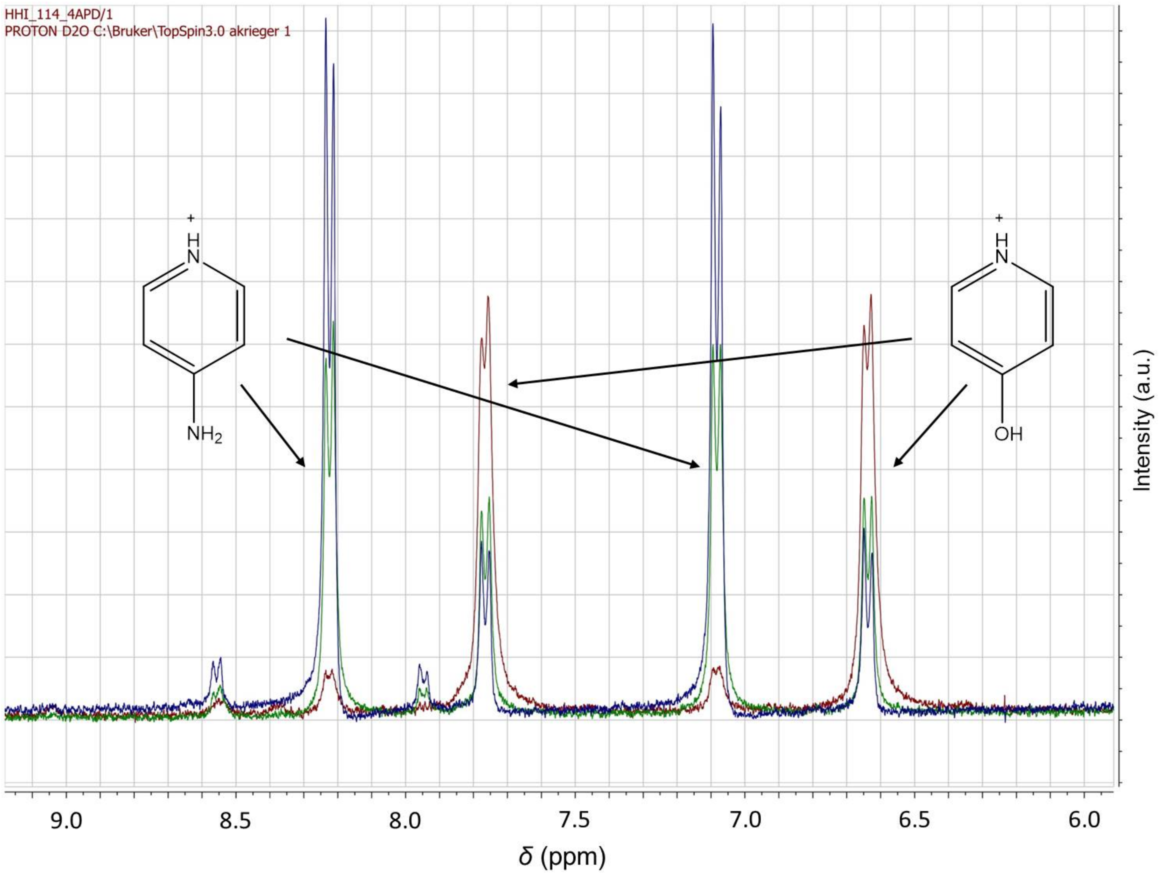

Figure 4.4: ^{1}H-NMR spectra of a 1:1 stochiometric mixture of 4-aminopyridine and NaNO$_2$ right after mixing (dark blue), after 3 min. (green) and after 90 min. (maroon) with signals from 4-aminopyridine and only 4-hydroxypyridine. NMR measurements were conducted by Ignaz Höhnlein.

Grafting 3-diazopyridine resulted in modified silicon electrodes, where the onset for the hydrogen evolution reaction (HER) was shifted towards more positive potentials [68], as denoted by the dashed blue arrow in figure 4.8. This improvement of the reactivity of the modified silicon electrodes for HER stood in contrast to the effect of grafting benzene derivatives such as 4-bromobenzene diazonium onto the same silicon electrodes. In figure 4.9 4-bromobenzene diazonium was grafted onto an H-terminated silicon electrode (dashed violet) in the same manner as 3-diazopyridine and it resulted in an onset shift of the HER on the modified electrode towards more negative potentials (violet) compared to its initially H-terminated surface (red). The latter observation is consistent with literature reports, where grafted layers of benzene derivatives such as 4-bromo- or 4-nitrobenzene acted as a blocking or passivating layer for electrochemical reactions ontop of the grafted Si(111) electrode [64, 66, 67].

In contrast, the positive effect on the onset of HER depicted in figure 4.8 of the grafted 3-pyridine layer ontop of silicon electrodes was noted as a new defining characteristic of the functionalization procedure with 3-diazopyridine; the size of the onset shift of HER was subsequently used as a quantitative characteristic to assess the "quality" of the grafted layer. The influence of potential control on the grafting process and of the concentration of the grafting species was investigated by varying the concentra-

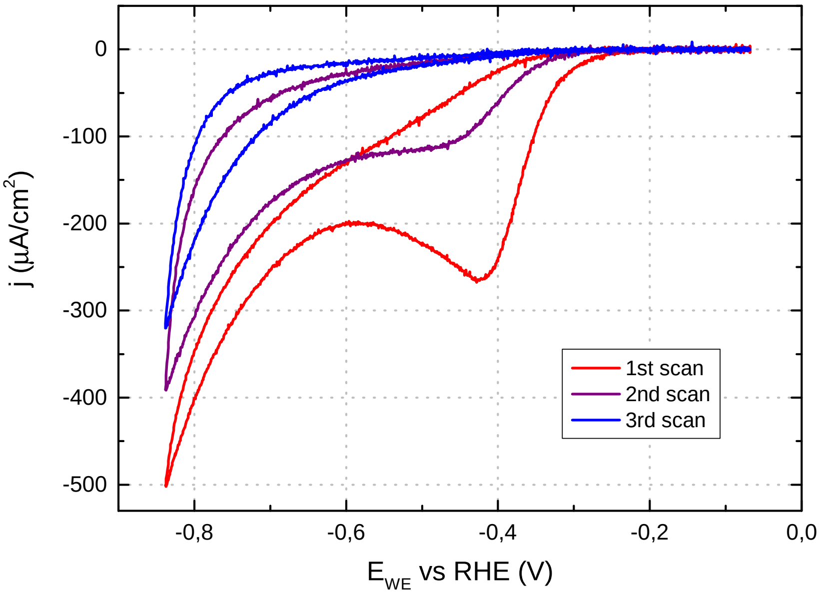

Figure 4.5: Three consecutive cyclic voltammograms (CVs) of an H-terminated silicon electrode in the unstirred grafting electrolyte. The potential cycles were started 30 s after the addition of $NaNO_2$. Electrolyte: 0.5 M H_2SO_4, 1.8 mM HF, 1 mM 3-aminopyridine, 1 mM $NaNO_2$, purged in Ar. Scan speed: 50 mV/s. Data from the bachelor thesis of Sebastian Lindner [68].

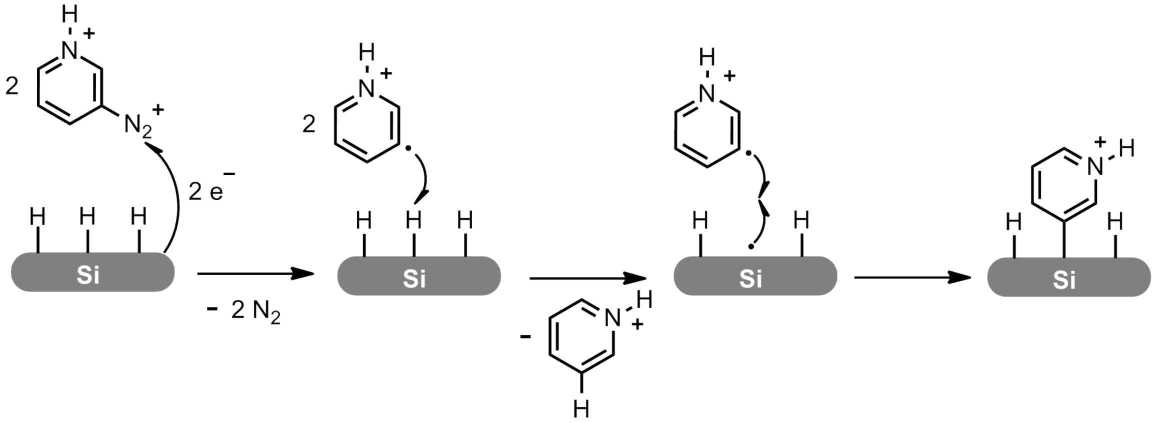

Figure 4.6: Schematic of the electrochemical grafting process of 3-diazopyridine on H-terminated Si.

tion of grafting species, the CV scan rates or, in the case of constant potential steps, the grafting potential and the charge drawn during grafting.

With respect to the onset shift of HER on the resulting modified electrodes, all four parameters exhibited a parameter range, where the reactivity increase was maximal, i.a. optimal values could be found regarding the potential control (constant set potential, Cv parameters etc.) during the grafting process with respect to the size of the HER onset shift afterwards. This observation corresponds to those during the grafting of diazopyridine on glassy carbon, where differences in the potential control methods like CV scan rates or potential steps led to more or less porous pyridine layers [111, 113]. The difference here is that the grafted 3-pyridine layer on silicon electrodes can lead to an increase in reactivity (positive HER onset shift) as well as a decrease in reactivity

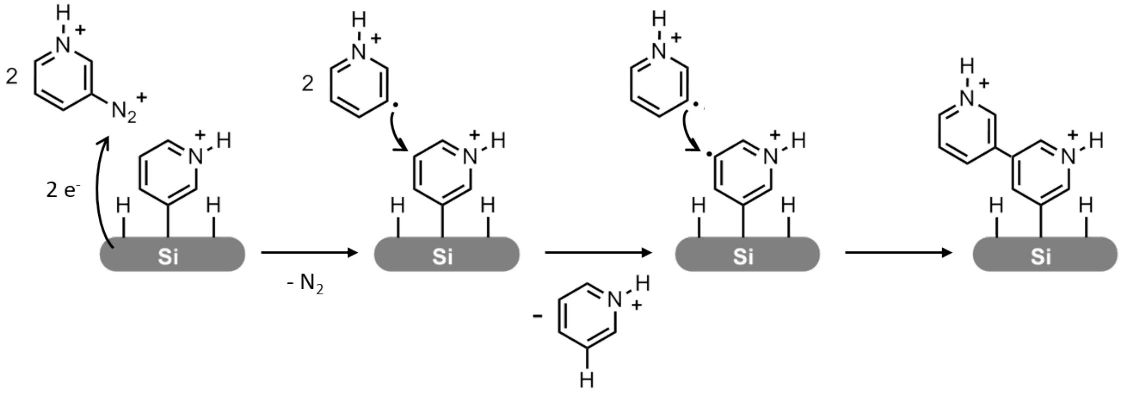

Figure 4.7: Schematic of the undesired side reaction during the electrochemical grafting process of 3-diazopyridine on silicon (see also [63]).

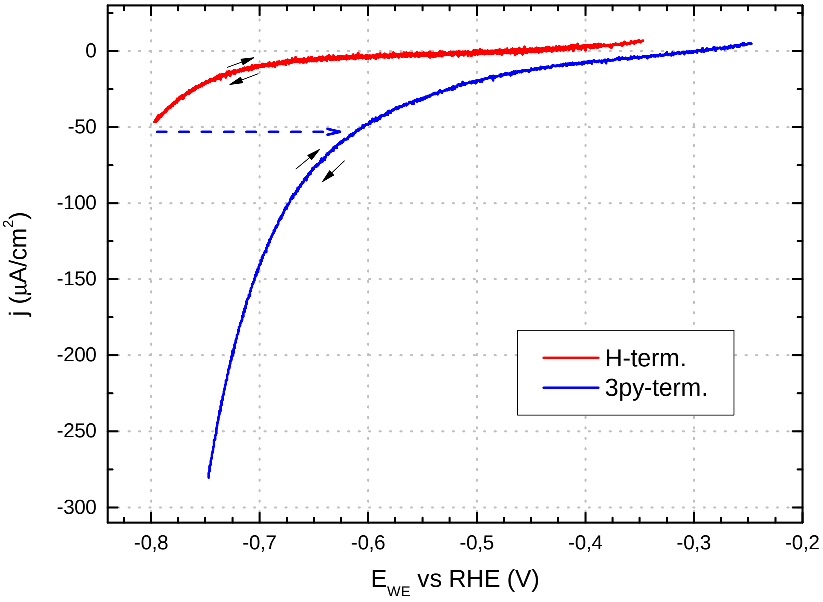

Figure 4.8: CV of a silicon electrode with hydrogen (H-) termination (red) and 3-pyridine (3py-) termination after functionalization via electrografting 1 mM 3-aminopyridine and 1 mM $NaNo_2$. Electrolyte: 0.1 M H_2SO_4, 1.8 mM HF, purged in Ar. Scan rate: 50 mV/s. Data from the bachelor thesis of Sebastian Lindner [68].

(negative HER onset shift) of the modified electrode, as seen in the two plots in figure 4.10, where the influence of the concentration of the grafting species on the resulting HER onset shift is exemplarily shown. On glassy carbon electrodes only the blocking properties of the grafted layer was observed [113]. Slower scan rates as well as longer potential steps tended to yield more compact, less porous layers [69, 113]. The onset shift for HER was either negligible or negative when the thickness of the grafted layer was too big or the layer too compact, similar to the plot on the left in figure 4.10.

It was found that the grafting step potential (right side of fig. 4.11) needed to be more cathodic than the peak potential of -0.42 V for increased reactivity. Also, at even lower step potentials, the formation of multilayers was believed to increase because of a presumed higher layer thickness, either via covalent bonds between pyridine molecules (see the surface polymerization in figure 4.7) or via azo-bridges [69, 113]. Interestingly, the effect on the reactivity of the grafted electrodes did not clearly correspond to the

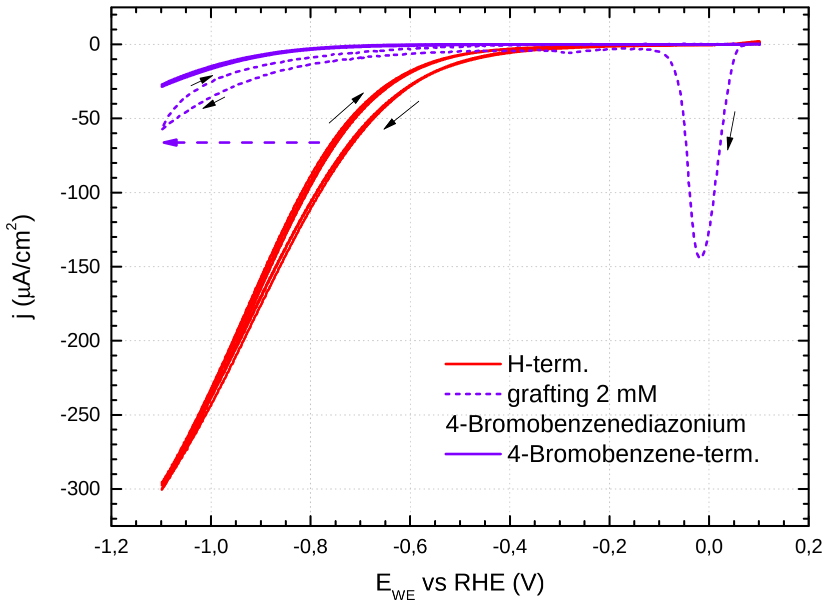

Figure 4.9: Effect of grafting 2 mM 4-bromobenzene diazonium salt onto an illuminated p-type silicon electrode (violet dashed) can be seen in the negative shift of the HER onset, when comparing the CVs of the initially H-terminated silicon electrode (red) with the CV of the 4-bromobenzene terminated electrode (violet solid). Electrolyte: 0.1 M H_2SO_4 + 1.8 mM HF, purged with Ar. Scan rate: 50 mV/s, 100 mV/s during grafting (violet dashed). Data from the bachelor thesis of Sebastian Lindner [68].

amount of surface polymerization. To limit the multilayer formation, grafting experiments were conducted with 3-amino-4-methylpyridin and 3-amino-5-methylpyridin, i.e. aminopyridine, where the C4/C6 carbon atoms in the pyridine ring, where polymerization would take place, were methylated. The thickness of the resulting layers was decreased to 1/10 compared to the layers grafted with unmethylated 3-diazopyridine as obtained from XPS measurements described later 4.2, but the corresponding HER onset shifts were significantly smaller compared to unmethylated 3-pyridine-terminated electrodes, which produced a thicker 3-pyridine layer [70]. The best surface activation was achieved using a two step process with an initial potential step to -0.74 V vs. RHE for 30 s, followed by 10 cyclic potential scans between -0.24 V and -0.64 V vs. RHE with a scan rate of 50 mV/s, as seen in figure 4.12. It may be tentatively suggested that the constant potential step at a potential more cathodic than the grafting peak at ≈ -0.42 V vs RHE, around the onset of HER, together with moderately fast potential ramps generates a comparatively porous grafted layer on top of the silicon electrodes, while slower CV scan rates and step potentials which are more positive than the HER onset tend to yield more compact layers [69].

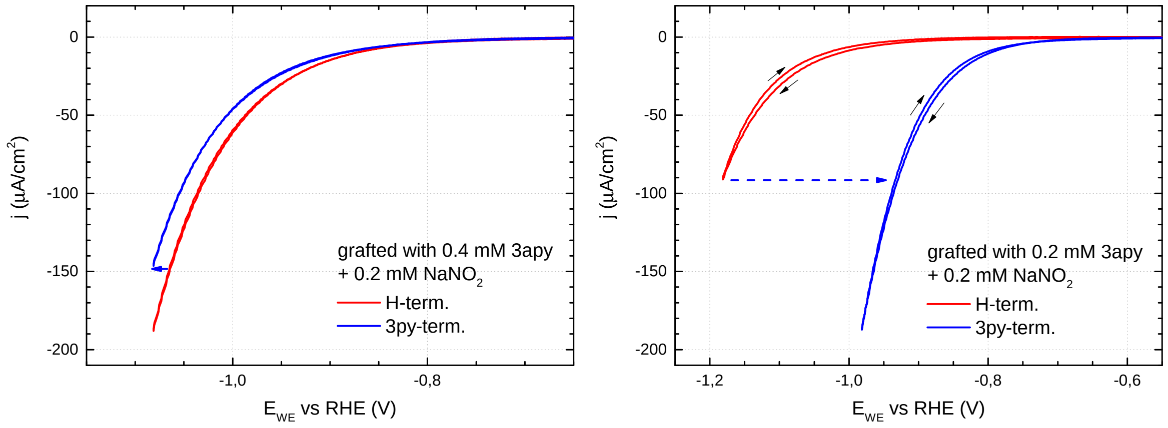

Figure 4.10: Effect of the 3-aminopyridine concentration on the resulting HER onset shift of the grafted silicon electrode. Left: CVs depicting the negative shift in HER onset on a silicon electrode with its initial H-termination (red) and after grafting with 0.4 mM 3-aminopyridine and 0.4 mM $NaNO_2$ (blue). Right: CVs depicting the positive shift in HER onset on a different silicon electrode with its initial H-termination (red) and after grafting with 0.2 mM 3-aminopyridine and 0.2 mM $NaNO_2$ using the same potentiostatic parameters as in the case of 0.4 mM 3-aminopyridine (blue). Electrolyte: 0.5 M H_2SO_4, purged in Ar. Scan rate: 100 mV/s.

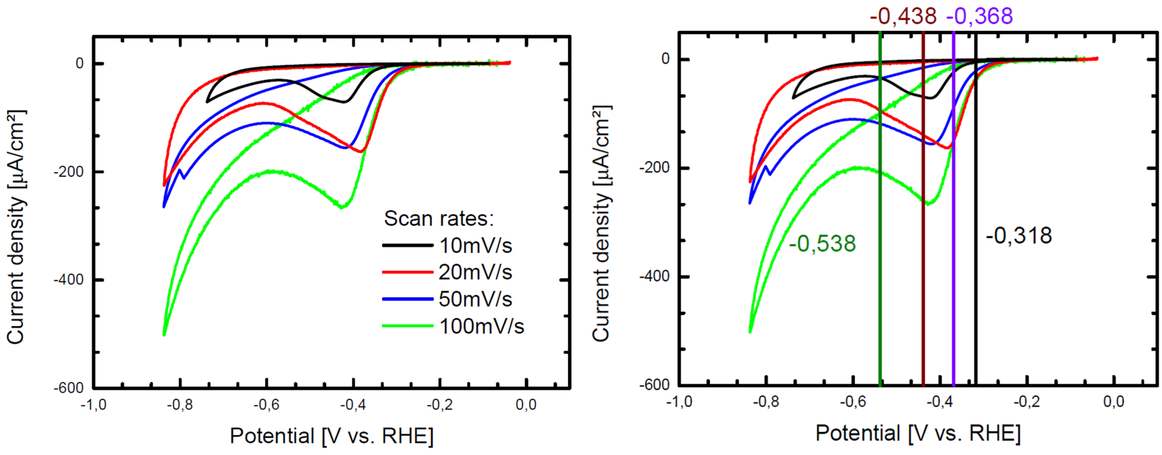

Figure 4.11: Left: Grafting CVs (1st cycle) at different scan rates. Right: Potentials chosen for electrograting using a constant potential step. Electrolyte: 0.5 M H_2SO_4, 1.8 mM HF, 1 mM 3-aminopyridine, 1mM $NaNO_2$, purged in Ar. Original figure from the bachelor thesis of Anton Tosilini [69].

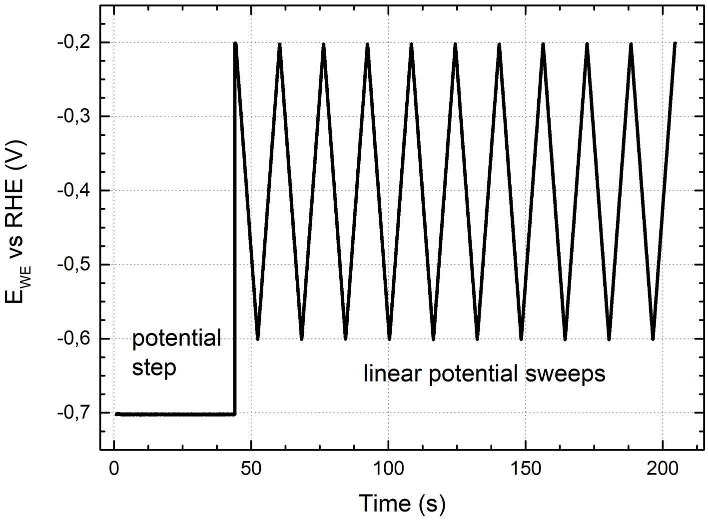

Figure 4.12: Potential profile of the described two step grafting process.

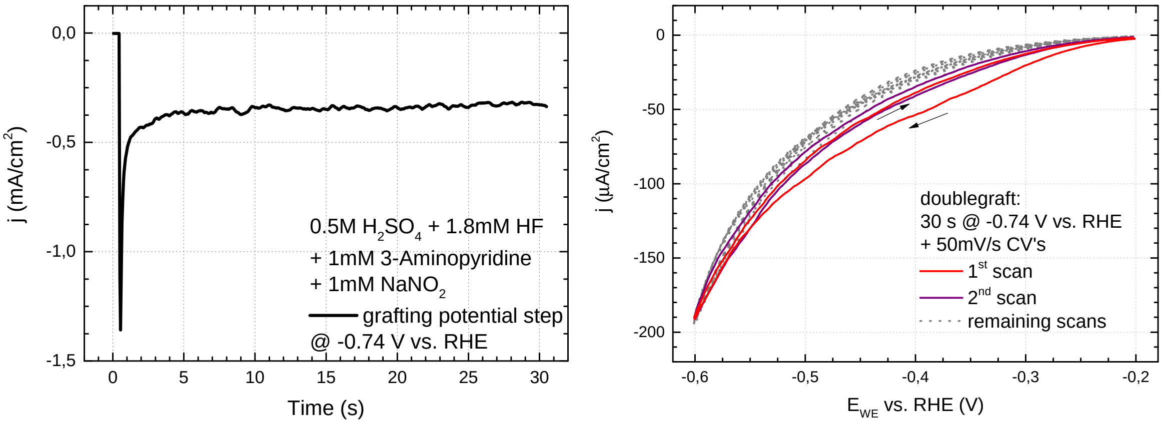

Figure 4.13: Left: Grafting current during the potential step at -0.738 V 30 s after the addition of $NaNO_2$; Right: Subsequent cyclic voltammograms following the potential step in the unstirred grafting electrolyte. Electrolyte: 0.5 M H_2SO_4, 1.8 mM HF, 1 mM 3-aminopyridine, 1mM $NaNO_2$, purged in Ar. Scan rate: 50 mV/s.

Synthesis of diazopyridine tetrafluoridoborate ($C_5H_5N\text{-}N_2^+BF_4^-$)

In collaboration with the WACKER-Chair of Macromolecular Chemistry, Chemistry Department, Technical University of Munich, a method was developed for the synthesis of diazopyridine tetrafluoridoborate ($C_5H_5N\text{-}N_2^+BF_4^-$) or diazonium salt, which was sufficiently stable in ambient air. Tobias Helbig[2] developed the synthesis, which is described in the following:

- 5.00 g aminopyridine (53.1 mmol, 1.0 equivalent (eqv.)) is dissolved in 50.0 ml fluoroboric acid (H_3OBF_4, 48 %) and cooled to 5 °C.
- 5.50 g $NaNO_2$ (79.7 mmol, 1.5 eqv.) is gradually added over the course of 1 h and the mixed solution stirred for 3 h.
- The resulting dispersion is filtered with a Büchner funnel and washed with ≈ 10 ml fluoroboric acid (48 %).
- The filtered, white, solid powder is finally dried in vacuum. In the end this process yields 6.15 g diazopyridine tetrafluoroborate (31.9 mmol, 60 %).

With this synthesis method, 3-, but also 4- and 2-diazopyridine tetrafluoroborate diazonium salts were produced, which were stored in the dark in the refrigerator. While the 4- and 2-diazopyridine salts remained active up to month-long storage and retained their initial white color, 3-diazopyridine salt seemed to decompose more quickly (in the course of 2 weeks) and developed a yellow tint. The decomposition process was accelerated by exposing the salt to light and humidity each time when the salt containers were opened.

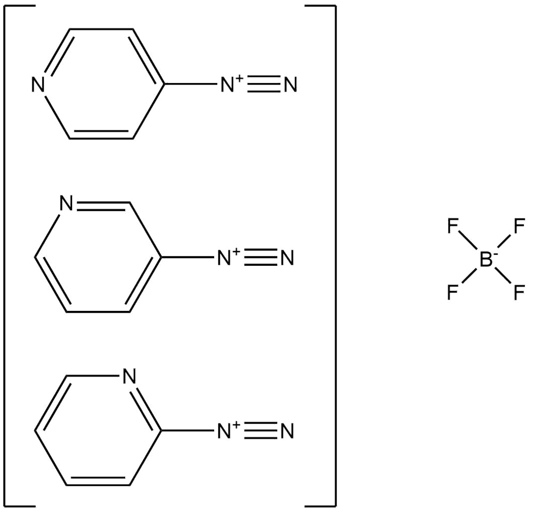

Figure 4.14: Diagram of synthesized 4-, 3-, and 2-diazopyridine tetrafluoridoborate.

The new diazopyridine salts were used as a replacement for aminopyridine and $NaNO_2$ in the grafting solution and the silicon samples were grafted using the established grafting process shown in fig. 4.12. Compared to the prior *in situ* generated

---

[2] WACKER-Chair of Macromolecular Chemistry, Chemistry Department, Technical University of Munich

diazopyridine, the resulting grafting CVs shown in fig. 4.15 exhibit a less clear current response or a peak-like current curve from the reduction of the diazopyridine salts. The reduction peak at -0.42 V vs. RHE is not visible any more, and only a smaller peak at -0.34 V vs. RHE is discernible. It shows a diminishing behaviour in subsequent scans in an unstirred grafting solution. Otherwise the main characteristics consist of a rather stable reduction current between -0.30 V and -0.60 V before the onset of HER more negative of -0.60 V vs RHE.

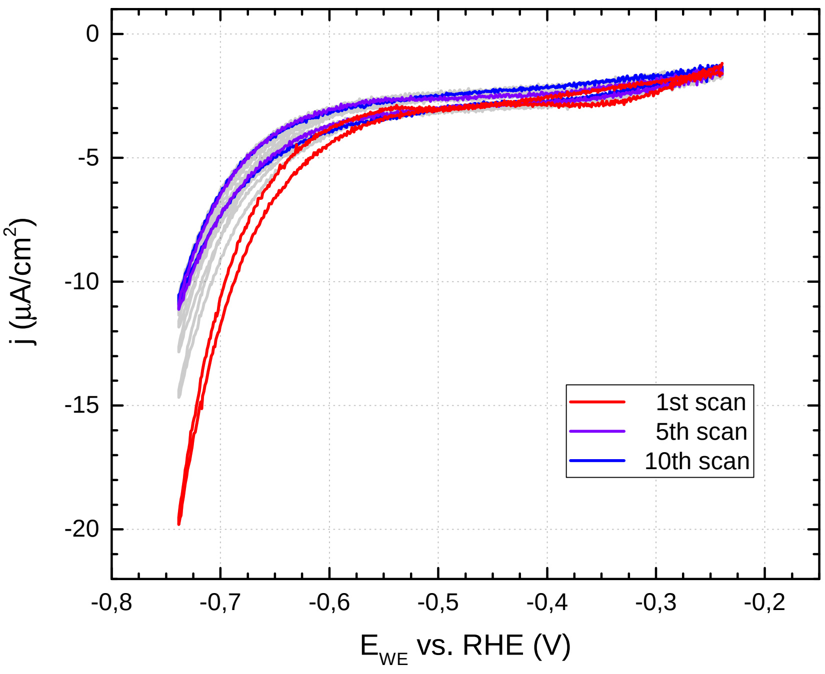

Figure 4.15: Grafting CV of an electrolyte containing 1 mM 3-diazopyridine tetrafluoroborate. Electrolyte: 0.5 M H_2SO_4, 1.8 mM HF, 3-diazopyridine tetrafluoroborate, purged in Ar. Scan rate: 50 mV/s.

The subdued reduction current response during grafting of diazopyridine salts compared to grafting with *in situ* generated diazopyridine could point towards a lower effective concentration of the synthesized diazopyridine in the electrolyte after insertion of the salt. Typically, the amounts of inserted salt tend to be higher than the equivalent amounts of inserted aminopyridine and $NaNO_2$, with their ratio (varying with age and decomposition state of the salts) between 2:1 up to 10:1 in order to achieve a similar HER onset shift. A reason could be that the synthesized diazopyridine salt also decomposes during storage to hydroxypyridine similar to the in-situ generated diazopyridine (cf. the NMR spectra in figure 4.1). NMR measurements of the diazopyridine salt dissolved in solution showed only faint signals, even in high concentration.

After the grafting procedure samples were retrieved from the grafting electrolyte, cleaned again using the aforementioned cleaning protocol (see section 3.2) and either stored in air or etched again before further measurements.

4.2 XPS characterization of the grafted samples

To characterize the grafted 3-pyridine layer on top of the silicon electrodes, grafted samples were analysed using X-ray photospectroscopy (XPS). All H-terminated samples were new and unused samples, which were cleaned and etched before introduction into the vacuum chamber of the XPS instrument, while all 3-pyridine-terminated samples were first grafted, electrochemically characterized and then subsequently cleaned and etched before transferring them into the vacuum chamber.

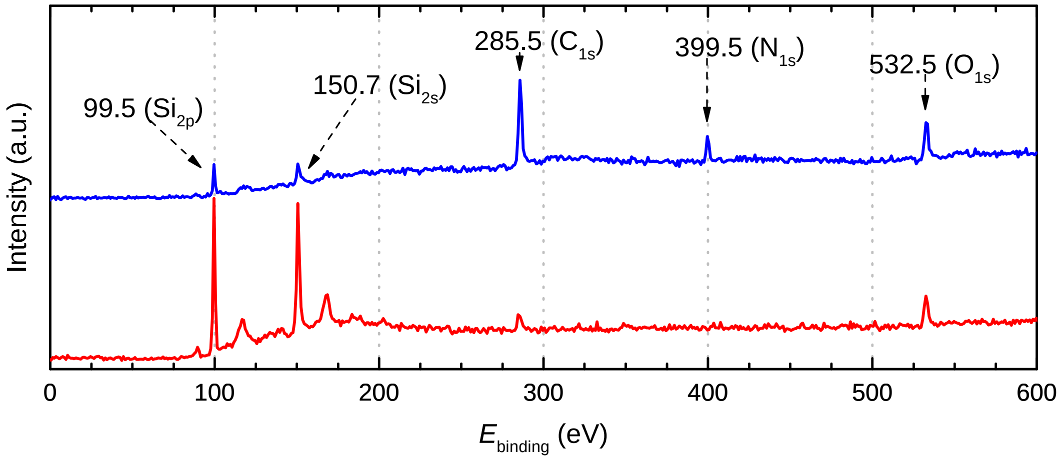

Figure 4.16: XP overview spectra of a silicon sample with H-termination (red) and with 3-pyridine-termination after the grafting process (blue).

In figure 4.16 two overview XP spectra are depicted, one from an H-terminated silicon surface (red) and one from the modified sample with a 3-pyridine layer, similar to the grafted electrode depicted in figure 5.1 (blue). Comparing these two spectra, the presence of pyridine on the surface of the grafted sample is clearly seen by the emergence of peaks corresponding to nitrogen (N_{1s} in pyridine: 399.5 eV) and carbon (C_{1s}: 285.5 eV) [79].

The detailed single spectrum of the nitrogen N_{1s} region in figure 4.17 reveals one main peak at 399.5 eV and a smaller peak shifted to higher binding energy at 400.3 eV. While the main peak can be attributed to the nitrogen atom in pyridine [79, 116], the additional N_{1s} peak shifted by $\approx +1$ eV to higher binding energy may be traced back to azo (N=N) bridges, which are formed by the binding of diazopyridine on already grafted pyridine molecules [113], as illustrated in figure 4.18.

The area under the azo-N_{1s} peak amounts to about 15 % of the total N_{1s} signal and is, thus, smaller than the relative size previously reported for the grafting of diazopyridine on glassy carbon [113, 117, 118], which showed the azo sub-peak with an area of 22 % of the pyridine N_{1s} peak area. In contrast to the reported grafted glassy carbon electrodes, all 3-pyridine-terminated samples were cleaned and etched after the grafting process and a second time after their electrochemical characterization, so the covalent binding as well as the azo bridge binding on the immobilized pyridine are strong enough to withstand these treatment steps, while one can assume that there are no (merely) adsorbed pyridine molecules left on the silicon surface. The presence of the azo-N_{1s} signal validates the assumption that the azo bridges possess a similar robustness towards the etching procedure with fluoride containing solutions as the Si-C bonds.

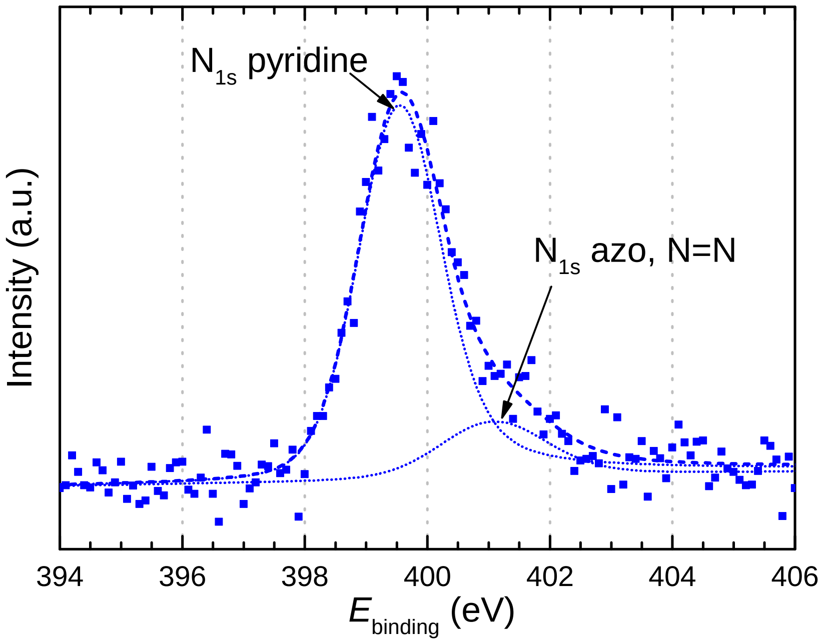

Figure 4.17: N_{1s} XP detail spectrum of the 3-pyridine-terminated silicon sample (blue). Dotted lines denote single peak fits, whereas the dashed line denotes the cumulative fit of the data.

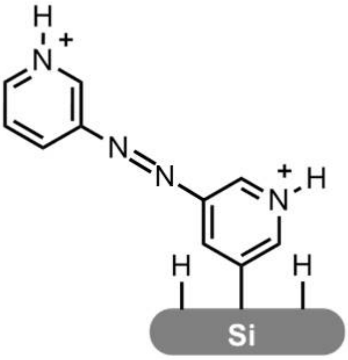

Figure 4.18: Illustration of the coupling of pyridine molecules through azo (N=N) bridge formed during the grafting process.

In figure 4.19 detailed spectra of the Si_{2p} region of the H-terminated silicon sample (red) and the one grafted with 3-diazopyridine (blue, same samples as in fig. 4.16) are shown. Comparing the different surface terminations of the silicon sample, the Si_{2p} peak around 99.5 eV is strongly attenuated in case of the 3-pyridine-terminated silicon sample. The second peak around 102.7 eV points to a partial formation of silicon oxide (SiO_2) [119] on the surface due to oxidation of the grafted sample, as this sample was measured after electrochemical measurements without an additional etching step in fluoride containing solutions. Another possible explanation for this peak are residuals of a silicone paste used for sample assembly on a previous sample holder, since the energy shift is comparable to literature values of both, silicone and SiO_2 species [79]. The same can be said for the enhanced oxygen signal (O_{1s}: 532.5 eV) in the survey XP spectrum of the grafted silicon sample shown in figure 4.16, whose energy can also be attributed to both, silicone and SiO_2. Small patches of silicone paste were present

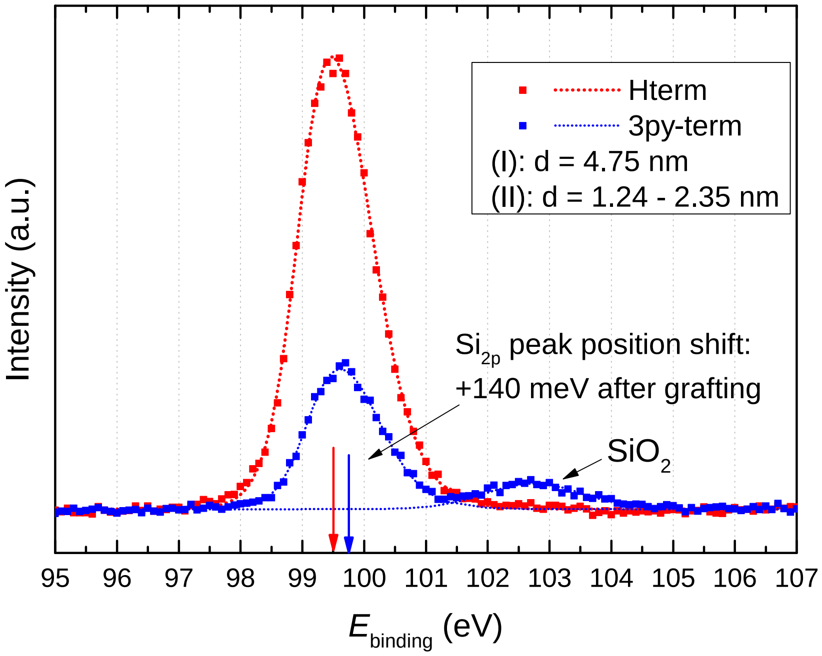

Figure 4.19: Si 2p XP detail spectra of silicon samples with H-termination (red) and with 3-pyridine-termination after the grafting process (blue). Dotted lines denote single peak fits.

around the edges of the samples, which were not completely removed before the XPS measurements in order to minimize possible contamination sources of the modified surface. Nonetheless, the main part of the O_{1s} peak around 532.5 eV visible in figure 4.16 should be attributed to adsorbed H_2O on the surface due to the cleaning steps as well as the electrochemical measurements the samples were subjected to prior to their transfer into the vacuum chamber, not only to SiO_2 or silicone residues on the surface. The binding energy of the Si_{2p} photo electrons of the 3-pyridine-terminated sample is shifted to higher energies relative to the peak of the H-terminated sample. This shift could originate from the different surface termination as well as from the silicon oxide residing on the surface [120].

Thickness estimation of the 3-pyridine layer

The thickness of the grafted 3-pyridine layer was estimated using two approaches. For the first approach (I) the intensity of the Si_{2p} peak ${I_{\mathrm{Si2p}}}^{\mathrm{H}}$ of an ungrafted, H-terminated sample was compared to the intensity of the Si_{2p} peak of the grafted sample, ${I_{\mathrm{Si2p}}}^{\mathrm{Py}}$. The relative attenuation of the peak intensity or the reduction of the peak area can be described by an exponential function where the exponent is dependent on the attenuation length of the Si_{2p} photoelectrons (i.e., the attenuation length of electrons with the kinetic energy of $E_{\mathrm{kin}} = h\nu - E_{\mathrm{b,Si2p}}$) in an organic layer, $\lambda_{\mathrm{OL}}(E_{\mathrm{b,Si2p}})$, and the layer thickness d [66, 121].

$$\frac{{I_{\mathrm{Si2p}}}^{\mathrm{Py}}}{{I_{\mathrm{Si2p}}}^{\mathrm{H}}} = \exp\left(\frac{-\mathrm{d}}{\lambda_{\mathrm{OL}}(E_{\mathrm{b,Si2p}})}\right)\sin\Theta \tag{4.2}$$

Θ denotes the detector angle relative to the sample, which was kept at $\Theta = 90°$, i.e., perpendicular to the sample for all measurements. For $\lambda_{\mathrm{OL}}(E_{\mathrm{b,Si2p}})$, as estimated from alkyl- and alkoxy-monolayers, the attenuation length amounts to $\lambda_{\mathrm{OL}}(E_{\mathrm{b,Si2p}}) = 3.95\,\mathrm{nm}$ [121].

For the second approach (II), the signals of the $\mathrm{C_{1s}}$ and $\mathrm{Si_{2p}}$ peaks of the grafted sample were considered. Its ratio can be correlated to the respective attenuation lengths $\lambda_{\mathrm{OL}}(E_{\mathrm{b,Si2p}})$ and $\lambda_{\mathrm{OL}}(E_{\mathrm{b,C1s}})$ in polyethylene as an equivalent of the pyridine layer, and the layer thickness d [122–124].

$$\frac{{I_{\mathrm{C1s}}}^{\mathrm{Py}}}{{I_{\mathrm{Si2p}}}^{\mathrm{Py}}} = \frac{{I_{\mathrm{C1s}}}^{\infty} \cdot \left(1 - \exp\left(\frac{-\mathrm{d}}{\lambda_{\mathrm{OL}}(E_{\mathrm{b,C1s}})}\right)\right)}{{I_{\mathrm{Si2p}}}^{\infty} \cdot \exp\left(\frac{-\mathrm{d}}{\lambda_{\mathrm{OL}}(E_{\mathrm{b,Si2p}})}\right)} \tag{4.3}$$

${I_{\mathrm{Si2p}}}^{\infty}$ stands for the photoelectron intensity of an idealized, clean, semi-infinite silicon crystal, whereas ${I_{\mathrm{C1s}}}^{\infty}$ stands for the photoelectron intensity of a semi-infinite, solid layer of the respective benzene derivative. The ratio of both values is estimated to be between 2.2 and 1 [122]. For a closed layer of polyethylene, the respective attenuation lengths are $\lambda_{\mathrm{OL}}(E_{\mathrm{b,C1s}}) = 3.67\,\mathrm{nm}$ and $\lambda_{\mathrm{OL}}(E_{\mathrm{b,Si2p}}) = 4.12\,\mathrm{nm}$ [124, 125]. The thickness of the 3-pyridine-layer from figure 4.19 was calculated as $\mathrm{d_{3py}} = 4.75$ nm (I) and $\mathrm{d_{3py}} \approx 1.24 - 2.35$ nm (II). A source of uncertainty is the fact that the modified sample in figure 4.19 was partly oxidized. Following the observations of the effect of oxidation on the performance of the grafted sample in section 5.2, the grafted sample is expected not to be fully covered by covalently grafted pyridine molecules. These ungrafted areas on the silicon surface are then prone to oxidation, which would lead to a composite layer on top of the silicon surface with parts covered by $\mathrm{SiO_2}$ and parts covered by grafted pyridine molecules. While the oxide-free ,i.e., ungrafted surface areas could yield a lower effective layer thickness from the XPS signals [121], the areas covered by $\mathrm{SiO_2}$ should increase the attenuation of the modified $\mathrm{Si_{2p}}$ peak ${I_{\mathrm{Si2p}}}^{\mathrm{Py}}$ due to the attenuation length of $\mathrm{SiO_2}$ ($\lambda_{\mathrm{SiO_2}}(E_{\mathrm{b,Si2p}}) = 3.78\,\mathrm{nm}$) being comparable or slightly lower than that of the organic (polyethylene) layer [125].

Nonetheless, these thickness values point towards a grafted 3-pyridine-layer consisting of more than a monolayer of immobilized pyridine molecules, assuming a monolayer thickness of $\mathrm{d_{ML}} \approx 0.4$ nm, which is slightly smaller than 4-bromobenzene [66] due to the missing endgroup such as Br-, $\mathrm{NO_2}$- etc. [13]. In comparison, the formation of a 4-bromobenzene monolayer after electrografting has been achieved, yielding a thickness of $\mathrm{d_{ML}} = 0.7\,\mathrm{nm}$ [66]. A thickness between $1.24 - 2.35$ nm fits to other thickness estimates of grafted layers of i.a. 4-nitrobenzene and phenyl/aryl derivatives on silicon substrates, as determined by XPS ($3.0 - 6.0$ nm [122]; $1.0 - 1.9$ nm [120]) and Rutherford backscattering spectroscopy (≈ 2.5 nm [64]). The actual 3-pyridine layer thickness should be lower without the partial oxidation of the grafted sample and its corresponding attenuation of the $\mathrm{Si_{2p}}$ peak and thus less than 2 to 3 monolayers. The thickness value for method (I) (see equation 4.2, i.e., the attenuation of the $\mathrm{Si_{2p}}$ peak) of 4.75 nm deviates more strongly. One additional source of uncertainty is the subsequent, separate measurement of the H-terminated sample. Here, the sample position and the position as well as the parameters of the X-ray source might have been changed compared to the measurement of the grafted sample.

For the XPS measurements depicted in figure 4.20, both the unmodified and the grafted sample were etched before the XPS measurement to negate the effect of silicon

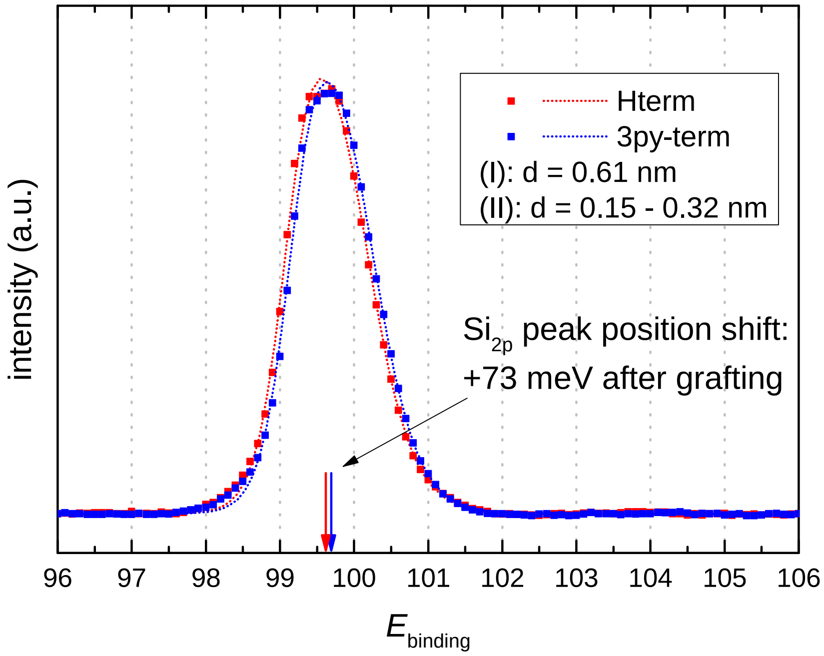

Figure 4.20: Si 2p XP detail spectra of silicon samples with H-termination (red) and with 3-pyridine-termination after the grafting process (blue). Dotted lines denote single peak fits.

oxide on the Si_{2p} peak, as one can see from the absence of the SiO_2 peak around 103 eV. Both samples were mounted onto the same XPS sample holder and measured using the same XPS parameters. Again, the binding energy of Si_{2p} peak energy of the 3-pyridine-terminated sample is shifted (less than in figure 4.19), now assumably without the effect of residual SiO_2 remaining on the surface. The resulting attenuation is much weaker compared to figure 4.19 and barely visible in the figure. This is reflected in the thickness estimations of $d_{3py} = 0.61$ nm (I) and $d_{3py} \approx 0.15 - 0.32$ nm (II) for the grafted sample, which would correspond to a modified silicon surface which is only partially covered by a 3-pyridine monolayer, thus leading to an effective layer thickness slightly below the value of a monolayer. The grafted samples from figures 4.19 (3py-Si ox) and 4.20 (3py-Si etched) differ in grafting solutions and concentrations (3py-Si ox: 1 mM 3-aminopyridine + 1 mM $NaNO_2$; 3py-Si etched: 1 mM 3-diazopyridine salt) but show similar electrochemical behaviour concerning the onset shift of HER in an acidic electrolyte (for 3py-Si ox in figure 4.19 ≈ +260 mV for HER onset; for 3py-Si etched in figure 4.20 ≈ +230 mV). At the end of chapter 4.1 it was mentioned that the same concentration of diazopyridine salt tended to yield a smaller effective concentration of diazopyridine in the solution compared to using in-situ generated diazopyridine, corresponding to a smaller grafting current during the grafting process (which, however, could also be due to the missing residual reduction current of $NaNO_2$). The resulting 3-pyridine layers also appear to be less thick when using diazopyridine salts. Together with the thickness determined by XPS and the total electrical charge drawn during electrografting process described in figure 4.13, a grafting yield $\eta_{g,3py}$ can be estimated from the total charge drawn during the grafting process $Q_{g,3py}$, the number of monolayers grafted, n_{ML}, and the minimal charge necessary to graft a monolayer Q_{ML}. The grafting charge $Q_{g,3py}$ was calculated by integrating the current during the potential step and the subsequent potential ramps. For grafted 4-nitrobenzene it has been estimated that, in order to form a fully closed monolayer on 1 cm^2 of Si (111) surface (the surface atom density on H-terminated Si (111) is $7.8 \cdot 10^{14}$ per 1 cm^2), at least $Q_{ML} = 128\,\mu Ccm^{-2}$ is needed to graft $3.9 \cdot 10^{14}$ molecules, which form the closest packed grafted monolayer for benzene ontop of Si (111) [64]. The ratio between the charge consumed to form the number of monolayers measured by XPS and the total charge drawn during electrografting is the grafting yield $\eta_{g,3py}$:

$$\eta_{g,3py} = \frac{n_{ML} \cdot Q_{ML}}{Q_{g,3py}} \tag{4.4}$$

The results for the 3-pyridine-terminated samples presented in figures 4.19 and 4.20 are listed in table 4.1.

	3py-Si ox (fig. 4.19)	3py-Si etched (fig. 4.20)
grafting species	0.1 mM 3-aminopyridine + 0.1 mM $NaNO_2$	2 mM 3-diazopyridine synthesized salt
$Q_{g,3py}$ (μCcm^{-2})	$1.31 \cdot 10^4$	775
d (I);(II) (nm)	4.75 ; 1.24 – 2.35	0.61 ; 0.15 – 0.32
n_{ML} (I);(II)	11.9 ; 3.1 – 5.9	1.5 ; 0.4 – 0.8
$\eta_{g,3py}$ (I);(II) (%)	11.6 ; 3.0 – 5.8	24.8 ; 6.6 – 13.2

Table 4.1: Drawn charge $Q_{g,3py}$, pyridine layer thickness d_{3py}, number of monolayers n_{ML} and the resulting grafting efficiency $\eta_{g,3py}$ for grafting processes of the 3-pyridine-terminated samples presented in figures 4.19 and 4.20

The grafting of the synthesized 3-diazopyridine salt resulting in the 3-pyridine terminated sample in figure 4.20 is about twice as efficient as the grafting of in situ generated 3-diazpyridine resulting in the grafted sample in figure 4.19. Compared to grafted layers of 4-nitrobenzene [122], the grafting yields for 3-diazopyridine $\eta_{g,3py}$ are up to 10 times smaller. Apparently, only a fraction of the charge drawn during electrografting is being consumed by generating 3-pyridine radicals, with the remaining charge going into side reactions like HER, reduction of residual O_2 [47, 126–128], and reduction of remaining, unreacted $NaNO_2$ in the case of in-situ generation of 3-diazopyridine [111].

In the end, a procedure to electrochemically graft 3-diazopyridine, either in situ generated or synthesized, onto H-terminated silicon electrodes has been developed, which yields a layer of covalently bound 3-pyridine molecules on the silicon surface. In XP spectra the presence of the pyridine termination was confirmed, while the grafted layer thickness is estimated to be slightly smaller than one monolayer, leading to a rather small grafting efficiency compared to other reported grafting procedures.

Control of the thickness and coverage of the grafted layers could be improved by the presence of radical scavengers such as DPPH (2,2-diphenyl-1-picrylhydrazyl), which was reported to limit the thickness of the grafted layer to a monolayer during the grafting of 4-nitrobenzene diazonium on glassy carbon electrodes [129–131]. The inclusion of such scavengers could lead to an increase of the robustness of the grafting procedure against changes in diazonium concentration, as well as an improved grafting efficiency $\eta_{g,3py}$, and should be considered for future grafting procedures for the reliable formation of a monolayer of grafted pyridine molecules on the silicon electrode.

Additionally, the detail spectra of the $\mathrm{Si_{2p}}$ in figures 4.19 and 4.20 show a shift of the peak position when comparing the $\mathrm{Si_{2p}}$ peak of an H-terminated sample with a modified, 3-pyridine-terminated sample. Changing the surface termination of silicon can lead to differences in the work function at the surface of the sample and the bending of the energy bands at the surface due to the coverage and composition of the surface termination, as well as differences in the dipole moments of the surface termination molecules [120, 122, 132, 133]. The examination of the surface energetics using XPS and (in the future possibly) ultraviolet photoelectron spectroscopy (UPS) measurements would be worthy of further investigation, in order to elucidate the effect of functionalized species on the energetics of the silicon electrode.

Chapter 5

Hydrogen Evolution Reaction (HER) on grafted silicon electrodes

Cyclic voltammograms of the silicon electrodes modified with grafted 3-pyridine molecules exhibited a significant *shift of the onset of the hydrogen evolution reaction (HER) towards more positive potentials, i.e., smaller overpotentials* compared to the initially H-terminated electrodes, as can be seen in figure 5.1.

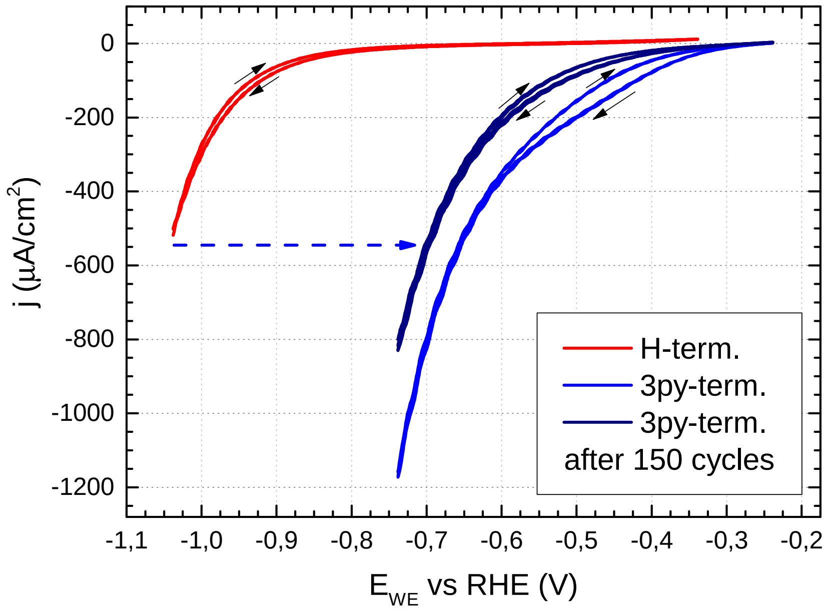

Figure 5.1: Cyclic voltammograms of an n-type silicon electrode with an H-terminated surface (red) and a surface modified with grafted 3-pyridine molecules in the above mentioned two-step grafting process (blue) showing the positively shifted onset of the HER in an acidic electrolyte. Hysteresis feature between -0.35 to -0.60 V nearly vanishes after 150 CV cycles (navy). Electrolyte: 0.5 M H_2SO_4 and 1.8 mM HF, purged with Ar. Scan rate: 100 mV/s.

The overpotential for the HER was decreased by up to 400 mV, reducing the overpotential necessary for a current density of 0.5 mA/cm^2 from -1.04 V to -0.64 V vs RHE. In addition to the overall shift of the HER onset, the grafted electrode exhibited a hysteresis in the potential range between -0.35 to -0.60 V, which was absent in case of the H-terminated silicon electrode. The hysteresis might originate from adsorped/chemisorped (diazo- or hydroxy-) pyridine molecules. After 150 CV cycles the hysteresis nearly vanished and the CV of the grafted electrode showed a remaining, exponentially increasing HER current response with increasing overpotential. Previously it was speculated that the hysteresis might originate from the reduction and oxidation of the bound protonated pyridine molecules/pyridyl radicals [134], but subsequent measurements could not reproduce this hysteresis feature. The small, negative regression of the HER onset shift after the 150 cycles (compare navy to blue CV in fig. 5.1) points towards a slight degradation of the grafted surface over time, which will be discussed later in more detail in section 5.2. Silicon electrodes grafted with 4-bromo- and 4-nitrobenzene are reported to also exhibit a hysteresis in their CVs after cleaning and etching procedures, but their cause has not been further investigated [66].

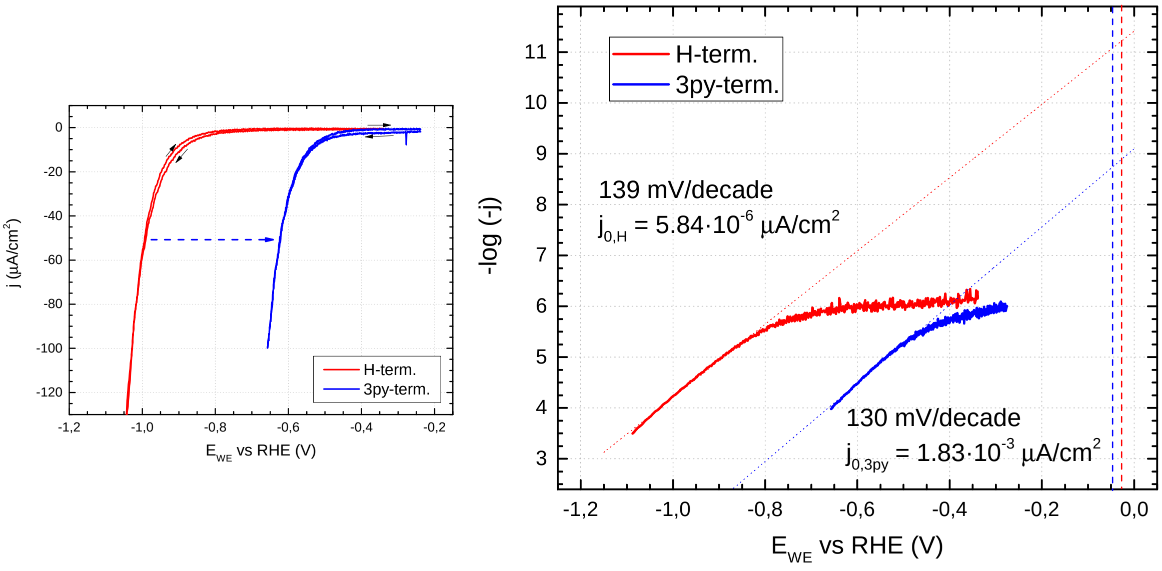

Figure 5.2: Left: CVs of a silicon electrode with an H-terminated surface (red) and a surface modified with a 3-pyridine layer (blue) ; Right: Tafel-like plot of the downward scans of the CVs of the H-terminated (red) and 3-pyridine-terminated electrode. Dashed lines indicate the flatband potentials of a similarly grafted silicon electrode, as obtained from Mott-Schottky plots (see figure 6.6). Electrolyte: 0.5 M H_2SO_4, purged with Ar. Scan rate: 100 mV/s.

The Tafel-like plots of the downward scans show a similar slope for the HER on the H-terminated (139 mV/decade) and 3-pyridine-terminated electrode (130 mV/decade). The exchange current density j_0 or the intersection of the linear fit of the Tafel-like plot with the corresponding flatband potentials E_{fb} (derived from figure 6.6 in the EIS chapter) for the grafted electrode ($j_{0,3py} = 1.83 \cdot 10^{-3}$ μA/cm^2) was strongly increased compared to its initial, H-terminated state ($j_{0,H} = 5.84 \cdot 10^{-6}$ μA/cm^2). By interpreting these j_0 values, it seems that the immobilized pyridine layer enhances the reactivity of the modified silicon electrode for the HER, resulting in an exchange current density that is over 400 times larger, but the reaction itself seems not be fundamentally changed by the surface modification. The slopes of the downward scans are comparable to values from literature, which range from 200 mV/decade to 140 mV/decade [48, 135] down to 117 mV/decade [47, 78], whereas the observed $j_{0,H}$ values are $\approx$10 [47] to $\approx$30 times smaller than literature values on H-terminated, n-type silicon electrodes [48, 136, 137], although cited values were recorded on Si (100) samples [136,137]. The shift of the onset potential for HER towards smaller overpotential on the 3-pyridine-terminated electrode is one of the largest, reported reactivity improvement for an organically modified silicon electrode and comparable to previous surface modifications on silicon electrodes with metal nano islands [138–150] and polymers with decorated metal particles [138, 151]. In contrast, the increased reactivity of the functionalized silicon electrodes investigated here stem from the purely organic, grafted 3-pyridine layer, without addition of any catalytically active metal particles. Reported onset shift of HER on modified silicon electrodes are collected in table 5.1.

	Substrate	Surface mod.	Electrolyte	ΔE_{HER} (mV)
[134]	n-Si etched	3-pyridine layer (this work)	0.5 M H_2SO_4, pH 0.3	400 @ 0.5 mA/cm^2
[139]	p-Si etched	Ag film	0.5 M K_2SO_4 + AcB[1] pH 4.7	350
[140]	p-Si etched	Pt deposited	0.5 M K_2SO_4[2]	130 @ 5 mA/cm^2
[138]	p-Si etched	Pt isles	1 M KCl + 0.1 M HCl pH 1	260
			1 M KCl + PhoB[3] pH 6.6	460
		$(PQ^{2+})_n \cdot n\mathrm{Pt}(0) \cdot 2n\mathrm{X}^{-}$[4]	1 M KCl + 0.1 M HCl pH 1	200
			1 M KCl + PhoB pH 7	340
[141]	p-Si etched	Cd isles	0.5 M H_2SO_4, pH 0.3	-200 @ 5 μA/cm^2
		Pb isles		-120 @ 20 μA/cm^2
		Co isles		50 @ 20 μA/cm^2
		Ni isles		180 @ 20 μA/cm^2
		Au isles		220 @ 20 μA/cm^2
		Pt isles		320 @ 20 μA/cm^2
[142]	pSi etched	Pt deposited	7.6 M HI	400
	n^+/p-Si	Pt deposited		600
		Pd deposited		300
[152]	pSi etched	RuO_2	2 M HCl	600
[153]	p-Si etched	$SiW_{12}O_{40}H_4$ modified	0.5 M H_2SO_4	500 @ 10 mA/cm^2

[143]	p-Si etched	Pt isles	1 M HCl, pH 0	450
		Au isles		450
		Pt & Au isles		500
[144]	p-Si etched	WO$_3$ layer	0.1 M H$_2$SO$_4$, pH 1	400
		Pt NP/WO$_3$ layer[5]		550
[154]	nSi etched	viologen (V$^+$)	0.1 M Na$_2$SO$_4$, pH 6	120
	pSi etched	Pt-V^{2+}		500
		3L[6]-Pt-V^{2+}		570
		5L[6]-Pt-V^{2+}		650
[145]	pSi nanowire	Pt NP	8.6 M HBr + 50 mM Br$^-$/Br$_2$	300 @ 10 mA/cm^2
[146]	p-Si etched	FeO$_x$ isles, aged [7]	0.1 M Na$_2$SO$_4$, pH 9	370
		Pt isles		350
		Pt/FeO$_x$ isles, aged		700
[147]	p-Si etched	Pt deposited	0.2 M KHP[8] + 0.5 M K$_2$SO$_4$ pH 4.5	550 @ 10 mA/cm^2
		Ni deposited		480 @ 10 mA/cm^2
		Ni-Mo deposited		500 @ 10 mA/cm^2
[155]	pSi etched	adsorbed Mo$_3$S$_4$	0.1 M HClO$_4$	650 @ 4 mA/cm^2
[151]	pSi etched	Pt$_{\text{complex}}$-SC11 layer[9]	50 mM H$_2$SO$_4$	500
[148]	p-Si etched	Au NS film[10]	0.5 M K$_2$SO$_4$ + H$_2$SO$_4$ pH 1	480 @ 10 mA/cm^2
		Pt NP film		670 @ 10 mA/cm^2
		Pt/Au NS film		670 @ 10 mA/cm^2
[149]	pSi nanowire	Pt NP atomic layer deposition	0.5 M Na$_2$SO$_4$ + H$_2$SO$_4$ pH 1	220
[150]	p-Si etched	Au isles	0.1 M H$_2$SO$_4$ pH 1	500
		Pt/Au isles		620
[156]	pSi etched	W$_2$C dep.	1 M H$_2$SO$_4$	350
		Pt dep.		700
		Ni-Mo dep.		450
		W$_2$C/Pt dep.		700

[157]	pSi etched	TiO_2 dep.	0.1 M B_i[11] + 1 M KCl pH 9.2	150 @ 10 mA/cm^2
		Ni dep.		270 @ 10 mA/cm^2
		TiO_2|Ni dep.		270 @ 10 mA/cm^2
		$TiNi_{cat}$[12]		500 @ 10 mA/cm^2
		Pt dep.		600 @ 10 mA/cm^2
[158]	pSi etched	TiO_2|hydrogenase[13]	50 mM MES[14], pH 6.0	300
[159]	pSi|mesoTi[15]	COP_3[16]	0.1 M acetic acid, pH 4.5	300[17]
		NiP[18]		300[17]
[160]	p-n^+|Ti	NiFe layered double hydroxide	1 M KOH	530
[161]	pSi etched	$Ni(TEOA)_2Cl_2$ [19] adsorbed	0.5 M H_2SO_4	400

Table 5.1: Table of reported surface modifications for silicon electrodes and their effect on the onset of HER ΔE_{HER} using the modified electrodes in aqueous electrolytes.

---

[1] Acetate buffer

[2] Independent of pH

[3] Phosphate buffer

[4] Redox Polymer with dispersed / incorporated Pt nanoparticles

[5] Nanoparticles

[6] layers of Pt-decorated viologen chains

[7] 10 h at 0.28 V vs RHE, ill.

[8] Potassium Hydrogen Phthalate

[9] 11-mercaptoundec-1-ene complexed with Pt particles

[10] Nanostructured film

[11] Borate ions

[12] dropcasting $TiNi_{pre}$ precursor molecule and cathodically activating $TiNi_{pre}$

[13] [NiFeSe]-hydrogenase isolated from Desulfomicrobium baculatum (Dmb)

[14] 2-(N-morpholino)ethanesulfonic acid

[15] mesoporous Ti layer deposited onto pSi

[16] cobalt diimine-dioxime, phosphonated molecular proton reduction catalyst

[17] compared to pSi|mesoTi

[18] DuBois-type, phosphonated molecular proton reduction catalyst

[19] Triethanolamine

5.1 HER on silicon electrodes grafted with 2- or 4-diazopyridine

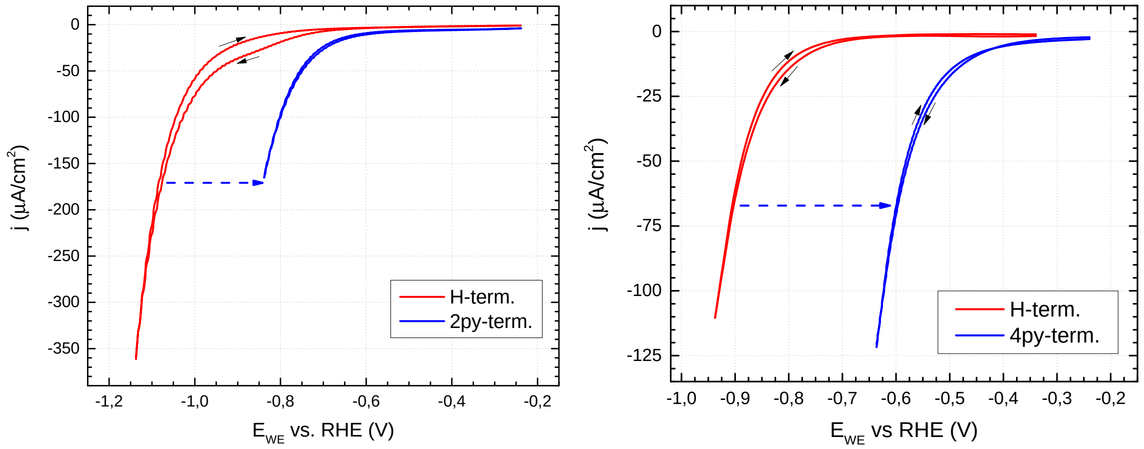

Figure 5.3: Left: Cyclic voltammograms of a silicon electrode with an H-terminated surface (red) and a surface modified with a 2-pyridine (blue) layer; Right: Cyclic voltammograms of a silicon electrode with an H-terminated surface (red) and 4-pyridine layer (blue). Electrolyte: 0.5 M H_2SO_4, purged with Ar. Scan rate: 50 mV/s.

Grafting 2- or 4-diazopyridine onto silicon electrodes yielded modified electrodes with increased reactivity which behave similarly as the 3-diazopyridine grafted electrodes. These pyridine layers were grafted using the respective diazopyridine salts that were synthesized by Tobias Helbig and Marc Kloberg[1] (see the synthesis steps in chapter 4.1). It would be interesting to see, if differences in the positive shift of HER onset could be observed due to the different orientation of the nitrogen atom of these diazopyridine molecules. Since the protonated nitrogen atom was proposed to act as a reaction center for HER [21, 22], differences in HER reactivity would point towards a reaction mechanism, where the orientation of the nitrogen atom in relation to the silicon surface influences its behaviour. However, the observed effect of grafted 2- and 4-pyridine layers on the silicon electrodes was well inside the range of reactivity increase found with 3-pyridine layers and did not show distinguishable characteristics.

5.2 Electrochemical stability of the HER onset shift on 3-pyridine-terminated silicon electrodes

After electrografting 3-diazopyridine onto silicon electrodes the pyridine molecules form a covalent bond with surface silicon atoms (or with other pyridine molecules), which should create a robust modified surface. Grafted electrodes retained their electrochemical behaviour after ultrasonification in H_2O and organic solvents like acetone, ethanol and isopropanol. In this regard the grafted layer on a silicon electrode shows similar stability as grafted pyridine layers on glassy carbon [111, 113] and grafted benzene derivatives on silicon electrodes [66, 67]. Figure 5.4 shows CVs of an electrode that

---

[1] both members of: WACKER-Chair of Macromolecular Chemistry, Technical University of Munich Chemistry Department

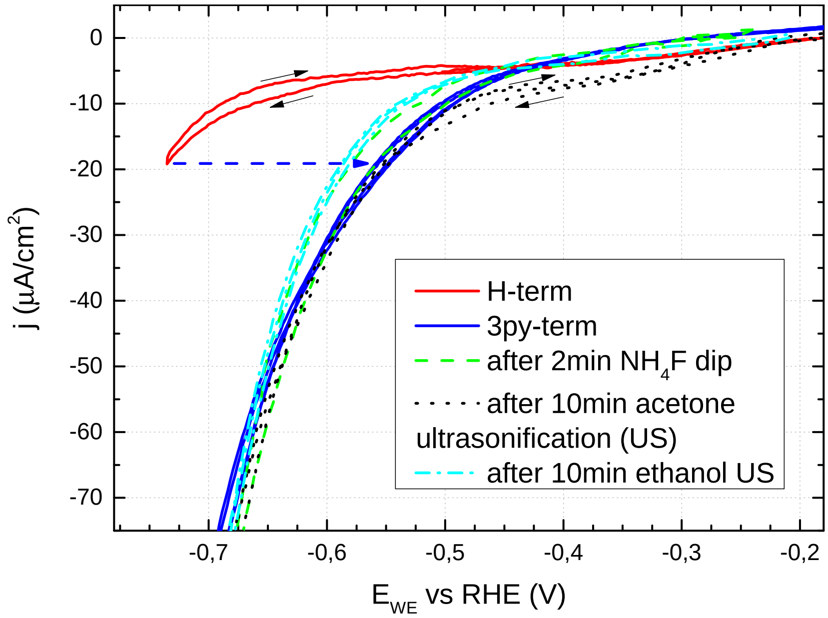

Figure 5.4: CVs of a grafted Si electrode (blue) after dipping in NH_4F (40%) (green), ultrasonicated for 10 minutes in acetone (black) and ethanol (cyan), compared to the CV of the initially H-terminated silicon electrode (red). Electrolyte: 0.1 M H_2SO_4 and 1.8 mM HF, purged with Ar. Scan rate: 50 mV/s. Data from the bachelor thesis of Sebastian Lindner [68].

was grafted, cleaned, etched, and afterwards measured in 0.1 M H_2SO_4 + 1.8 mM HF (blue). Then, it was subsequently rinsed with H_2O and dipped in NH_4F (40%) as an additional cleaning / etching step, rinsed again with H_2O and measured again in the aforementioned electrolyte (dashed green). This intermediate cleaning cycle was repeated with ultrasonication in acetone (dotted black) as well as ethanol (dashed dotted cyan). The onset shift of HER did not change after all of these cleaning cycles. The changes in the current step from -0.35 to -0.5 V vs RHE before the otherwise stable onset of HER might be attributed to remaining O_2 dissolved in the electrolyte during extraction and insertion of the sample [47, 126–128].

Silicon oxide formation is known to change the characteristics of a grafted layer [162]. It forms at "free" silicon surface sites (i.e. without surface termination such as hydrides or molecules) and grows isotropically into the bulk silicon und underneath the grafted surface area, thus roughening or fissuring it [64, 162]. After removal of this oxide via etching the remaining surface has a lower coverage of immobilized molecules, because some were attached to oxidized silicon atoms which were removed during etching. In the case of layers which inhibit reduction reactions, i.e. HER, such as benzene derivatives [66, 162], the lower molecule coverage led to smaller negative onset shift of the HER, which was previously shown in figure 4.9, thus diminishing the passivating effect of the grafted benzene layer on the HER. On electrodes modified with 3-pyridine an opposite trend was observed, when an anodic or oxidative potential was applied to the silicon electrode. As seen in figure 5.5 the improved onset of HER of the grafted electrode is diminished, once the n-type electrode is oxidized by a potential sweep above -0.2 V vs RHE to 0.75 V vs RHE in ambient light.

In figure 5.6, a grafted electrode with an observed HER onset shift (blue) was stored in air for two weeks and thus possessed a native oxide layer [48], when it again

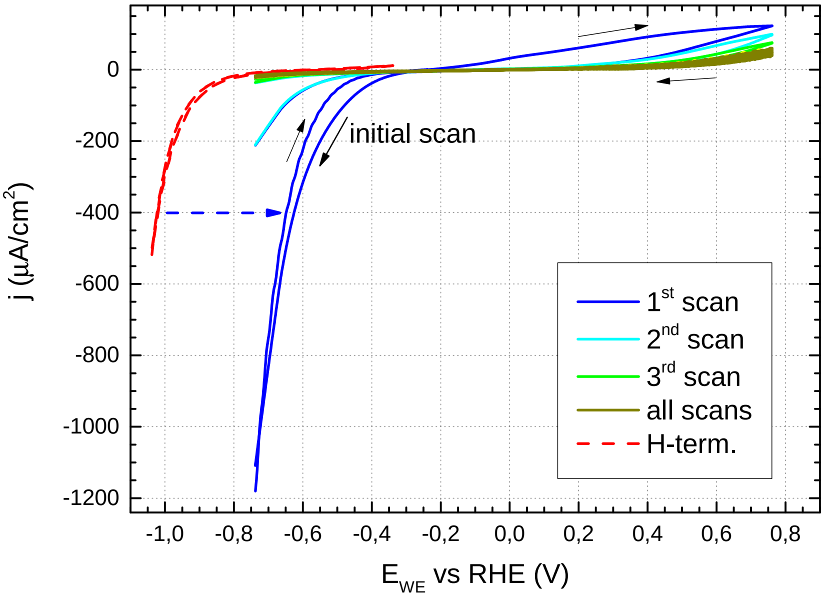

Figure 5.5: CV of a grafted silicon electrode (same sample as in fig. 5.1), whereby the potential was swept into the anodic / oxidizing region, with the first (blue), second (cyan) and following scans (dark yellow) in ambient light. As reference, the CV of the electrode in its initial, H-terminated state is also shown (dashed red). Electrolyte: 0.5 M H_2SO_4, purged with Ar. Scan rate: 50 mV/s

was electrochemically measured. Similar to figure 5.5 the resulting CV (cyan) showed a smaller onset shift for HER compared to its initial, H-terminated state (red). After etching the oxidized or aged sample, the improved onset of HER due to the grafted 3-pyridine-layer, that the sample showed before the oxidation / ageing, could be restored (green).

However, oxidation or ageing of the sample and subsequent etching of oxidized electrode could also lead to a diminishing of the HER onset improvement. Figure 5.7 shows a grafted sample which HER improvement is dimished after storage in air for two month and up to four cleaning / etching steps. Similar to the oxidation and the resulting fissuring of other grafted layers [162] a loss of grafted pyridine molecules on the aged, etched sample surface could explain the negative development of the HER onset shift. In an analogous manner to the 3-pyridine-termination, immobilized 4-bromo- and 4-nitrobenzene molecules led to a negative shift of the onset of HER on the grafted samples (see fig. 4.9) and the passivating or deactivating effect of these layers diminished after etching them in NH_4F, which led to defects in the grafted layer and therefore a reduction of the negative HER onset shift [65].

Apparently, the covalently bound pyridine layer is stable towards ultrasonification in water and organic solvents. But it is remarkable that oxidation of a grafted silicon electrode negates the HER onset improvement. In this regard it behaves similarly to an unmodified, H-terminated silicon electrode; the pyridine layer does not protect the silicon surface from oxidation, as it has been reported in publications of silicon electrodes grafted with phenyl derivatives which also show signs of silicon oxide after the functionalization [64,66,67,120,122,162]. The observations with oxidized, 3-pyridine-terminated samples not only point towards a rather porous pyridine layer, since a continuous layer

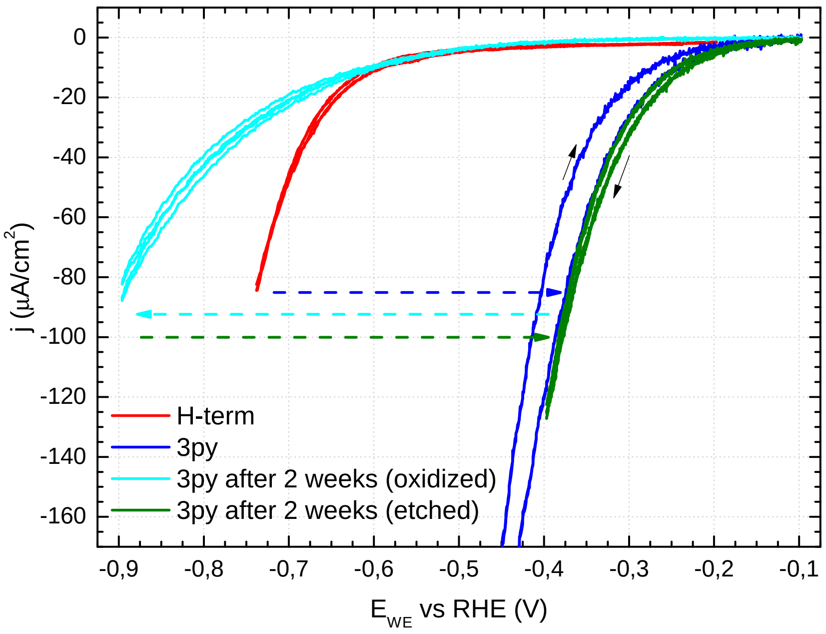

Figure 5.6: CVs of a grafted sample with H-termination (red), with 3-pyridine-termination (blue), as well as CVs of the grafted electrode after oxidation in air for two weeks (cyan) and subsequent etching of oxidized 3-pyridine-terminated sample. Electrolyte: 0.1 M H_2SO_4, purged with Ar. Scan rate: 100 mV/s.

should passivate the sample from oxidation. But it also appears that the improved onset of HER originates from an interaction of the grafted pyridine molecules with the non-functionionalized, H-terminated silicon surface itself rather than only from the grafted layer. Oxidation of the grafted pyridine molecules also could not explain the deactivation of the modified surface, as pyridine should not be oxidized in the potential range where silicon surface oxidation occurs but rather at more anodic values of $\approx$ 1.41 V vs SCE [18, 163].

5.3 HER on grafted silicon electrodes in weakly acidic electrolytes

To further investigate the effect of the grafted 3-pyridine layer on HER, the electrochemical behaviour of the grafted electrodes in electrolytes with a weakly acidic pH was examined. Silicon electrodes decorated with metal islands showed a shift in the onset of HER in neutral to alkaline electrolytes similar to or even larger than in acidic electrolytes (see table 5.1). Dissolved pyridine has a pK_a value of 5.3 [18] and thus is present in acidic electrolytes mainly as the positively charged pyridinium. The pK_a value of pyridine / pyridinium grafted on glassy carbon was estimated to be $pK_{a,gPy}$ $\approx$ 5 [113], which is very close to the value of dissolved pyridinium. Therefore, it can be assumed that the grafted pyridine layer at acidic pH values is also comprised of immobilized pyridinium molecules, which would deprotonate (back) to pyridine at pH values around and above 5. Signs of grafted pyridinium or its hydronated nitrogen atoms have also been observed as an additional peak shifted to higher binding energies in the nitrogen N_{1s} detail XP spectra on grafted glassy carbon electrodes [113].

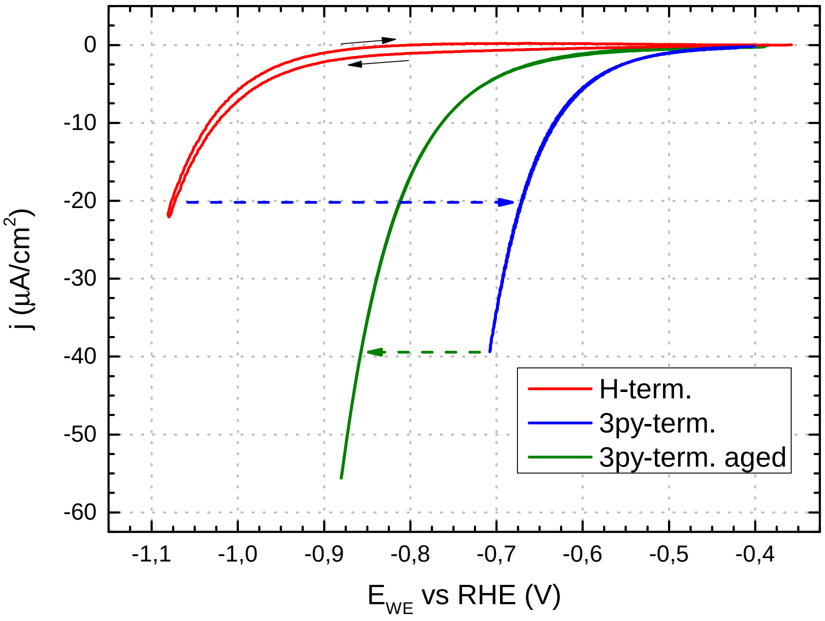

Figure 5.7: CVs of an electrode with H-termination (red) and 3-pyridine-termination after grafting (blue) and after two months long storage in air and final etching step (green). Electrolyte: 0.5 M H_2SO_4, purged with Ar. Scan rate: 50 mV/s.

Curiously, the improvement in the onset of HER on 3-pyridine-terminated silicon electrodes vanishes in an electrolyte with a weakly acidic pH, as can be seen in figure 5.8. In this plot, the first cycles of the CVs from the two samples are compared, one H-terminated (solid red), the other modified with a 3-pyridine-layer (dashed red, dashed and solid blue lines). The grafted electrode shows a positive HER onset shift of about + 200 mV in an acidic environment but practically no onset shift in an electrolyte with a pH $>$ 6. Only the first cycle of each CV of the measurements in the neutral electrolyte is shown, because the electrochemical behaviour or its current response of the electrodes did not stay constant during the usual time period of one CV measurement ($\approx$ 3 - 5 minutes), i.e., the voltammograms of different cycles did not stabilize during the time of several CV cycles. This instability varied with different electrolyte components and salts at the same bulk pH such as Na_2SO_4, universal buffer (Na_2HPO_4 + citric acid) and sodium acetate buffer, with K_2SO_4 showing the smallest degradation effect. As a first assumption, this could be linked to a degradation or roughening of the silicon surface due to alkaline etching [164], when the local pH at the electrode|electrolyte interface is shifted to alkaline values, when protons are consumed during HER.

The change in electrochemical behaviour of the grafted silicon electrodes when increasing the pH of the electrolyte mirrors that of a pyridine-grafted glassy carbon electrode reducing and oxidating ferricyanide $[Fe(CN)_6]^{3-/4-}$ [111, 113] (see fig. 5.9). On glassy carbon electrodes, the grafted pyridine layer acts as a blocking layer for the redox reaction, leading to subdued oxidation and reduction current peaks of the ferricyanide in electrolytes with higher pH values. However, the blocking properties of the pyridine layer are diminished when the pH of the electrolyte is consequently shifted to lower or more acidic values, to where the CV at pH 3 looks almost the same as the CV on a bare, ungrafted glassy carbon electrode. Using this dependence of the current response on the pH of the solution it was then shown that the blocking properties of the pyridine

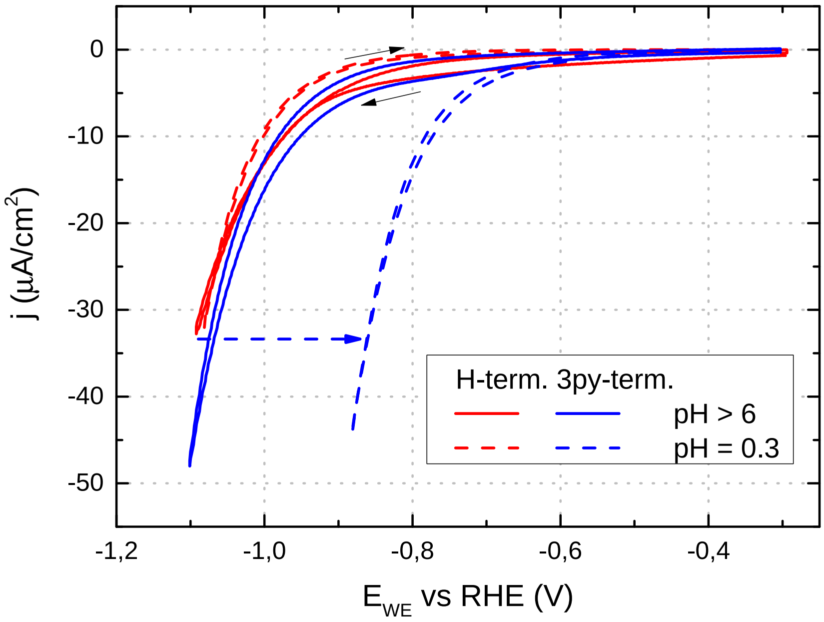

Figure 5.8: CVs of a silicon electrode with H-termination (red) and 3-pyridine-termination after grafting (blue) in acidic electrolyte (0.5 M H_2SO_4, purged with Ar, dashed lines) and neutral electrolyte (0.5 M K_2SO_4, pH > 6, purged with Ar, solid lines). Scan rate: 50 mV/s.

layer on top of glassy carbon depends on the state of protonation of the grafted pyridine molecules and the changing interaction of the pyridine / pyridinium layer with the $[Fe(CN)_6]^{3-/4-}$ anions. When protonated, the positively charged pyridinium molecules tended to pull the negatively charged $[Fe(CN)_6]^{3-/4-}$ molecules closer to the electrode, thus increasing the redox reaction current. In an analogous manner, it seems that the protonation of the pyridine molecules grafted onto silicon electrodes is essential for the resulting onset shift of the HER. Once deprotonated, the same grafted electrode does not exhibit the improvement of the HER onset any more in an electrolyte with pH > 6.

3-pyridine terminated silicon electrodes show an increased reactivity towards HER, i.e., a shift of its onset potential for HER towards a smaller overpotential in acidic electrolytes. This shift is linked to the protonation of the immobilized pyridine molecules to pyridinium, as the HER onset shift vanishes, when the pH of the electrolyte is higher than the pK_a of grafted pyridinium molecules. One possible cause would be the increase of the local proton concentration at the electrode|electrolyte interface due to the protonated 3-pyridinium layer at the surface. If half of the surface is covered by grafted pyridinium molecules as proposed in chapters 4.2 and 6.4, then there are $n_{3py} \approx 2.0 \cdot 10^{14}$ grafted 3-pyridinium molecules per 1 cm^2 Si (111) surface. With that, a local H^+ concentration from the pyridinium molecules can be calculated, together with the thickness of the 3-pyridine layer $d_{3py} = 4$ Å and the Avogrado number N_a:

$$[H^+]_{3py} = \frac{n_{3py} \cdot d_{3py}}{N_A} \approx 300\,\mathrm{M} \tag{5.1}$$

The local $[H^+]_{3py}$ concentration would be 600× higher than the bulk concentration of

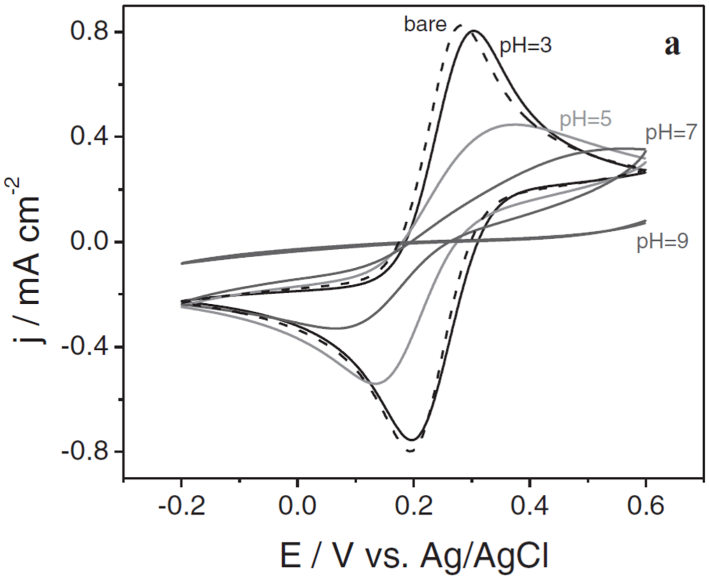

Figure 5.9: CVs of a grafted glassy carbon electrode in electrolytes with varying pH values containing 5 mM Fe(CN)$_6$ $^{3-/4-}$. Electrolyte: 0.1 M KCl, pH adjusted with HCl and KOH. Scan rate: 20 mV/s. Original plot taken from [113].

protons of 0.5 M. The resulting shift of the HER due to the pH change in front of the electrode would only amount to a part of the presented total HER onset shift:

$$\Delta \mathrm{E}_{\mathrm{H^+/H_2,pH}} = 2.77 \cdot (+59)\,\mathrm{mV} \approx 163\,\mathrm{mV} \tag{5.2}$$

Another cause for the increased reactivity might be linked to an improvement of the kinetic parameters for HER at the modified silicon surface, i.e., a lowered activation barrier, considering the slope of the Tafel plots does not seem to noticeably change with the grafted pyridinium molecules (see fig. 5.2). The reaction mechanism of HER on semiconducting electrodes poses numerous questions and electrochemical impedance spectrometry (EIS) measurements could provide valuable insight into the overall reaction and the effect of surface modifications on the reaction itself. This is discussed in the next chapter.

Chapter 6

Electrochemical Impedance Spectroscopy measurements of grafted silicon electrodes

To further investigate the effect of the grafted pyridine layer on silicon electrodes, Electrochemical Impedance Spectroscopy (EIS) measurements were conducted. The perturbation frequencies range from 10 kHz down to 50 mHz, while the potential in the cathodic region was set between the onset of HER (e.g. > -0.7 V vs RHE for H-terminated silicon electrodes) and ≈ -0.2 V vs RHE to reduce the influence of possible surface oxidation. Measurements were conducted starting from the cathodic potential limit and shifted to more anodic potentials. The perturbation amplitude E_p was ± 20 mV. Impedance values in the following are stated for an electrode area of 1 cm^2 if not otherwise mentioned.

6.1 Impedance measurements in the cathodic potential region

In the cathodic potential region a typical Nyquist plot of the impedance spectrum of an H-terminated silicon sample consists mainly of a half circle, as can be seen on the right of figure 6.1. This main feature can be fitted with an equivalent circuit consisting of two resistors (R_S, R_P) in series and a capacitor C_P connected in parallel to the resistor R_P (see figure 6.2). The dashed lines in the Nyquist plot in figure 6.1 show the corresponding fits of the data points depicted with the coloured squares.

R_S can be interpreted as the serial resistance of the electrochemical cell comprised of the resistances of the electrolyte, the contacts and the potentiostat. The half circle can be interpreted as a redox reaction such as HER taking place on the surface in the double layer, with $R_P \mathrel{\widehat{=}} R_{ct}$ denoting the charge transfer (CT) resistance of the assumed reaction through the electrochemical double layer in front of the electrode and $C_P \mathrel{\widehat{=}} C_{dl}$ as the capacitance of the double layer. Modifying the same silicon electrode (red in figure 6.1) with a 3-pyridinium-layer, the grafted electrode (blue in figure 6.1) also displays a half circle in the Nyquist plot which is, however, noticeably smaller than the one of the H-terminated surface, i.e., the resistance of R_P is greatly reduced. The reduction of R_{ct} could be seen in accordance to the improved HER on the grafted

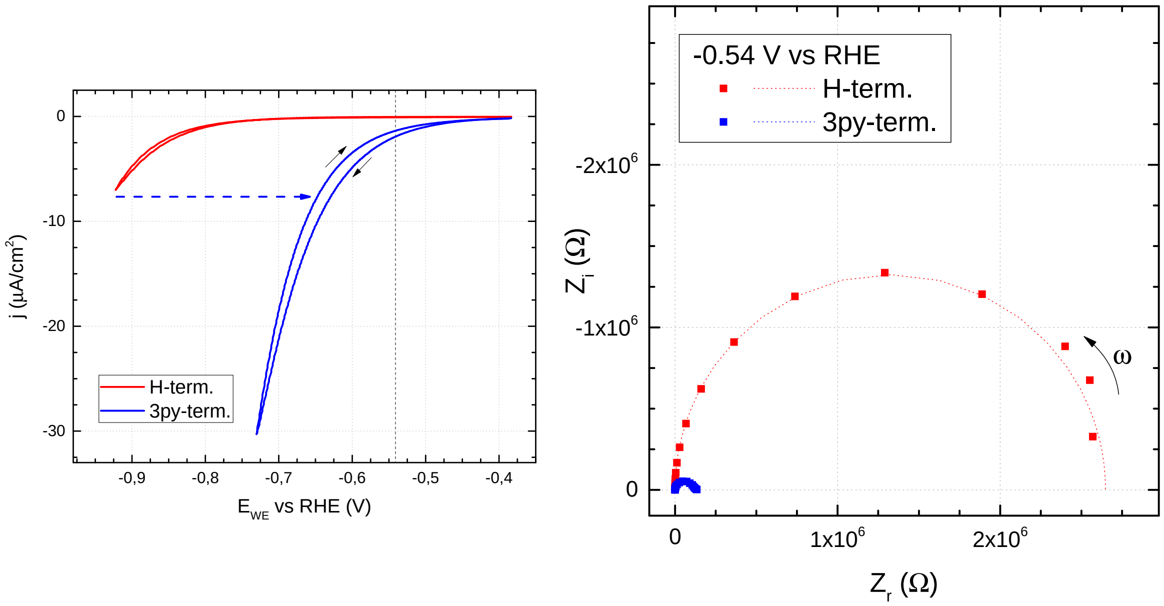

Figure 6.1: Left: CVs showing the effect of the grafted 3-pyridinium-layer on HER on the silicon electrode. The black dashed line marks the corresponding WE potential for the single EIS measurements. Scan rate: 10 mV/s ; Right: Nyquist plots of a silicon electrode with H-termination (red) and with 3-pyridinium-termination (blue) at -0.54 V vs RHE. Dotted lines show the corresponding fits of the data points. Electrolyte: 0.1 M H_2SO_4, purged with Ar.

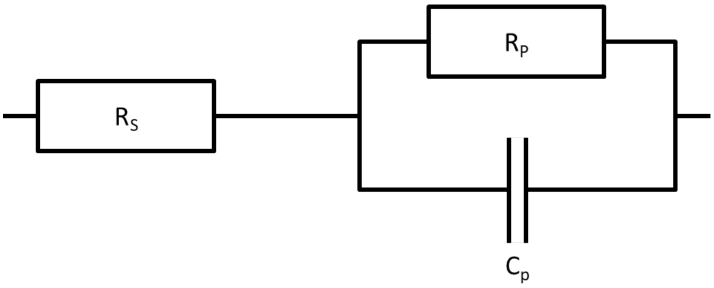

Figure 6.2: Equivalent circuit used to fit the recorded EIS spectra in figure 6.1

silicon electrode described in the previous chapter, as it would denote a more facile charge transfer through the double layer.

In figure 6.3 the values for C_P were taken from the individual fits of the Nyquist plots recorded at different potentials and plotted versus the potential of the electrode E_{WE}. The H-terminated silicon electrode shows a sloped C_P vs E_{WE} curve, which exhibits a sigmoidal shape, starting around -0.15 V vs RHE (Fig. 6.3, red curve). While the shape of the C_P vs E_{WE} curve for the grafted, 3-pyridinium-terminated electrode stays similar, $C_{P,3py}$ is increased compared to $C_{P,H}$ over most of the aforementioned cathodic potential region. Similar to the charge transfer resistance, since the onset of HER is improved on the grafted silicon electrode, as seen in the left side of figure 6.1, this increase in capacitance could also be attributed to the grafted 3-pyridinium layer as in the previous chapter 5. This connection was further explored with EIS measurements in electrolytes with a weakly acidic pH (see figure 6.4). The measurement were conducted after the corresponding CVs shown in figure 5.8 in the previous chapter. The measured

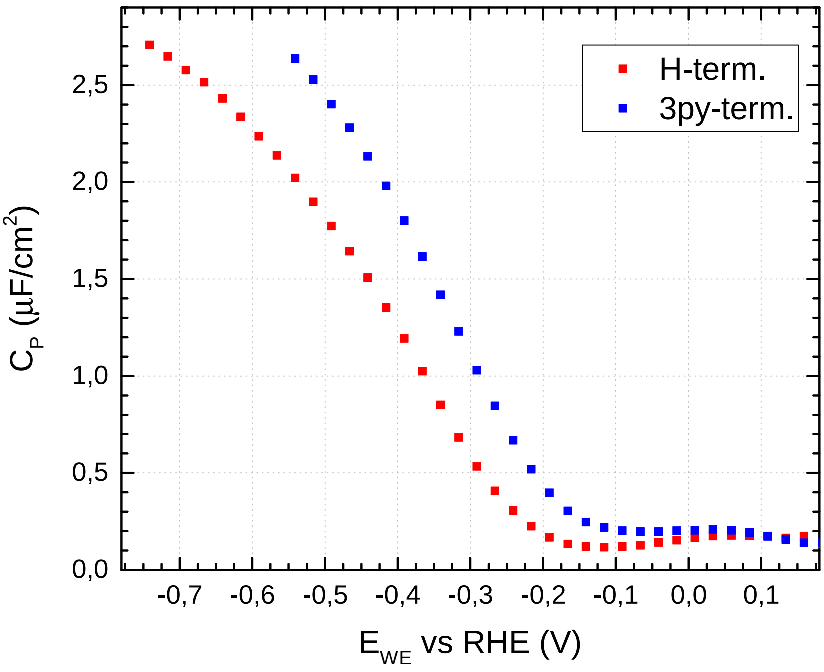

Figure 6.3: Plots of the parallel capacitance C_P vs E_{WE} of a silicon electrode with H-termination (red) and 3-pyridinium-termination (blue). Electrolyte: 0.1 M H_2SO_4, purged with Ar.

potential ranges were chosen in accordance to the initial and turning potentials of the CVs, which did not cover the less cathodic parts of the C_P vs E_{WE} curve compared to the curves in figure 6.3.

In a weakly acidic electrolyte with a pH higher than the pK_a value of pyridinium, thus with deprotonated grafted 3-pyridine molecules, the C_P vs E_{WE} curve of the grafted silicon electrode exhibits lower capacitance values than the curve of an H-terminated silicon electrode. Other than a general increase of C_P compared to the measurements in 0.5 M H_2SO_4, the change of C_P due to the grafted pyridine layer matches more closely the reported decrease of the total capacitance of silicon electrodes after grafting them with (electrochemically passivating) organic molecules such as 4-bromobenzene and 4-nitrobenzene, as displayed in the reference figure on the right of figure 6.4. For comparison, the potential scale on the top in figure 6.4 is noted vs a mercury/mercury sulfate reference electrode (MSE) instead of RHE. The inset in the reference figure show the same effect of the grafted 4-bromo- or 4-nitrobenzene layers on the HER as in figure 4.9, namely a negative onset shift of the HER compared to an H-terminated silicon electrode. In contrast to this behaviour, the CVs in the weakly acidic electrolyte of the 3-pyridine-terminated electrode did not show a negative shift of the HER onset as much as an unchanged HER onset for the silicon electrode grafted with deprotonated pyridine molecules. Again, the protonation of the immobilized pyridine molecules seems to be the cause for the higher differential capacitance that the grafted 3-pyridinium-terminated silicon electrodes exhibit in the cathodic potential region compared to other reported functionalized electrodes. The increase in capacitance can apparently be negated by deprotonating the pyridinium molecules in electrolytes with pH higher than the pK_a of pyridinium in the same way the positive onset shift of HER can be negated.

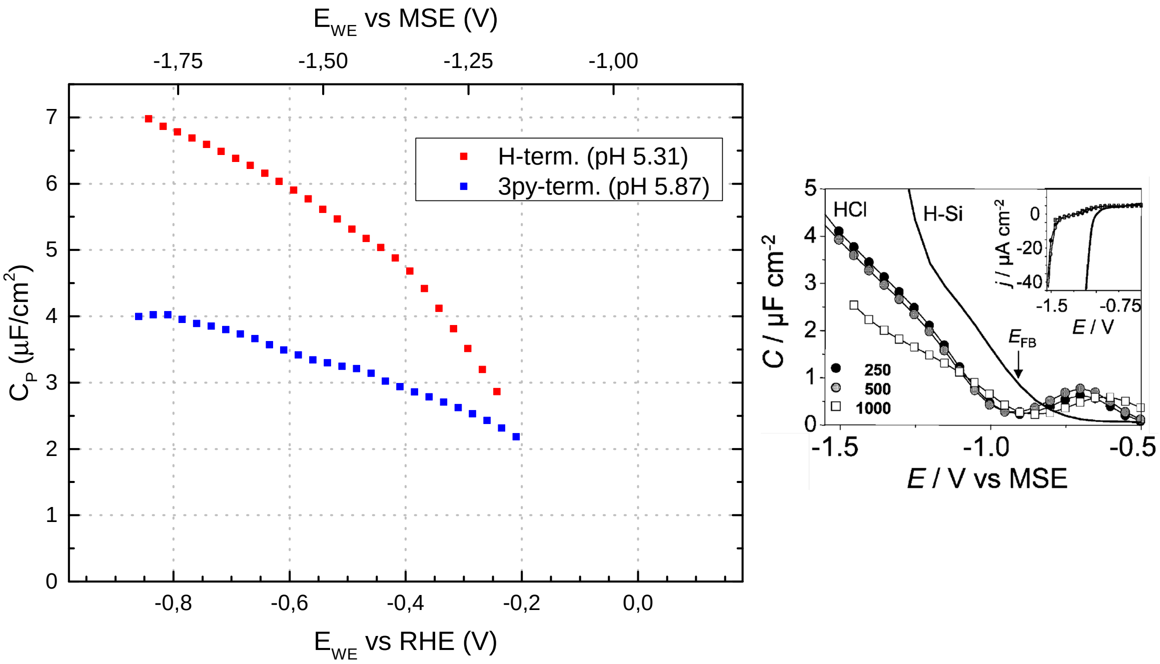

Figure 6.4: Left: C_P-E_{WE} plots of a silicon electrode with H-termination (red) and 3-pyridine-termination (blue) in an electrolyte with a weakly acidic pH. Electrolyte: 0.5 M K_2SO_4; pH: 5.31 (H-termination) and 5.81 (3-pyridine-termination); purged with Ar. Potentials also plotted vs MSE for comparison with reference figure on the right. Right: C-E_{WE} plots of silicon electrodes with H-termination (solid) and after electrografting 4-bromobenzene diazonium salt, using a grafting charge of 250, 500, 1000 $\mu C/cm^2$. Electrolyte: 0.1 M HCl, pH 1, purged with Ar. Original figure from [64].

6.1.1 EIS measurements at HER

In addition, EIS measurements were conducted at potentials, where hydrogen evolved on the electrodes with a faradaic current density of $\approx 20\ \mu A/cm^2$ in an acidic electrolyte (cf. figure 6.5). Over a large range of frequencies the resulting Nyquist plots of both H-terminated and 3-pyridinium-terminated electrodes (at similar current densities) look very similar to the ones shown in figure 6.1 and can be modelled with the same equivalent circuit shown in figure 6.2. This means, at a comparable current density there are no signs in the EIS spectra which point towards a different reaction mechanism taking place at the grafted silicon electrode (blue) compared to the initially H-terminated electrode before grafting (red), albeit requiring less overpotential. When the grafted electrode was measured at the same potential (navy) as the H-terminated electrode, then the half circle of the Nyquist plot was greatly reduced in size, i.e. the charge transfer resistance R_{CT} is greatly reduced, similar to figure 6.1, together with a corresponding increase of the faradaic reaction current. In contrast to the main half circle, the origin of the linearly increasing part of the spectrum at high frequencies remains unclear, but it seems unaffected by the grafted 3-pyridinium layer. Like in figure 5.2, the HER as the main reaction occurring on the modified silicon electrode seems to take place in the same manner as on the H-terminated silicon electrode, only with its onset shifted towards smaller overpotentials.

Noticably, the values for the parallel capacitance C_p after the onset of HER are lowered for the grafted silicon electrode compared to the H-terminated electrode, both

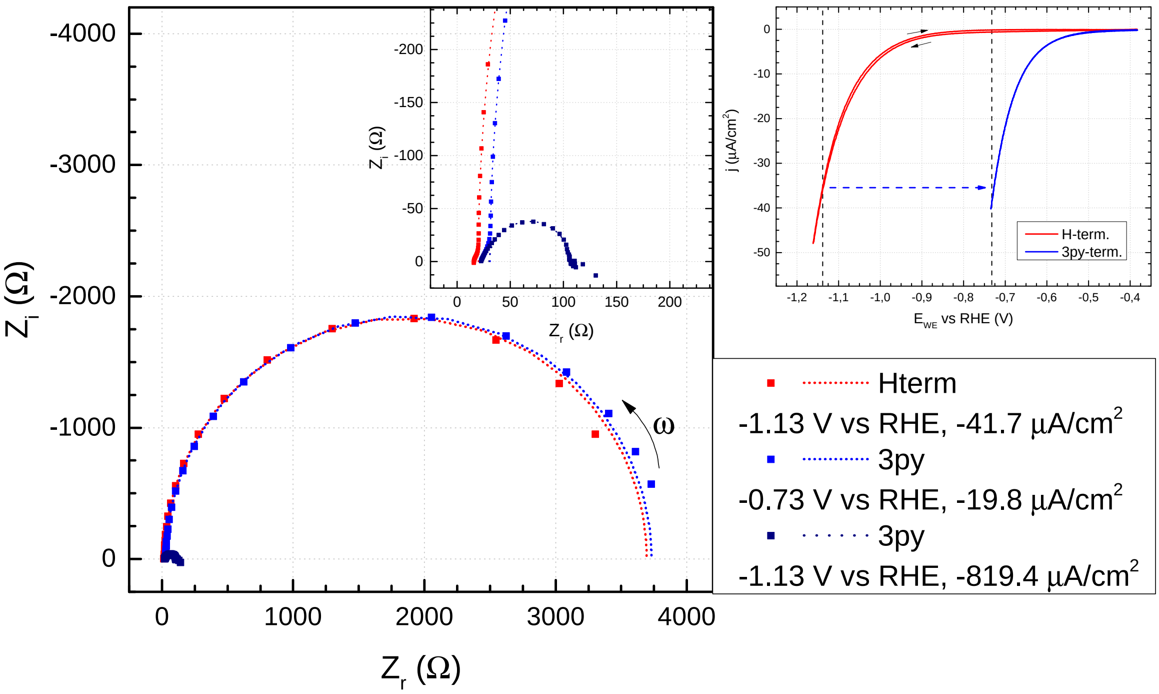

Figure 6.5: Left: Nyquist plots of a silicon electrode with H-termination (red) and with 3-pyridinium-termination at a comparable faradaic current $\approx -20\,\mu\mathrm{A/cm}^2$ (blue) as well as at the same potential (-1.13 V vs RHE) (navy, inset). Dotted lines show the corresponding fits of the data points. Right: CVs showing the effect of the grafted 3-pyridinium-layer on the HER on the silicon electrode. The black dashed lines mark the corresponding potentials for the single EIS measurements. Electrolyte: 0.5 M H_2SO_4, purged with Ar. Scan rate: 50 mV/s

for the measurements at the same potential and at similar current densities. The EIS measurement of the grafted silicon electrode after HER onset thus shows a capacitive behaviour different from the general increase of C_p for grafted electrodes in the cathodic region *before* the onset of HER (fig. 6.3). The deviation is believed to stem from the beginning HER current and its effect on the impedance of the interface [162, 165]. As described in the discussion section 6.4, the sigmoidal shape of the C_P vs E_{WE} curve is excepted to saturate around a plateauing capacitance value independent of the more cathodic potentials, but C_P vs E_{WE} curves systematically deviate from that proposed behaviour when, as in figure 6.3, the C_P vs E_{WE} curves continues to rise with more cathodic potential. This deviation might be caused by the changing charge transfer impedance once faradaic current from HER sets in. R_{CT} values from the EIS spectra before HER onset from figure 6.3 are in fact 10-30 times larger than the values derived from the EIS measurement after onset of HER. This decrease of the faradaic part of the RC impedance of the double layer could lead to the change in C_P, but needs further investigation.

In summary, grafted, 3-pyridinium-terminated silicon electrodes show a similar qualitative behaviour in the EIS measurements in the cathodic potential region compared to their initially H-terminated state, but a *decrease* of the charge transfer resistance R_{CT} across the double layer and an *increase* of the total capacitance C_p. In contrast, the grafted 3-pyridine-layer on glassy carbon electrodes is reported to lead to an increase of the charge transfer resistance, which is explained by the grafted

	H-term.	3py-term., same j	3py-term., same E_{WE}
R_S	20 Ω	31 Ω	30 Ω
R_{CT}	3.67 kΩ	3.70 kΩ	77 Ω
C_p	3.9 μF	1.8 μF	2.1 μF

Table 6.1: Fit values of the EIS spectra in figure 6.5 using the equivalent circuit 6.2 of the H-terminated silicon electrode (left column), the 3-pyridinium-terminated electrode at a comparable current density $\approx -20\,\mu A/cm^2$ (middle column), and finally the 3-pyridinium-terminated electrode at the same potential (-1.13 V vs RHE) as the H-terminated electrode (right column).

molecules forming a blocking layer for the redox reaction of ferricyanide $[Fe(CN)_6]^{3-/4-}$ [111, 113, 166]. Similarly, silicon electrodes are reported to show a decrease of their total capacitance compared to unmodified H-terminated electrodes when modified with a passivating or blocking layer of organic molecules, such as 4-bromobenzene and 4-nitrobenzene [64], which are similarly sized molecules compared to pyridine. Other grafted silicon and glassy carbon electrodes also exhibited a lowering of their total capacitance of the electrode|electrolyte interface after surface modification with organic molecules [165, 167, 168]. In contrast to those reports, for glassy carbon electrodes grafted with carboxyphenyl groups the capacitance at open circuit potential in 0.1 M KCl containing 5 mM $K_3Fe(CN)_6$/5 mM $K_4Fe(CN)_6$/0.1 M phosphate buffer (pH 7) was reported to increase [166]. The increase of the total capacitance of the 3-pyridinium-terminated silicon electrode electrode might point towards an opposite effect of the pyridine / pyridinium layer compared to the benzene layers on silicon electrodes, which is further addressed in section 6.4.

6.2 Mott Schottky plots

EIS measurements were also conducted at potentials positive of the OCP. In the anodic potential region electrons as the majority charge carriers in the n-type silicon electrodes are depleted, leading to positive band banding at the surface. In this depletion region one can make use of the Mott Schottky (MS) equation to determine the flatband potential E_{fb} and the doping density N_D:

$$\frac{A^2}{C_{SC}^2} = \frac{2}{e\epsilon_{Si}\epsilon_0 N_D}(E_{WE} - E_{fb} - \frac{kT}{e}) \tag{6.1}$$

A is the area of the electrode, e the elemental charge, ϵ_{Si} the permittivity of silicon ($\epsilon_{Si} = 11.9$ [48]), N_D the doping density, $E_{WE} - E_{fb}$ the potential of the silicon electrode relative to its flatband potential E_{fb}, k the Boltzmann constant and T the temperature. When we assume that most of the potential drop over the electrode|electrolyte interface occurs in the space charge layer and none in the Helmholtz layer, i.e., C_{SC} is much smaller than C_H and thus dominates the total capacitance, then we can denote $C_P \mathrel{\widehat{=}} C_{SC}$ and use the same equivalent circuit in figure 6.2 to fit the EIS spectra in the anodic region, which show a similar half circle shape in their corresponding Nyquist plots. For the MS plots the measurements were conducted between ≈ 0.3 V and 1 V vs RHE.

For potentials below $E_{WE} \leq 0.3$ V deviations from the linear behaviour of the MS plot have been reported due to surface states on the silicon electrode in contact with the electrolyte [47], and are omitted for the fitting. Since the electrolyte used in these EIS measurements do not contain HF, the electrodes unpreventably oxidized when biased to anodic potentials, which again led to deviations from the linear behaviour at more anodic potentials. Hence, the surface oxidation limited MS measurements at more positive potentials for $E_{WE} > 0.8$ V vs RHE, where the obtained C_{SC} values were also omitted for fitting.

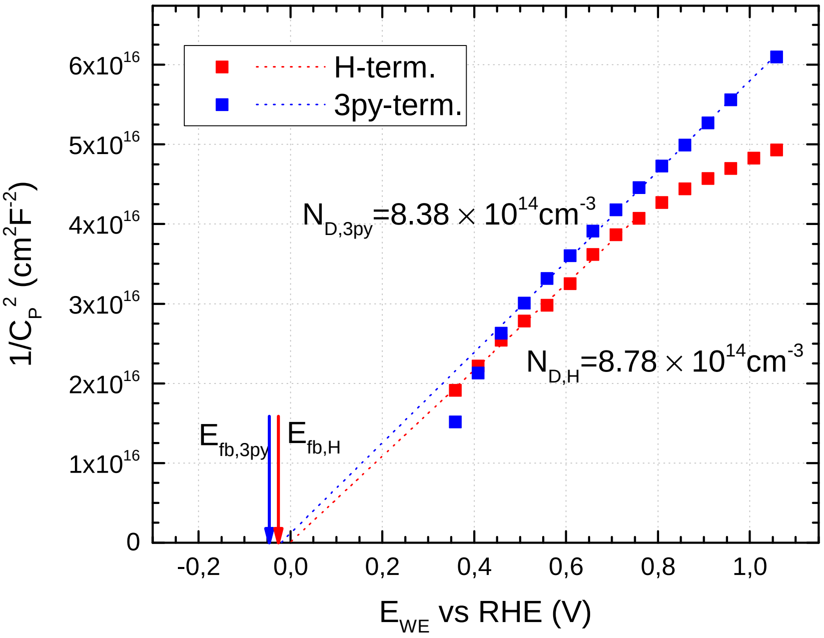

Figure 6.6: MS plots of the silicon electrode from figure 6.1 with initial H-termination (red) and 3-pyridinium-termination after grafting (blue). C_P values obtained from fitting the EIS spectra using the equivalent circuit 6.2. Electrolyte: 0.1 M H_2SO_4, purged with Ar.

The MS plots (figure 6.6) show a flatband potential for the H-terminated silicon electrode of $E_{fb,H} = -27$ mV vs RHE which is in good agreement with literature values ranging from -140 mV up to +40 mV vs RHE [47, 64, 169–171]. The doping density as determined from equation 6.1, $N_D = 8.78 \times 10^{14}$ cm^{-3}, also correnspods well with the values of the manufacturer for the specific resistance $1 - 10\,\Omega$cm for the silicon wafers used in this thesis. The grafted electrode exhibits only a slightly changed flatband potential $E_{fb,3py}$ of about -20 mV more negative than $E_{fb,H}$. However, the values varied from sample to sample up to $\Delta E_{fb} \approx \pm 80$ mV in their flatband potential after functionalization, with the mean value of all samples exhibiting $\Delta E_{fb,all} \approx -10$ mV. Some samples also exhibited a small positive shift of the flatband potential, as seen in figure 6.13. For grafted benzene derivatives a shift in flatband potential up to +200 mV has been reported [120], but it has also been reported that such a shift vanished in electrolytes containing HF [64].

As can be seen in figure 6.7, the same small shift of $E_{fb,3py}$ towards more negative potentials compared to $E_{fb,H}$ was observed when conducting the MS measurements in weakly acidic electrolytes with a pH higher than the pK_a of pyridine. These measurements were conducted following the measurements in figure 5.8 and 6.4 on the same

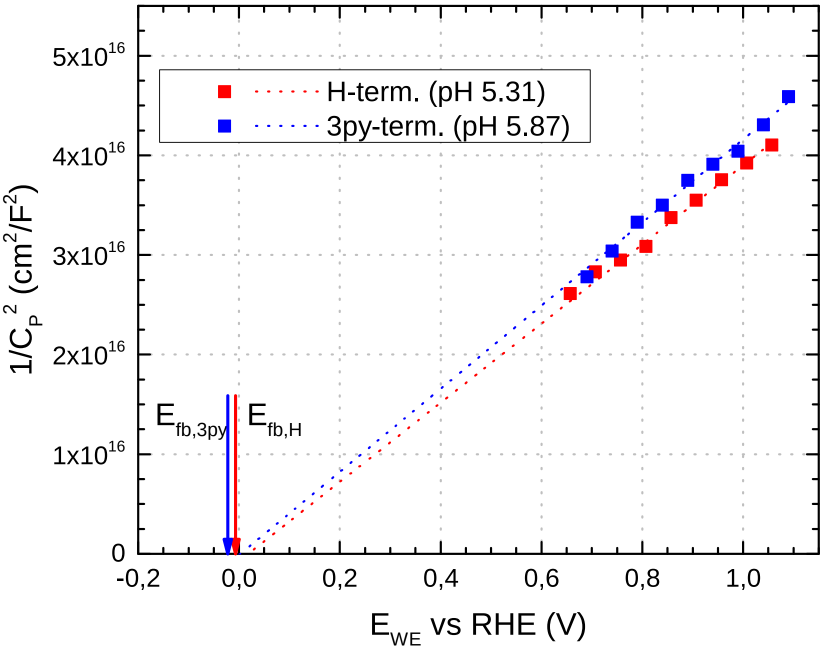

Figure 6.7: MS plots of the silicon electrode from figure 6.4 with initial H-termination (red) and 3-pyridine-termination after grafting (blue); Electrolyte: 0.5 M K_2SO_4, purged with Ar, pH 5.31 (H-term.), pH 5.81 (3py-term.)

silicon electrodes. The flatband potentials seem to shift in a Nernstian behaviour together with the RHE [171], although smaller, non-Nernstian shift values have also been reported in the literature [98, 172]. Again, the flatband potential was slightly -15 mV more negative with the 3-pyridine-termination after grafting, indicating that the shift of the flatband potential ΔE_{fb} might be independent of the pH of the solution and thus independent of the protonation / deprotonation state of the grafted pyridinium / pyridine layer.

The 3-pyridine-termination does not appear to drastically change the flatband potential compared to the initial H-termination on silicon electrodes. The onset shift of the HER due to the 3-pyridine layer of $> +400$ mV therefore cannot be explained by such a shift of the flatband potential of the modified electrode, especially since the shift of the flatband potential is towards slightly more negative potentials and seemingly independent of the protonation state of the grafted pyridine layer.

6.3 Discussion: Effect of the 3-pyridinium-termination on the surface energy band positions

With the gathered values of flatband potential and doping density from the MS plots, one can attempt to assemble the energy band diagram at the surface of the silicon electrodes and the effect the grafted 3-pyridinium-termination has on the band edge positions of the now modified silicon electrode. The main guiding energy value in order to examine the surface energy band diagram is the Fermi energy E_F, which can then be placed inside the band gap in relation to the position of the band edges. In the bulk of an n-doped silicon substrate at room temperature ($\approx$ 300 K) one can determine the position of E_F within the band gap in relation to the conduction band edge, using the doping density $\mathrm{N_D}$ obtained in the fitting of MS plot (see chapter 6.2):

$$E_\mathrm{F} = E_\mathrm{cb}^\mathrm{b} - \mathrm{kT} \ln \frac{\mathrm{N_C}}{\mathrm{N_D}} \Rightarrow E_\mathrm{cb}^\mathrm{b} - E_\mathrm{F} = \mathrm{kT} \ln \frac{\mathrm{N_C}}{\mathrm{N_D}} \tag{6.2}$$

with the bulk band edge of the conduction band E_cb^b, Boltzmann constant k, temperature T and effective density of states in the conduction band $\mathrm{N_C}$ [77]. The latter is given by:

$$\mathrm{N_C} = 2 \cdot \left(\frac{2\pi \mathrm{m}_e \mathrm{kT}}{h^2} \right)^{3/2} = 2 \cdot 10^{19}\,\mathrm{cm}^{-3} \tag{6.3}$$

with the mass of an electron m_e and the Planck constant h. With the known value for the electron affinity $\chi_\mathrm{Si} = 4.05\,\mathrm{eV}$ [48] the work function $\Phi_\mathrm{Si,b}$, i.e., the energy difference between the vacuum level E_vac and the Fermi energy E_F, of n-doped bulk silicon can be calculated:

$$\Phi_\mathrm{Si,b} = E_\mathrm{vac} - E_\mathrm{F} = \chi_\mathrm{Si} + (E_\mathrm{cb}^\mathrm{b} - E_\mathrm{F}) \tag{6.4}$$

At the surface, for example of the initially H-terminated silicon electrode, band bending leads to a shift of the band edges compared to E_F. When in contact with the electrolyte, the open circuit potential $\mathrm{E_{ocp}}$ of the electrode can be used to determine the work function $\Phi_\mathrm{Si,s}$ of the surface. Because at the open circuit potential the electrochemical potential of electrons at the surface of the electrode (E_F) is the same as in the electrolyte, the energy distance from E_F in the electrolyte to the vacuum level $\Phi_\mathrm{ocp,H}$ should be the same at the surface of the silicon electrode $\Phi_\mathrm{Si,s}$. With the absolute potential of the SHE ($\mathrm{E^0_{H^+/H_2}} = 4.44\,\mathrm{V}$ [73]), the work function $\Phi_\mathrm{ocp,H}$ can be calculated.

$$\Phi_\mathrm{ocp,H} = |\, e^- \cdot (\mathrm{E_{ocp,H}}(\mathrm{vs\,SHE}) + 4.44\,\mathrm{V})| = 4.149\,\mathrm{eV} \tag{6.5}$$

with the elemental charge e. $\Phi_\mathrm{ocp,H} \mathrel{\hat{=}} \Phi_\mathrm{Si,s}$ then can be compared to the work function $\Phi_\mathrm{Si,b}$ in the bulk of the n-doped silicon electrode. Unfortunately, $\mathrm{E_{ocp}}$ values were not consistently recorded for each electrode or surface termination. In the following the $\mathrm{E_{ocp}}$ values from another measurement set are exemplarily used, $\mathrm{E_{ocp,H}} = -0.291$ V vs SHE for the initially H-terminated silicon electrode and $\mathrm{E_{ocp,3py}} = -0.166$ V vs. SHE for the 3-pyridinium-terminated electrode resulting from the grafting process. Reported $\mathrm{E_{ocp,H}}$ values for n-doped H-terminated silicon electrodes are listed in table 6.2, where the above mentioned values fit in.

Silicon electrodes grafted with substituted benzene molecules were reported to show a shift of their respective $\mathrm{E_{ocp}}$ values of up to $\Delta\mathrm{E_{ocp}} \approx +110\,\mathrm{mV}$ compared to an H-terminated silicon sample [120], a shift similar to the values for $\mathrm{E_{ocp,3py}} - \mathrm{E_{ocp,H}}$ given above. Any differences in work function between $\Phi_\mathrm{Si,b}$ and $\Phi_\mathrm{Si,s}$ can then be assigned to the sum of the band bending E_bb

$$E_\mathrm{bb} = e^- \cdot (\mathrm{E_{fb}} - \mathrm{E_{ocp}}) \tag{6.6}$$

and a surface potential step δ, which corresponds to a change of the electron affinity of the surface. Controlling δ would allow for a tailoring of the electron affinity of

$E_{ocp,H}$ (V vs SHE)	Electrolyte	
-0.160	3.3 M NH_4F, pH 2	[98]
-0.180	1 M HF	[173]
-0.220	0.01 M H_2SO_4	[174]
-0.3	1 M HCl + 25 mM HF	[175]
-0.3	10 M NH_4F	[162]
-0.4	2 M HF	[136,137]

Table 6.2: Selection of $E_{ocp,H}$ values for n-doped H-terminated silicon electrodes in aqueous electrolytes.

Fig. 4.20	H-terminated	3py-terminated	data origin
E_{ocp}	-0.291 V vs SHE	-0.166 V vs SHE	
E_{fb}	-0.139 V vs SHE	-0.162 V vs SHE	MS plots (CU, f = 1 kHz)
N_D	$8.22 \cdot 10^{14}$ cm^{-3}	$8.15 \cdot 10^{14}$ cm^{-3}	MS plots (CU, f = 1 kHz)
E_{bb}	-0.152 eV	-0.004 eV	
δ	-0.004 eV	-0.027 eV	

Table 6.3: Surface potential step δ of the H-terminated and 3-pyridine-terminated samples from fig. 4.20 including the values used for its calculation.

the surface to better suit the desired application of the modified electrode, e.g. electrochemical reactions such as HER or CO_2 reduction [120,122,132,133]. An *increase* in δ would correspond to an effective *increase* of any redox potential of a chemical species in the electrolyte and therefore an effective *decrease* of an applied potential at the electrode|electrolyte interface, i.e. the potential drop ϕ_H in the double layer, thus leading to a lower reaction current at the same applied potential and vice versa.

$$\begin{aligned}\delta &= \Phi_{ocp,H} - E_{bb} - \Phi_{Si,b} = \\ &= \Phi_{ocp,H} - E_{bb} - \chi_{Si} - (E^{b}_{cb} - E_F)\end{aligned} \tag{6.7}$$

In table 6.3 the values used for the calculation of the band bending E_{bb} and the surface potential step δ stemming from the measurement data from figure 4.20, are listed.

The qualitative energy diagrams of the H-terminated and 3-pyridinium-terminated are shown in figures 6.8 and 6.9, respectively.

At open circuit potential in an acidic electrolyte (such as 0.1 M H_2SO_4 used in these measurements), the band bending is negative for the H-terminated silicon sample, corresponding to reports on similar n-doped silicon samples in NH_4F [49,98,162,175] and oxygen-free H_2O + 50 mM ammonium sulfite [176], i.e., there is a weak accumulation region near the electrode|electrolyte interface. $E_{bb,H} = -0.152$ eV is in the range of the reported values from -0.14 eV [98] up to -0.28 eV [176] and -0.50 eV [162]. After grafting, the 3-pyridinium-terminated sample appears to show nearly no band bending. These observations fit with the reported investigation of (slightly oxidized) p-doped silicon electrodes electrografted with substituted benzene molecules [120]. The grafted, modified surfaces also showed less band bending when immersed in an acidic electrolyte (0.1 M $HClO_4$). The surface potential $\delta_H = -0.004$ eV is close to zero

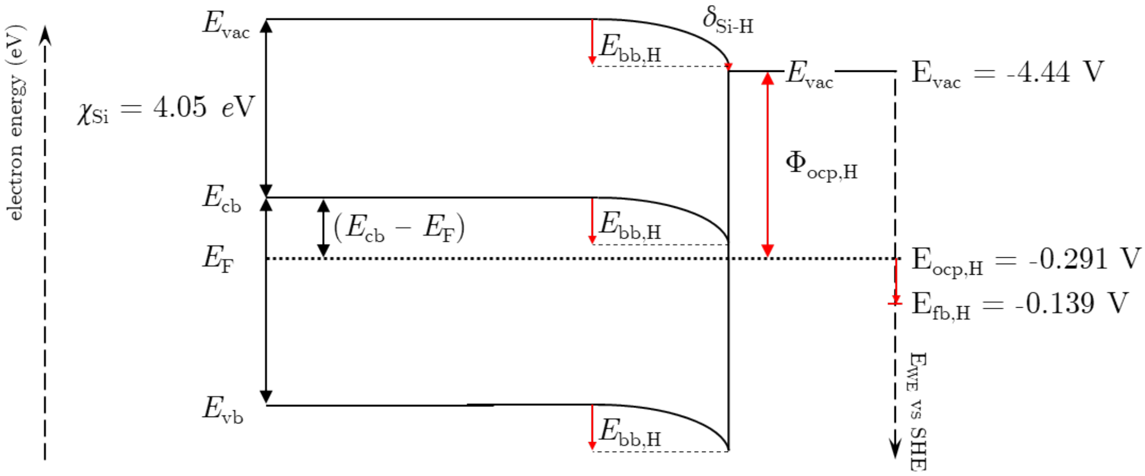

Figure 6.8: Energy level diagram of n-type silicon sample with H-termination (red) from the values from table 6.3.

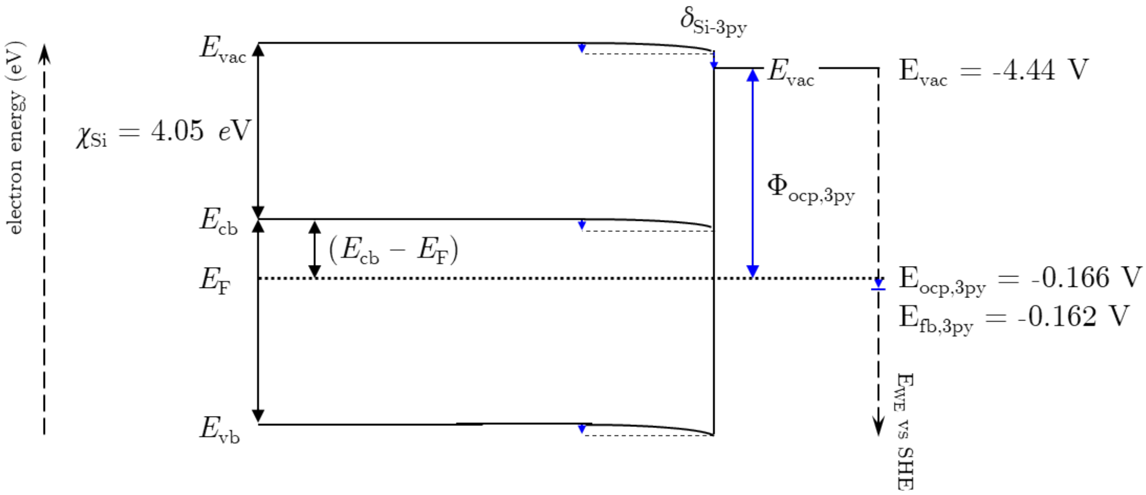

Figure 6.9: Energy level diagram of n-type silicon sample with 3-pyridine-termination after the grafting process (blue) from the values from table 6.3.

for the H-terminated silicon electrode and only changes to a slightly more negative value $\delta_{3py} = -0.027$ eV with 3-pyridinium termination. Similarly, p-doped (slightly oxidized), H-terminated silicon electrodes are reported to show only a small, negative surface potential δ (-0.01 eV), but the ones grafted with substituted benzene molecules exhibited surface potential steps up to -0.23 eV [120]. The resulting surface potential step with 3-pyridinium-termination changes only slightly and would only marginally (or not at all) contribute to the presented shift of the HER onset in chapter 5.

The same calculations of the surface potential step can be performed using XPS and UPS data concerning the changing binding energy of the Si_{2p} peaks in figure 4.20. Now the comparison is between the energy difference from the Si_{2p} level up to the vacuum energy E_{vac} using bulk values of silicon, and the sum of the observed binding energy $E_{b,Si2p}$ and the work function $\Phi_{Si,s}$:

$$\mathrm{BE}^{v}_{\mathrm{Si2p}} + E_{\mathrm{g}} + \chi_{\mathrm{Si}} + \delta \;=\; E_{\mathrm{b,Si2p}} + E_{\mathrm{bb}} + \Phi_{\mathrm{Si,s}} \tag{6.8}$$

with the bulk valence band maximum $\mathrm{BE}^{v}_{\mathrm{Si2p}} = 98.74$ eV [119, 122] and the band gap $E_{\mathrm{g}} = 1.12$ eV [177]. The band bending can be calculated by comparing the bulk energy difference from the $\mathrm{Si_{2p}}$ level up to the Fermi energy E_{F} and the observed binding energy $E_{\mathrm{b,Si2p}}$.

$$\mathrm{BE}^{v}_{\mathrm{Si2p}} + E_{\mathrm{g}} - (E^{\mathrm{b}}_{\mathrm{cb}} - E_{\mathrm{F}}) \;=\; E_{\mathrm{b,Si2p}} + E_{\mathrm{bb}} \tag{6.9}$$

Matching results have been reported regarding band bending energies of grafted p-type silicon electrodes [120]. Ultimately, the protonation of the grafted 3-pyridine molecules has to be considered and kept constant when comparing different samples in the same manner as in previous chapters. The values on which the energy level diagrams in figures 6.9 and 6.8 are based on in table 6.3 stem from EIS measurements in an acidic electrolyte; the grafted 3-pyridinium molecules are protonated. The effect of the additional positive charge of the pyridinium molecules will certainly change the energetics of the grafted silicon surface|electrolyte interface analogous to the change in other electrochemical properties described in the following chapters 5.3, 6.1 and 7. In order to match the energetics measured using either EIS or XPS, the state of the grafted pyridine layer has to be kept constant during both measurements, as it is in the other reported measurements of grafted organic layers comprised of molecules which cannot be protonated [120]. For future studies, these corresponding EIS and XPS/UPS characterizations of the modified silicon electrode would be an intriguing way to investigate of the effect of the grafted layer on the surface energy levels.

6.4 Discussion: Fitting the capacitance vs potential (C vs E_{WE}) curves and investigating its origin

As seen in figure 6.3, negative of E_{fb} the fitted values of the parallel capacitance Cp versus E_{WE} curve of the silicon electrodes in an acidic electrolyte display a sigmoidal shape with an exponential rise around the flatband potential E_{fb} and a flattened increase slightly before the onset of the HER. This behaviour of the total capacitance C_P per 1 cm^2 can be fitted with a series connection of two capacitors, the potential dependent capacitance of the space charge layer C_{SC} of the semiconducting silicon electrode, and the capacitance of the Helmholtz layer C_H [64, 78, 162, 165, 167, 178].

$$1/C_P = 1/C_{SC} + 1/C_H \tag{6.10}$$

with the (classical) Poisson-Boltzmann approximation of C_{SC} under accumulation conditions ($E_{WE} < E_{fb}$) [177]:

$$C_{SC} = \sqrt{\frac{e^2 \epsilon_{Si} \epsilon_0 N_D}{2kT}} \exp\left(-e\frac{E_{WE} - E_{fb}}{2kT}\right) \tag{6.11}$$

where e is the elemental charge, ϵ_{Si} the permittivity of silicon ($\epsilon_{Si} = 11.9$ [48]), N_D the doping density, k the Boltzmann constant, T the absolute temperature and $E_{WE} - E_{fb}$ the potential of the silicon electrode relative to its flatband potential E_{fb}. Furthermore, C_H is derived from the model of the Helmholtz double layer. The charge at the surface of the electrode Q_H has the same magnitude as the charge of the space charge layer $Q_{SC}+Q_H = 0$. The ions in the Helmholtz layer comprise a compact layer of hydrated counterions, in this case hydrated forms of protons such as H_3O^+ or ${H_{12}O_6}^+$ [179, 180].

$$C_H = \frac{\epsilon_H \epsilon_0}{d_H} \tag{6.12}$$

where ϵ_H is the relative permittivity of the (highly ordered) H_2O layer between electrode and the counterions ($\approx$ 6 [74,181,182]) and d_H the width of the Helmholtz layer, usually the radius of at least one hydration shell of the hydrated protons ($\geq$ 3 Å [183]). C_H is considered to be independent of the applied potential in the potential range used (i.e., the potential drop in the double layer $\Delta\phi_H$ being less than $< 10^7$ V/m [184–186]).

As seen in the reference figure on the right of figure 6.4 from [64] and in the figures in 6.10 from [93, 167], silicon electrodes grafted with a passivating or blocking layer consisting of molecules such as benzene derivatives and alkenes show a decrease of its total capacitance after the electrografting process. This decrease is modelled by the insertion of a new capacitance C_{ML} stemming from the dielectric molecular layer in series, therefore decreasing the total capacitance of the grafted electrode|electrolyte interface $C_{tot,g}$ [64, 162, 165, 167, 178].

$$1/C_{tot,g} = 1/C_{SC} + 1/C_{ML} + 1/C_H \tag{6.13}$$

The inclusion of C_{ML} modelled as an additional plate capacitor (see equation 6.14) is believed to lead to a replacement or exclusion of H_2O and other electrolyte components [187, 188] by the dielectric organic molecular layer with its dielectrial constant ϵ_{ML}, thus inserting a new set of idealized capacitor "plates" between the silicon surface and the counterions in the Helmholtz layer, which leads to a decrease of the total capacitance

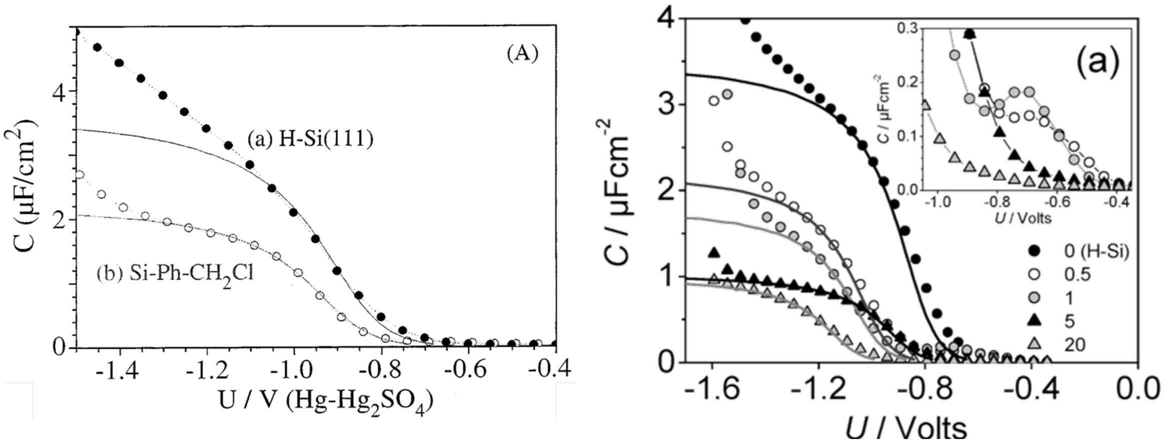

Figure 6.10: Reported fits of C_{tot} vs E_{WE} plots for differently terminated n-Si surfaces. Left: C-E_{WE} plots of n-type silicon electrodes with H-termination (black dots) and after grafting with diazobenzene with a CH_2Cl substitution (open circles). Black lines are the corresponding fits. Original figure is from [93]. Right: C-E_{WE} plots of n-type silicon electrodes with H-termination (black dots) and after grafting with diazoalkenes with different chain lengths (all other symbols). Black lines are the corresponding fits. Original figure is from [167]. U denotes the potential of the working electrode E_{WE} vs MSE. Impedances were measured at f = 1 kHz.

$C_{tot,g}$ of the modified interface [64, 178]. For the calculation of C_{ML} (eq. 6.14) the distance of the capacitor plates is the height of the immobilized molecules.

$$C_{ML} = \frac{\epsilon_{ML}\epsilon_0}{d_{ML}} \tag{6.14}$$

Since the electrodes grafted with pyridine show an *increase* of the total capacitance C_P compared to its initial, H-terminated surface, the question arises how this change in C_P can be modelled, since the addition of a serially connected C_{ML} stated above cannot lead to an increase of the total capacitance. Therefore, only C_H and C_{SC} of equation 6.10 are used to fit the C-E_{WE} plots.

Equation 6.10 is fitted to the rising part of the C-E_{WE} plots between $\approx$ 0.5 - – 2.0 μF/cm^2 in figure 6.11 in order to acquire the Helmholtz capacitance C_H. Comparing the C_P vs E_{WE} plots of the initial, H-terminated silicon electrode with the grafted, 3-pyridinium-terminated electrode, the changes in C_P can either arise from a shift in the flatband potential of the electrode or the Helmholtz capacitance. At more cathodic potentials, the onset of the HER current across the electrode|electrolyte interface distorts the capacitance values [93, 165, 178], while at potentials near the flatband potential E_{fb} the plot displays an additional, peak-like feature around $\approx$ +50 mV vs RHE (similar to the reference figure on the right side of figure 6.4), which is believed to correspond to surface states on the silicon surface [171, 189], possibly originating from hydrogen diffusion into the subsurface region of the silicon electrode. When using fluorine containing electrolytes, this capacitance peak is reported to disappear [64, 167]. The space charge capacitance C_{SC} depends on the flatband potential E_{fb} as well as the doping density of the silicon electrode N_D. While both values could be taken from the fitting results of the MS plots, C_P with both values fixed could only be fitted poorly. The best fit is achieved when using N_D from the MS plot fit and E_{fb} as an additional fit parameter. The fit results are tabulated in table 6.4.

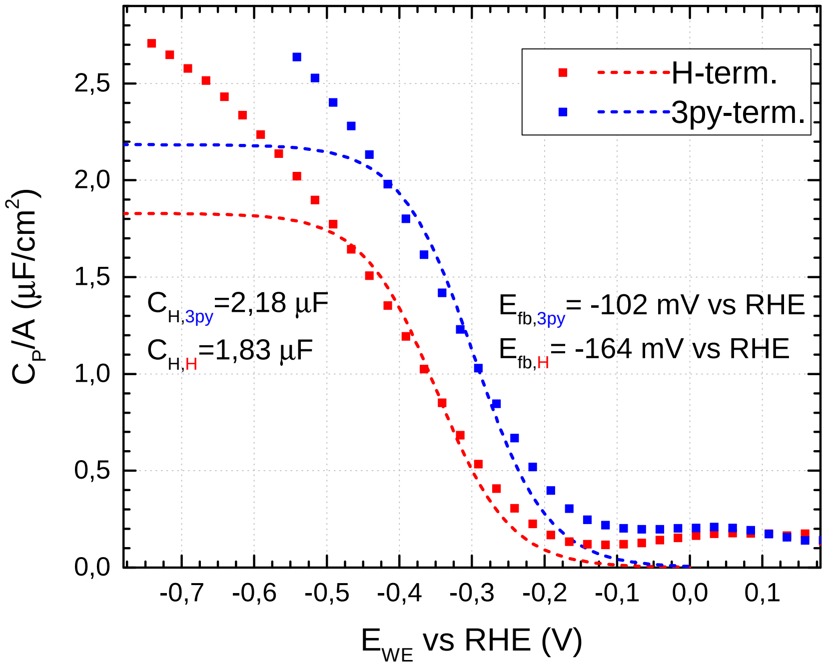

Figure 6.11: Fit of the C-E_{WE} plots from 6.4 using equation 6.10 for C_P.

C_H for the H-terminated silicon electrode derived here is on the low side compared to similar electrode systems [64, 162, 178] but falls within the reported range of values of the Helmholtz layer capacitance at an H-terminated n-type silicon electrode in an aqueous electrolyte [64, 162, 167, 190, 191] from 0.5 [192] and 1.5 $\mu F/cm^{-2}$ [193] up to 7 $\mu F/cm^{-2}$ [178]. Changing the surface termination from hydrogen to 3-pyridinium seems to not only lead to a shift of the flatband potential $\Delta E_{fb,C-E}$ of $\approx +62$ mV compared to $\Delta E_{fb,MS} \approx +80$ mV as obtained from the MS plots, but also to a slight increase of the Helmholtz capacitance C_H. As can be seen in table 6.4 the values for the flatband potentials $E_{fb,C-E}$ from the fit of the C_P vs E_{WE} plots deviate from the MS plot derived $E_{fb,MS}$ by up to ≈ -145 mV for unknown reasons. Other reports showed a match of E_{fb} using both fitting methods [64].

Further comparisons of the presented fitting method with the results of similarly grafted silicon electrodes [64, 93, 167] need to include an adaption of the capacitance values. In the cited papers the total capacitance C_{tot} is calculated using an impedance measurement at a fixed frequency of 1 kHz, reasoning there is a frequency range where the impedance is almost fully capacitive [165, 167], i.e., the phase of the impedance φ is higher than $> 80°$. In that case, the total capacity can be calculated from the imaginary part of the impedance Z_i [72].

$$C_{tot} = \frac{1}{\omega Z_i} = \frac{1}{2\pi f |Z| \sin(\varphi)} \tag{6.15}$$

where f is the frequency of the impedance measurement and |Z| the absolute value of the impedance. In two exemplary Bode plots of the EIS spectrum at -0.516 and -0.316 V vs RHE in figure 6.12, one can see the frequency range where the impedance is mostly capacitive, i.e., all filled circles lie under the dashed line marking $\varphi = 80°$. The two potentials span the potential range in which the CU plots were fitted.

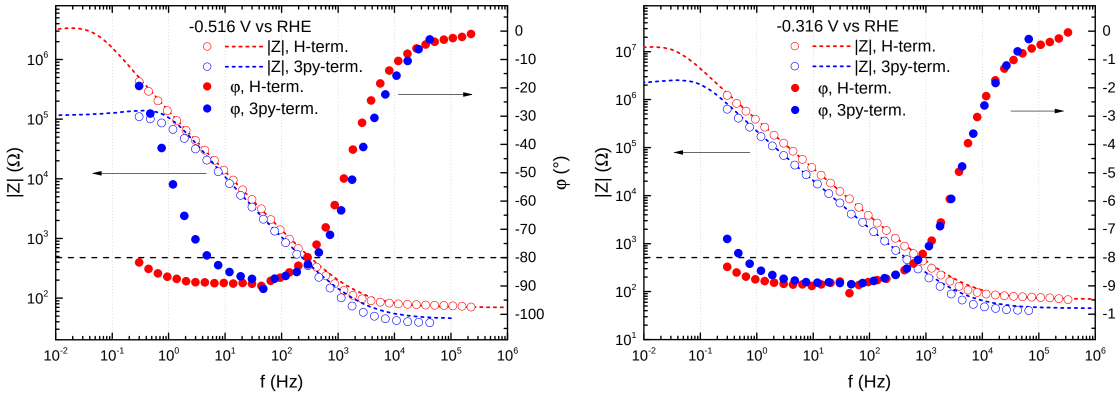

Figure 6.12: Bode plots of two EIS spectra from figure 6.3 with measurements of the H-terminated (red) and the grafted, 3-pyridine-terminated (blue) silicon electrode at -0.516 V vs RHE (left) and -0.314 V vs RHE (right). Circles denote the total impedance |Z| while the filled dots denotes the phase φ of the impedance.

Since between -0.516 and -0.316 V vs RHE the total impedance is mostly capacitive at f = 1 kHz, the imaginary part of the impedance Z_i at f = 1 kHz of each EIS spectrum from figure 6.11 is extracted and converted into the total capacitance C_{tot} using equation 6.15. The resulting C_{tot} vs E_{WE} plots are shown in figure 6.13 and subsequently fitted using the same equation 6.10 as in figure 6.11. Again, the fit results are listed in table 6.4.

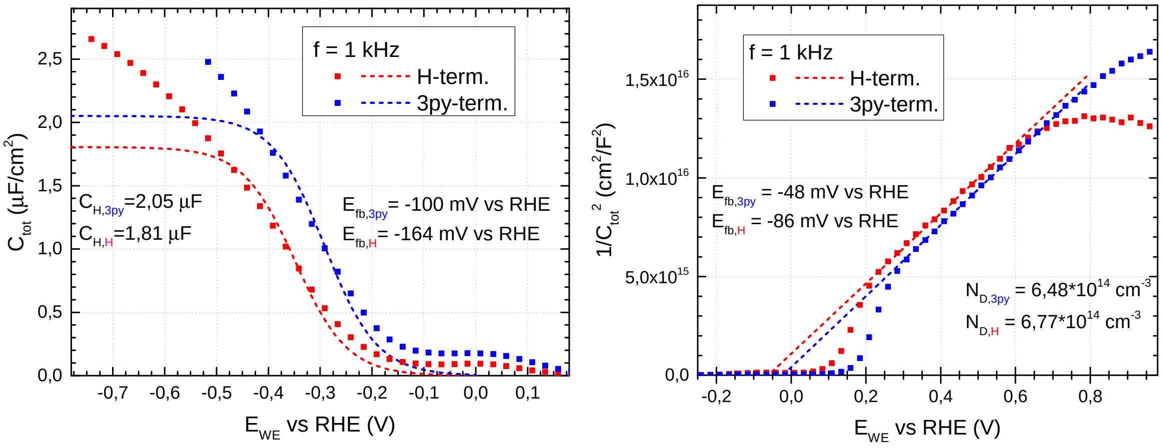

Figure 6.13: Left: Fit of the C_{tot} vs E_{WE} plots with Z_i values at f = 1 kHz from the EIS spectra plotted in figure 6.4 using equation 6.10. Right: Fit of the MS plots with Z_i values at f = 1 kHz from the EIS spectra plotted in figure 6.4 using equation 6.1. Silicon electrode with initial H-termination (red) and final 3-pyridinium-termination after grafting (blue).

The total capacitance vs potential plots match the plots for fitted parallel capacitance C_P, but the results feature the same problems of a rather small Helmholtz capacitance C_H for the silicon electrode with H-termination and the cathodic shift of the flatband potentials of ≈ -80 mV compared to the MS derived values $E_{fb,MS}$, though the shift is smaller compared to the values from figure 6.11. The C-E_{WE} plots are, again, fitted reasonably well using equation 6.10 in the rising part of the plots but deviate near the flatband potential and at more cathodic potentials near the onset of HER.

The fit results point towards both a shift of the flatband potential E_{fb} and an appar-

Fig. 6.11	C_H	$E_{fb,C-E}$	$E_{fb,MS}$
C_p, full spectra	(μF/cm^2)	(mV vs RHE)	(mV vs RHE)
H-term.	1.83 ± 0.05	-164	-37
3py-term.	2.18 ± 0.07	-102	43

Fig.6.13	C_H	$E_{fb,C-E}$	$E_{fb,MS}$
C_{tot}, f = 1 kHz	(μF/cm^2)	(mV vs RHE)	(mV vs RHE)
H-term.	1.81 ± 0.05	-164	-86
3py-term.	2.05 ± 0.07	-100	-48

Table 6.4: Fitted values for the Helmholtz capacitance C_H and flatband potential E_{fb} of the C-E_{WE} plots from figures 6.11 and 6.13 as well as fitted E_{fb} values from the corresponding MS plots.

ent increase of the Helmholtz capacitance stemming from the change in surface termination of the silicon electrodes from its H-termination to the 3-pyridinium-termination after grafting. The flatband potential of the 3-pyridinium-terminated silicon electrode is more anodic than with H-termination, in contrast to the results from the MS plots in figure 6.6 and 6.3. The increase of the Helmholtz capacitance is intriguing, as it conventionally has been assumed to stay constant for silicon electrodes grafted with blocking or passivating organic molecules [64,93,165,178]. As shown before, the C-E_{WE} plots in K_2SO_4 at a pH > 5 display a decrease of the total capacitance after changing the surface termination from hydrogen to 3-pyridine as also reported for other organic layers in the literature. Using the same equations as in figure 6.13 the C-E_{WE} plots in K_2SO_4 are also fitted, with the resulting values listed in table 6.5.

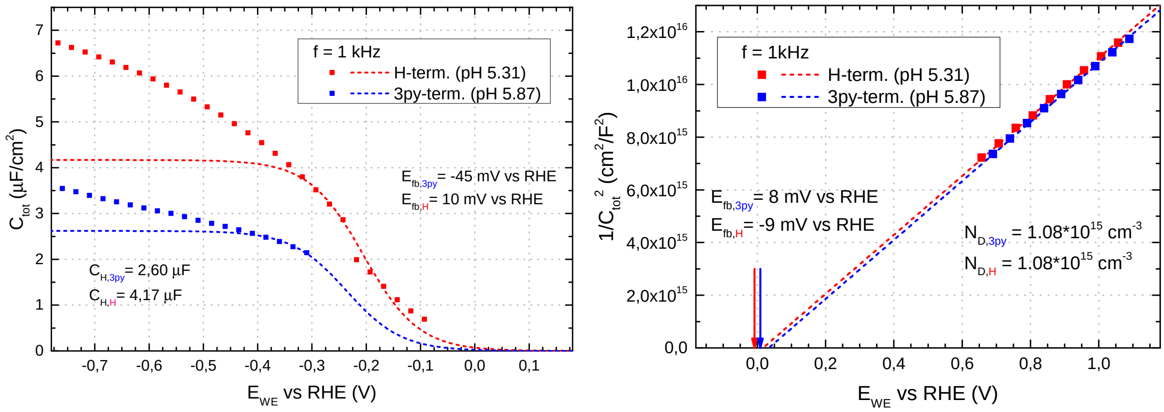

Figure 6.14: Left: Fit of the C_{tot} vs E_{WE} plots with Z_i values at 1 kHz from 6.4 using equation 6.10. Right: Fit of the MS plots with Z_i values at 1 kHz from 6.4 using equation 6.1. Silicon electrodes with initial H-termination (red) and final 3-pyridine-termination after grafting (blue).

Again, there is a systematic cathodic shift of the flatband potentials determined using the MS plot or the C-E_{WE} fittings, although the differences are smaller compared to the results in table 6.4. $E_{fb,MS}$ values also show an almost negligible shift after changing surface termination. As mentioned before (see figure 6.4) the potential range for the EIS measurement in the weakly acidic electrolyte was already in the HER region, which is especially evident in the potential range chosen for the 3-pyridine-terminated sample. Therefore, the fit of that C-E_{WE} plot contains much uncertainty and should be treated with caution.

Fig.6.14 C_{tot}, f = 1 kHz	C_H (μF/cm^2)	$E_{fb,C-E}$ (mV vs RHE)	$E_{fb,MS}$ (mV vs RHE)
H-term.	4.17 ± 0.07	10	-9
3py-term.	2.62 ± 0.03	-45	8

Table 6.5: Fitted values for the Helmholtz capacitance C_H and flatband potential E_{fb} of the CE_{WE} plots from figures 6.14 as well as fitted E_{fb} values from the corresponding MS plots.

The fit of the C-E_{WE} plots at f = 1 kHz shown in figure 6.14 results in a decrease of the modified Helmholtz layer capacitance $C_{H,3py}$ compared to $C_{H,H}$ of the H-terminated electrode, which can then be further deconvoluted into the additional capacitance of the molecular layer C_{ML} as shown in equation 6.13. Using the assumption of an unchanged Helmholtz capacitance [93], the capacitance of the 3-pyridine layer C_{3py-L} can be calculated by assuming analogously to equation 6.13, that the sum of the inverse of C_{3py-L} and $C_{H,H}$ yields the inverse of the modified Helmholtz layer capacitance $C_{H,3py}$ of the 3-pyridine-terminated electrode listed in table 6.5:

$$1/C_{H,3py} = 1/C_{H,H} + 1/C_{3py-L} \Rightarrow C_{3py-L} = 7.05\,\mu F/cm^2 \tag{6.16}$$

Now equation 6.14 can be applied to yield the thickness of the grafted 3-pyridine layer, if the relative permittivity ϵ_{3py} of a grafted 3-pyridine layer can be assumed to be similar to other grafted organic layers such as grafted alkyl monolayers (ϵ_{ML} = 3.3 [165]), self-assembled n-alkyl thiol monolayers on Au/Cr/silicon electrodes (2.6 [188]) or solid polyethylene (2.3 [194]). In publications investigating grafted (substituted) benzene layers, usually ϵ_{ML} = 2.3 is used [64, 93], which will be used in the following for ϵ_{3py} because of the comparable size of a grafted pyridine molecule to grafted benzene. With this assumption the following thickness $d_{3py,C-E}$ is obtained:

$$d_{3py,C-E} = 2.9\,\text{Å} \tag{6.17}$$

The resulting layer thickness $d_{3py,CE}$ is smaller than the presumed height of a grafted pyridine molecule of $d_{3py} \approx 4$ Å, which could point towards a modified silicon surface only partially covered by grafted pyridine molecules, similar to the thickness estimations using XPS in chapter 4.2. For figure 4.20 an average height of the grafted layer of less than half of the height of one molecule was calculated ($d_{3py,XPS}$ = 1.5–3.2 Å). Assuming a heterogeneously mixed layer of either grafted pyridine or solvent molecules (H_2O) in front of the silicon electrode, the capacitance of such a layer can calculated with an *effective relative permittivity* ϵ_{eff} and d_{3py} = 4 Å [64, 93, 165].

$$C_{3py-L} = \frac{\epsilon_{eff}\epsilon_0}{d_{3py}} \Rightarrow \epsilon_{eff} = 3.2 \tag{6.18}$$

ϵ_{eff} originates from the effective medium theory for heterogeneous thin films [195, 196] and describes the effective relative permittivity of a film, when it consists of a mixture of two phases 1 and 2, each with its own relative permittivity ϵ_1, ϵ_2. In our case, phase 1 is the grafted pyridine layer with ϵ_{3py} = 2.3, while phase 2 is comprised of the ordered

H_2O molecules where $\epsilon_H \approx 6$, as it is the case in the Helmholtz layer. The assumed heterogeneous surface layer is sketched in figure 6.15.

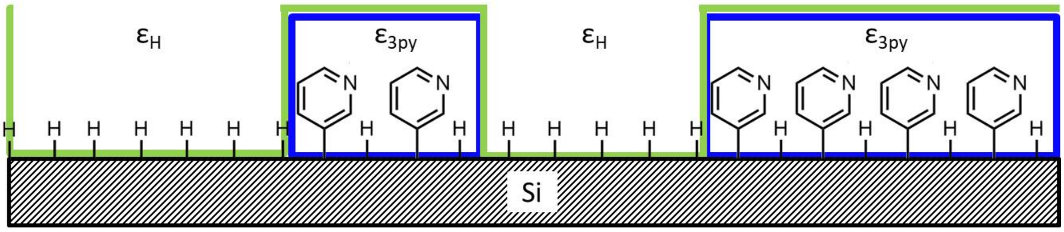

Figure 6.15: Sketch of the assumed heterogeneously mixed surface layer with phase 1 comprised of grafted pyridine molecules with ϵ_{3py} (blue area) and the solvent phase 2 comprised of H_2O with ϵ_H (green area) in front of the silicon electrode (shaded black).

The resulting effective relative permittivity ϵ_{eff} can then be correlated to the relative permittivity values of the two phases and the volume fraction f_{3py} occupied by the grafted pyridine molecules using equation 6.19.

$$0 = f_{3py}\frac{\epsilon_{3py} - \epsilon_{eff}}{\epsilon_{3py} + 2\epsilon_{eff}} + (1 - f_{3py})\frac{\epsilon_H - \epsilon_{eff}}{\epsilon_H + 2\epsilon_{eff}} \tag{6.19}$$

The volume fraction f_{3py} is 1 when the organic monolayer is densely packed, i.e. every second surface silicon atom is grafted with a pyridine molecule, leading to a (2×1) structure on the Si(111) surface and a maximum surface density of 3.9×10^{14} pyridine molecules per 1 cm^2 [64]. With the values given above the volume fraction is

$$f_{3py} = 0.84 \tag{6.20}$$

which agrees well with the number of monolayers $n_{ML} \approx 0.8$ derived from the measured thickness of the grafted 3-pyridine layer using XPS in table 4.1, as well as results from other partially covered silicon surfaces grafted with substituted benzene Bz-R, with substitutions R such as $R = C_{12}H_{25}$ ($f_{ML} = 0.54$), $R = CH_3$ ($f_{ML} = 0.76$) [93], $R = CH_2Br$ ($f_{ML} = 0.76$) [64]. It is smaller than the volume fraction derived for densely packed grafted layers of 4-bromobenzene ($f_{ML} \approx 1$ [64]). One reason for the decreased packing of the 3-pyridine layer could be a difference in molecular dipole moment compared to 4-bromobenzene [93, 122, 174]. The attractive forces between the dipole moment of differently substituted diazonium cations and their reduced radicals with the cathodically biased hydrophobic H-terminated silicon surface might necessitate the additional rotation of the radicals in order for the radical carbon atom of the pyridine ring to face the H-terminated silicon surface perpendicularly, thus decreasing the grafting efficiency and the resulting coverage. Figure 6.16 from [122, 174] shows the proposed situation for 4-methoxybenzene diazonium in contrast to 4-nitrobenzene diazonium, which reaches similarly high grafting coverage as 4-bromobenzene [64].

Finally one might speculate if the effective medium theory for heterogeneous thin films can also be utilized to explain the apparent *increase* of the Helmholtz capacitance of a silicon electrode with 3-pyridinium-termination in an acidic electrolyte, as seen in figure 6.13 and 6.11. In that case, $C_{H,3pyH}$ may again be described by the same equation given for the initial Helmholtz capacitance $C_{H,H}$ of the H-terminated silicon electrode, only now with an effective relative permittivity $\epsilon_{eff,3pyH}$.

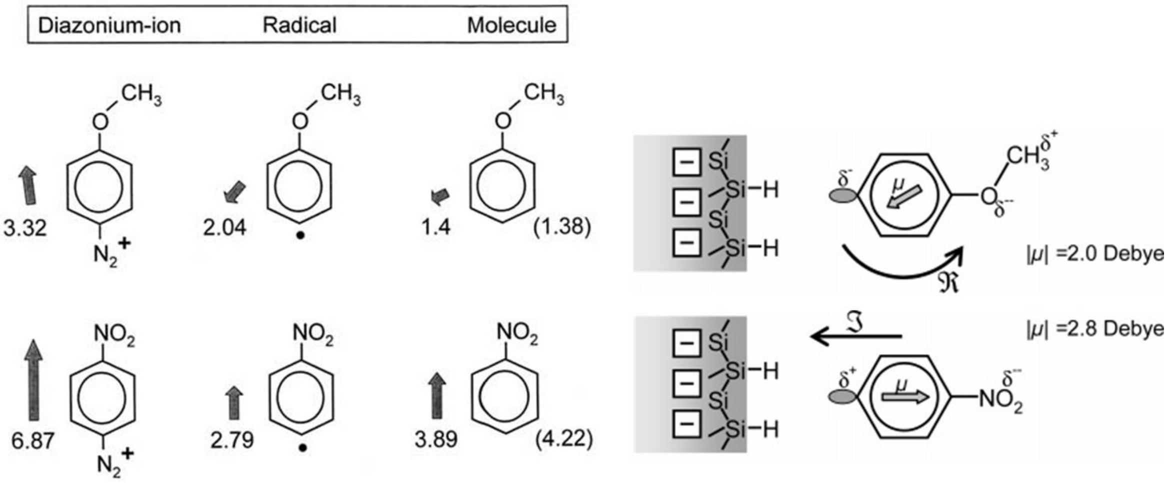

Figure 6.16: Left side: calculated directiosn (grey arrow, arrowheads point towards the negatively charge side) and strengths (length of the arrow) of the dipole moments of 4-nitrobenzene and 4-methoxybenzene diazonium in its ionic (left), radical (middle) and molecular state (right). Original figure from [174]. Right side: torsional force $-\mathfrak{R}$ needed to rotate the 4-methoxybenzene radical away from the preferred dipole moment alignment with the negatively charged surface, in order for the radicalized side to face the surface. The radicalized side possesses a partial negative charge δ^{-} in addition to the larger partial negative charge of the methoxy endgroup δ^{--} and the radical would rather rotate with $\mathfrak{R}$ to the side. In contrast, the dipole moment of 4-nitrobenzene in all forms is favourable to its orientation perpendicular to the silicon surface and experiences some electrostatic pull $\mathfrak{I}$. Original figure from [122].

$$\mathrm{C_{H,3pyH}} = \frac{\epsilon_{\mathrm{eff,3pyH}} \cdot \epsilon_0}{\mathrm{d_{eff}}} \tag{6.21}$$

Presuming that $\mathrm{C_H} = 7\,\mu\mathrm{Fcm^{-2}}$ and $\epsilon_\mathrm{H} = 6$ from [178] best match the presented system, one obtains a Helmholtz layer thickness $\mathrm{d_H} = 7.6$ Å. The thickness $\mathrm{d_{eff}}$ of the composite, effective capacitor could be assumed to be at least the Helmholtz layer thickness together with the difference in height of the surface termination molecules pyridine ($\mathrm{d_{3py}} \approx 4$ Å) and hydrogen ($\mathrm{d_{Si-H}} = 1.5$ Å [13]), as sketched in figure 6.17.

$$\mathrm{d_{eff}} \geq \mathrm{d_H} - \mathrm{d_{Si-H}} + \mathrm{d_{3py}} \approx 12.1\,\text{Å} \tag{6.22}$$

The ratio of the Helmholtz capacitances of the H-terminated and 3-pyridine-terminated silicon electrodes can then be used to determine the ratio between the effective relative permittivity $\epsilon_{\mathrm{eff,3pyH}}$ and the relative permittivity of H_2O ϵ_H.

$$\frac{\mathrm{C_{H,3pyH}}}{\mathrm{C_H}} = \frac{\epsilon_{\mathrm{eff,3pyH}} \cdot \mathrm{d_H}}{\epsilon_\mathrm{H} \cdot \mathrm{d_{eff}}} \quad \Rightarrow \quad \epsilon_{\mathrm{eff,3pyH}} = \epsilon_\mathrm{H} \underbrace{\frac{\mathrm{C_{H,3pyH}} \cdot \mathrm{d_{eff}}}{\mathrm{C_H} \cdot \mathrm{d_H}}}_{\widehat{=}c} \tag{6.23}$$

Ideally, the same sample would be measured in weakly acidic and acidic electrolytes in order to first establish the volume fraction of the deprotonated 3-pyridine layer and then use $\mathrm{f_{3py}} \widehat{=} \mathrm{f_{3pyH}}$ for the determination of the unknown relative permittivity of the protonated 3-pyridinium layer ϵ_{3pyH}. When using $\mathrm{f_{3py}} = 0.84$ from above (6.20), equation 6.19 could then be modified using equation 6.23, this time with the two phases being protonated 3-pyridine-layer with ϵ_{3pyH} and H-terminated layer with ϵ_H:

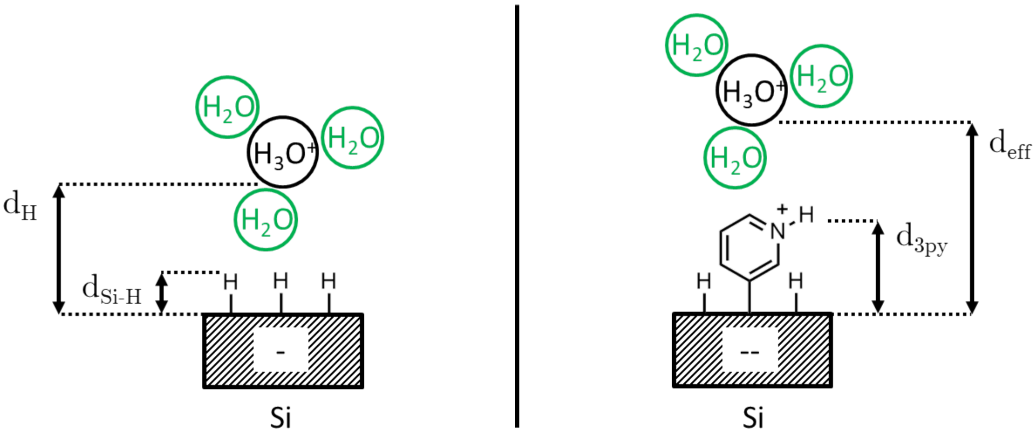

Figure 6.17: Assumed arrangements of counterions/protons found at a silicon surface spot with H-termination (left) and with 3-pyridinium termination (right). Black arrows indicate the distances between the charged silicon surface and $H_9O_4^+$ counterprotons and the heights of the different surface terminations.

$$0 = f_{3py} \cdot \frac{\epsilon_{3pyH} - \epsilon_H \cdot c}{\epsilon_{3pyH} + 2\epsilon_H \cdot c} + (1 - f_{3py}) \cdot \frac{1-c}{2+c} \tag{6.24}$$

Using the C_H values from table 6.4 of the C-E$_{WE}$ plots at f = 1 kHz to calculate c, the relative permittivity of the 3-pyridinium layer would be significantly larger than ϵ_H:

$$\epsilon_{3pyH} = 9.7 \tag{6.25}$$

Presuming this is the relative permittivity for the modified Helmholtz layer augmented by the grafted 3-pyridinium layer, the next step would be to connect ϵ_{3pyH} to the surface density of grafted, immobilized 3-pyridinium molecules n_{3pyH} per 1 cm^2. The increase in relative permittivity compared to its initial value $\epsilon_H \approx 6$ could depend on a reduction of the orientation of the ordered H_2O molecules inside the Helmholtz layer, where the dipole moments of the water molecules are forced to align to the electric field on the inside of the Helmholtz plate capacitor [197]. Simulations of ions and H_2O molecules as dipoles approaching a charged membrane suggest an asymptotic rise of $\epsilon_{H,sim}$ to the bulk value $\epsilon_{H_2O} = 78$ [13] from the electrode|electrolyte interface towards a distance of $\approx$ 10 Å. The same effect can be reached by reducing the effective surface charge at the simulated membrane [197, 198].

Simulating the total capacitance of the modified silicon electrode|electrolyte interface

The grafted, positively charged 3-pyridinium molecules can on the one hand shield the negatively charged silicon surface in the cathodic potential range considered; the layer effectively becomes part of the imagined, positively charged "plate" of the idealized Helmholtz plate capacitor with a negatively charged silicon "plate". The shielding might reduce the concentration of counterions in the double layer by effectively replacing them, which would lead to an increase of ϵ_{3pyH} at the 3-pyridinium-terminated interface [197]. On the other hand, it can also affect the charge accumulation in the space charge layer inside the silicon electrode near the interface, causing, e.g., changes in the band bending of the modified electrode compared to an H-terminated electrode, which does not possess such an additional layer of immobilized charged molecules. The change in the space charge layer due to the grafted pyridinium layer can likewise lead to a change in the electrochemical double layer composition. The cumulative effect of the charged 3-pyridinium layer could be responsible for the increased reactivity of the electrode towards HER. Together with Munir Salman[1], an attempt to simulate the total capacitance from the potential drop across the interface is undertaken. The total potential drop $\Delta\phi_{\mathrm{tot}}(\mathrm{q})$ from the bulk of the silicon electrode to the bulk of the electrolyte was calculated for the H-terminated silicon electrode following [78],

$$\Delta\phi_{\mathrm{tot,H}}(\mathrm{q}) \;=\; \Delta\phi_{\mathrm{sc}}(\mathrm{q}) + \Delta\phi_{\mathrm{H}}(\mathrm{q}) \;=\; -(\mathrm{E_{WE}} - \mathrm{E_{fb}}) \tag{6.26}$$

which comprises the potential drop in the space charge layer under accumulation (q<0) $\Delta\phi_{\mathrm{sc}}(\mathrm{q})$,

$$\Delta\phi_{\mathrm{sc}}(\mathrm{q}) \;=\; \frac{2\mathrm{kT}}{e}\ln\left(\frac{-\mathrm{q}}{\sqrt{2\mathrm{kT}\epsilon_{\mathrm{Si}}\epsilon_0\mathrm{N_D}}}\right), \tag{6.27}$$

and the potential drop in the Helmholtz layer $\Delta\phi_{\mathrm{H}}(\mathrm{q})$:

$$\Delta\phi_{\mathrm{H}}(\mathrm{q}) \;=\; \mathrm{q}\cdot 1/\mathrm{C_H}\,; \quad \mathrm{C_H} \;=\; \frac{\epsilon_{\mathrm{H}}\epsilon_0}{\mathrm{d_H}}, \tag{6.28}$$

all depending on the total charge q, assuming charge conservation [78]:

$$\mathrm{q} \;=\; \mathrm{q_{sc}} \;=\; \mathrm{q_H} \tag{6.29}$$

Analogous to equation 6.10, the described potential drop fits the equivalent circuit of two capacitors connected in series as seen on the left of figure 6.18.

To yield the total capacitance $\mathrm{C_{tot}}(\mathrm{q})$ of the interface equations, $\phi_{\mathrm{tot}}(\mathrm{q})$ is differentiated with respect to q and inverted.

$$\mathrm{C^{H}_{tot,sim}}(\mathrm{q}) \;=\; \left(\frac{\partial\phi_{\mathrm{tot,H}}(\mathrm{q})}{\partial\mathrm{q}}\right)^{-1} \tag{6.30}$$

For the grafted, 3-pyridinium-terminated silicon electrode, the assumed equivalent circuit changes to the one on the right side of figure 6.18. The Helmholtz layer in front of the electrode is then split up into a part of the modified silicon surface which is still H-terminated and has a Helmholtz capacitance $\mathrm{C_H}$, and a part of the surface which is covered by a pyridinium layer with its own capacity $\mathrm{C_{py}}$ connected in series with a modified Helmholtz layer with a capacity $\mathrm{C_{3pyH}}$. The potential drop across the two parts connected in parallel is the same for both branches (eq. 6.31 iv)). The charges on $\mathrm{C_H}$ and $\mathrm{C_{py}}$, $\mathrm{q_{H'}}$ and $\mathrm{q_{py}}$ respectively, add up to yield q' on the space charge capacitor (eq. 6.31 i)). It is at the modified Helmholtz layer where the additional charge of the protonated 3-pyridinium molecules $\mathrm{Q_{pyH^+}}$ is inserted (eq. 6.31 ii)), where it has an effect on the charge and thus the capacitance of the space charge layer (see eq. 6.27). The equations governing the potential drop across the 3-pyridinium-modified interface are given by:

---

[1] Non-equilibrium Chemical Physics Group, Physics Department, Technical University Munich

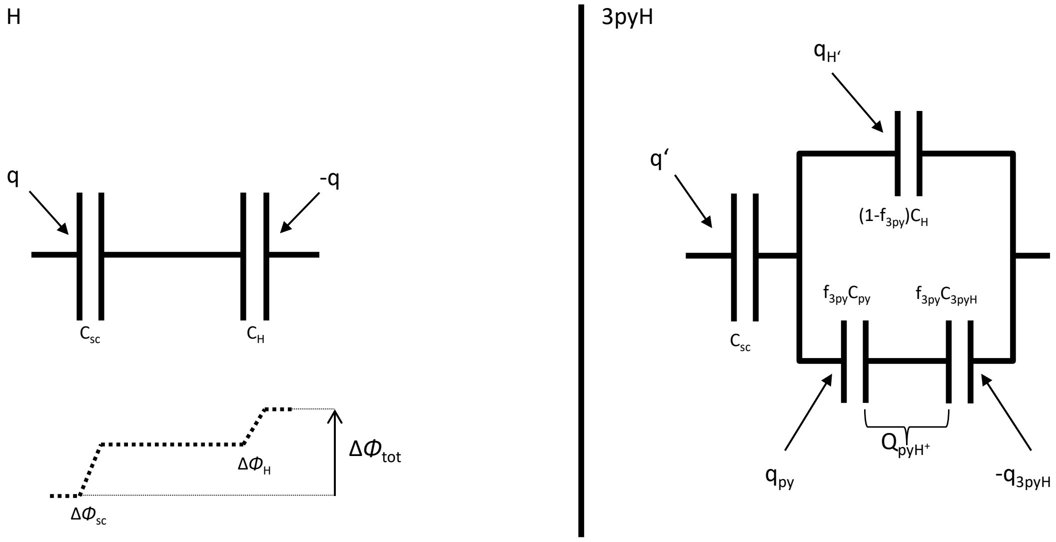

Figure 6.18: Equivalent circuits used to simulate the potential drop $\Delta\phi_{\mathrm{tot}}$ of the unmodified, H-terminated silicon electrode|electrolyte interface (left) and the grafted, 3-pyridinium-terminated interface (right). Q_{pyH^+} denotes the additional charge of the protonated pyridinium molecules stored between the capacitors $f_{3py}C_{py}$ and $f_{3py}C_{3pyH}$. On the left side the total potential drop $\Delta\phi_{\mathrm{tot}}$ over the two capacitors connected in series is depicted.

$$\begin{aligned}
\text{i)}\quad & q' = q_{H'} + q_{py} \\
\text{ii)}\quad & Q_{pyH^+} = q_{3pyH} - q_{py} \\
\text{iii)}\quad & \Delta\phi_{tot,3py} = \Delta\phi_{sc} + \Delta\phi_{H'} \\
\text{iv)}\quad & \Delta\phi_{H'} = \Delta\phi_{py} + \Delta\phi_{3pyH}
\end{aligned} \tag{6.31}$$

The capacitance values on the 3-pyridinium-terminated part correspond to the volume fraction $\sim f_{3py}$ of the total surface of the electrode, while the capacitance of the H-terminated electrode part correspond to $\sim (1 - f_{3py})$ (eq. 6.20).

$$\begin{aligned}
\text{v)}\quad & \Delta\phi_{H'} = \frac{q_{H'}}{(1-f_{3py})\cdot C_H}\,; \quad C_H = \frac{\epsilon_H\epsilon_0}{d_H} \\
\text{vi)}\quad & \Delta\phi_{py} = \frac{q_{py}}{f_{3py}\cdot C_{py}}\,; \quad C_{py} = \frac{\epsilon_{3py}\epsilon_0}{d_{3py}} \\
\text{vii)}\quad & \Delta\phi_{3pyH} = \frac{q_{3pyH}}{f_{3py}\cdot C_{3pyH}}\,; \quad C_{3pyH} = \frac{\epsilon_{3pyH}\epsilon_0}{d_{eff}}
\end{aligned} \tag{6.32}$$

The values for the thickness d_H, d_{3py}, d_{eff} as well as relative permeabilities ϵ_H, ϵ_{3py} and ϵ_{3pyH} are taken from prior equations 6.12, 6.22, 6.21 and 6.24. Similarly, the charge of the protonated pyridinium molecules can be calculated by multiplying the charge of a closed monolayer of grafted pyridinium molecules (surface density in chapter 4.2 from [64]) with f_{3py}:

$$Q_{pyH^+} = f_{3py}\cdot e\cdot 3.9\times 10^{14}\mathrm{cm}^{-2} \tag{6.33}$$

with the positive elemental charge e, since pyridinium is positively charged. Again, the total capacitance of the 3-pyridinium-terminated silicon electrode is derived from the total potential drop across the interface:

$$C^{3py}_{tot,sim}(q) = \left(\frac{\partial \phi_{tot,3py}(q')}{\partial q'}\right)^{-1} \tag{6.34}$$

The resulting $C^{H}_{tot,sim}$ vs E_{WE} and $C^{3py}_{tot,sim}$ vs E_{WE} plots are shown in figure 6.19. The model yields a $C^{3py}_{tot,sim}$ versus E_{WE} curve for a partially 3-pyridinium-terminated silicon electrode with some promising features similar to the C_{tot} vs E_{WE} curves in figure 6.14. With increasing f_{3py} values, the $C^{3py}_{tot,sim}$ curve is shifted towards more positive potentials due to the additional charge originating from the immobilized pyridinium molecules Q_{pyH^+}, while for $f_{3py} = 0$, i.e., no 3-pyridinium-termination, the total capacitance of the electrode is the same for both models. The same can be seen in the positive shift of the flatband potential of the grafted silicon electrode compared to H-terminated electrodes as listed in table 6.5. Since the capacitance of the space charge layer $C_{sc} = \partial q_{sc}/\partial\Delta\phi_{sc}$ is dependent its charge, the increase of $q_{sc} \widehat{=} q'$ from the immobilized pyridinium molecules Q_{pyH^+} should lead to an increase in C_{sc} near the flatband potential, where the total capacitance is dominated by C_{sc}; therefore a significant part of the total potential is dropped in the space charge layer (see equation 6.26), where an increase of C_{sc} corresponds to a positive shift in flatband potential.

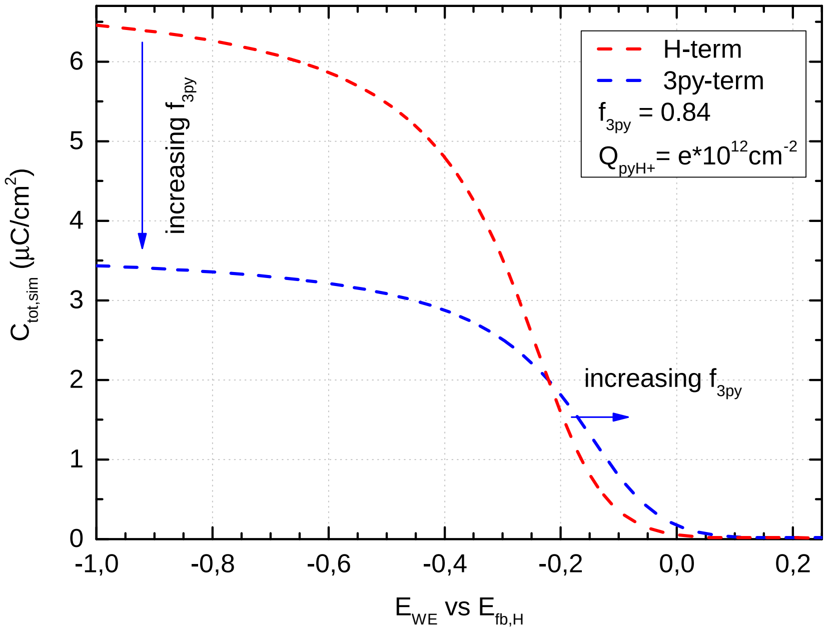

Figure 6.19: $C^{H}_{tot,sim}$ (red dashed) and $C^{3py}_{tot,sim}$ (blue dashed) plotted against $E_{WE} - E_{fb,H}$ curves(potential scale is the same for the $C_{tot,3py}$ plot) based on simulation data using the set of equations in 6.26, 6.30, 6.34, 6.31, 6.32. Arrows indicate the direction of the change between the two curves with increase values of f_{3py}, i.e., when a larger part of the silicon electrode is 3-pyridinium-terminated.

Unfortunately, at the same time with increasing volume fraction f_{3py} of the 3-pyridinium-terminated part of the electrode, the $C^{3py}_{tot,sim}$ curve saturates at a lower value compared to $C^{H}_{tot,sim}$. The potential-independent part of the total capacitance, i.e., the capacitance of the modified Helmholtz layer, is smaller compared to the corresponding value for the H-terminated silicon electrode, once $f_{3py} > 0$. This behaviour does not match the experimentally determined results in figure 6.14 for 3-pyridinium-terminated silicon electrodes. Additionally, the positive shift of the $C^{3py}_{tot,sim}$ curve of ≈ 100 mV for the derived volume fraction value of $f_{3py} = 0.84$ is only achievable, if the charge of a closed layer of pyridinium is strongly reduced. In the plot it is 100 times smaller than assumed in equation 6.33; otherwise the $C^{3py}_{tot,sim}$ curve is shifted to several Volts more positive. This is a strong hint that either the implementation of the additional charge of the pyridinium molecules is not correct or the coverage of charged pyridinium molecules on the modified surface is significantly smaller than f_{3py}. For instance, while in the presented model the charge of the pyridinium layer Q_{pyH^+} effects the space charge layer, it does not directly influence the capacity of the modified Helmholtz capacitor C_{3pyH}. As stated before, this additional charge should correlate to the calculated increase in the relative permittivity of the modified Helmholtz layer ϵ_{3pyH}, but in the presented model this correlation is kept constant.

The presented attempt at modelling the total capacitance of the interface was only partially successful in reproducing the change in total capacitance of the interface once the surface termination is changed from hydrogen to 3-pyridinium. Further investigations and augmentations of the interface model and its equivalent circuit are needed to incorporate more features of the C_{tot} vs E_{WE} curves. Especially the effect of the charge of the grafted pyridinium layer on the composition and width of the double layer and the shielding of that charge due to the species in the double layer would be of significant interest, as would be the application of the Poisson-Boltzmann equation on the whole, 1D-extended silicon|pyridinium|electrolyte interface. In the end, these inquiries were deemed to be beyond the scope of this thesis.

Chapter 7

CO_2 reduction reaction (CO_2RR) on grafted silicon electrodes

Finally, we were interested in the performance of the grafted, 3-pyridinium-terminated silicon electrodes towards the CO_2 reduction reaction (CO_2RR). Two electrolytes were used for the investigation of CO_2RR on grafted silicon electrodes. 0.5 M HCl was used as an electrolyte with a low, acidic pH, while 0.5 M KCl was used as the electrolyte with a weakly acidic pH. HCl was used instead of H_2SO_4, because electrolyte samples based on sulfuric acid led to a more noisy baseline in the NMR spectra due to a possible interaction of the sulfate ions with the water suppression method deployed. 0.5 M KCl has been commonly used in publications, which observed methanol and other reduction products of the CO_2RR on metal [19,21,24–26,199] and semiconductor electrodes [32,33] with dissolved pyridine. Together with CO_2 as purge gas and dissolved pyridine in the electrolyte the pH of the solution could also have a small buffer capacity around pH 5.3 due to the presence of pyridine/pyridinium and CO_2/hydrogen carbonate (HCO_3^-) as acid/base pairs [21].

7.1 CO_2RR on grafted Si electrodes in acidic electrolytes

The 3-pyridinium-terminated silicon electrodes show improved reactivity towards HER in acidic electrolytes like 0.5 M H_2SO_4 and 0.5 M HCl saturated with CO_2, as can be seen in figure 7.1. The presence of CO_2 did not change the onset shift of the HER on the grafted silicon electrodes, so signs of CO_2RR could not be deduced from the CV data alone.

To investigate CO_2RR on H-terminated and modified silicon electrodes and the formation of possible reduction products, galvanostatic bulk electrolysis measurements of electrodes with both surface terminations were conducted at a set current density and subsequent product analysis of the electrolyte and the gas overhead were carried out via NMR and GC. Figure 7.2 shows the E_{WE} vs t plots of the bulk electrolysis for an H-terminated (red) and a modified, 3-pyridinium-terminated silicon electrode (blue).

At a current density of -31.7 μA/cm^2, both E_{WE} vs t curves in the left plot of fig. 7.2 show an initial increase in overpotential until they settle after 5 min. The potential values after 10 min are similar but slightly higher than the ones on the CVs in figure

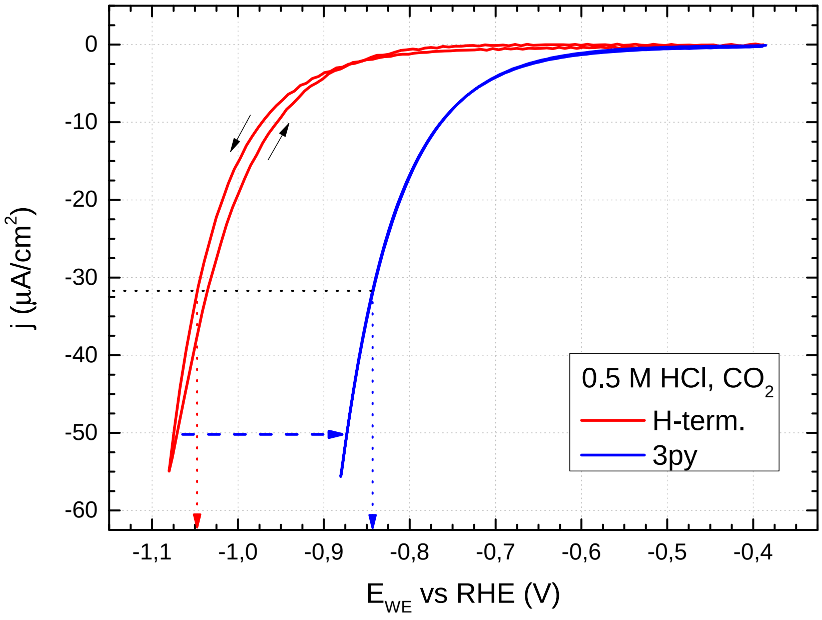

Figure 7.1: CVs showing the effect of the grafted 3-pyridine-layer on HER on an n-type silicon electrode in CO_2 containing electrolyte. Electrolyte: 0.5 M HCl, purged with CO_2. Scan rate: 50 mV/s.

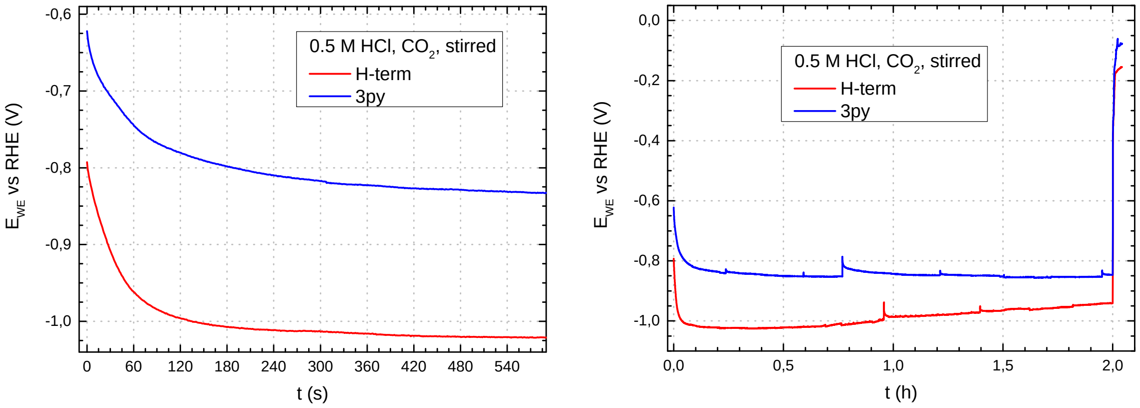

Figure 7.2: Galvanostatic bulk electrolysis of an H-terminated silicon electrode (red) and a 3-pyridinium-terminated electrode (blue). Samples were characterized before electrolysis via CVs shown in figure 7.1. Left: First 10 minutes of electrolysis. Right: Complete plot of the applied potential during the 2 h long electrolysis. At the end of the measurement after 2 h the potential of the electrodes were switched to OCP. Electrolysis current density for both samples: -31.7 $\mu A/cm^2$. Electrolyte: 0.5 M HCl, purged with CO_2 before electrolysis. Electrolyte was stirred during electrolysis

7.1, marked at the black dashed line. The potential of the electrode modified with 3-pyridinium is consistently shifted to a ≈ -200 mV smaller overpotential compared the H-terminated electrode and reaches the steady potential plateau after a slightly longer electrolysis time. On a timescale of 2 hours the grafted electrode stays at this steady potential aside from some peaks due to bubble desorption from its surface, while the H-terminated silicon electrode shows a slow dccline of the applied overpotential during electrolysis starting after about 30 min. This potential shift towards lower overpotentials during HER could be caused by the HER itself. It has been reported that, after long electrolysis measurements at high overpotentials of < -3 V vs RHE, illuminated p-type silicon electrodes showed noticably improved reactivity for the HER [200]. This behaviour was correlated to the formation of a subsurface hydride layer, where evidence of the absorbed hydrogen atoms under the surface of the electrode has been found via Fourier-transform Infrared spectroscopy (FTIR) measurement [201]. If the lowering of the overpotential during the electrolysis on the H-terminated electrode was also caused by the HER and the subsequent surface hydride formation, then this process does not seem to take place on the grafted, 3-pyridinium-terminated silicon electrode. After the electrolysis, the grafted sample shows a positive shift of OCP potential compared to the H-terminated electrode of ≈ +80 mV ($E^{\mathrm{final}}_{\mathrm{ocp,H}} = -0.162$ V vs RHE; $E^{\mathrm{final}}_{\mathrm{ocp,3py}} = -0.086$ V vs RHE) similar to the OCP values used in the previous chapter 6.3 and table 6.3. The positive OCP shift was apparently unchanged after the electrolysis.

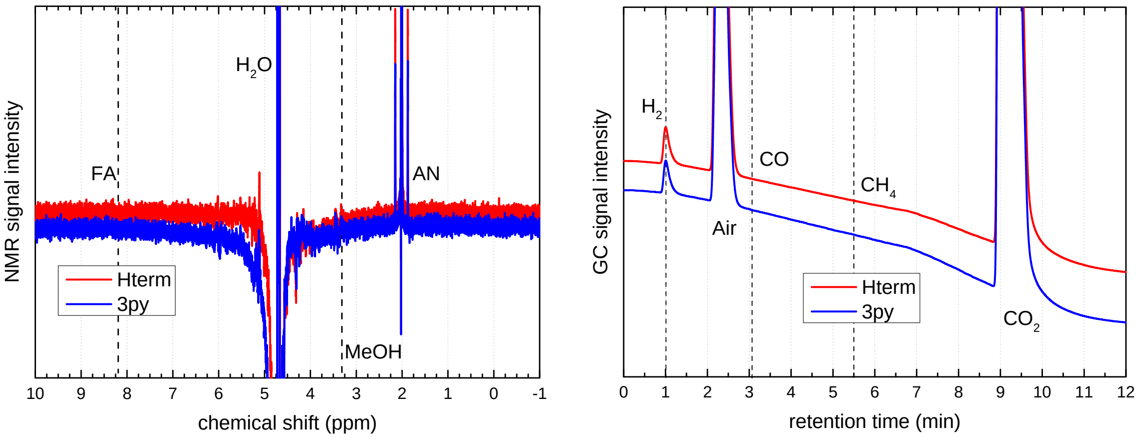

Figure 7.3: Left: NMR signals from electrolysis samples of the bulk electrolysis on H-terminated (red) and 3-pyridinium-terminated silicon electrodes (blue) from figure 7.2. Black dashed lines show the expected chemical shifts for formic acid (FA), methanol (MeOH) and acetonitrile (AN); Right: GC signals from (manually injected) gas overhead samples after bulk electrolysis measurements on H-terminated (red) and 3-pyridinium-terminated silicon electrodes (blue) from figure 7.2. Besides peaks for produced hydrogen (H_2) only residual peaks of air (O_2, N_2) and CO_2 are visible. No other gaseous CO_2 reduction products (CO, CH_4) were detected.

Product analysis of the gas overhead using the procedures described in chapter 3.5 revealed *no CO_2 reduction products* such as carbon monoxide (CO) or methane (CH_4) in the GC spectrum. Electrolyte samples measured using ^{1}H-NMR (figure 7.3) also showed no liquid products such as formic acid (FA) and methanol (MeOH). The H_2 signals relative to the main CO_2 peak are almost the same for the H-terminated and the 3-pyridinium-terminated electrode, with slightly more H_2 gas signal detected during the electrolysis on the H-terminated electrode (H-term.: 1.2 %; 3py-term.: 1.0 %). Since no other reduction products were detected, this discrepancy could also be caused by the inconsistency of manual gas sample injection used for these two measurements. The larger gas volume injected during the manual injection compared to the automated injection procedure tended to lead to an overload of GC column, which caused deviations in peak form and area of CO_2 as the main gas component. These deviations could then lead to changes in the relative peak area of the H_2 peak. The small, noise-like deviations from the baseline in the NMR spectrum in the region of methanol (≈3.34 ppm) stem from the worsening water suppression method due of the high proton concentration in the electrolyte and the remaining H_2O signal (≈ 4.8 ppm), i.e., they do not point towards trace amounts of detected methanol. For NMR measurements of electrolyte samples with an acidic pH, acetonitrile (AN) was used as an internal calibration species instead of pyridine (see left side of figure 7.3). The chemical shifts of pyridine shifted in an acidic sample in such a way that it masked the potential peak of formic acid.

7.2 CO_2RR on grafted Si electrodes in weakly acidic electrolytes

CO_2RR on grafted Si electrodes in 0.5 M HCl as an acidic electrolyte yielded no CO_2 reduction products. One of the reasons for the missing CO_2 reduction products could be the low concentration of dissolved CO_2 of ≈ 38.7 mM (20°C) / ≈ 33.5 mM (25°C) in the electrolyte [202, 203]. Due to the much higher concentration of H^+ compared to dissolved CO_2 at pH ≤ 1, HER from protons could be the favored reaction across the electrode|electrolyte interface und thus be the dominating reaction in the acidic electrolyte. In more neutral and alkaline pH ranges the HER from protons subsides and is replaced by water splitting, which possesses much slower reaction kinetics. For example, on Pt the exchange current density of HER from H_2O is 10 times smaller in alkaline than in acidic electrolytes [204, 205]. Electrolysis measurements were therefore conducted in a weakly acidic electrolyte (0.5 M KCl) with a pH around 5. The pH was chosen to be close to the $pK_{a,gPy} = 5$ of grafted pyridinium [113] in order to minimize HER while at the same time to ensure pyridinium still being present on the surface of the grafted silicon electrode.

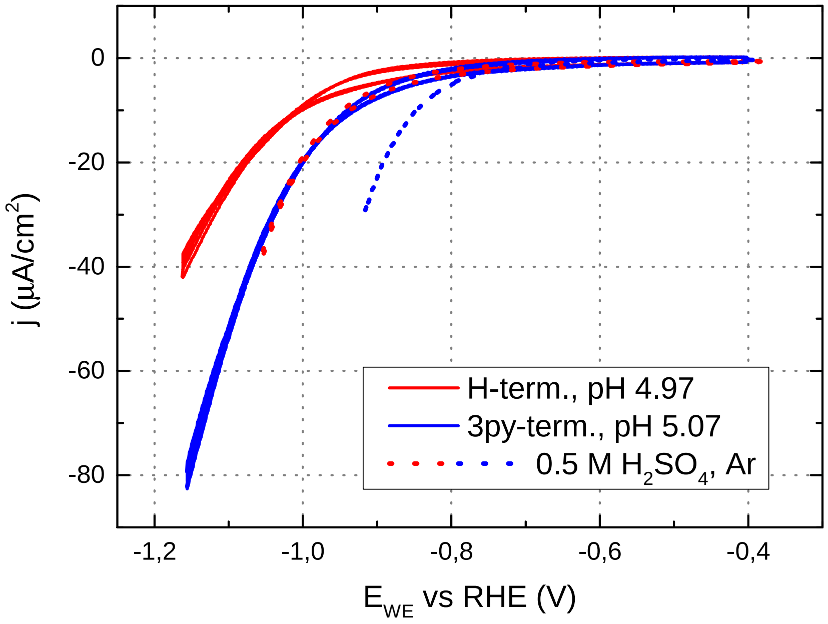

Figure 7.4: Left: CVs of H-terminated (red) and 3-pyridine-terminated silicon electrodes (blue) before the electrolysis. Dotted lines denote CVs of the grafted sample in 0.5 M H_2SO_4, purged in Ar, before (dotted, red) and after grafting (dotted, blue). Electrolyte: 0.5 M KCl, purged with CO_2. pH before electrolysis: 4.97 (H-terminated, red), 5.07 (3-pyridine-terminated, blue);

As can be seen in the CV in figure 7.4, both the H-terminated silicon electrode as well as the grafted, 3-pyridine-terminated electrode again show an exponential rise of current several hundreds of mV negative of RHE. Similar to figure 5.8 the onset shift of the 3-pyridinium-terminated electrode visible in an acidic electrolyte (dashed CVs) vanishes in the weakly acidic KCl electrolyte with pH $\approx$ 5, irrespective if the solution is saturates with Ar or CO_2. One of the main characterics of the pyridine mediated CO_2RR was the reported redox potential around RHE [19, 21, 32]. Since around RHE there is no significant current observable, a different potential range was chosen for the bulk electrolysis measurements. Similar to reported electrolysis measurements on silicon electrodes [50, 53, 206] a potential of $\approx$ -1.16 V vs RHE was held constant during the electrolysis, i.e. the electrolysis measurements in weakly acidic electrolytes were potentiostatic instead of galvanostatic as in figure 7.5 in HCl. The intention of this change is to make the electrolysis results more comparable to literature results of CO_2RR bulk electrolysis on unmodified silicon electrodes listed in table 7.1.

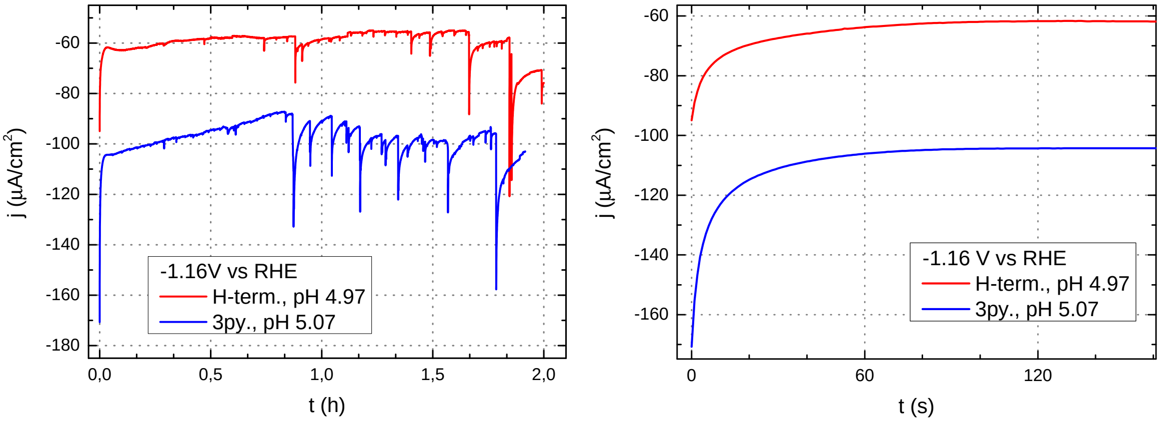

Figure 7.5: Left: Potentiostatic bulk electrolysis of silicon electrodes with H-termination (red) and 3-pyridine-termination after the grafting process (blue). Right: Beginning of potentiostatic bulk electrolysis of silicon electrodes with H-termination (red) and 3-pyridine-termination after the grafting process (blue). Electrolyte: 0.5 M KCl, purged with CO_2. pH before electrolysis: 4.97 (H-terminated, red), 5.07 (3-pyridine-terminated, blue).

Analogous to the galvanostatic electrolysis measurements in HCl (figure 7.2), at the start of the potentiostatic electrolysis in KCl (figure 7.5) the current drops significantly until settling around values higher than the ones obtained in the CVs, i.e., the current at the cathodic turnaround potential. Because of the higher current density bubble formation at the electrode intensified compared to the measurements in HCl, leading to multiple current spikes during the electrolysis. The H-terminated silicon electrode shows a trend towards higher current density over the time period of the electrolysis, though this trend is less clear to see compared to figure 7.2 due to the current spikes. The 3-pyridine-terminated sample shows the same trend towards higher currents at the end of the 2 h long electrolysis, but it also has a section in the j vs t curve till 0.8 h / 48 min, where the current density falls linearly. During the electrolysis the majority of the surface of the electrode was at times covered by gas bubbles, which could effectively lead to a decrease of electrode area and thus a (linear) decrease in reaction current. The bubble formation rate was also more pronounced on the grafted than on the H-terminated sample, which might partially explain the larger current spikes compared the ones present on the j vs t curve for the H-terminated electrode.

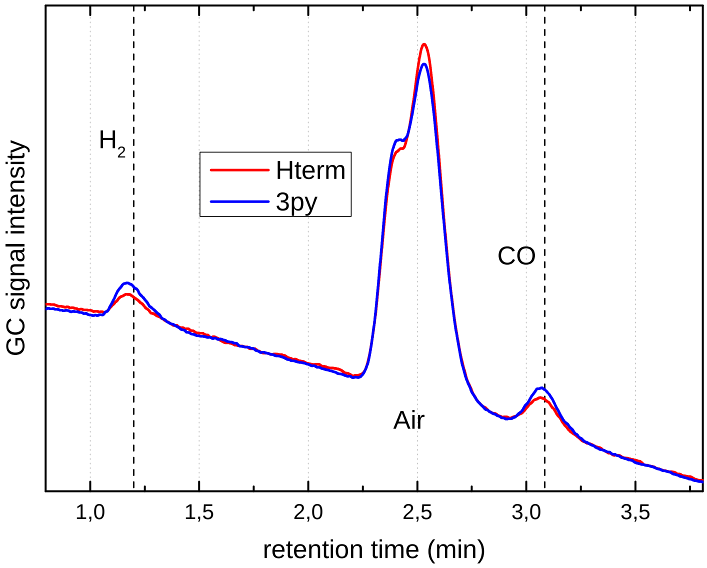

Figure 7.6: GC signals from gas overhead samples after electrolysis measurements on H-terminated (red) and 3-pyridine-terminated silicon electrodes (blue) from figure 7.5 in weakly acidic KCl. H_2 and CO were detected.

Sampling of the gas overhead after electrolysis in the GC (figure 7.6) show H_2 and, in addition, CO gas as a product of the CO_2RR. The 3-pyridine-terminated sample produced a slightly higher ratio of the two product gases for hydrogen: H_2:CO (79% : 21%), compared to the H-terminated electrode (76% : 24%).

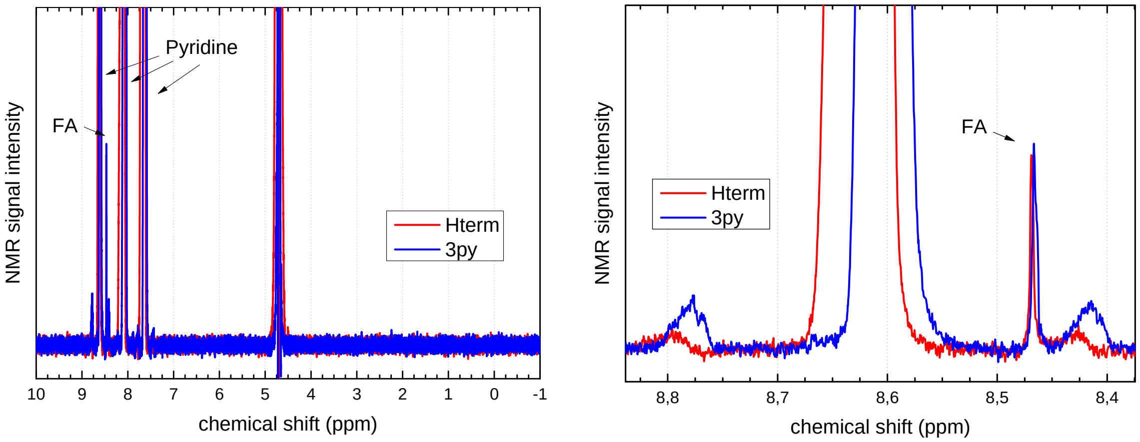

Figure 7.7: Left: NMR signals from electrolysis samples of bulk electrolysis on H-terminated (red) and 3-pyridine-terminated silicon electrodes (blue) from figure 7.5 in weakly acidic KCl. Besides pyridine (10 mM) as the calibration species only FA is detected; Right: Zoom into the FA region of NMR signals from of bulk electrolysis on H-terminated (red) and 3-pyridine-terminated silicon electrodes (blue) from figure 7.5 in weakly acidic KCl.

In the KCl based electrolyte at a pH around 5, formic acid (FA) was detected in the NMR spectrum (figure 7.7) as the only liquid product of CO_2RR. The changes in chemical shifts in the NMR spectra (i.e. the different shifts of the pyridine peak at 8.60 / 8.64 ppm in the right NMR spectrum of figure 7.7) arise from differences in pH of the

NMR samples. With the total amount of produced formic acid (H-term.: 375 nmol; 3py-term.: 350 nmol) the faradaic efficiency $\eta_{\mathrm{f,FA}}$ for the CO_2 conversion into formic acid can be calculated,

$$\eta_{\mathrm{f,FA}} = \frac{\mathrm{nF} \cdot 2}{\mathrm{Q_{EL}}} \tag{7.1}$$

with n being the number of moles of formic acid, F the Faraday constant and $\mathrm{Q_{EL}}$ the total charge drawn during the electrolysis. For the formation of one formic acid molecule, 2 electrons are needed. Although more charge was drawn on the grafted sample during the 2 h long electrolysis, the amount of formic acid produced via CO_2 reduction on the 3-pyridine-terminated electrode was slightly smaller compared to amount produced on the H-terminated electrode (350 to 375 nmol), leading to a worse faradaic efficiency (15.8 % compared to 26.7 %). The rest of the electrolysis charge can then assigned to the gaseous products H_2 and CO corresponding to their ratio, since both molecules consume 2 electrons for the formation of one product gas molecule, respectively. For the measurements in figure 7.5 the faradaic efficiency for H_2 evolution improved from 55.8 % for H-terminated electrode to 66.7 % for the 3-pyridine-terminated electrode. For CO production faradaic efficiencies are very similar, namely 17.6 % and 17.5 % for H-terminated and 3-pyridine-terminated electrodes, respectively. The product distribution and faradaic efficiency are comparable to CO_2 reduction conducted on unmodified silicon electrodes in aqueous and nonaqueous electrolytes [50–53, 206]. In the same manner as in HCl, functionalizing a silicon electrode with *a grafted 3-pyridine-layer does not improve its reactivity towards CO_2 reduction in a weakly acidic electrolyte with a pH $\approx$ 5.* In fact, the grafted layer led to a decrease of detected CO_2 reduction products (44.2 % to 33.3 %), most significantly for formic acid.

It is known that the use of an unbuffered electrolyte such as 0.5 M KCl can lead to a rise of the local pH at the surface (as well as the bulk pH over the duration of the electrolysis, if the electrolyte volume is small enough) compared to the initial bulk pH of 5. In unbuffered electrolytes the local pH can be shifted from a bulk pH value as low as 4 up to beyond 10 during reductive electrolysis, such as HER on Pt electrodes even at comparatively small current densities [207, 208]. At these alkaline local pH values two problems could arise for the CO_2RR on grafted silicon electrodes. First, in alkaline solutions silicon electrodes can be etched [164, 209], leading to a change of the surface during the electrolysis, for example a degradation of the 3-pyridine-layer via etching pyridine-terminated silicon surface atoms, thus removing grafted pyridine molecules (similar to the situation described in [162]). This surface change affects the electrochemical effect of the grafted layer on the CO_2 reduction. Together with the aforementioned formation of (sub)surface hydrides during cathodic electrolysis both H-terminated and grafted silicon electrodes irreversibly changed their electrochemical behaviour during the electrolysis and electrolysis measurements on the same electrode could not be repeated. Second, for the CO_2RR mediated with dissolved pyridine most proposed reaction mechanisms focus on the protonated pyridinium molecule as the catalytically active species [21, 22, 210]. With a pKa of around 5 [113], there would be very few to no grafted pyridinium molecules present on the silicon surface at an alkaline local pH. The protonation of the grafted pyridine layer has been shown to be the main reason for the improved onset of the HER of the 3-pyridinium-terminated silicon electrodes in previous chapters 5.3 and 6.1. In order to minimise the local pH shift to higher, alkaline values, a last set of electrolysis measurements were conducted where the applied reduction potential was pulsed.

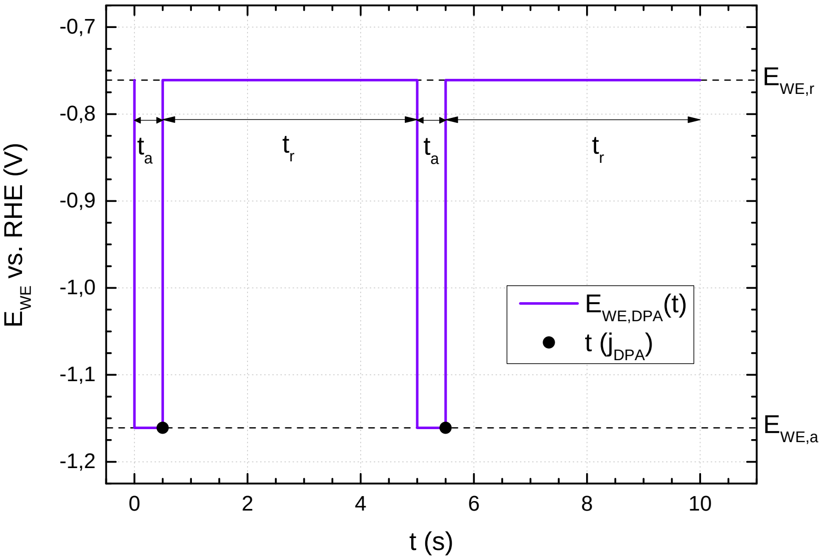

Figure 7.8: Potential control for the pulsed electrolysis or "Differential Pulsed Amperometry" (DPA).

Using the "Differential Pulsed Amperometry" (DPA) measurement protocol on the Biologic SP 300 Potentiostat, the applied potential was toggled between the reduction potential $E_{WE,a}$ = -1.16 V and a 400 mV more positive rest potential $E_{WE,r}$ = -0.76, where the faradaic current is negligible (see figure 7.8). For each reduction pulse of t_a = 0.5 s the potential stayed at $E_{WE,r}$ for t_r = 4.5 s. Together with additional convection due to stirring of the electrolyte, the local pH should shift back to the bulk pH during the resting time t_r at $E_{WE,r}$ after it had been increased by the reduction pulse. The current j_{DPA} was recorded at the end of each reduction pulse to minimise the capacitive contribution of the current, denoted t (j_{DPA}) in figure 7.8. The total reduction charge for each pulse is calculated by multiplying j_{DPA} with the pulse length t_a, assuming j_{DPA} is mostly faradaic.

The resulting electrolysis j vs t curves in figure 7.9 still exhibit the main features of the potentiostatic electrolysis measurements shown in figure 7.5, namely a current drop at the beginning and a general trend towards higher currents over the duration of the 2 h long electrolysis. If the initial drop in reduction current stems from a depletion of reactants (protons and CO_2) in the double layer in front of the electrode, the pulsed potential control with the given parameters and the additional stirring could not mitigate this change in the chemical composition of the double layer. The pulse and rest time were optimised as a compromise between the length of the electrolysis, as the samples tended to degrade over longer measurement times, and the overall charge drawn, as the pulsed electrolysis led to a total charge of only 15 % of the drawn charge during (constant) bulk electrolysis. Such a decrease of the produced amounts of CO_2 reduction products made their detection difficult, as they were near the sensitivity limits of the product analysis tools deployed in this thesis.

For the H-terminated silicon electrode, formic acid was produced in addition to H_2 and a negligably small amount of CO close to the detection limit of the GC (figure

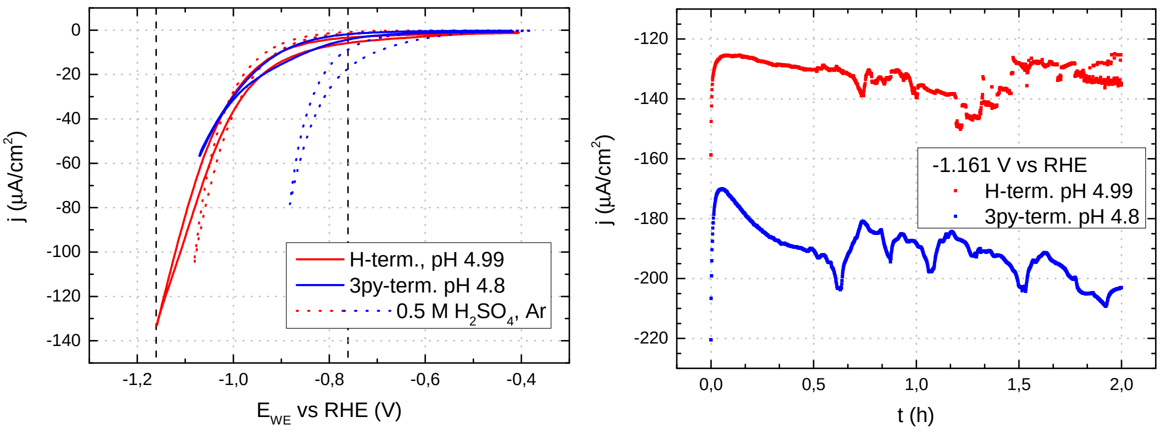

Figure 7.9: Left: CVs of a H-terminated (solid red) and a 3-pyridine-terminated silicon electrodes (solid blue) before the electrolysis. Dotted lines denote CVs of the grafted sample in 0.5 M H$_2$SO$_4$, purged in Ar, before (dotted red) and after grafting (dotted blue). Right: Potentiostatic DPA electrolysis of silicon electrodes with H-termination (red squares) and 3-pyridine-termination (blue squares). Electrolyte: 0.5 M KCl, purged with CO$_2$. pH before electrolysis: 4.99 (H-terminated, red), 4.8 (3-pyridine-terminated, blue)

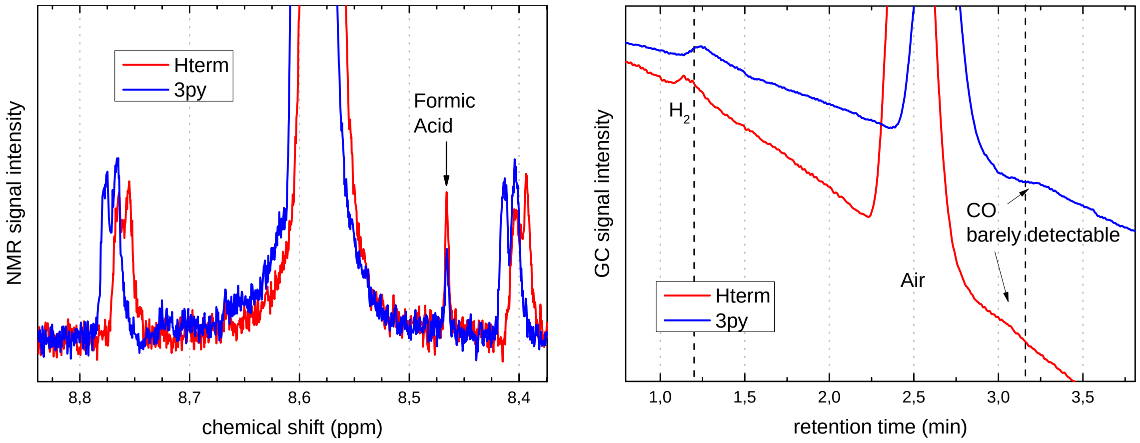

Figure 7.10: Left: NMR spectra of electrolysis samples from the DPA electrolysis on H-terminated (red) and 3-pyridine-terminated silicon electrodes (blue) from figure 7.9 in weakly acidic KCl. Besides pyridine (10 mM) as the calibration species only FA is detected; Right: GC signals from gas overhead samples from the DPA electrolysis on H-terminated (red) and 3-pyridine-terminated silicon electrodes (blue) from figure 7.9 in weakly acidic KCl. H$_2$ and CO were detected in both measurements.

7.10). Again, the changes in chemical shifts in the NMR spectra (most noticeable in the pyridine peaks) arise from differences in pH of the NMR samples. As in figure 7.7, the grafted electrode produced a smaller amount of formic acid despite the reduction charge drawn during the pulsed electrolysis being larger. Compared to the measurement series with constant potential in figure 7.5 the pulsed electrolysis led to a higher H$_2$ to CO ratio (H-terminated: 93.5 % : 6.5 %; 3-pyridine-terminated: 94.4 % : 5.6 %) and slightly higher faradaic efficiency for formic acid production on H-terminated electrodes versus slightly lower faradaic efficiency for FA on 3-pyridine-terminated electrodes. The product analysis results from all described bulk electrolysis measurements are listed in table (7.1), together with results from literature.

Fig.	Si surface mod.	Electrolyte	Q_{EL} (C)[1]	E_{WE} vs RHE (V)
7.2	H-term.	0.5 M HCl + CO_2, pH 0.3	-0.144	-1.007 (avg.)
	3py-term.	0.5 M HCl + CO_2, pH 0.3	-0.144	-0.860 (avg.)
7.5	H-term.	0.5 M KCl + CO_2, pH 4.97	-0.271	-1.163
	3py-term.	0.5 M KCl + CO_2, pH 5.07	-0.427	-1.163
7.9	H-term.	0.5 M KCl + CO_2, pH 4.99	-0.060	-1.163
	3py-term.	0.5 M KCl + CO_2, pH 4.8	-0.087	-1.163
Literature data				
[206]	pSi (ill.) PANI[2]	0.1 M Li_2SO_4 + CO_2 pH $\approx$ 6.3	-56.7	-1.284
[50]	pSi (ill.) H-term.	0.5 M Na_2SO_4 + CO_2 pH > 6	-231	-1
[51]	pSi (ill.) H-term.	0.3 M TBAP[3] in MeOH[4] + CO_2	–	-1.7 vs. Ag/AgCl
[52]	pSi (ill.) H-term.	0.1 M TBAP + 3.0 M H_2O in AN[5] + CO_2	-10	-2.7 vs. Ag/AgCl
[53]	pSi (ill.) H-term.	0.1 M $KHCO_3$ + CO_2 pH 7	-1.2 /cm^2	-0.613

Fig.	H_2 : CO	FA (nmol)	H_2 (%)[6]	CO (%)[6]	FA (%)[6]	other products	CO_2 (%)[7]
7.2	–	–	100	–	–	–	0
	–	–	100	–	–	–	0
7.5	76 : 24	375	55.8	17.6	26.7	–	44.2
	79.2 : 20.8	350	66.7	17.5	15.8	–	33.3
7.9	93.5 : 6.5	94.8	65.1	4.5	30.4	–	34.9
	94.4 : 5.6	57.3	82.3	4.9	12.8	–	17.7
Literature data							
[206]	–	$5.05 \cdot 10^4$	–	–	17.1	Formaldehyde	27.7
[50]	–	–	–	–	$\approx$ 18	Formaldehyde[8]	$\approx$ 18
[51]	82 : 17	–	82	17	–	$HCOOCH_3$	30.3
[52]	96.7 : 1.7	–	87.8	1.5	2.1	CH_4	5.1
[53]	85.5 : 14.0	–	73.5	12.0	4.3	CH_4	16.7

Table 7.1: Bulk electrolysis of CO_2 on silicon electrodes and subsequent product analysis. Literature data is included for comparison.

---

[1] Charge drawn during electrolysis

[2] Polyaniline, $(C_6H_4NH)_n$

[3] Tetrabutylammonium perchlorate

[4] Methanol

[5] Acetonitrile

[6] Faradaic efficiency

[7] Faradaic efficiency for the sum of all CO_2 reduction products

[8] Traces

7.3 Discussion: The evolving role of pyridine / pyridinium for the CO_2RR

The neutral to negative effect of the grafted 3-pyridine layer on the CO_2RR on silicon electrodes seems to fit into the emergence of critital reports from other groups investigating the pyridine mediated CO_2 reduction reaction. The first diverging views on the proposed homogeneous reaction mechanism arose with density function theory (DFT) calculations, which stated that the neutral pyridinyl radical, proposed as the catalytically active species [21], was electrochemically inert and the reduction potential of pyridinium ($\leq$ -1.2 V vs SCE) should have been much lower than experimentally observed ($\approx$ -0.6 V vs SCE) [211–213]. Likewise, the reaction was surface sensitive, thus negating its initially assumed homogeneous nature. It was reported that certain electrode materials could not reduce CO_2 with pyridine present in the electrolyte, like gold (Au) [214] and glassy carbon [215]. This behaviour was similar to the shift of the reduction peak of pyridine in acetonitrile, where the potential scaled linearly with the overpotential needed for the same HER current of the respective electrode materials measured [46]. As both Au and glassy carbon electrodes need rather high overpotentials for HER compared to Pt and H-terminated Pd electrodes, the availability of surface hydride was then proposed to play a crucial role in the (now) pyridine-"mediated" CO_2 reduction on, for example, Pt electrodes [210]. In operando FTIR measurements in our group on Au and Pt electrodes in acidic electrolytes containing pyridine showed, that the main difference between Au and Pt was the amount of adsorbed hydronium and Zundel cations, thus amount of adsorbed protons on the surface of Pt [216]. Similarly, DFT calculations on semiconducting electrodes, like p-GaP, which showed a high faradaic efficiency for CO_2 reduction to methanol, focused on the H-termination of its surface under electrolysis conditions [217]. While CO_2RR was improved with *dissolved* pyridine to yield methanol and other reduction products, electrochemical systems reducing CO_2 where pyridine was immobilized on the surface of the electrode have also been reported. Pyridine derivatives incorporated in metal/alloy powder electrodes like Pd [218], Cu-Pt [219] and Cu-Pd [220] led to these electrodes reducing CO_2 to methanol with high efficiency and much reduced overpotential required. Gold electrodes covered with 4-pyridinylethanemercaptan [221] and copper electrodes covered with a poly(4-vinyl pyridine) film [222] showed a significant increase in their faradaic efficiency for reducing CO_2 to formic acid despite the negative results of CO_2RR on gold and copper with dissolved pyridine [214].

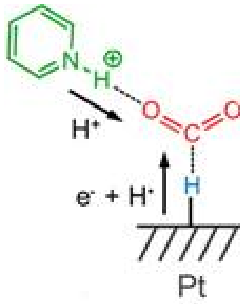

Figure 7.11: Proposed reaction scheme for pyridinium-mediated reduction of CO_2 on Pt with surface hydrides. Original figure from [210].

The effect of pyridine on the electrochemical CO_2 observed in this thesis and concomitantly conducted studies in other groups is summarized in table 7.2.

Electrode	Electrolyte sat. with CO_2	Effect of pyridine on CO_2 reduction	
Pd	0.5 M Na_2SO_4 + 10 mM Py pH 5.3	MeOH (30%) Formaldehyde	[19]
	0.5 M KCl, pH 5.4	MeOH (36%)	[218][1]
Pd-Cu	0.5 M KCl, pH 5.4	MeOH (26%) EtOH	[220][1]
Pt-Cu	0.5 M KCl, pH 5.4	MeOH (36%)[2] EtOH (25%)[3]	[219][1]
Pt	0.5 M KCl + 10 mM Py, pH 5.3	MeOH (22%) FA (11%)	[21]
	0.5 M KCl + 10 mM Py, pH 4.8	MeOH PrOH	[23]
	0.1 M KNO_3 + 10 mM Py pH 5.3	no products	[223]
	0.5 M KCl + 10 mM Py, pH 5.3	MeOH (14%)	[24]
	0.5 M KCl + 10 mM Py, pH 5.3	MeOH[4]	[81]
	0.5 M KCl + 10 mM Py, pH 5.3[5]	MeOH (7%) EtOh, PrOH, BuOH	[25]
	0.1 M $LiClO_4$[6] + 10mM Py pH 5.5	MeOH (30%)	[26]
	0.5 M KCl + 10 mM Py, pH 5.3	FA (2%)	[224]
	0.5 M KCl + 10 mM Py, pH 4.7	no products	[225]
	0.5 M KCl + 10 mM Py, pH 5.3	no products	[27]
	0.5 M KCl + 10 mM Py, pH 5.3	no products	[215]
	0.5 M KCl + 10 mM Py, pH 5.3	no products[7]	[226]
GC	0.1 M $LiClO_4$[6] + 10 mM Py pH 5.5	MeOH (7%) FA	[26]
	0.5 M KCl + 10 mM Py, pH 5.3	no products	[215]
Au	0.1 M NaF + 10 mM Py	no products	[214]
	0.1 M $KHCO_3$, pH 6.8	FA (21%) CO (12%)	[221][8]
	0.5 M KCl + 10 mM Py, pH 5.3	no products	[215]
Cu	0.1 M $KHCO_3$, pH 6.8	FA (40%)	[222][9]
Sn	0.5 M KCl + 30 mM Py, pH 5.3	FA (32%)	[199]
Pt-Au[10]	0.1 M $KHCO_3$, pH 4.0	MeOH (39%)	[227][10]

Cu_2O/ZnO	0.5 M $KHCO_3$, pH 5	MeOH (26%)	[228]
p-GaP	0.5 M KCl + 10 mM Py, pH 5.3	MeOH (96%)	[32]
	0.5 M KCl + 10 mM Py, pH 5.3	MeOH (55%)	[36][12]
$CuInS_2$	0.1 M acetate buffer + 10 mM Py pH 5.2	MeOH (97%)	[37]
CdTe/FTO	0.1 M $NaHCO_3$[13] + 10 mM Py pH 5	MeOH (61%)	[35]
Cu_2O	0.1 M acetate buffer + 30 mM Py pH 5.2	EtOH	[38]

Table 7.2: Reported bulk electrolysis data of CO_2 on various electrodes in electrolytes containing pyridine.

---

[1] Pyridine derivates incorporated

[2] -0.6 V vs SCE

[3] -1.2 V vs SCE

[4] Trace

[5] CO_2 overpressure up to 50 bar

[6] CH_3CN/H_2O 40% (v/v)

[7] Piperidine

[8] Gold electrodes covered with 4-pyridinylethanemercaptan

[9] Copper electrodes covered with a poly(4-vinyl pyridine) film

[10] Nanoparticles

[11] Self-assembled monolayer of 2-pyridinethiol film

[12] GaP passivated by TiO_2

[13] + citrate acid buffer

Recently, several other publications appeared, in which CO_2RR on Pt with pyridine dissolved in the electrolyte were investigated. In these studies, no reduction products were detected [215, 223, 225] besides formic acid and trace amounts of CO [224]. In our group, methanol as a CO_2 reduction product was either only detectable in trace amounts [81] or not detected at all, together with any other CO_2 reduction products [27, 226], when using the same or comparable electrolysis parameters compared to literature reports of successful CO_2RR. Saveant et al. showed that the current increase seen in figure 1.4 previously mainly attributed to CO_2 reduction [21] could be explained by the HER driven by protons dissociated from pyridinium (fig. 7.12, blue CV) superpositioned to the HER driven by protons stemming from carbonic acid in the CO_2 saturated electrolyte (fig. 7.12, green CV).

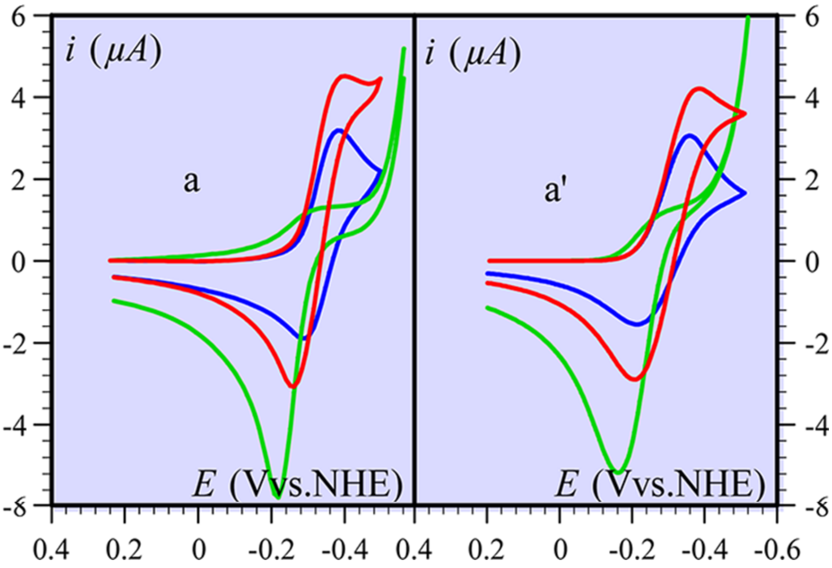

Figure 7.12: Experimental (left) and simulated (right) CVs of a Pt electrode in 0.1 M KNO_3 with 10 mM pyridine (blue), purged with CO_2 (green), and finally with both pyridine and CO_2 (red). Beware of inverted sign of the current density, cathodic current densities are denoted as positive. Original figure from [223].

In electrolytes with a weakly acidic pH around 5, both weak acids pyridinium and carbonic acid act as proton sources, which can lead to a current peak before HER from water splitting starts to occur. FTIR experiments during and after CV scans or electrolysis measurements on Pt found little to no indications concerning the mediation or catalysis of CO_2 reduction by pyridine or pyridinium besides signals stemming from the adsorption of CO [225], formate [224] and from of the hydrogenation of pyridinium [229]. The signs of pyridine hydrogenation were also found in our group in FTIR measurements on a Pt electrode in an acidic electrolyte with dissolved pyridine [216]. All the while, the use of an unbuffered electrolyte such as 0.5 M KCl in most of the prior electrolysis measurements led to questions of the validity of reaction mechanisms surrounding pyridinium as the targeted mediating or catalytically active species, since with any noticable reduction current density the local pH of the electrolyte at the electrode|electrolyte interface would shift towards alkaline values [207, 208], thus leading to the deprotonation of pyridinium back to pyridine.

These aspects prompted a collaboration with Dr Pierre-Yves Olu[1], in which bulk electrolysis measurements were conducted in a carefully designed electrochemical setup with the goal to minimise the shift of the local pH in front of the electrode [226].

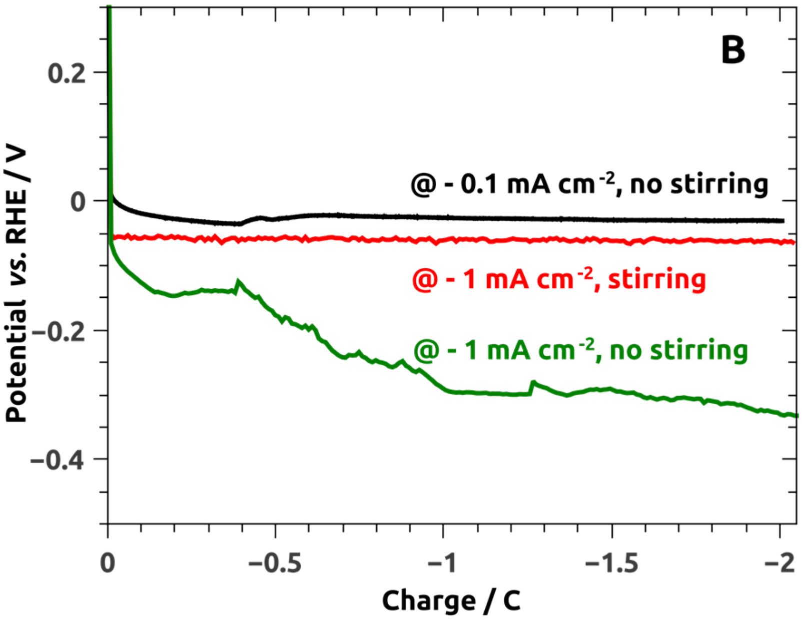

Figure 7.13: Galvanostatic measurement of a Pt mesh electrode at -0.1 mA/cm^2 without stirring (black), at -1 mA/cm^2 without (green) and with stirring (red). Electrolyte: 1 M KCl + 10 mM Py, purged with CO_2.

In figure 7.13 the effect of the local pH shift can be seen. Under galvanostatic conditions, a current density of -0.1 mA/cm^2 leads to a stable electrode potential of -10 mV vs RHE without stirring, while for -1 mA/cm^2 the potential decreases with increasing measurement time and charge transferred, indicating a shift of the local pH in front of the electrode towards higher, alkaline values, as the proton concentration in the double layer cannot be supported by the mass transport of protons from the bulk under stagnant conditions. When additional stirring is provided, the current vs time curve for -1 mA/cm^2 stays constant at about -60 mV vs RHE, thus showing no signs of a local pH shift. The potential difference between the two cases is $\approx$ 240 mV, which would correspond to a local pH shift of 4.2 units. Without stirring and at a current density of -0.1 mA/cm^2, it could therfore be ensured that the predominant reactants for the pyridine mediated CO_2RR were indeed CO_2 and pyridinium as proposed in the aforementioned reaction mechanisms [21,210] instead of HCO_3^- and pyridine, as present at an alkaline local pH value of $\geq$ 9.2. In these measurements the present pyridinium underwent full hydrogenation during electrolysis in CO_2 saturated 0.5 M KCl with a pH $\approx$ 5 at mild reductive conditions ($\approx$ 0 V vs RHE) and was the sole reduction product besides H_2, with no CO_2 reduction products detectable. In an acidic electrolyte, almost all of the pyridinium as the predominant pyridine species was hydrogenated to piperidine (confirming the trend in [216]), whereas in an alkaline electrolyte no piperidine was detected, since there is no pyridinium present in an alkaline electrolyte environment. The hydrogenation of pyridine to piperidine is independent of the presence of CO_2 in

---

[1] Non-equilibrium Chemical Physics group, Physics Department, Technical University Munich

the electrolyte. With these results, pyridinium can be ruled out as a probable catalyst for the CO_2RR in near-neutral, weakly acidic electrolytes while hydrogenated pyridine species such as piperidine also do not seem to show catalytic properties for the CO_2RR.

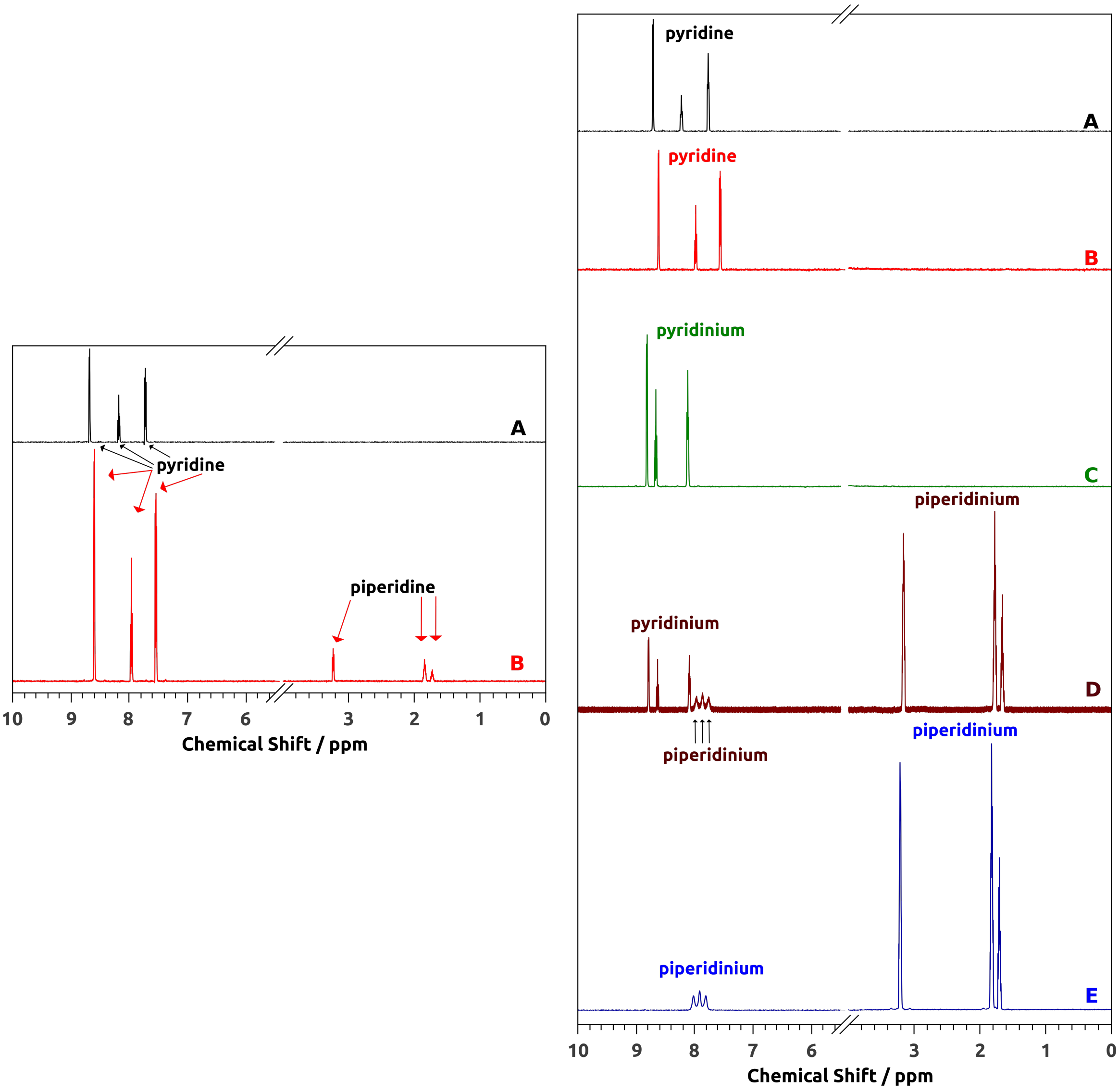

Figure 7.14: Left: ^{1}H-NMR of electrolyte samples before (A) and after (B) -15 C electrolysis on Pt mesh at -0.1 mA cm^{-2}. Electrolyte: 1 M KCl + 10 mM Py electrolyte (initial pH = 5.3), CO_2-saturated. Piperidine peaks emerge after the electrolysis in the NMR spectrum. Right: ^{1}H-NMR of N_2-saturated 1 M KCl + 10 mM Py electrolyte (initial pH = 7.5) before (A) and after (B) -15 C electrolysis on Pt mesh at -0.1 mA cm^{-2}. In the alkaline electrolyte pyridine is not hydrogenated and there are no signs of piperidine. ^{1}H-NMR of N_2-saturated 1 M KCl + 0.2 M HCl + 10 mM PyH^+ electrolyte (initial pH = 0.7) before (C) and after -5 C (D) and -15 C (E) electrolysis on Pt mesh at -0.1 mA c^{-2}. In the acidic electrolyte almost all pyridine is hydrogenated into piperidine. In all NMR spectra there are no signs of other species, such as CO_2RR products.

1,2-dihydropyridine as a partially hydrated pyridine molecule was reported to show no observable interaction with added $^{13}CO_2$ and H_2O when measured in NMR along with other organic hydride donors (OHD) [230], supporting the independence of the hydrogenation of pyridine from the CO_2RR. It is doubtful in light of these findings, that pyridinium on its own takes some significant part in the reduction process of CO_2; rather pyridine could provide a still unexplained synergy effect on the reduction reaction of CO_2 in neutral and alkaline electrolytes. Molecules similar to pyridine, i.e., with a nitrogen moiety, have been reported to show similar enhancing properties for the CO_2RR like imidazole [34], pyrazine [24], picoline [199] and pyridoxine (Vitamin B6) [231]. Substituted pyridine derivates, such as the precursor molecule 4-aminopyridine used in this thesis, showed even higher faradaic efficiencies for the methanol and formic acid production from CO_2 reduction than pyridine when dissolved in electrolytes [232]. The mediating nature of pyridine and similar molecules on the electrochemical CO_2 reduction needs to be further explored with an emphasis on elucidating the underlying reaction mechanism on the substrate or electrode used for the reduction and the effect of the actual (local) electrochemical environment at the electrode|electrolyte interface, i.e., local pH shift and the composition of chemical species present, on the reaction. Only then can the effect of pyridine on the reaction system be deduced. In light of the results of the 3-pyridine grafted silicon electrodes for CO_2RR, it can be stated that a grafted pyridine layer on top of a silicon electrode does not enhance or catalyse the electrochemical CO_2 reduction. Immobilized pyridine might possibly play an indirect role, such as inhibiting competing side reactions or stabilizing intermediate species during the CO_2RR, but the as described grafted pyridine layer does not show this kind of CO_2RR-promoting properties.

Chapter 8

Summary

In this thesis, the surface modification of H-terminated n-type silicon electrodes with immobilized pyridine molecules was investigated in order to elucidate the effect of the functionalized pyridine layer on the reactivity of the silicon electrodes with respect to the hydrogen evolution and CO_2 reduction reaction, where pyridine was reported to lower the required overpotential and improve the efficiency and selectivity of the reduction reaction towards methanol production.

A suitable electrochemical procedure was developed to graft 3-diazopyridine (either in situ generated or as a synthesized diazonium salt) covalently onto a planar, H-terminated n-Si electrode. The resulting layers were shown to be resistant against various aqueous and organic solvents but did not prevent the unfunctionalized surface atoms from oxidizing. Likewise, such functionalized silicon electrodes could be indirectly damaged by the chemical etching of the underlying oxidized silicon substrate in fluoride containing solutions. XPS measurements in conjunction with EIS measurements confirmed the presence of grafted pyridine molecules on the modified silicon electrodes with a partial surface coverage of less than a monolayer.

The grafted silicon electrodes were shown to be activated toward the hydrogen evolution reaction, for which the onset potential of the HER is reduced substantially by up to $\approx$+400 mV compared to an H-terminated silicon electrode, which is, to the knowledge of the author, one of the highest achieved overpotential reduction caused by an organic surface modification on silicon substrates, and rivals results for metallic surface modifications. The positive HER onset shift is predicated on the protonation of the grafted pyridine or pyridinium molecules in an acidic electrolyte, as the onset shift vanishes in weakly acidic solutions with a pH higher than the $pK_a \approx 5$ of the grafted pyridine layer.

In EIS measurements, the grafted 3-pyridinium-terminated silicon electrodes exhibited a higher total capacitance than in their prior H-terminated state in an acidic environment, while the capacitance of the functionalized electrode was lowered in a weakly acidic solution with a pH $\geq$ 5, again pointing towards the modification of the electrode|electrolyte interface with a layer of the immobilized, protonated pyridinium molecules. This layer of charged pyridinium molecules is presumed to influence the composition of the Helmholtz layer in front of the silicon electrode as well as the thickness of the space charge layer, which could result in the higher double layer capacitance, and subsequently higher total capacitance of a modified electrode.

In contrast to the increased reactivity for HER, the grafted 3-pyridine layer showed no detectable enhancement of the CO_2 reduction reaction during the bulk electrolysis both in acidic and weakly acidic electrolytes, i.e., when the immobilized pyridine molecules were protonated or deprotonated. This neutral to negative behaviour of the grafted pyridine layer seems to fit into the emergence of a critical view concerning the favourable effects of pyridine on the CO_2 reduction reaction presented in literature. Further studies on the CO_2RR on Pt electrodes led to the conclusion, that reactions involving pyridine like its de-/protonation or hydrogenation seem to take place independent of the CO_2 reduction and no CO_2 reduction products were detected in an electrolyte containing pyridine. For HER, the grafting of 3-diazopyridine turned out to be an intriguing method to tune the energetics and electrocatalytic properties of the silicon|electrolyte interface and thereby its reactivity towards HER. The method could be expanded to other (metallo)organic molecules with (known) electrocatalytic activities towards desired reactions, which could in turn lead to functionalized (silicon) photoelectrodes "activated" towards numerous electrochemical reactions.

During the duration of the thesis, parts of the results were published:

- [134] Li, Q., Schönleber, K., Zeller, P., Höhlein, I., Rieger, B., Wintterlin, J., and Krischer, K. (2015). Activation of silicon surfaces for H_2 evolution by electrografting of pyridine molecules. Surface Science, 631, 185-189.
- [226] Olu, P. Y., Li, Q., and Krischer, K. (2018). The True Fate of Pyridinium in the Reportedly Pyridinium-Catalyzed Carbon Dioxide Electroreduction on Platinum. Angewandte Chemie, 130(45), 14985-14988.

Bibliography

[1] K. Krischer and K. Schönleber, *Physics of Energy Conversion*. Walter de Gruyter GmbH & CO KG, 2015.

[2] Global temperature mean from Goddard Institute for Space Studies, NASA; https://tinyurl.com/y7wblyk5

[3] “CO_2 ppm curve from 1700 to 2019 Jan. at Mauna Loa Observatory, https://scripps.ucsd.edu/programs/keelingcurve/,”

[4] C. MacFarling Meure, D. Etheridge, C. Trudinger, P. Steele, R. Langenfelds, T. van Ommen, A. Smith, and J. Elkins, “Law Dome CO_2, CH_4 and N_2O ice core records extended to 2000 years BP,” *Geophysical Research Letters*, vol. 33, no. 14, 2006.

[5] R. S. Haszeldine, “Carbon capture and storage: how green can black be?,” *Science*, vol. 325, no. 5948, pp. 1647–1652, 2009.

[6] D. Leung, G. Caramanna, and M. M. Maroto-Valer, “An overview of current status of carbon dioxide capture and storage technologies,” *Renewable and Sustainable Energy Reviews*, vol. 39, pp. 426–443, 2014.

[7] K. Damen, A. Faaij, and W. Turkenburg, “Health, safety and environmental risks of underground CO_2 storage - overview of mechanisms and current knowledge,” *Climatic Change*, vol. 74, no. 1-3, pp. 289–318, 2006.

[8] M. M. May and K. Rehfeld, “ESD Ideas: Photoelectrochemical carbon removal as negative emission technology,” *Earth System Dynamics*, vol. 10, no. 1, pp. 1–7, 2019.

[9] J. Rogelj, M. Schaeffer, M. Meinshausen, R. Knutti, J. Alcamo, K. Riahi, and W. Hare, “Zero emission targets as long-term global goals for climate protection,” *Environmental Research Letters*, vol. 10, no. 10, p. 105007, 2015.

[10] C. Keeling, S. Piper, R. Bacastow, M. Wahlen, T. Whorf, M. Heimann, and H. Meijer, “Atmospheric CO_2 and $^{13}CO_2$ exchange with the terrestrial biosphere and oceans from 1978 to 2000: observations and carbon cycle implications,” in *A history of atmospheric CO_2 and its effects on plants, animals, and ecosystems*, pp. 83–113, Springer, 2005.

[11] R. K. Pachauri, M. R. Allen, V. R. Barros, J. Broome, W. Cramer, R. Christ, J. A. Church, L. Clarke, Q. Dahe, P. Dasgupta, *et al.*, *Climate change 2014: synthesis*

report. Contribution of Working Groups I, II and III to the fifth assessment report of the Intergovernmental Panel on Climate Change. IPCC, 2014.

[12] Total Final Energy Consumption (TFC) by source, IEA; https://tinyurl.com/y7o3a5lr

[13] W. M. Haynes, ed., *CRC handbook of chemistry and physics.* CRC Press, 2014.

[14] B. Kumar, M. Llorente, J. Froehlich, T. Dang, A. Sathrum, and C. P. Kubiak, "Photochemical and Photoelectrochemical Reduction of CO_2," *Annu. Rev. Phys. Chem.*, vol. 63, p. 541, 2012.

[15] Y. Hori, K. Kikuchi, and S. Suzuki, "Production of CO and CH_4 in electrochemical reduction of CO_2 at metal electrodes in aqueous hydrocarbonate solution," *Chemistry Letters*, vol. 1, pp. 1695–1698, 1985.

[16] K. P. Kuhl, E. R. Cave, D. N. Abram, and T. F. Jaramillo, "New insights into the electrochemical reduction of carbon dioxide on metallic copper surfaces," *Energy & Environmental Science*, vol. 5, no. 5, pp. 7050–7059, 2012.

[17] K. P. Kuhl, T. Hatsukade, E. R. Cave, D. N. Abram, J. Kibsgaard, and T. F. Jaramillo, "Electrocatalytic conversion of carbon dioxide to methane and methanol on transition metal surfaces," *Journal of the American Chemical Society*, vol. 136, no. 40, pp. 14107–14113, 2014.

[18] A. Bard and H. Lund, *Encyclopedia of the Electrochemistry of the Elements. Organic Section, Vol XV.* CRC press, 1985.

[19] G. Seshadri, C. Lin, and A. B. Bocarsly, "A new homogeneous electrocatalyst for the reduction of carbon dioxide to methanol at low overpotential," *Journal of Electroanalytical Chemistry*, vol. 372, p. 145, 1994.

[20] K. Ohkawa, K. Hashimoto, A. Fujishima, Y. Noguchi, and S. Nakayama, "Electrochemical reduction of carbon dioxide on hydrogenstoring materials: Part 1. the effect of hydrogen absorption on the electrochemical behavior on palladium electrodes," *Journal of Electroanalytical Chemistry*, vol. 345, no. 1-2, pp. 445–456, 1993.

[21] E. Barton-Cole, P. Lakkaraju, D. Rampulla, A. Morris, E. Abelev, and A. Bocarsly, "Using a one electron shuttle for the multielectron reduction of CO_2 to methanol: kinetic mechanistic and structural insight," *J. Am. Chem. Soc.*, vol. 132, p. 11539, 2010.

[22] A. J. Morris, R. T. McGibbon, and A. B. Bocarsly, "Electrocatalytic carbon dioxide activation: The rate-determining step of pyridinium-catalyzed CO_2 reduction," *ChemSusChem*, vol. 4, no. 2, pp. 191–196, 2011.

[23] N. R. de Tacconi, W. Chanmanee, B. H. Dennis, F. M. MacDonnell, D. J. Boston, and K. Rajeshwar, "Electrocatalytic reduction of carbon dioxide using Pt/C-TiO_2 nanocomposite cathode," *Electrochemical and Solid-State Letters*, vol. 15, no. 1, pp. B5–B8, 2011.

[24] E. Portenkirchner, C. Enengl, S. Enengl, G. Hinterberger, S. Schlager, D. Apaydin, H. Neugebauer, G. Knör, and N. S. Sariciftci, "A comparison of pyridazine and pyridine as electrocatalysts for the reduction of carbon dioxide to methanol," *ChemElectroChem*, vol. 1, no. 9, pp. 1543–1548, 2014.

[25] S. I. Rybchenko, D. Touhami, J. D. Wadhawan, and S. K. Haywood, "Study of pyridine-mediated electrochemical reduction of CO_2 to methanol at high CO_2 pressure," *ChemSusChem*, vol. 9, no. 13, pp. 1660–1669, 2016.

[26] P. K. Giesbrecht and D. E. Herbert, "Electrochemical reduction of carbon dioxide to methanol in the presence of benzannulated dihydropyridine additives," *ACS Energy Letters*, vol. 2, no. 3, pp. 549–555, 2017.

[27] A. Heine, "Pyridine-catalysed carbon dioxide reduction to methanol on platinum surfaces," master's thesis, Technische Universität München, Physik-Department, E19a, Nonequilibrium Chemical Physics, 2017.

[28] Y. Hori, H. Wakebe, T. Tsukamoto, and O. Koga, "Electrocatalytic process of CO selectivity in electrochemical reduction of CO_2 at metal electrodes in aqueous media," *Electrochimica Acta*, vol. 39, no. 11-12, pp. 1833–1839, 1994.

[29] M. Z. Kamrath, R. A. Relph, and M. A. Johnson, "Vibrational predissociation spectrum of the carbamate radical anion, $C_5H_5N^-CO_2^-$, generated by reaction of pyridine with $(CO_2)_m^-$," *Journal of the American Chemical Society*, vol. 132, no. 44, pp. 15508–15511, 2010.

[30] F. Riboni, E. Selli, M. Hoffmann, and A. COlussi, "Homogeneous reduction of CO_2 by photogenerated pyridinyl radicals," *The Journal of Physical Chemistry A*, vol. 119, no. 19, pp. 4433–4438, 2014.

[31] D. N. Abram, K. P. Kuhl, E. R. Cave, and T. F. Jaramillo, "Platinum and hybrid polyaniline–platinum surfaces for the electrocatalytic reduction of CO_2," *MRS Communications*, vol. 5, no. 2, pp. 319–325, 2015.

[32] E. E. Barton, D. M. Rampulla, and A. B. Bocarsly, "Selective solar driven reduction of CO_2 to methanol using a catalyzed p-GaP based photoelectrochemical cell," *J. Am. Chem. Soc.*, vol. 130/20, p. 6342, 2008.

[33] K. A. Keets, E. Barton-Cole, A. J. Morris, N. Sivasankar, K. Teamey, P. S. Lakkaraju, and A. B. Bocarsly, "Analysis of pyridinium catalyzed electrochemical and photoelectrochemical reduction of CO_2: Chemistry and economic impact," 2012.

[34] A. B. Bocarsly, Q. D. Gibson, A. J. Morris, R. P. L'Esperance, Z. M. Detweiler, P. S. Lakkaraju, E. L. Zeitler, and T. W. Shaw, "Comparative study of imidazole and pyridine catalyzed reduction of carbon dioxide at illuminated iron pyrite electrodes," *ACS Catalysis*, vol. 2, no. 8, pp. 1684–1692, 2012.

[35] J. H. Jeon, P. M. Mareeswaran, C. H. Choi, and S. I. Woo, "Synergism between CdTe semiconductor and pyridine–photoenhanced electrocatalysis for CO_2 reduction to formic acid," *RSC Advances*, vol. 4, no. 6, pp. 3016–3019, 2014.

[36] G. Zeng, J. Q., Z. Li, P. Pavaskar, and S. B. Cronin, “CO_2 reduction to methanol on TiO_2-passivated GaP photocatalysts,” *ACS Catalysis*, vol. 4, no. 10, pp. 3512–3516, 2014.

[37] J. Yuan and C. Hao, “Solar-driven photoelectrochemical reduction of carbon dioxide to methanol at $CuInS_2$ thin film photocathode,” *Solar Energy Materials and Solar Cells*, vol. 108, pp. 170–174, 2013.

[38] J. Yuan and Y. Wang, “Photoelectrochemical reduction of carbon dioxide to methanol at $CuS/CuO/CuInS_2$ thin film photocathodes,” *Journal of The Electrochemical Society*, vol. 164, no. 13, pp. E475–E479, 2017.

[39] M. Halmann, “Photoelectrochemical reduction of aqueous carbon dioxide on p-type gallium phosphide in liquid junction solar cells,” *Nature*, vol. 275, pp. 115–116, 1978.

[40] T. Inoue, A. Fujishima, S. Konishi, and K. Honda, “Photoelectrocatalytic reduction of carbon dioxide in aqueous suspensions of semiconductor powders,” *Nature*, vol. 277, no. 5698, pp. 637–638, 1979.

[41] D. Canfield and K. Frese Jr, “Reduction of carbon dioxide to methanol on n- and p-GaAs and p-InP. effect of crystal face, electrolyte and current density,” *Journal of the Electrochemical Society*, vol. 130, no. 8, pp. 1772–1773, 1983.

[42] K. W. Frese and D. Canfield, “Reduction of CO_2 on n-GaAs electrodes and selective methanol synthesis,” *Journal of The Electrochemical Society*, vol. 131, no. 11, pp. 2518–2522, 1984.

[43] W. M. Sears and S. R. Morrison, “Carbon dioxide reduction on gallium arsenide electrodes,” *The Journal of Physical Chemistry*, vol. 89, no. 15, pp. 3295–3298, 1985.

[44] R. Memming and G. Schwandt, “Electrochemical properties of gallium phosphide in aqueous solutions,” *Electrochimica Acta*, vol. 13, no. 6, pp. 1299–1310, 1968.

[45] K. Frese, M. Madou, and S. Morrison, “Investigation of photoelectrochemical corrosion of semiconductors. 1,” *The Journal of Physical Chemistry*, vol. 84, no. 24, pp. 3172–3178, 1980.

[46] K. Yasukouchi, I. Taniguchi, H. Yamaguchi, and M. Shiraishi, “Cathodic reduction of pyridinium ion in acetonitrile,” *Journal of Electroanalytical Chemistry and Interfacial Electrochemistry*, vol. 105, no. 2, pp. 403–408, 1979.

[47] S. Jakob, *The n-Si (111):H Surface in contact with an Aqueous Electrolyte: Surface States, Electrochemical Charge Transfer, and Nanoscale Structuring.* PhD thesis, Technical University Munich Physics Department, 2013.

[48] X. G. Zhang, *Electrochemistry of silicon and its oxides.* Kluwer Academic, 2001.

[49] M. Hugelmann, *Erzeugung und Charakterisierung metallischer Nanostrukturen auf n-Si (111): H-Einkristalloberflächen.* PhD thesis, 2004.

[50] L. Junfu and C. Baozhu, “Photoelectrochemical reduction of carbon dioxide on a p^+/p^-Si photocathode in aqueous electrolyte,” *Journal of Electroanalytical Chemistry*, vol. 324, no. 1-2, pp. 191–200, 1992.

[51] K. Hirota, D. A. Tryk, T. Yamamoto, K. Hashimoto, M. Okawa, and A. Fujishima, “Photoelectrochemical reduction of CO_2 in a high-pressure CO_2+methanol medium at p-type semiconductor electrodes,” *The Journal of Physical Chemistry B*, vol. 102, no. 49, pp. 9834–9843, 1998.

[52] Y. Nakamura, R. Hinogami, S. Yae, and Y. Nakato, “Photoelectrochemical reduction of CO_2 at a metal-particle modified p-Si electrode in non-aqueous solutions,” in *Studies in Surface Science and Catalysis*, vol. 114, pp. 565–568, Elsevier, 1998.

[53] R. Hinogami, Y. Nakamura, S. Yae, and Y. Nakato, “An Approach to Ideal Semiconductor Electrodes for Efficient Photoelectrochemical Reduction of Carbon Dioxide by Modification with Small Metal Particles,” *J. Phys. Chem. B*, vol. 102, pp. 974–980, 1998.

[54] W. Shockley and H. J. Queisser, “Detailed balance limit of efficiency of pn junction solar cells,” *Journal of Applied Physics*, vol. 32, no. 3, pp. 510–519, 1961.

[55] S. Rühle, “Tabulated values of the Shockley–Queisser limit for single junction solar cells,” *Solar Energy*, vol. 130, pp. 139–147, 2016.

[56] S. Kirner, P. Bogdanoff, B. Stannowski, R. van de Krol, B. Rech, and R. Schlatmann, “Architectures for scalable integrated photo driven catalytic devices - a concept study,” *International Journal of Hydrogen Energy*, vol. 41, no. 45, pp. 20823–20831, 2016.

[57] F. Urbain, J.-P. Becker, V. Smirnov, J. Ziegler, F. Yang, B. Kaiser, W. Jaegermann, S. Hoch, A. Maljusch, U. Rau, *et al.*, “Influence of the operating temperature on the performance of silicon based photoelectrochemical devices for water splitting,” *Materials science in semiconductor processing*, vol. 42, pp. 142–146, 2016.

[58] J. M. Buriak, “Organometallic Chemistry on Silicon and Germanium Surfaces,” *Chem. Rev.*, vol. 102, no. 5, pp. 1272–1306, 2002.

[59] I. Grill Master’s thesis, Technical University Munich Physics Department, 2012. Bachelor Thesis.

[60] S. Schwaminger, “Immobilization of pyridine derivates on surfaces for the photocatalytic CO_2 activation,” Master’s thesis, Technical University Munich Chemistry Department, 2013.

[61] Y. Liu, S. Yamazaki, S. Yamabe, and Y. Nakato, “A mild and efficient Si (111) surface modification via hydrosilylation of activated alkynes,” *Journal of Materials Chemistry*, vol. 15, no. 46, pp. 4906–4913, 2005.

[62] C. Galli, “Radical reactions of arenediazonium ions: an easy entry into the chemistry of the aryl radical,” *Chemical Reviews*, vol. 88, no. 5, pp. 765–792, 1988.

[63] J. Pinson and F. Podvorica, "Attachment of organic layers to conductive or semiconductive surfaces by reduction of diazonium salts," *Chemical Society Reviews*, vol. 34, no. 5, pp. 429–439, 2005.

[64] P. Allongue, C. H. de Villeneuve, G. Cherouvrier, R. Cortes, and M.-C. Bernard, "Phenyl layers on H-Si(111) by electrochemical reduction of diazonium salts: monolayer versus multilayer formation," *J. Electroanal. Chem*, vol. 550-551, p. 161, 2003.

[65] C. H. de Villeneuve, J. Pinson, F. Ozanam, J. N. Chazalviel, and P. Allongue, "Molecular grafting on Si (111) surfaces: An electrochemical approach," *MRS Online Proceedings Library Archive*, vol. 451, 1996.

[66] C. H. de Villeneuve, J. Pinson, M. C. Bernard, and P. Allongue, "Electrochemical Formation of Close-Packed Phenyl Layers on Si(111)," *J. Phys. Chem. B*, vol. 101, p. 2415, 1997.

[67] P. Allongue, C. H. De Villeneuve, J. Pinson, F. Ozanam, J. Chazalviel, and X. Wallart, "Organic monolayers on Si (111) by electrochemical method," *Electrochimica Acta*, vol. 43, no. 19-20, pp. 2791–2798, 1998.

[68] S. Lindner, "Functionalization of silicon surfaces for artificial photosynthesis," Master's thesis, Technical University Munich Physics Department, 2013. Bachelor Thesis.

[69] A. Tosolini, "Electrochemical modification of silicon surfaces for the production of solar fuels," Master's thesis, Technical University Munich Physics Department, 2014. Bachelor Thesis.

[70] M. Windscheid, "Investigation of structure and catalytic activity of organic monolayers on single crystalline silicon for artificial photosynthesis," Master's thesis, Technical University Munich Physics Department, 2014. Bachelor Thesis.

[71] W. Schmickler, *Interfacial Electrochemistry.* Oxford University Press, Inc., 1996.

[72] A. J. Bard and L. R. Faulkner, *Electrochamical Methods - Fundamentals and Applications.* John Wiley & Sons, Inc., 2001.

[73] S. Trasatti, "The absolute electrode potential: an explanatory note," *Pure & Appl. Chem.*, vol. 58/7, p. 955, 1986.

[74] J. O. Bockris, A. K. N. Reddy, and M. Gamboa-Aldeco, *Modern aspects of electrochemistry*, vol. 2A. Kluwer Academic / Plenum Publishers, New York, 2000.

[75] J. S. Duncan, *Introduction to colloid and surface chemistry.* Butterworth-Heinemann Ltd, 4 ed., 1992.

[76] M. A. Brown, A. Goel, and Z. Abbas, "Effect of electrolyte concentration on the stern layer thickness at a charged interface," *Angewandte Chemie International Edition*, vol. 55, no. 11, pp. 3790–3794, 2016.

[77] P. Würfel and U. Würfel, *Physics of solar cells: from basic principles to advanced concepts.* John Wiley & Sons, 2009.

[78] A. Natarajan, G. Oskam, and P. C. Searson, “The potential distribution at the semiconductor/solution interface,” *The Journal of Physical Chemistry B*, vol. 102, no. 40, pp. 7793–7799, 1998.

[79] G. E. Mullenberg, ed., *Handbook of X-ray Photoelectron Spectroscopy.* Perkin-Elmer Corp., 1992.

[80] P. van der Heide, *X-ray Photoelectron Spectroscopy: An introduction to Principles and Practices.* Wiley, 2011.

[81] M. Daimer, “An electrochemical study of the pyridine catalyzed CO_2 reduction on platinum electrodes,” master’s thesis, Technische Universität München, Physik-Department, E19a, Nonequilibrium Chemical Physics, 2015.

[82] H. M. McNair and J. M. Miller, *Basic gas chromatography.* John Wiley & Sons, 2011.

[83] Calculation of Chromatographic Resolution, https://tinyurl.com/ya9b3qv5

[84] K. Shinada, S. Horiike, S. Uchiyama, R. Takechi, and T. Nishimoto, “Development of new ionization detector for gas chromatography by applying dielectric barrier discharge,” *Shimadzu Hyoron*, vol. 69, pp. 255–263, 2012.

[85] S. Kanazawa, M. Kogoma, T. Moriwaki, and S. Okazaki, “Stable glow plasma at atmospheric pressure,” *Journal of Physics D: Applied Physics*, vol. 21, no. 5, p. 838, 1988.

[86] J. J. Hopfield, “Absorption and emission spectra in the region λ 600- 1100,” *Physical Review*, vol. 35, no. 9, p. 1133, 1930.

[87] J. W. Akitt and B. E. Mann, *NMR and Chemistry: An introduction to modern NMR spectroscopy.* Crc Press, 2000.

[88] H. Günther, *NMR spectroscopy: basic principles, concepts and applications in chemistry.* John Wiley & Sons, 2013.

[89] W. Demtröder, *Experimentalphysik 4.* Springer, 1998.

[90] Beispiel zur Fourier-Transformation, https://tinyurl.com/y9jbuhjm

[91] P. Giraudeau, V. Silvestre, and S. Akoka, “Optimizing water suppression for quantitative NMR-based metabolomics: a tutorial review,” *Metabolomics*, vol. 11, no. 5, pp. 1041–1055, 2015.

[92] R. T. Mckay, “How the 1D-NOESY suppresses solvent signal in metabonomics NMR spectroscopy: An examination of the pulse sequence components and evolution,” *Concepts in Magnetic Resonance Part A*, vol. 38, no. 5, pp. 197–220, 2011.

[93] P. Allongue, C. H. de Villeneuve, S. Morin, R. Boukherroub, and D. D. M. Wayner, "The preparation of flat Si(111) surfaces in 40% NH_4F revisited," *Electrochim. Acta*, vol. 45, p. 4591, 2000.

[94] M. L. Munford, R. Cortes, and P. Allongue, "The preparation of ideally ordered flat H-Si (111) surfaces," *Sensors and Materials(Japan)*, vol. 13, no. 5, pp. 259–269, 2001.

[95] T. Nagai, A. Imanishi, and Y. Nakato, "Scratch induced nano-wires acting as a macro-pattern for formation of well-ordered step structures on H-terminated Si (1 1 1) by chemical etching," *Applied surface science*, vol. 237, no. 1-4, pp. 533–537, 2004.

[96] G. Higashi, Y. Chabal, G. Trucks, and K. Raghavachari, "Ideal hydrogen termination of the Si (111) surface," *Applied physics letters*, vol. 56, no. 7, pp. 656–658, 1990.

[97] S. Watanabe, K. Horiuchi, and T. Ito, "Atomic step structure on vicinal HSi (111) surface formed by hot water immersion," *Japanese journal of applied physics*, vol. 32, no. 8R, p. 3420, 1993.

[98] P. Allongue, V. Kieling, and H. Gerischer, "Etching mechanism and atomic structure of H-Si (111) surfaces prepared in NH_4F," *Electrochimica Acta*, vol. 40, no. 10, pp. 1353–1360, 1995.

[99] S.-E. Bae, M.-K. Oh, N.-K. Min, S.-H. Paek, S.-I. Hong, and C.-W. J. Lee, "Preparation of atomically flat Si (111)-H surfaces in aqueous ammonium fluoride solutions investigated by using electrochemical, in situ EC-STM and ATR-FTIR spectroscopic methods," *Bulletin of the Korean Chemical Society*, vol. 25, no. 12, pp. 1822–1828, 2004.

[100] P. Jakob and Y. Chabal, "Chemical etching of vicinal Si (111): Dependence of the surface structure and the hydrogen termination on the pH of the etching solutions," *The Journal of Chemical Physics*, vol. 95, no. 4, pp. 2897–2909, 1991.

[101] H. Hessel, A. Feltz, M. Reiter, U. Memmert, and R. Behm, "Step-flow mechanism versus pit corrosion: scanning-tunneling microscopy observations on wet etching of Si (111) by HF solutions," *Chemical physics letters*, vol. 186, no. 2-3, pp. 275–280, 1991.

[102] F. Casablanca, "Functionalization of the n-Si(111):H surface with pyridine molecules: a voltammetric and electrochemical scanning tunneling microscopy study," Master's thesis, Technische Universität München, Physik-Department, E19a, Nonequilibrium Chemical Physics, 2017.

[103] C. P. Wade and C. E. D. Chidsey, "Etch-pit initiation by dissolved oxygen on terraces of H-Si(111)," *Appl. Phys. Lett.*, vol. 71, p. 1679, 1997.

[104] S. Doniach and M. Sunjic, "Many-electron singularity in X-ray photoemission and X-ray line spectra from metals," *Journal of Physics C: Solid State Physics*, vol. 3, no. 2, p. 285, 1970.

[105] A. Bandarenka and G. A. Ragoisha, *Progress in Chemometrics Research.* Nova Science Publishers, New York, 2005.

[106] T. L. Maier, “Characterization of gold/copper nanostructures on silicon electrodes for applications in photoelectrochemical CO_2 conversion,” master’s thesis, Technische Universität München, Physik-Department, E19a, Nonequilibrium Chemical Physics, 2017.

[107] M. Delamar, R. Hitmi, J. Pinson, and J.-M. Saveant, “Covalent modification of carbon surfaces by grafting of functionalized aryl radicals produced from electrochemical reduction of diazonium salts,” *Journal of the American Chemical Society*, vol. 114, no. 14, pp. 5883–5884, 1992.

[108] C. Bourdillon, M. Delamar, C. Demaille, R. Hitmi, J. Moiroux, and J. Pinson, “Immobilization of glucose oxidase on a carbon surface derivatized by electrochemical reduction of diazonium salts,” *Journal of Electroanalytical Chemistry*, vol. 336, no. 1-2, pp. 113–123, 1992.

[109] P. Allongue, M. Delamar, B. Desbat, O. Fagebaume, R. Hitmi, J. Pinson, and J.-M. Savéant, “Covalent modification of carbon surfaces by aryl radicals generated from the electrochemical reduction of diazonium salts,” *Journal of the American Chemical Society*, vol. 119, no. 1, pp. 201–207, 1997.

[110] R. N. Butler, “The Diazotozation of Heterocyclic Primary Amines,” *Chem. Rev.*, vol. 75, no. 2, pp. 241–257, 1975.

[111] J. Agullo, S. Canesi, F. Schaper, M. Morin, and D. Bélanger, “Formation and reactivity of 3-diazopyridinium cations and influence on their reductive electrografting on glassy carbon,” *Langmuir*, vol. 28, p. 4889, 2012.

[112] E. Kalatzis, “Reactions of N-Heteroaromatic Bases with Nitrous Acid. Part 1. Diazotisation and Nitrosation of α- and γ-Amino-derivatives in Dilute Acid Solutions,” *J. Chem. Soc. (B)*, pp. 273–277, 1967.

[113] J. Agullo, M. Morin, and D. Bélanger, “Modification of glassy carbon electrode by electrografting of in situ generated 3-diazopyridinium cations,” *J. Electrochem. Soc.*, vol. 159/9, p. 758, 2012.

[114] C. Combellas, F. Kanoufi, J. Pinson, and F. I. Podvorica, “Time-of-flight secondary ion mass spectroscopy characterization of the covalent bonding between a carbon surface and aryl groups,” *Langmuir*, vol. 21, no. 1, pp. 280–286, 2005.

[115] J. Genders, D. Hartsough, and D. Hobbs, “Electrochemical reduction of nitrates and nitrites in alkaline nuclear waste solutions,” *Journal of applied electrochemistry*, vol. 26, no. 1, pp. 1–9, 1996.

[116] M. Barber, J. Connor, M. Guest, I. Hillier, M. Schwarz, and M. Stacey, “Bonding in some donor–acceptor complexes involving boron trifluoride. study by means of ESCA and molecular orbital calculations,” *Journal of the Chemical Society, Faraday Transactions 2: Molecular and Chemical Physics*, vol. 69, pp. 551–558, 1973.

[117] S. Baranton and D. Bélanger, “In situ generation of diazonium cations in organic electrolyte for electrochemical modification of electrode surface,” *Electrochimica Acta*, vol. 53, no. 23, pp. 6961–6967, 2008.

[118] A. Yeşildağ and D. Kekinci, “Covalent attachment of pyridine-type molecules to glassy carbon surfaces by electrochemical reduction of in situ generated diazonium salts. Formation of ruthenium complexes on ligand-modified surfaces,” *Electochim. Acta*, vol. 55, pp. 7000–7009, 2010.

[119] F. Himpsel, G. Hollinger, and R. Pollak, “Determination of the Fermi-level pinning position at Si (111) surfaces,” *Physical Review B*, vol. 28, no. 12, p. 7014, 1983.

[120] T. Cottineau, M. Morin, and D. Bélanger, “Surface band structure of aryldiazonium modified p-Si electrodes determined by X-ray photoelectron spectroscopy and electrochemical measurements,” *RSC Advances*, vol. 3, no. 45, pp. 23649–23657, 2013.

[121] X. Wallart, C. H. de Villeneuve, and P. Allongue, “Truly quantitative XPS characterization of organic monolayers on silicon: Study of alkyl and alkoxy monolayers on H-Si (111),” *J. Am. Chem. Soc.*, vol. 127(21), p. 7871, 2005.

[122] R. Hunger, W. Jaegermann, A. Merson, Y. Shapira, C. Pettenkofer, and J. Rappich, “Electronic structure of methoxy-, bromo-, and nitrobenzene grafted onto Si (111),” *The Journal of Physical Chemistry B*, vol. 110, no. 31, pp. 15432–15441, 2006.

[123] P. Sherwood, *Auger and X-ray photoelectron spectroscopy*, vol. 1. Chichester, England, 1990.

[124] S. Tanuma, C. J. Powell, and D. R. Penn, “Calculations of electron inelastic mean free paths. V. data for 14 organic compounds over the 50–2000 eV range,” *Surface and Interface Analysis*, vol. 21, no. 3, pp. 165–176, 1994.

[125] C. J. Powell and A. Jablonski, “NIST electron inelastic-mean-free-path database 71, version 1.0,” tech. rep., 1999.

[126] P. Hugelmann and W. Schindler, “In-situ voltage tunneling spectroscopy at electrochemical interfaces,” *The Journal of Physical Chemistry B*, vol. 109, no. 13, pp. 6262–6267, 2005.

[127] T. Koop, W. Schindler, A. Kazimirov, G. Scherb, J. Zegenhagen, T. Schulz, R. Feidenhans’l, and J. Kirschner, “Electrochemical cell for in situ X-ray diffraction under ultrapure conditions,” *Review of scientific instruments*, vol. 69, no. 4, pp. 1840–1843, 1998.

[128] K. Jüttner, “Oxygen reduction electrocatalysis by underpotential deposited metal atoms at different single crystal faces of gold and silver,” *Electrochimica Acta*, vol. 29, no. 11, pp. 1597–1604, 1984.

[129] T. Menanteau, E. Levillain, and T. Breton, “Electrografting via diazonium chemistry: from multilayer to monolayer using radical scavenger,” *Chemistry of Materials*, vol. 25, no. 14, pp. 2905–2909, 2013.

[130] T. Menanteau, E. Levillain, and T. Breton, “Spontaneous grafting of nitrophenyl groups on carbon: effect of radical scavenger on organic layer formation,” *Langmuir*, vol. 30, no. 26, pp. 7913–7918, 2014.

[131] T. Menanteau, E. Levillain, A. J. Downard, and T. Breton, “Evidence of monolayer formation via diazonium grafting with a radical scavenger: electrochemical, AFM and XPS monitoring,” *Physical Chemistry Chemical Physics*, vol. 17, no. 19, pp. 13137–13142, 2015.

[132] T. He, H. Ding, N. Peor, M. Lu, D. Corley, B. Chen, Y. Ofir, Y. Gao, S. Yitzchaik, and J. Tour, “Silicon/molecule interfacial electronic modifications,” *Journal of the American Chemical Society*, vol. 130, no. 5, pp. 1699–1710, 2008.

[133] D. C. Gleason-Rohrer, B. S. Brunschwig, and N. S. Lewis, “Measurement of the band bending and surface dipole at chemically functionalized Si (111)/vacuum interfaces,” *The Journal of Physical Chemistry C*, vol. 117, no. 35, pp. 18031–18042, 2013.

[134] Q. Li, K. Schönleber, P. Zeller, I. Höhlein, B. Rieger, J. Wintterlin, and K. Krischer, “Activation of silicon surfaces for H_2 evolution by electrografting of pyridine molecules,” *Surface Science*, vol. 631, pp. 185–189, 2015.

[135] R. M. Candea, M. Kastner, R. Goodman, and N. Hickok, “Photoelectrolysis of water: Si in salt water,” *Journal of Applied Physics*, vol. 47, no. 6, pp. 2724–2726, 1976.

[136] V. Bertagna, C. Plougonven, F. Rouelle, and M. Chemla, “p-and n-type silicon electrochemical properties in dilute hydrofluoric acid solutions,” *Journal of the Electrochemical Society*, vol. 143, no. 11, pp. 3532–3538, 1996.

[137] V. Bertagna, F. Rouelle, G. Revel, and M. Chemla, “Electrochemical and radiochemical study of copper contamination mechanism from HF solutions onto silicon substrates,” *Journal of The Electrochemical Society*, vol. 144, no. 12, pp. 4175–4182, 1997.

[138] R. N. Dominey, N. S. Lewis, J. A. Bruce, D. C. Bookbinder, and M. S. Wrighton, “Improvement of photoelectrochemical hydrogen generation by surface modification of p-type silicon semiconductor photocathodes,” *Journal of the American Chemical Society*, vol. 104, no. 2, pp. 467–482, 1982.

[139] Y. Nakato, T. Ohnishi, and H. Tsubomura, “Photo-electrochemical behaviors of semiconductor electrodes coated with thin metal films,” *Chemistry Letters*, vol. 4, no. 8, pp. 883–886, 1975.

[140] Y. Nakato, S. Tonomura, and H. Tsubomura, “The catalytic effect of electrodeposited metals on the photo-reduction of water at p-type semiconductors,” *Berichte der Bunsengesellschaft für physikalische Chemie*, vol. 80, no. 12, pp. 1289–1293, 1976.

[141] M. Szklarczyk and J. O. Bockris, "Photoelectrocatalysis and electrocatalysis on p-silicon," *The Journal of Physical Chemistry*, vol. 88, no. 9, pp. 1808–1815, 1984.

[142] Y. Nakato, Y. Egi, M. Hiramoto, and H. Tsubomura, "Hydrogen evolution and iodine reduction on an illuminated np junction silicon electrode and its application to efficient solar photoelectrolysis of hydrogen iodide," *The Journal of Physical Chemistry*, vol. 88, no. 19, pp. 4218–4222, 1984.

[143] Y. Nakato, H. Yano, S. Nishiura, T. Ueda, and H. Tsubomura, "Hydrogen photoevolution at p-type silicon electrodes coated with discontinous metal layers," *J. Electroanal. Chem.*, vol. 228, pp. 97–108, 1987.

[144] K. H. Yoon, D. K. Seo, Y. S. Cho, and D. H. Kang, "Effect of Pt layers on the photoelectrochemical properties of a WO_3/p-Si electrode," *Journal of applied physics*, vol. 84, no. 7, pp. 3954–3959, 1998.

[145] K.-Q. Peng, X. Wang, X.-L. Wu, and S.-T. Lee, "Platinum nanoparticle decorated silicon nanowires for efficient solar energy conversion," *Nano Letters*, vol. 9, no. 11, pp. 3704–3709, 2009.

[146] X. Lu, T. Minegishi, , and J. K. Kazunari Domen, "Improvement of photoelectrochemical properties by surface modification with iron oxide on p-type Si electrodes for hydrogen evolution from water," *Japanese Journal of Applied Physics*, vol. 50, no. 8R, p. 085702, 2011.

[147] J. R. McKone, E. L. Warren, M. J. Bierman, S. W. Boettcher, B. S. Brunschwig, N. S. Lewis, and H. B. Gray, "Evaluation of Pt, Ni, and Ni–Mo electrocatalysts for hydrogen evolution on crystalline Si electrodes," *Energy Environ. Sci.*, vol. 4, pp. 3573–3583, 2011.

[148] J. Kye, M. Shin, B. Lim, J. Jang, I. Oh, and S. Hwang, "Platinum monolayer electrocatalyst on gold nanostructures on silicon for photoelectrochemical hydrogen evolution," *ACS nano*, vol. 7, no. 7, pp. 6017–6023, 2013.

[149] P. Dai, J. Xie, M. T. Mayer, X. Yang, J. Zhan, and D. Wang, "Solar hydrogen generation by silicon nanowires modified with platinum nanoparticle catalysts by atomic layer deposition," *Angewandte Chemie*, vol. 125, no. 42, pp. 11325–11329, 2013.

[150] M. Metzler, A. Thorwart, S. Zeller, T. Diemant, R. Behm, and T. Jacob, "Electroless deposition of Au/Pt/Pd nanoparticles on p-Si(111) for the light-induced hydrogen evolution reaction," *Catalysis Today*, vol. 244, pp. 3 – 9, 2015.

[151] T. Masuda, H. Fukumitsu, S. Takakusagi, W. Chun, T. Kondo, K. Asakura, and K. Uosaki, "Molecular catalysts confined on and within molecular layers formed on a Si (111) surface with direct Si–C bonds," *Advanced Materials*, vol. 24, no. 2, pp. 268–272, 2012.

[152] W. Gissler and A. McEvoy, "Photoelectrochemical effects on p-silicon of ruthenium dioxide thin films," *Solar energy materials*, vol. 10, no. 3-4, pp. 309–316, 1984.

[153] B. Keita and L. Nadjo, “Activation of electrode surface: Electrocatalysis of the photoelectrochemical generation of hydrogen at p-type Si,” *Journal of electroanalytical chemistry and interfacial electrochemistry*, vol. 199, no. 1, pp. 229–237, 1986.

[154] T. Masuda, K. Shimazu, and K. Uosaki, “Construction of Mono- and Multimolecular Layers with Electron Transfer Mediation Function and Catalytic Activity for Hydrogen Evolution on a Hydrogen-Terminated Si(111) Surface via Si-C Bond,” *J. Phys. Chem. C*, vol. 112, pp. 10923–10930, 2008.

[155] Y. Hou, B. L. Abrams, P. C. Vesborg, M. E. Björketun, K. Herbst, L. Bech, A. M. Setti, C. Damsgaard, T. Pedersen, O. Hansen, *et al.*, “Bioinspired molecular cocatalysts bonded to a silicon photocathode for solar hydrogen evolution,” *Nature materials*, vol. 10, no. 6, p. 434, 2011.

[156] S. P. Berglund, H. He, W. D. Chemelewski, H. Celio, A. Dolocan, and C. B. Mullins, “p-Si/W_2C and p-Si/W_2C/Pt photocathodes for the hydrogen evolution reaction,” *Journal of the American Chemical Society*, vol. 136, no. 4, pp. 1535–1544, 2014.

[157] Y.-H. Lai, H. Park, J. Zhang, P. Matthews, D. Wright, and E. Reisner, “A Si photocathode protected and activated with a Ti and Ni composite film for solar hydrogen production,” *Chemistry–A European Journal*, vol. 21, no. 10, pp. 3919–3923, 2015.

[158] C.-Y. Lee, H. S. Park, J. C. Fontecilla-Camps, and E. Reisner, “Photoelectrochemical H_2 evolution with a hydrogenase immobilized on a TiO_2-protected silicon electrode,” *Angewandte Chemie International Edition*, vol. 55, no. 20, pp. 5971–5974, 2016.

[159] J. J. Leung, J. Warnan, D. H. Nam, J. Z. Zhang, J. Willkomm, and E. Reisner, “Photoelectrocatalytic H_2 evolution in water with molecular catalysts immobilised on p-Si via a stabilising mesoporous TiO_2 interlayer,” *Chemical science*, vol. 8, no. 7, pp. 5172–5180, 2017.

[160] L. Zhao, J.H.and Cai, H. Li, X. Shi, and X. Zheng, “Stabilizing silicon photocathodes by solution-deposited Ni–Fe layered double hydroxide for efficient hydrogen evolution in alkaline media,” *ACS Energy Letters*, vol. 2, no. 9, pp. 1939–1946, 2017.

[161] W. Zhou, F. Niu, S. S. Mao, and S. Shen, “Nickel complex engineered interface energetics for efficient photoelectrochemical hydrogen evolution over p-Si,” *Applied Catalysis B: Environmental*, vol. 220, pp. 362–366, 2018.

[162] P. Allongue, C. H. de Villeneuve, and J. Pinson, “Structural characterization of organic monolayers on Si$< 111 >$ from capacitance measurements,” *Electrochimica acta*, vol. 45, no. 20, pp. 3241–3248, 2000.

[163] W. Turner and P. Elving, “Electrooxidation in pyridine at pyrolytic graphite electrode.,” *Analytical Chemistry*, vol. 37, no. 4, pp. 467–469, 1965.

[164] O. J. Glembocki, R. E. Stahlbush, and M. Tomkiewicz, “Bias-dependent etching of silicon in aqueous KOH,” *Journal of the Electrochemical Society*, vol. 132, no. 1, pp. 145–151, 1985.

[165] H.-Z. Yu, S. Morin, D. D. Wayner, P. Allongue, and C. de Villeneuve, “Molecularly tunable “organic capacitors” at silicon/aqueous electrolyte interfaces,” *The Journal of Physical Chemistry B*, vol. 104, no. 47, pp. 11157–11161, 2000.

[166] C. Saby, B. Ortiz, G. Y. Champagne, and D. Bélanger, “Electrochemical modification of glassy carbon electrode using aromatic diazonium salts. 1. blocking effect of 4-nitrophenyl and 4-carboxyphenyl groups,” *Langmuir*, vol. 13, no. 25, pp. 6805–6813, 1997.

[167] P. Gorostiza, C. de Villeneuve, Q. Sun, F. Sanz, X. Wallart, R. Boukherroub, and P. Allongue, “Water exclusion at the nanometer scale provides long-term passivation of silicon (111) grafted with alkyl monolayers,” *The Journal of Physical Chemistry B*, vol. 110, no. 11, pp. 5576–5585, 2006.

[168] A. Faucheux, A. Gouget-Laemmel, C. de Villeneuve, R. Boukherroub, F. Ozanam, P. Allongue, and J.-N. Chazalviel, “Well-defined carboxyl-terminated alkyl monolayers grafted onto H- Si (111): packing density from a combined AFM and quantitative IR study,” *Langmuir*, vol. 22, no. 1, pp. 153–162, 2006.

[169] A. Reitzle, F. Renner, T. Lee, J. Zegenhagen, and D. Kolb, “Electrochemical growth of copper on well-defined n-Si (1 1 1): H surfaces,” *Surface science*, vol. 576, no. 1-3, pp. 19–28, 2005.

[170] R. Krumm, B. Guel, C. Schmitz, and G. Staikov, “Nucleation and growth in electrodeposition of metals on n-Si (111),” *Electrochimica acta*, vol. 45, no. 20, pp. 3255–3262, 2000.

[171] G. Schlichthörl and L. Peter, “Deconvolution of the impedance of the silicon/electrolyte interface by potential-modulated-microwave measurements,” *Journal of the Electrochemical Society*, vol. 141, no. 12, pp. L171–L173, 1994.

[172] M. Madou, B. Loo, K. Frese, and S. R. Morrison, “Bulk and surface characterization of the silicon electrode,” *Surface Science*, vol. 108, no. 1, pp. 135–152, 1981.

[173] G. Li, E. Kneer, B. Vermeire, H. Parks, S. Raghavan, and J. Jeon, “A comparative electrochemical study of copper deposition onto silicon from dilute and buffered hydrofluoric acids,” *Journal of The Electrochemical Society*, vol. 145, no. 1, pp. 241–246, 1998.

[174] P. Hartig, T. Dittrich, and J. Rappich, “Surface dipole formation and nonradiative recombination at p-Si (111) surfaces during electrochemical deposition of organic layers,” *Journal of Electroanalytical Chemistry*, vol. 524, pp. 120–126, 2002.

[175] V. Bertagna, R. Erre, F. Rouelle, and M. Chemla, “Ionic components dependence of the charge transfer reactions at the silicon/HF solution interface,” *Journal of Solid State Electrochemistry*, vol. 4, no. 1, pp. 42–51, 1999.

[176] F. Bensliman, M. Aggour, A. Ennaoui, and M. Matsumura, “Electrochemical method for evaluation of structural perfection of hydrogen-terminated Si (111) surface,” *Japanese Journal of Applied Physics*, vol. 39, no. 12A, p. L1206, 2000.

[177] S. M. Sze and K. K. Ng, *Physics of semiconductor devices.* John wiley & sons, 2006.

[178] P. Allongue, J.-N. Chazalviel, C. Henry de Villeneuve, and F. Ozanam, “Analysis of capacitance potential measurements at the silicon- electrolyte interface revisited,” *The Journal of Physical Chemistry C*, vol. 111, no. 14, pp. 5497–5499, 2007.

[179] T. P. Silverstein, “The aqueous proton is hydrated by more than one water molecule: Is the hydronium ion a useful conceit?,” *Journal of Chemical Education*, vol. 91, no. 4, pp. 608–610, 2014.

[180] E. S. Stoyanov, I. V. Stoyanova, and C. A. Reed, “The structure of the hydrogen ion (H^+_{aq}) in water,” *Journal of the American Chemical Society*, vol. 132, no. 5, pp. 1484–1485, 2010.

[181] R. Rampolla, R. Miller, and C. Smyth, “Microwave absorption and molecular structure in liquids. XXV. measurements of dielectric constant and loss at 3.1-mm wavelength by an interferometric method,” *The Journal of Chemical Physics*, vol. 30, no. 2, pp. 566–573, 1959.

[182] J. R. Macdonald and C. A. Barlow Jr, “Theory of double-layer differential capacitance in electrolytes,” *The Journal of Chemical Physics*, vol. 36, no. 11, pp. 3062–3080, 1962.

[183] M. Tuckerman, K. Laasonen, M. Sprik, and M. Parrinello, “Ab initio molecular dynamics simulation of the solvation and transport of hydronium and hydroxyl ions in water,” *The Journal of chemical physics*, vol. 103, no. 1, pp. 150–161, 1995.

[184] F. Booth, “The dielectric constant of water and the saturation effect,” *The Journal of Chemical Physics*, vol. 19, no. 4, pp. 391–394, 1951.

[185] F. Booth, “Dielectric constant of polar liquids at high field strengths,” *The Journal of Chemical Physics*, vol. 23, no. 3, pp. 453–457, 1955.

[186] H. Wang and L. Pilon, “Accurate simulations of electric double layer capacitance of ultramicroelectrodes,” *The Journal of Physical Chemistry C*, vol. 115, no. 33, pp. 16711–16719, 2011.

[187] M. Anderson, M. Evaniak, and M. Zhang, “Influence of solvent on the interfacial structure of self-assembled alkanethiol monolayers,” *Langmuir*, vol. 12, no. 10, pp. 2327–2331, 1996.

[188] M. Porter, T. Bright, D. Allara, and C. Chidsey, “Spontaneously organized molecular assemblies. 4. structural characterization of n-alkyl thiol monolayers on gold by optical ellipsometry, infrared spectroscopy, and electrochemistry,” *Journal of the American Chemical Society*, vol. 109, no. 12, pp. 3559–3568, 1987.

[189] S. Jakob and W. Schindler, “Surface states of wet chemically etched n-Si (1 1 1): H surfaces,” *Electrochimica Acta*, vol. 88, pp. 659–663, 2013.

[190] P. Hoffmann, G. Oskam, and P. Searson, “Analysis of the impedance response due to surface states at the semiconductor/solution interface,” *Journal of applied physics*, vol. 83, no. 8, pp. 4309–4323, 1998.

[191] X. Bin, T. K. Mischki, C. Fan, G. Lopinski, and D. Wayner, “Electrochemical characterization of Si (111) modified with linear and branched alkyl chains,” *The Journal of Physical Chemistry C*, vol. 111, no. 36, pp. 13547–13553, 2007.

[192] A. Natarajan, G. Oskam, and P. C. Searson, “Characterization of silicon surfaces in HF solution using microwave reflectivity,” *Journal of applied physics*, vol. 83, no. 4, pp. 2112–2120, 1998.

[193] J.-N. Chazalviel, “Electrochemical transfer via surface states: a new formulation for the semiconductor/electrolyte interface,” *Journal of The Electrochemical Society*, vol. 129, no. 5, pp. 963–969, 1982.

[194] V. Lanza and D. Herrmann, “The density dependence of the dielectric constant of polyethylene,” *Journal of Polymer Science*, vol. 28, no. 118, pp. 622–625, 1958.

[195] D. Aspnes, “Optical properties of thin films,” *Thin solid films*, vol. 89, no. 3, pp. 249–262, 1982.

[196] D. Bruggeman, “Berechnung verschiedener physikalischer Konstanten von heterogenen Substanzen. II. Dielektrizitätskonstanten und Leitfähigkeiten von Vielkristallen der nichtregulären Systeme,” *Annalen der Physik*, vol. 417, no. 7, pp. 645–672, 1936.

[197] E. Gongadze, U. van Rienen, V. Kralj-Iglič, and A. Iglič, “Langevin Poisson-Boltzmann equation: Point-like ions and water dipoles near a charged surface,” *General physiology and biophysics*, vol. 30, no. 2, p. 130, 2011.

[198] E. Gongadze, U. Rienen, and A. Iglič, “Generalized stern models of the electric double layer considering the spatial variation of permittvity and finite size of ions in saturation regime,” *Cellular & molecular biology letters*, vol. 16, no. 4, p. 576, 2011.

[199] R. Parajuli, J. B. Gerken, K. Keyshar, I. Sullivan, N. Sivasankar, K. Teamey, S. S. Stahl, and E. B. Cole, “Integration of anodic and cathodic catalysts of earth-abundant materials for efficient, scalable CO_2 reduction,” *Topics in Catalysis*, vol. 58, no. 1, pp. 57–66, 2015.

[200] P. De Mierry, A. Etcheberry, R. Rizk, P. Etchegoin, and M. Aucouturier, “Defects induced in p-type silicon by photocathodic charging of hydrogen,” *Journal of The Electrochemical Society*, vol. 141, no. 6, pp. 1539–1546, 1994.

[201] K. Mandal, F. Ozanam, and J.-N. Chazalviel, “In situ infrared evidence for the electrochemical incorporation of hydrogen into Si and Ge,” *Applied physics letters*, vol. 57, no. 26, pp. 2788–2790, 1990.

[202] J. J. Carroll, J. D. Slupsky, and A. E. Mather, “The solubility of carbon dioxide in water at low pressure,” *Journal of Physical and Chemical Reference Data*, vol. 20, no. 6, pp. 1201–1209, 1991.

[203] D. Zhenhao, S. Rui, Z. Chen, and I.-M. Chou, “An improved model for the calculation of CO_2 solubility in aqueous solutions containing Na^+, K^+, Ca^{2+}, Mg^{2+}, Cl^-, and ${SO_4}^{2-}$,” *Marine Chemistry*, vol. 98, no. 2, pp. 131 – 139, 2006.

[204] V. Bagotzky and N. Osetrova, “Investigations of hydrogen ionization on platinum with the help of micro-electrodes,” *Journal of Electroanalytical Chemistry and Interfacial Electrochemistry*, vol. 43, no. 2, pp. 233–249, 1973.

[205] W. Sheng, H. A. Gasteiger, and Y. Shao-Horn, “Hydrogen oxidation and evolution reaction kinetics on platinum: acid vs alkaline electrolytes,” *Journal of The Electrochemical Society*, vol. 157, no. 11, pp. B1529–B1536, 2010.

[206] B. Aurian-Blajeni, I. Taniguchi, and J. Bockris, “Photoelectrochemical reduction of carbon dioxide using polyaniline-coated silicon,” *Journal of Electroanalytical Chemistry and Interfacial Electrochemistry*, vol. 149, no. 1-2, pp. 291–293, 1983.

[207] I. Katsounaros, J. C. Meier, S. O. Klemm, A. A. Topalov, P. U. Biedermann, M. Auinger, and K. J. Mayrhofer, “The effective surface pH during reactions at the solid–liquid interface,” *Electrochemistry COmmunications*, vol. 13, no. 6, pp. 634–637, 2011.

[208] M. Auinger, I. Katsounaros, J. C. Meier, S. O. Klemm, P. U. Biedermann, A. A. Topalov, M. Rohwerder, and K. J. Mayrhofer, “Near-surface ion distribution and buffer effects during electrochemical reactions,” *Physical Chemistry Chemical Physics*, vol. 13, no. 36, pp. 16384–16394, 2011.

[209] P. Allongue, V. Costa-Kieling, and H. Gerischer, “Etching of silicon in NaOH solutions II. electrochemical studies of n-Si (111) and (100) and mechanism of the dissolution,” *Journal of the Electrochemical Society*, vol. 140, no. 4, pp. 1018–1026, 1993.

[210] M. Z. Ertem, S. J. Konezny, C. M. Araujo, and V. S. Batista, “Functional role of pyridinium during aqueous electrochemical reduction of CO_2 on Pt (111),” *The journal of physical chemistry letters*, vol. 4, no. 5, pp. 745–748, 2013.

[211] J. Tossell, “Calculation of the properties of molecules in the pyridine catalyst system for the photochemical conversion of CO_2 to methanol,” *Computational and Theoretical Chemistry*, vol. 977, no. 1-3, pp. 123–127, 2011.

[212] J. A. Keith and E. A. Carter, “Theoretical insight into Pyridinium-based photoelectrocatalytic reduction of CO_2,” *JACS*, vol. 134, p. 7580, 2012.

[213] J. A. Keith and E. A. Carter, “Theoretical insights into electrochemical CO_2 reduction mechanisms catalyzed by surface-bound nitrogen heterocycles,” *The journal of physical chemistry letters*, vol. 4, no. 23, pp. 4058–4063, 2013.

[214] A. J. Lucio and S. K. Shaw, “Pyridine and pyridinium electrochemistry on polycrystalline gold electrodes and implications for CO_2 reduction,” *The Journal of Physical Chemistry C*, vol. 119, no. 22, pp. 12523–12530, 2015.

[215] E. Lebègue, J. Agullo, and D. Bélanger, “Electrochemical behavior of pyridinium and N-Methyl pyridinium cations in aqueous electrolytes for CO_2 reduction,” *ChemSusChem*, vol. 11, no. 1, pp. 219–228, 2018.

[216] A. Moteabbed, “Surface enhanced infrared absorption spectroscopy of pyridine assisted CO_2 reduction,” master’s thesis, Technische Universität München, Physik-Department, E19a, Nonequilibrium Chemical Physics, 2017.

[217] M. Lessio, T. P. Senftle, and E. A. Carter, “Is the surface playing a role during pyridine-catalyzed CO_2 reduction on p-GaP photoelectrodes?,” *ACS Energy Letters*, vol. 1, no. 2, pp. 464–468, 2016.

[218] H.-P. Yang, S. Qin, H. Wang, and J.-X. Lu, “Organically doped palladium: a highly efficient catalyst for electroreduction of CO_2 to methanol,” *Green Chemistry*, vol. 17, no. 12, pp. 5144–5148, 2015.

[219] H.-P. Yang, Y.-N. Yue, S. Qin, H. Wang, and J.-X. Lu, “Selective electrochemical reduction of CO_2 to different alcohol products by an organically doped alloy catalyst,” *Green Chemistry*, vol. 18, no. 11, pp. 3216–3220, 2016.

[220] H.-P. Yang, S. Qin, Y.-N. Yue, L. Liu, H. Wang, and J.-X. Lu, “Entrapment of a pyridine derivative within a copper–palladium alloy: a bifunctional catalyst for electrochemical reduction of CO_2 to alcohols with excellent selectivity and reusability,” *Catalysis Science & Technology*, vol. 6, no. 17, pp. 6490–6494, 2016.

[221] Y. Fang and J. C. Flake, “Electrochemical reduction of CO_2 at functionalized Au electrodes,” *Journal of the American Chemical Society*, vol. 139, no. 9, pp. 3399–3405, 2017.

[222] S. Ponnurangam, C. M. Yun, and I. V. Chernyshova, “Robust electroreduction of CO_2 at a poly (4-vinylpyridine)-copper electrode,” *ChemElectroChem*, vol. 3, no. 1, pp. 74–82, 2016.

[223] C. Costentin, J. C. Canales, B. Haddou, and J.-M. Savéant, “Electrochemistry of acids on platinum. application to the reduction of carbon dioxide in the presence of pyridinium ion in water,” *Journal of the American Chemical Society*, vol. 135, no. 47, pp. 17671–17674, 2013.

[224] M. Dunwell, Y. Yan, and B. Xu, “In situ infrared spectroscopic investigations of pyridine-mediated CO_2 reduction on Pt electrocatalysts,” *ACS Catalysis*, vol. 7, no. 8, pp. 5410–5419, 2017.

[225] H. Dridi, C. Comminges, C. Morais, J.-C. Meledje, K. B. Kokoh, C. Costentin, and J.-M. Savéant, “Catalysis and inhibition in the electrochemical reduction of CO_2 on platinum in the presence of protonated pyridine. new insights into mechanisms and products,” *Journal of the American Chemical Society*, vol. 139, no. 39, pp. 13922–13928, 2017.

[226] P.-Y. Olu, Q. Li, and K. Krischer, “The true fate of pyridinium in the reportedly pyridinium-catalyzed carbon dioxide electroreduction on platinum,” *in preparation*, 2018.

[227] A. A. Ensafi, H. A. Alinajafi, M. Jafari-Asl, and B. Rezaei, “Self-assembled monolayer of 2-pyridinethiol @ Pt-Au nanoparticles, a new electrocatalyst for reducing of CO_2 to methanol,” *Journal of Electroanalytical Chemistry*, vol. 804, pp. 29–35, 2017.

[228] J. Albo, G. Beobide, P. Castaño, and A. Irabien, “Methanol electrosynthesis from CO_2 at Cu_2O/ZnO prompted by pyridine-based aqueous solutions,” *Journal of CO_2 Utilization*, vol. 18, pp. 164–172, 2017.

[229] C. Kronawitter, Z. Chen, P. Zhao, X. Yang, and B. Koel, “Electrocatalytic hydrogenation of pyridinium enabled by surface proton transfer reactions,” *Catalysis Science & Technology*, vol. 7, no. 4, pp. 831–837, 2017.

[230] T. E. Elton, G. E. Ball, M. Bhadbhade, L. D. Field, and S. B. Colbran, “Evaluation of organic hydride donors as reagents for the reduction of carbon dioxide and metal-bound formates,” *Organometallics*, vol. 37, no. 21, pp. 3972–3982, 2018.

[231] J. H. Lee, S. J. Lauw, and R. D. Webster, “The electrochemical reduction of carbon dioxide (CO_2) to methanol in the presence of pyridoxine (vitamin B6),” *Electrochemistry COmmunications*, vol. 64, pp. 69–73, 2016.

[232] E. E. Barton-Cole, M. F. Baruch, P. Robert, M. T. Kelly, P. S. Lakkaraju, E. L. Zeitler, and A. B. Bocarsly, “Substituent effects in the pyridinium catalyzed reduction of CO_2 to methanol: further mechanistic insights,” *Topics in Catalysis*, vol. 58, no. 1, pp. 15–22, 2015.

Appendix

Origin of plot data

- 3.9, 20180605, 0.5 M KCl, sample from H-terminated silicon electrode
- 4.8: Archiv/lindner/3Amminopyridine nSi/20130703_neu, nSi, Electrolyte: 0.1 M H_2SO_4, 1.8 mM HF, purged in argon (Ar). Scan rate: 50 mV/s.
- 4.9: Archiv/lindner/Bromobenzene pSi/20130514, p-Si, Electrolyte: 0.1 M H_2SO_4 + 1.8 mM HF, purged with Ar. Scan rate: 50 mV/s, 100 mV/s during grafting (violet dashed).
- 4.10 20180208 left: 1 2 right: 3 4 , nSi, Electrolyte: 0.5 M H_2SO_4, purged in Ar. Scan rate: 100 mV/s, left: double graft with 0.4 mM 3apy + $NaNO_2$, right: double graft with 0.2 mM 3apy + $NaNO_2$
- 4.12,4.13: 20140319, nSi, Electrolyte: 0.5 M H_2SO_4, 1.8 mM HF, 1 mM 3-aminopyridine, 1mM $NaNO_2$, purged in Ar. Scan rate: 50 mV/s
- 4.15 20160216, nSi, Electrolyte: 0.5 M H_2SO_4, 1.8 mM HF, 3-diazopyridine tetrafluoridoborate, purged in Ar. Scan rate: 50 mV/s.
- 4.16 20140319, paper [134]
- 4.17 20140319, paper [134]
- 4.19 20140319, paper [134]
- 4.20 XPS/20170313, inset: 20170313, nSi, Electrolyte: 0.5 M H_2SO_4, purged with Ar. Scan rate: 10 mV/s.
- 5.1 20140304, nSi, Electrolyte: 0.5 M H_2SO_4 and 1.8 mM HF, purged with Ar. Scan rate: 100 mV/s
- 5.2 20160216, nSi, Electrolyte: 0.5 M H_2SO_4, purged with Ar. Scan rate: 100 mV/s
- 5.3, left: 20160822, nSi, Electrolyte: 0.5 M H_2SO_4, purged with Ar. Scan rate: 50 mV/s ; right: 20150825, nSi, Electrolyte: 0.5 M H_2SO_4, purged with Ar. Scan rate: 100 mV/s.
- 5.4, Archiv/lindner/130710/Probe 1, nSi, Electrolyte: 0.5 M H_2SO_4, purged with Ar. Scan rate: 50 mV/s

- 5.5, 20140304, nSi, Electrolyte: 0.5 M H_2SO_4, purged with Ar. Scan rate: 50 mV/s
- 5.6, 20140425, nSi, Electrolyte: 0.1 M H_2SO_4, purged with Ar. Scan rate: 100 mV/s.
- 5.7, 20180622, sample from 20180420, nSi, Electrolyte: 0.5 M H_2SO_4, purged with Ar. Scan rate: 50 mV/s
- 5.8, 20180520, nSi, acidic electrolyte (0.5 M H_2SO_4, purged with Ar, dashed lines) and neutral electrolyte (0.5 M K_2SO_4, $pH > 6$, purged with Ar, solid lines). Scan rate: 50 mV/s
- 6.1, 20170607, nSi, Electrolyte: 0.1 M H_2SO_4, purged with Ar. Scan rate: 10 mV/s
- 6.3, 20170320, nSi, Electrolyte: 0.1 M H_2SO_4, purged with Ar.
- 6.4, 20180520, nSi, Electrolyte: 0.5 M K_2SO_4; pH: 5.31 (H-termination) and 5.81 (3-pyridine-termination); purged with Ar.
- 6.5, 20180409, nSi, Electrolyte: 0.5 M H_2SO_4, purged with Ar. Scan rate: 50 mV/s
- 6.6, 20170607, nSi, Electrolyte: 0.1 M H_2SO_4, purged with Ar.
- 6.7, 20180520, nSi, Electrolyte: 0.5 M K_2SO_4, purged with Ar, pH 5.31 (H-term.), pH 5.81 (3py-term.)
- 6.3, values from 20170407
- 7.1,7.2,7.3, 20180622, nSi, Electrolyte: 0.5 M HCl, purged with Ar or CO_2. Scan rate: 50 mV/s.
- 7.4,7.5,7.6,7.7, nSi, H-term. 20180430, 3py-term. 20180504, Electrolyte: 0.5 M KCl, purged with CO_2. pH before electrolysis: 4.97 (H-terminated, red), 5.07 (3-pyridine-terminated, blue)
- 7.9, nSi, 20180609, 3py sample from 20180607, Electrolyte: 0.5 M KCl, purged with CO_2. pH before electrolysis: 4.99 (H-terminated, red), 4.8 (3-pyridine-terminated, blue).
- 6.19 thesis/pyridin_ cap4_ ctot.txt ; export from Mathematica work book thesis/pyridin_ cap4.nb

Acknowledgements

First and foremost, I would like to thank Professor Dr Katharina Krischer for the opportunity to write my PhD thesis on such an interesting topic under her great supervision and guidance. During my eight years at the Non-equilibrium Chemical Physics group, starting as a work student, and throughout my diploma and, finally, PhD thesis, she guided me through every step with her unrivalled enthusiasm and curiosity for all the minutiae while not losing sight of the bigger picture. Her expertise, enthusiasm and, simply, care created an awesome scientific and working environment where I was glad to be a part of. I would also like to thank PD Dr Werner Schindler, who lent me his expertise, attention to details and insights to push my experiments to reach a new and more consistent level. I would like to thank Dr Konrad Schönleber for mentoring me during my diploma thesis and also leading me towards the topics of my eventual PhD thesis, and Dr Pierre-Yves Olu for the fruitful discussions and our subsequent collaboration on the resulting publication. Likewise, I would like to thank Markus Haß and Siegfried Schreier for your expertise (and patience) for the building/realization of my experimental setups, as well as Munir Salman for our collaboration on the simulation of the grafted interface and for being a great office mate during the writing of the thesis.

To the entire Non-equilibrium Chemical Physics group, I would like to thank you all for the great working environment and for being my home away from home for these last eight years. Special thanks to Simon Filser, with whom I walked most of the way during the PhD thesis together (attending conferences, sharing lab benches and office desks, etc.), for his camaraderie and support along the way.

I would like thank Ignaz Höhlein, Tobias Helbig, Marc Julian Kloberg and Professor Dr. Bernhard Rieger (WACKER Chair of Macromolecular Chemistry, Chemistry Department, Technical University Munich) for our collaboration on the in situ generation and, later, synthesis of diazopyridine, which was a necessary precondition for the grafting process described in this thesis. For my introduction into the field of XPS and a major part of the XPS measurements of the grafted silicon samples, I would like to thank Patrick Zeller and Professor Dr. Joost Wintterlin (AK Wintterlin, Chemistry Department, Ludwig-Maximilian-Universität München). For my introduction into the field of NMR and our discussions concerning the interpretation of our NMR spectra, I would like to thank Professor Dr. Wolfgang Eisenreich (Chair of Biochemistry, Chemistry Department, Technical University Munich).

Finally, I would like to thank my parents, for everything.